A HIGH TIME RESOLUTION STUDY OF THE RADIO EMISSION FROM PULSARS

A THESIS SUBMITTED TO AUCKLAND UNIVERSITY OF TECHNOLOGY
IN PARTIAL FULFILMENT OF THE REQUIREMENTS FOR THE DEGREE OF
DOCTOR OF PHILOSOPHY

Supervisor
A. Prof. W. van Straten
Dr. C. Tiburzi
Prof. T. S. Gulyaev

31.03.2023

By
Nat Primak
School of Engineering, Computer and Mathematical Sciences

Abstract

This thesis reports on the foundation, establishment, development, and initial outcomes of the large-scale pulsar radio emission statistics survey (PRESS), which was initiated and carried out during this PhD project. The research started by developing and testing novel methods of analysing single-pulse polarisation fluctuation, based on the theory developed by van Straten (2009) and van Straten and Tiburzi (2017). For this pioneering effort, we used an existing set of single-pulse polarisation observations recorded at the Arecibo radio telescope (Hankins & Rankin, 2010). By analysing the covariances between the Stokes parameters in these archival data, we discovered several rare polarisation phenomena.

In particular, the Arecibo data included a highly sensitive observation of the first-discovered pulsar, PSR B1919+21 (also known as PSR J1921+2153), which allowed us to perform a direct comparison between our statistical approach and more traditional methods of analysis. For example, principal component analysis of the matrix of covariances between the Stokes parameters led to the discovery of an unexpected oblate spheroidal distribution of the polarisation vector. This was confirmed using a scatter plot in the Poincaré sphere, which revealed a toroidal distribution of polarisation vectors centered near the origin of the Poincaré sphere. Further temporal and spectral analysis of the polarization fluctuations led us to discover that the polarisation vectors cycle around the toroidal axis of revolution synchronously with the drifting sub-pulse modulation of the total intensity, an effect that has been observed in only one other study (Edwards, 2004).

Prior to launching the observation campaign for PRESS, we experimentally verified a novel equation that describes sensitivity to the variance of modulated radio emission using single pulse observations of PSR J0437-4715 (Osłowski et al., 2014). After a brief description of the observing campaign that was carried out using Murriyang, the 64-m Parkes radio telescope, we present an overview of the current state of the PRESS data processing pipeline, including encountered challenges and solutions implemented

during pipeline development. This part of the thesis primarily describes our efforts to validate the quality of the outputs produced by the data processing pipeline and the challenges presented by Radio Frequency Interference.

Finally, we report on the preliminary results of a single-pulse statistical analysis of PRESS observations of PSR J1921+2153. The techniques, tools, and data presented in this thesis create new opportunities for future single pulse studies of radio pulsar emission.

Contents

List of Tables

List of Figures

Attestation of Authorship

I hereby declare that this submission is my own work and that, to the best of my knowledge and belief, it contains no material previously published or written by another person nor material which to a substantial extent has been accepted for the qualification of any other degree or diploma of a university or other institution of higher learning.

My contributions to the research described in Chapter 3 and Chapter 4 are the following.

For Chapter 3, I applied the principal component analysis to all pulsars of the freely available Arecibo data set P1260 and generated 3D plots with 2D projections of polarisation vectors distributions; thoroughly examined outcomes and selected interesting cases for further studies; found toroidal distributions of polarisation vectors in 3D plots for pulsar PSR B1919+21; examined and proved the validity of the findings; applied longitude-offset cross-correlations for each Stokes parameter (for various reference longitudes) and longitude-resolved cross-correlations for Stokes Q, U, V to study temporal and spatial behaviours of the polarisation vectors; contributed to discussions of the observed phenomena.

For Chapter 4, I contributed to the discussions that led to establishing the PRESS project; during the planning stage, I verified the radiometer equation for the sample mean variance (which was derived by A.Prof. Willem van Straten) using observational data; contributed to discussions of the strategies of the PRESS survey and source selection; managed the observing campaign by scheduling pulsar observations, looking after the source completion, and managing the observing rosters; processed all observed pulsars and found issues that led to further development of the data processing pipeline; tested all pipeline changes and developments with selected pulsars, found and reported issues, and when issues were resolved, I did quality verification of the processing step; after each improvement of the automatic RFI mitigation algorithm, I repeated the manual cleanup for each frequency sub-band and verified data quality; finally, I obtained preliminary results for pulsar PSR B1919+21 and compared the PRESS results with our predictions and the Arecibo data.

Signature of candidate

Publications

Primak, N., Tiburzi, C., van Straten, W., Dyks, J. & Gulyaev, S., (2022), A&A, 657, A34, *"The polarisation of the drifting sub-pulses from PSR B1919+21"*

Acknowledgements

The work presented in this thesis would not have been possible without my supervisors. First and foremost I would like to express my deepest gratitude to my supervisor and mentor Dr Willem van Straten, Associate Professor for the Institute of Astronomy and Space Research at Auckland University of Technology (AUT). Words cannot express how grateful I am for all the time and patience in answering my numerous questions, explaining concepts, and discussing research issues. I am deeply grateful for all the valuable feedback on my written texts and for understanding my natural struggle with the written word. Willem's enthusiasm for pulsars is contagious, and his mastery of coding is inspiring. I am forever grateful for the possibility to learn from him.

I would like to thank and express my deepest appreciation to Dr Caterina Tiburzi for being my co-supervisor and mentor. This person is a "Perpetual mobile engine" in a human form: Caterina's never-ending bursting energy and enthusiasm make things happen (even if previously everyone believed that they were impossible) and speed-up work and all the processes we were dealing with. I thank Caterina for all the help and guidance throughout my PhD.

I would also like to thank Professor Sergei Gulyaev who has taken the role of my mentor AUT supervisor. I am very grateful for all his helpful advice throughout the duration of my PhD and help in resolving my problems, big and small.

Special thanks to Patricia Sallis, administrator of the Institute of Astronomy and Space Research, for dealing with all matters of bureaucracy throughout my PhD time, for all the encouragement, positive attitude to all matters, and support.

Many thanks to Dr Barry Dowdeswell, my friend and coffee-buddy, for reading my thesis and for extremely valuable encouragement in my difficult times.

I would like to use the opportunity to express my gratitude to the PRESS observing team: Willem van Straten, Caterina Tiburzi, Ramesh Bhat, Vivek Venkatraman Krishnan, Golam Shaifullah, Fabian Jankowski, Lucy Oswald, and Aditya Parthasarathy. Together with conducting observations of pulsars for the PRESS project our incredible team members successfully tackled various challenges and issues, contributed with valuable advice, and generated ideas that improved the observing campaign. From all my heart - a big thank you, team.

I also like to express my gratitude to the ATNF support of the PRESS observations. Especially I would like to thank Stacy Mader for his incredible UWL software support and troubleshooting of software and technical failures during observing sessions in an efficient and fast way. I would like to thank Jimi Green for allocating us some extra observing time (so-called "Green time"); George Hobbs and John Sarkissian for help and support with UWL and the Parkes telescope respectively.

Chapter 1

Introduction

1.1 Pulsar generalities

Pulsars were first discovered at radio frequencies by Jocelyn Bell (Hewish et al., 1968) who was studying the interplanetary scintillation[1] of quasars with her supervisor, Anthony Hewish, and for that purpose the team constructed a radio telescope at the Mullard Radio Astronomy Observatory, in Cambridge, United Kingdom. Pulsars are rapidly-rotating neutron stars with high magnetic field strengths (of the order of 10^{12} – 10^{15} Gauss), spinning around their rotational axes with angular velocities from Hertz to kiloHertz, and emitting beams of radiation that are detectable across the electromagnetic spectrum, from radio to γ-rays. Neutron stars are compact objects, with radii of about 10 kilometers, masses ranging from 1.5 to 2 Solar masses ($M_{\odot}$; e.g., Bombaci, 1996), and extreme inner densities that are inferred to be of the order of 4×10^{17} kg/m^3 (e.g., Bombaci, 1996).

The existence of neutron stars was theoretically predicted long before the discovery of the "Rapidly Pulsating Radio Sources"[2] (Hewish et al., 1968). Baade and Zwicky

---

[1] Scintillation is discussed in Section 1.2.3.

[2] Initially pulsars were named "Little Green Men", in association with possible alien signals, but later these sources were identified as neutron stars and renamed

(1934) proposed that some massive stars (8 - 15 $M_{\odot}$) at the end of their evolution undergo a core-collapse Supernova event and turn into neutron stars. Following the rapid collapse of the massive core the densities inside neutron stars were supposed to be up to 10^{17} kg/m^3 and magnetic fields up to 10^{15} G, as predicted by Oppenheimer and Volkoff (1939) using a simple equation of state. At that time it was thought that neutron stars could not be observed because of their tiny sizes and absence of effective emission mechanism.

Only a few months after pulsars were discovered (Hewish et al., 1968), these sources were linked to neutron stars (Pilkington et al., 1968). After this connection, the detected radio pulses were explained as beamed radiation that comes approximately from the region above the magnetic poles, and sweeps through our line of sight. The magnetic axis is misaligned with respect to the rotational axis, thus we observe the radiation beam in a manner similar to the light from a lighthouse (as shown on Fig. 1.1).

Soon after the discovery of the first pulsar, named B1919+21 (from its B1950 equatorial coordinates), two other young pulsars were found in the Vela and Crab Supernova Remnants (SNR), which supported the Supernova origin of such objects.

1.1.0.1 Neutron star origins

The supernova phenomenon was known and studied for a long time before the discovery of pulsars. There are several types of Supernovae - Ia, Ib, Ic, and II, which are observationally distinguished by specifics of their spectra and light curves (which depend on the initial mass of the exploding star, or ”progenitor star“, e.g., Woosley, 1987; Woosley & Weaver, 1992). Supernovae type-Ia (SN-Ia) happen within a binary system where one of the two stars is a White Dwarf that accretes mass from its main-sequence companion until it reaches a Chandrasehkar limit[3], i.e., a ”critical mass“, when electron degeneracy pressure fails to prevent the White Dwarf collapse. Supernovae

---

[3] Which is the mass limit for the stable White Dwarf star, and is about 1.4 M$_{\odot}$ (e.g., Clayton, 1983).

type-II (SN-II) are associated with single massive stars; when the energy supplied by nuclear fusion no longer supports the core against gravitational pressure, the core collapses within seconds, releasing an enormous amount of energy (e.g., Woosley & Weaver, 1992). During the collapse, the core temperature increases rapidly, causing the release of high-energy gamma-rays that disintegrate iron nuclei into free neutrons and helium nuclei. That, in turn, launches the conditions under which inverse beta-decay ($p^+ + e^- \rightarrow n + \nu_e$) occurs, i.e., when protons and electrons merge together into neutrons, emitting a neutrino that carries away a large amount of energy with it. This leads to further collapse, which ends with a massive SN-II explosion after the rebound of the collapsing matter that produces an outward shock-wave. Conservation of angular momentum during collapse increases the rotation rate, driving neutron star rotation periods into ranges of seconds or even milliseconds.

Only SN-II can create neutron stars (e.g., Woosley & Weaver, 1986). Neutron stars are created from stars with initial masses in general of about 8 - 15 $M_{\odot}$, while progenitor stars with smaller mass create white dwarf. When the initial stellar mass is more than 15 $M_{\odot}$, the final product of the SN-II event is a black hole[4], or its core might even disintegrate. Neutron star progenitors have core masses ranging between $1.9 M_{\odot}$ to 2.5 $M_{\odot}$ (e.g., Woosley & Weaver, 1986; Ergma & van den Heuvel, 1998).

During the collapse the magnetic flux of the star is conserved and the initial magnetic field strength increases by a factor by which the cross-sectional area falls. Thus, after the collapse, young neutron stars should have very strong dipolar magnetic fields (e.g., Wheaton et al., 1979). After the SN-II explosion the outer shell of the parent star is blasted away forming a SNR.

Currently about 300 SNRs are known. They are found in various electromagnetic wave-ranges and catalogued by various surveys, such as: "A Catalogue of Galactic

---

[4] Or a rapidly-spinning neutron star that later will collapse into a BH, (e.g., Vietri & Stella, 1998; Baiotti et al., 2005).

Supernova Remnants" [5] (Green, 2017), the MOST Supernova Remnant Catalogue (MSC)[6], or "Chandra Supernova Remnant Catalog" [7]. A lot of young pulsars are found either inside the SNR or nearby, and by extrapolating their proper motion back to the inferred age of the supernova, it is possible to show that initially it was inside the SNR.

1.1.1 General properties of pulsars

Figure 1.1 presents a schematic diagram of a pulsar. It shows a neutron star with its magnetic field lines, which spins with angular velocity Ω. Pulsar magnetic and rotational axes are generally misaligned by a certain angle, which causes pulsar emission to be observed as pulses. The radio emission is beamed along the magnetic axis. The cylindrical surface that surrounds closed magnetic field lines is called the "light cylinder": at distances greater than $\sim c/\Omega$, co-rotation would force the magnetospheric plasma to move at a velocity higher than the light speed, which is not possible.

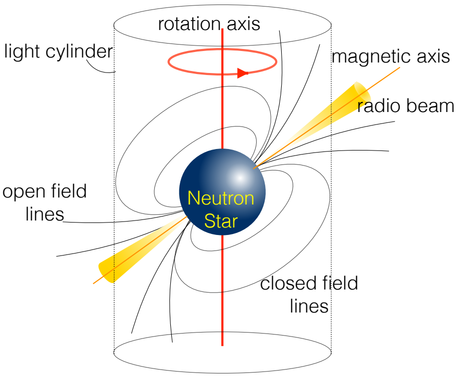

Figure 1.1: Schematic diagram of a simplified pulsar model. Here a thin orange diagonal line depicts the magnetic axis; the thick red vertical axis shows the rotational axes of the pulsar. When the beam of radio emission (yellow cones aligned with magnetic axis) crosses the line of sight of the observer, the radio telescope registers a pulse. It is analogous to the flash of light that we see when the beam from a lighthouse crosses our line of sight.

Since the earliest pulsar observations, it was noticed their radio emission is highly

---

[5] https://www.mrao.cam.ac.uk/surveys/snrs/

[6] http://www.physics.usyd.edu.au/sifa/Main/MSC

[7] https://hea-www.cfa.harvard.edu/ChandraSNR/

polarized, especially in terms of linear polarization (e.g., Stinebring et al., 1984). For some pulsars the polarization angle (PA) shows an S-shaped swing across the pulse profile, as depicted in Figure 1.2 panel A. Radhakrishnan and Cooke (1969) and Lyne et al. (1971) explained such phenomenon through the Rotating Vector Model (RVM). In this model the orientation of the magnetic field lines within the radiation beam defines the PA. When the pulsar rotates, the line of sight crosses the magnetic field lines which results in a change of the PA orientation (see Figure 1.2, panel B). The longitude- (or phase-) resolved PA curve then can be described as:

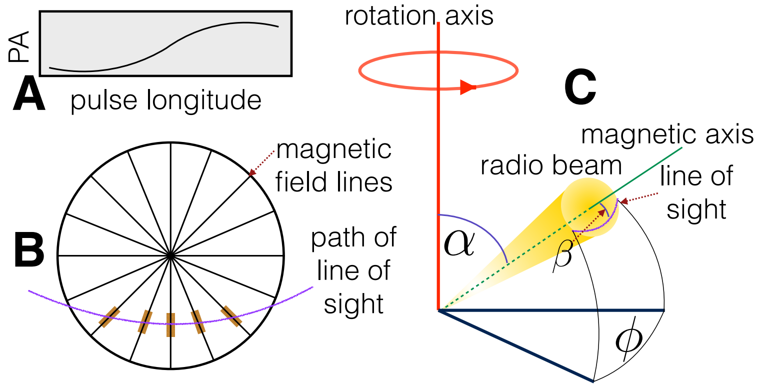

Figure 1.2: Schematic diagram of the simplified RVM model. Panel A schematically depicts S-shaped PA distribution across the pulse longitude. Panel B represents view to the emission beam above the magnetic pole. The black lines are magnetic field line and they intersect in the center which is magnetic field axes. The purple line is the line of sight, and the orange blocks correspond to the polarisation orientation. Panel C shows a geometry of the pulsar emission beam, where rotation axis shown with red, magnetic axis shown with green lines, and the angle between them is α. The line of sight is shown with purple line and β is the angle between it and the magnetic axes. Longitude ϕ belongs to the pulse window.

$$\Psi = \frac{\sin\alpha \sin(\phi - \phi_0)}{\sin(\alpha+\beta)\cos\alpha - \cos(\alpha+\beta)\sin\alpha\cos(\phi-\phi_0)} \tag{1.1}$$

Here Ψ is the position angle at pulse longitude ϕ_0. The pulse longitude ϕ, angle between magnetic and rotational axis α, and impact parameter, i.e., minimum angle between the line of sight and the magnetic axis β are shown in Figure 1.2 panel C. However, this simplified model does not explain all observed diversity of the pulsar polarisation phenomena.

1.1.1.1 The spin evolution of pulsars

Generally, pulsars are considered to be solid spheres rotating with a certain period P. From their births and for the next few million years pulsars emit their own rotational kinetic energy as magnetic dipole radiation. This process produces an observable spin-down rate $\dot{P}$. Both P and $\dot{P}$ can be measured with high precision through the 'pulsar timing' technique.

The spin evolution of the neutron star population is typically examined by plotting their period vs spin-down rate in a P – $\dot{P}$ diagram, as shown in Figure 1.3. From the diagram, it is clear that a distinction exists between "normal" or "slow pulsars" (those with $P \sim 0.5$ s and $\dot{P} \sim 10^{-15}$ s s^{-1}) and the "millisecond pulsars" ($P \lesssim 10$ ms and $\dot{P} \sim 10^{-20}$ s^{-1}). For those two populations the differences in spin-period and spin-down rate imply different formation scenarios and evolutionary histories, as well as different magnetic field strengths.

Some authors examined pulsar evolution with time in the P – $\dot{P}$ diagram (e.g., Ridley & Lorimer, 2010, Gullón et al., 2014), however, the exact pulsar evolution is still a debated topic. Generally speaking, a probable evolutionary path for a "normal pulsar" would be:

- Birth with short spin-periods and high spin-down rate. On the P – $\dot{P}$ diagram such pulsars are in the upper-left corner.
- A rapid spin-down into the "population of normal pulsars" on a time scale of 10^5 – 10^6 yr.
- After about 10^7 yr the spin of the pulsar has slowed down to the point radio waves cannot be emitted anymore and, thus, the pulsar becomes too faint to be detected in radio frequencies and it is considered extinct.

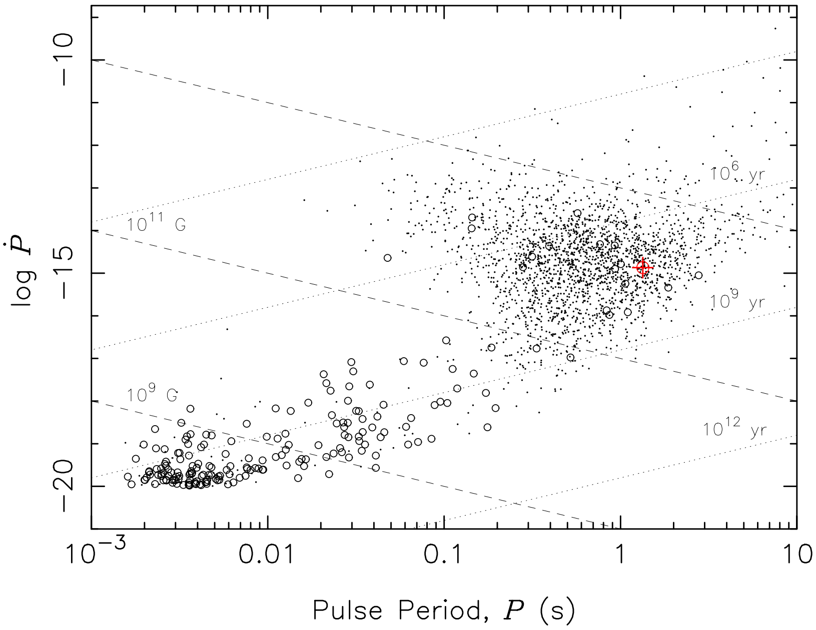

Figure 1.3: $P - \dot{P}$ diagram for the pulsar population known by the end of 2022. General pulsar population is shown by dots. Pulsars that are known to be a part of binary system are represented by open circles. The dashed lines (that go from left to right downwards) represent magnetic field strengths, the dotted lines (that go from left to right upwards) represent constant ages. The red cross-hair points to the PSR B1919+21. This diagram is generated with the *PSRCHIVE* software (van Straten et al., 2012), and the data for the $P - \dot{P}$ diagram is taken from the ATNF Pulsar Catalogue (Manchester et al., 2005).

In some circumstances, a neutron star can be newly spun-up, becoming a so-called "recycled" pulsar. This happens when a pulsar has a companion star (the first pulsar in a binary system was discovered by Hulse & Taylor, 1975). Depending on the characteristics of the binary system, the companion star can overflow its Roche lobe[8], transferring matter and angular momentum to its neutron star companion (spin-up by accretion was described, for example, by Davidson & Ostriker, 1973). This process shifts the pulsar to the lower-left corner of the $P - \dot{P}$ diagram.

---

[8] Roche lobe is a region in a binary stars system, in which the orbiting material around a star is gravitationally bound to that star. The region has a rain-drop shape with the apex of the raindrop pointing towards the other star. After a star's surface extends beyond its Roche lobe, the material and the angular momentum can transfer into the other object's Roche lobe via the first Lagrangian point.

1.1.1.2 Characteristic age

As mentioned, pulse periods are observed to increase with time; i.e., $\dot{P} = \frac{dP}{dt} > 0$, owing to magnetic dipole radiation, (e.g., Jackson, 1962, Lorimer & Kramer, 2012). A magnetic dipole with a magnetic dipole moment m, rotating with *angular velocity* $\Omega = 2\pi P^{-1}$ about an axis misaligned with the dipole, emits electromagnetic radiation (magnetic dipole radiation) at its rotational frequency.

The total power of magnetic dipole radiation is

$$\dot{E}_{dip} = \frac{2}{3} m^2 \Omega^4 c^{-3} \sin^2 \alpha, \tag{1.2}$$

where α is the angle between the magnetic dipole moment and the spin axis (Lorimer & Kramer, 2012).

The radiated energy E dominates the loss of angular (rotational) kinetic energy of the rotating body: $E_{rot} = \frac{1}{2} I \Omega^2$. The rate at which kinetic energy is lost (its *spin-down luminosity*) is

$$\dot{E} = \frac{dE_{rot}}{dt} = \frac{1}{2} \frac{dI\Omega^2}{dt} = I\Omega\dot{\Omega} = 4\pi^2 I \dot{P} P^{-3} \tag{1.3}$$

where $I = kMR^2$ - is the moment of inertia, R is the radius of the neutron star, and k is an inertial constant that depends on the shape and composition of the body (e.g., $k = \frac{2}{5}$ for a sphere of uniform density).

The spin-down and rotational energy loss evolution can be parameterized assuming:

$$\dot{P} = KP^{2-n}, \tag{1.4}$$

where n is the breaking index ($n = 3$ for dipole). Integrating Equation 1.4 yields the age of pulsar

$$T = \frac{P}{(n-1)\dot{P}} \Big[1 - \Big(\frac{P_0}{P} \Big)^{n-1} \Big] \tag{1.5}$$

Here P_0 is the spin period of the pulsar at its birth. Assuming that $P_0 \ll P$, and that the spin down happens only due to the dipole radiation, we can simplify Equation 1.5, and derive the *characteristic age*:

$$\tau = \frac{P}{2\dot{P}} \tag{1.6}$$

1.1.1.3 Inferred surface magnetic field

As discussed above, the main reason for a pulsar's loss of rotational energy is magnetic dipole radiation. Thus, the surface magnetic field plays significant role in the observed properties and characteristics of a pulsar.

It is not possible to directly measure the magnetic field strength of a pulsar given only observations at radio frequencies. However, cyclotron resonance[9] in the very thin hydrogen atmosphere of a neutron star creates absorption lines in X-ray spectra, enabling direct measurements of the surface magnetic field (e.g., Trümper et al., 1978, Wheaton et al., 1979). Cyclotron resonances that can be observed in the 0.1 - 1 keV band are caused by magnetic fields of $10^{10} - 10^{14}$ G. In observations of the magnetar SGR J1806-20 by Ibrahim et al. (2002), a cyclotron resonance feature was discovered with a narrow 5-keV absorption line, which was interpreted as a proton-cyclotron resonance due to a 10^{15} G magnetic field.

Radio observations of pulsars can be used to *infer* the surface magnetic field strength if we assume that the spin down is primarily due to dipole braking. In this way, we can derive the surface magnetic field strength from the evolution of the rate of energy loss (Equation 1.2). For that we need to relate the magnetic dipole moment $\mathbf{m}$ and the magnetic field strength: $\mathbf{B} \approx \frac{\mathbf{m}}{R^3}$ (with R being the pulsar radius, e.g. Lorimer & Kramer, 2012). We get the *characteristic magnetic field* at the pulsar surface:

---

[9] Cyclotron resonance describes the interaction of charged particles with external forces in the magnetic field of the neutron star. This phenomenon can be used as a probe of the magnetic field.

$$\mathbf{B_{sur}} = \sqrt{\frac{3c^3}{8\pi^2}\frac{I}{R^6 \sin^2\alpha}P\dot{P}} \tag{1.7}$$

This equation is a first-order approximation of the surface magnetic field strength, because α usually is unknown, the radius and the moment of inertia of the neutron star are usually uncertain, and other processes are contributing to the pulsar's spin-down at various degrees. Some authors, for example Shapiro and Teukolsky (1983) and Usov and Melrose (1995) suggest that B_{sur} is actually the magnetic field at the magnetic equator, but at the magnetic poles the field strength should be a factor of two higher.

1.2 Pulsar emission properties

1.2.1 Spectra of pulsars

An important aspect of pulsar emission is that the radiation intensity changes with frequency. Measuring peak flux density[10], or the mean flux density[11], as a function of observing frequency yields pulsar spectral energy distributions (SED) or *flux spectra*. Studies of radio spectra can be used to reveal important physical properties of individual pulsars. For example, the turn-off frequency allows to estimate properties of pulsar's magnetosphere (Petrova, 2002). Studies of radio spectra can also be used to reveal the group properties of pulsars in the Galaxy. For example, we can derive the luminosity function and, from that, information on the birth rate of the population of neutron stars in our Galaxy (e.g., Cordes & Chernoff, 1998). Spectra can also be used to differentiate between various models for the pulsar emission mechanism and/or physics related to geometry and environment (e.g., Maron et al., 2000, Kijak & Maron, 2004, Kijak et al., 2007, Jankowski et al., 2018).

---

[10] The peak flux density is the maximum flux density of the average pulse profile

[11] The mean flux density is the integrated flux density of the pulse profile averaged over the pulse period

Sieber (1973) first studied the SEDs of 27 pulsars and found that the spectra are steep and well approximated by a power-law:

$$S_\nu \propto \nu^A, \tag{1.8}$$

where S_ν is the flux density at frequency ν and A is a spectral index.

After that more studies of pulsar spectra followed and confirmed the steep power-law for pulsars spectra. Lorimer et al. (1995) studied SEDs of 280 pulsars based on flux densities of five observing frequencies between 0.4 and 1.6 GHz. Their average spectral index was $A = -1.6 \pm 0.3$. Jankowski et al. (2018) confirmed that spectral index by studying 441 pulsars.

Maron et al. (2000) extended the frequency range up to 5 GHz, and obtained a mean value of $A = -1.8 \pm 0.2$. They found that about 10% of the pulsars in the sample were best fit by a "broken" power-law, with two different spectral indexes (A_1 and A_2) for lower and higher frequencies respectively. Typically $\mid A_2 \mid > \mid A_1 \mid$ with the spectral break happening at an observing frequency ~ 1 GHz.

A new kind of pulsar was discovered thanks to spectral studies, i.e., pulsars whose spectral peak happens at about 1 GHz (e.g., Kijak & Maron, 2004, Kijak et al., 2007, Jankowski et al., 2018). The nature of such "Gigahertz-Peaked Spectra" (GPS) pulsars is still unclear, and it is not known if the spectrum is intrinsic to the pulsar, or to the circumstellar environment (e.g., Maron et al., 2000).

1.2.2 Morphology of the pulsar signals

During pulsar observations any radio telescope receives a sequence of pulses spaced by a certain time interval. Figure 1.4 shows a series of pulses from pulsar PSR B0301+19 observed at the Arecibo radio telescope. Although the rotational period of each pulsar is stable, the amplitude and shape of each single pulse usually vary significantly.

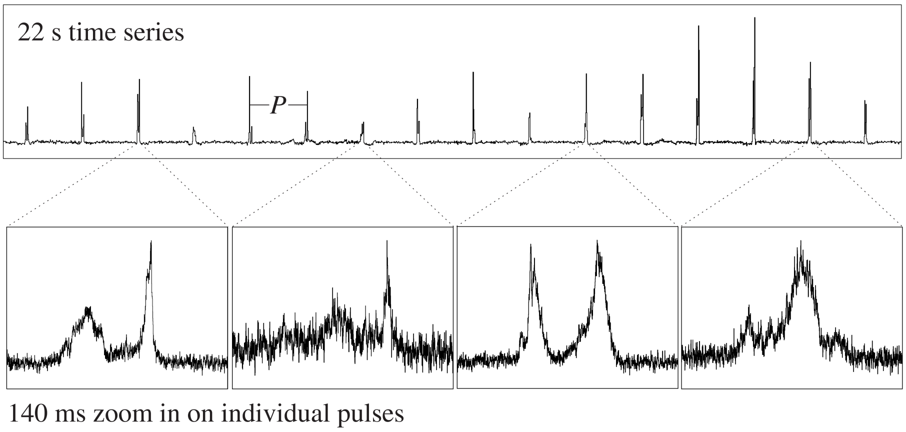

Figure 1.4: Pulsar time series observed during 22 s. Single-pulse data taken at Arecibo for PSR B0301+19. The horizontal axis is time (both in the main figure and the inserts). The vertical axis is power. Image is taken from Lorimer and Kramer (2012).

In single-pulse studies, when the pulse period is known and the pulsar is sufficiently bright, pulse sequences are depicted in a more compact and informative way by stacking pulses on top of each other as it is shown in Figure 1.5, left panel. When a large number of single pulses are added together, a stable pulse profile is obtained (Figure 1.5, right panel). For most pulsars, this *averaged profile* is a unique characteristic of that certain pulsar at a particular frequency. The stability of pulsar averaged profiles has been thoroughly investigated for large samples of pulsars (e.g., Helfand et al., 1975, Kaspi & Wolszczan, 1993).

There is also an observed evolution of averaged profile shapes as a function of observing frequency. For example, the pulse width (or duty cycle) of normal pulsars predominantly increases towards lower observing frequencies. It has been proposed that this effect is due to the fact that the emission that we observe at higher frequencies is produced much closer to the neutron star than the emission at lower frequencies

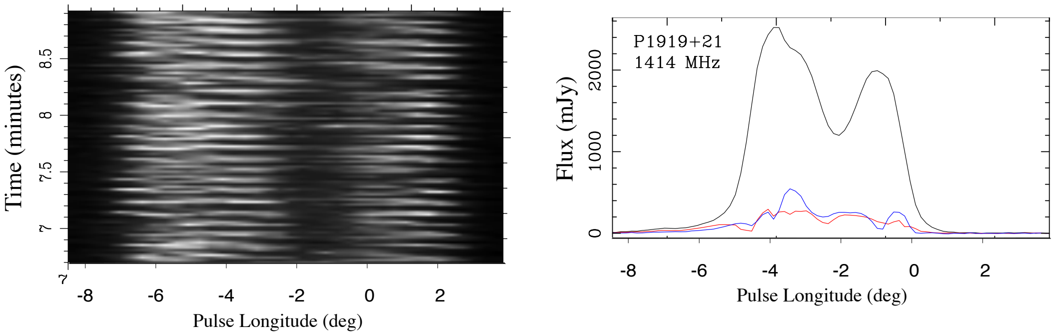

Figure 1.5: Pulse stack and averaged pulse profile in total intensity for the pulsar PSR B1919+21. Left panel depicts pulse stack in the 2-D depiction where grey-scale denotes intensity (white is the highest value); right panel depicts averaged pulse profile, where black is a total intensity, red is linear polarisation, and blue is circular polarisation.

Komesaroff (1970). Later, that explanation laid the basis of the *radius-to-frequency mapping* model (Cordes, 1978).

1.2.3 Interstellar medium effects

As the radio signal from a pulsar travels toward Earth, it propagates through the interstellar medium (ISM), which is composed of gas in ionic, atomic, and molecular form, as well as a magnetic field, dust and cosmic rays. The free electrons in the ISM cause effects such as dispersion, interstellar scattering, scintillation, and Faraday rotation.

1.2.3.1 Dispersion

When electromagnetic waves pass through any medium (material) rather than a vacuum, they experience dispersion. When we observe pulsars over a certain (broad) bandwidth, we receive seemingly broadened pulses. However, if we display the intensity as a function of observing frequency, the pulsar signal appears to "sweep" (see Figure 1.6). This happens because the radio signal has a frequency dependent time delay[12] when

---

[12] i.e., radiation of the higher frequency arrives earlier than the lower frequencies

it propagates through the ISM due to the fact that, in any material (e.g., plasma or glass), the refractive index depends on the radio frequency. This phenomenon is called *dispersion*.

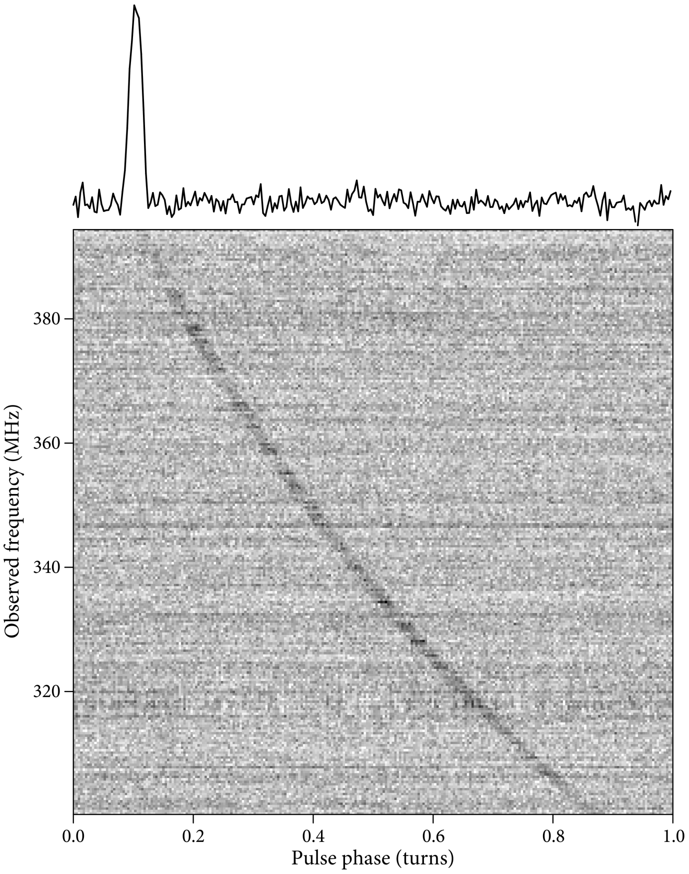

Figure 1.6: Example of dispersion for PSR J1800+5034 from Lorimer and Kramer (2012). Upper panel shows the de-dispersed band-integrated pulse profile. The bottom panel shows the uncorrected dispersive delay as a function of frequency.

The delay in time of arrival of the pulsar signal can be expressed as (e.g., Lorimer & Kramer, 2012)

$$\Delta t = \frac{\mathrm{DM}}{k\nu^2}, \tag{1.9}$$

where ν is observing frequency, $k \simeq 2.41 \times 10^{-4}\ \mathrm{cm^{-3}\ pc\ MHz^{-2}\ s^{-1}}$ is the dispersion constant[13], and DM parameter is the *Dispersion Measure*. The DM relates the frequency of the emission to the extra amount of time (comparing to electromagnetic wave traveling in vacuum) required to reach the observer due to dispersion, and is a column density of free electrons.

$$\mathrm{DM} = \int_0^L n_e dl \tag{1.10}$$

where L is the distance to the pulsar and n_e is the number density of electrons. The DM is expressed in $\mathrm{pc/cm^3}$ and is one of the tools for determining the distance to a pulsar when combined with a model of the Galaxy's free electron density (e.g., Yao et al., 2017).

1.2.3.2 Interstellar Scattering and Scintillation

The ionized ISM affects signals from pulsars in other ways as well. The inhomogeneous and turbulent ISM causes multipath propagation of a signal, such that some rays are delayed in time relative to those traveling more direct paths. Interference between delayed signals causes long-timescale and/or short-timescale *scintillation*, i.e., time- and frequency-dependent flux density variations of the signal from a pulsar analogous to the "twinkling" of stars caused by the turbulent terrestrial atmosphere. Moreover, multipath propagation causes a strongly frequency-dependent ($\propto \nu^{A_{iss}}$) exponential-like scattering tail of the pulse (e.g., Scheuer, 1968), as it is shown in Figure 1.7 from Pennucci et al. (2015).

---

[13] Here a more commonly quoted quantity is given, e.g., Kulkarni (2020)

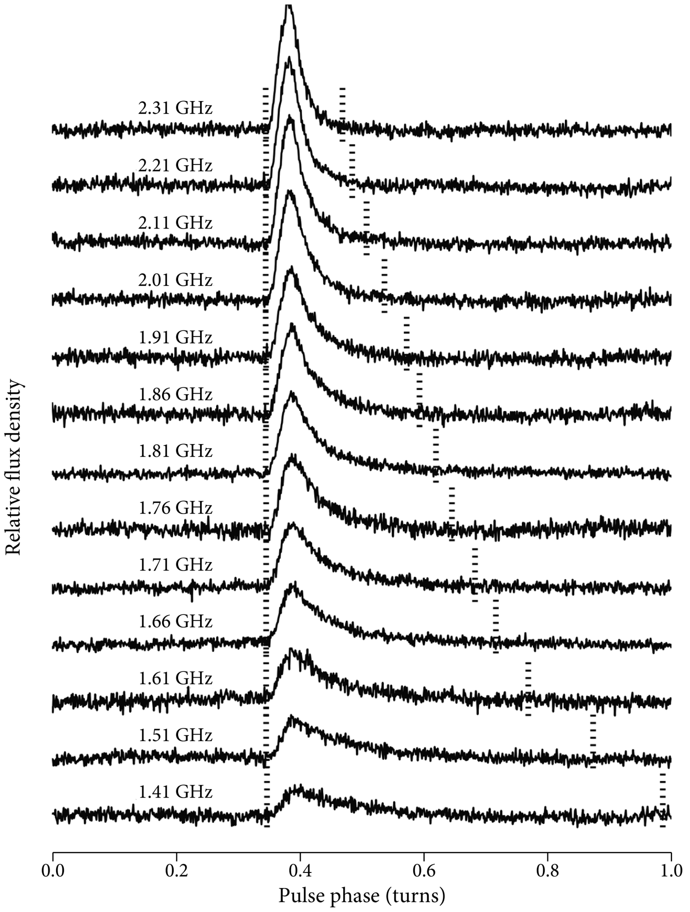

Figure 1.7: Example of the pulse broadening caused by scattering for magnetar PSR J1745-2900

The value of the spectral power-law exponent A_{iss}[14] depends on nature of the ISM and how it is modeled. For example, in the *thin screen model* the observed scattering occurs in a plane between the observer and the pulsar (e.g., Scheuer, 1968; Williamson, 1972). This approach gives A_{iss} = 4, (e.g., Rickett, 1977).

More recent multi-frequency studies (e.g., Löhmer et al., 2004; Lewandowski et al., 2013, 2015; Geyer et al., 2017) found that for different pulsars A_{iss} can vary between 1.3 and 5.6. According to Geyer et al. (2017) A_{iss} may evolve with frequency.

---

[14] A subscript “iss” stands for interstellar scintillation.

1.2.3.3 Faraday Rotation

When polarized light travels through ionised parts of the ISM that are permeated by a magnetic field **B**, the linear polarization plane is rotated by a certain angle. This phenomenon is called *Faraday rotation*.

The observed linearly polarized wave can be viewed as a superposition of left- and right-handed circularly polarized waves (LCP and RCP respectively). LCP and RCP waves propagate through a magnetized plasma with different group velocities owing to birefringence; i.e., the index of refraction differs for LCP and RCP (e.g., Condon & Ransom, 2016). In the magnetospheric ISM the relative delay between the two circular modes results in a rotation of the orientation of the linear polarisation plane by an angle proportional to the wavelength squared; i.e.,

$$\Delta\Psi = \mathrm{RM}\ \lambda^2, \tag{1.11}$$

The parameter RM is known as the **rotation measure**, which is proportional to the integral of the line-of-sight component $\mathrm{B}_{||}$ of the magnetic field, weighted by n_e (both of which vary along the line of sight):

$$\mathrm{RM} = \frac{e^3}{2\pi m_e^2 c^4} \int_0^L n_e B_{||} dl \tag{1.12}$$

where e and m_e are the charge and mass of the electron, c is the speed of light in vacuum, and L is the distance to the pulsar (e.g., Lorimer & Kramer, 2012). RM has units of $\mathrm{rad/m^2}$.

1.2.4 Brief review of emission models

During the decades following the discovery of pulsars, physical models of the pulsar emission mechanism were proposed that laid the basis for most current theories. Each model works to some degree; they may explain observed properties for particular class of pulsar, but fail to describe all observed phenomena. A very good overview of the current state of the art is presented by Melrose and Rafat (2017).

Below is a very brief summary of some theories of the pulsar radio emission mechanism that are applied in modern research.

Coherent Curvature Emission (CCE). This hypothesis was first suggested as a plausible description of the pulsar emission mechanism (e.g., Komesaroff, 1970 and Ruderman & Sutherland, 1975). It is based on the motion of charged particles along curved magnetic field lines at relativistic speeds (with Lorentz factor of order $\gamma \sim 10^2 - 10^3$), and thus they emit curvature radiation.

Relativistic Plasma Emission (RPE). Ginzburg et al. (1969) first suggested a mechanism that is based on a beam instability, where waves are excited by a resonant kinetic plasma beam instability, and non-linear interaction between the waves produces the escaping radiation[15]. Others have further developed this model (e.g., Gedalin & Machabeli, 1982, Lominadze et al., 1983), but it is also highly debated (e.g., Melrose & Gedalin, 1999).

Anomalous Doppler Emission (ADE). Pulsar radiation may be generated by certain plasma electromagnetic instabilities due to the strong magnetic field, which constrains electrons to move only along the field lines, causing an anisotropy that is a source of free energy. It was proposed by Lyutikov (1999) that it may be cyclotron-Cherenkov instability that drives the anomalous Doppler resonance.

Linear Acceleration Emission (LAE). This hypothesis considers emission from a charged particle that accelerates parallel to its velocity primarily caused by large-amplitude structures oscillating on short length scales (e.g., Melrose et al., 2009, Reville & Kirk, 2010).

Free-electron Maser Emission (FEM). Maser emission mechanisms were proposed

---

[15] It works in analogy with solar radio-emission.

as a source of the pulsar's radiation by some researchers (e.g., Rowe, 1995, Schopper et al., 2002) and, as Lorimer and Kramer (2012) wrote, may be "interpreted as negative absorption". Because LAE and FEM need a separate mechanism to generate the necessary large-amplitude structures, some researches suggest to consider them as the second stage of the RPE (e.g., Melrose & Rafat, 2017).

In principle, additional information that can shed light on the nature and origin of the pulsar emission mechanism can be gained by studying the single pulse phenomena of the pulsar emission.

1.3 Single pulse phenomena

The average profile and single pulses from pulsars provide complementary information about pulsar physics. The single pulses, or subpulses, demonstrate complex behaviour both in each individual pulsar and while comparing between different pulsars; however, some common phenomena and general properties of single-pulse emission have been identified.

1.3.1 Sub-pulse drifting

At the dawn of pulsar studies, (e.g., Drake & Craft, 1968, Sutton et al., 1970) it was observed that, for some pulsars, the "on-pulse window" is populated by narrow subpulses that move systematically in pulse longitude over the course of several rotations of the pulsar (see for example Figure 1.8), a phenomenon known as *sub-pulse drifting*. Drifting subpulses are thought to be present in almost half of the pulsar population, (e.g., Weltevrede et al., 2006, Basu et al., 2016 and Basu et al., 2019). Weltevrede et al. (2006) studied a sample of 187 pulsars at 21 cm, and found 55% of them to show subpulse drifting. Basu et al. (2016) added 22 more drifting pulsars to known set, and Basu et al.

(2019) classified all known pulsars with sub-pulse drifting at that time. Such drifting phenomena can occur in other pulsars as well, but due to low S/N, instrumentation or other limitations, they are not yet detected (e.g., Edwards & Stappers, 2002; Weltevrede, 2016).

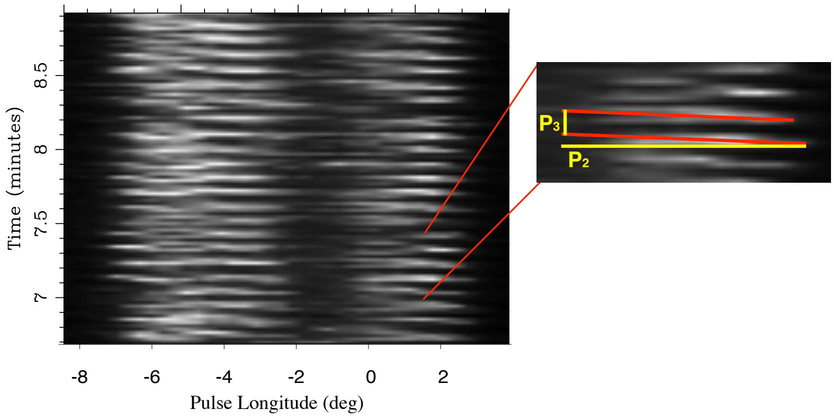

Figure 1.8: Arecibo data for PSR B1919+21, showing drifting sub-pulses (left panel) and zoomed view with examples of drift periods P_2 and P_3 marked with yellow colour and drift bands marked with red lines (right panel). Each row plots the total intensity of a single pulse, with time increasing on the vertical axis. The horizontal axis show pulse longitude. The grey-scale denotes flux density (white depicts the highest values). Drifting subpulses are seen as sloping bands of intensity.

To characterize the drifting subpulse phenomena, a series of periodicities are defined. In addition to the spin period of the pulsar (P_1), we usually identify other two periods: 1) the longitudinal interval or separation between successive drift bands (P_2); and 2) the modulation interval, or drift cycle, expressed in pulsar rotations between drift bands (P_3). The ratio between these periods P_2/P_3 (i.e., slope of the drifting pattern) is the drift rate.

The origin of drifting subpulses is still debated. It could be determined by the emission mechanism of the pulsar, or it could also arise during propagation in the pulsar magnetosphere. One scenario, known as the “rotating carousel” model (Ruderman & Sutherland, 1975; Rankin, 1993; Rankin et al., 2006), suggests that the observed radiation is produced by outflowing streams of charged particles that circulate around the magnetic pole due to $\mathbf{E} \times \mathbf{B}$ drift, where $\mathbf{E}$ and $\mathbf{B}$ are the electric and magnetic fields in the vicinity of the polar cap. Owing to a carousel-like motion of the streams, they drift across the primary beam of the pulsar, such that the associated sub-pulses appear to shift in pulse longitude as a function of time.

The phenomenology in drifting subpulses is rich (a classification and description of different types of drifting can be found, for example, in Basu et al., 2019) and some pulsars that exhibit drifting also demonstrate associations with other phenomena, such as *polarization-mode changing* and in some cases *nulling* (e.g., Wright & Fowler, 1981; Hankins & Wolszczan, 1987; Vivekanand & Joshi, 1997; Redman et al., 2005; Basu & Mitra, 2018).

1.3.2 Orthogonally Polarised Modes

A remarkable phenomenon in pulsar emission is the occurrence of the so-called orthogonally polarized modes (OPMs), as it is not uncommon for pulsars to alternate between two modes of polarised emission at the same phase longitude, first detected as bi-modal distributions of the polarization angle (Ψ), with two peaks offset by 90° (e.g., Ekers & Moffet, 1969; Manchester et al., 1975; Backer et al., 1976). In Poincaré space the modes appear as antiparallel distributions situated on opposite sides of the sphere (van Straten & Tiburzi, 2017).

Early studies of OPMs also found deviations from orthogonality (e.g., Edwards & Stappers, 2004); i.e., the Stokes vectors are not anti-parallel. OPMs have been studied through the application of different methods (see Section 1.6), and their origin is still debated. For example, some researchers suggest that it is originating in the pulsar emission itself, others suggest that it arises during the propagation through the pulsar magnetosphere. Deviations from orthogonality can be explained, for example, with the existence of two momentarily-orthogonal modes whose orientation varies in time due to coherent wave-coupling effect (e.g., Cordes et al., 1978). Other explanations involve a superposition of two modes that are not orthogonal (e.g., they may originate on different lines of magnetic field), which is caused by birefringence (e.g., Stinebring et al., 1984).

OPMs can be studied using the fourth-order statistics of the electric fields. McKinnon (2004) and Edwards and Stappers (2004), investigated OPMs using the 3×3 matrix of covariances between the Stokes Q, U, V parameters. Later, van Straten (2009) and van Straten and Tiburzi (2017) expanded this approach to use a 4×4 covariance matrix of the Stokes parameters, thereby increasing the interpretive power of the approach (see more in Section 1.7).

1.3.3 Mode Changing and Nulling

Some pulsars show more than one stable drift mode with different drift periods (e.g., Huguenin et al., 1970; Vivekanand & Joshi, 1997; Smits et al., 2007; McSweeney et al., 2017). The average profile for different modes of drifting also differs (Backer, 1970). In general, the alternation between different stable average profiles is referred to as *mode changing*.

Since the majority of pulsars are faint and therefore cannot be studied using techniques that depend upon detection of individual pulses, it is not clear how common mode changing is across the pulsar population. However, as it was noted by Rankin (1986), pulsars that exhibit mode changing have common behaviours. They usually exhibit complex average pulse profiles and complex changes in subpulse modulation characteristics which follow transitions between modes.

A number of mode changing pulsars (and a fraction of other pulsars as well) also exhibit nulling (e.g., Hankins & Wolszczan, 1987; Redman et al., 2005; Kloumann & Rankin, 2010; Basu et al., 2017), which consists in a sudden reduction[16] of their

---

[16] i.e., flux drops below the detection threshold of the instrument

emission, followed by a reappearance of the radiation (Backer, 1970). Such nulling phenomena may last from a few rotations of the pulsar to months for intermittent pulsars (Wang et al., 2007). Examples of nulling are taken from Wang et al. (2007) and shown in Figure 1.9.

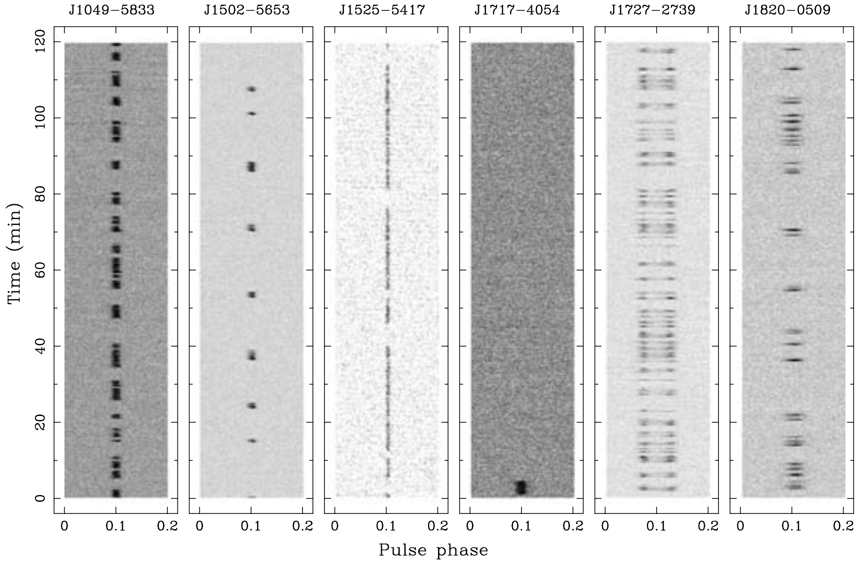

Figure 1.9: The figure shows phase-time plots for six pulsars which demonstrate nulling phenomena. Here for each pulsar x-axis are pulse phase, y-axis are integration time in minutes, and the gray-scale depicts flux density from zero (white) to the maximum observed value (black).
This image is taken from Wang et al. (2007).

Later it was found that nulls in pulsar emission occur simultaneously at all radio frequencies and to all pulse components at the same time; partial nulling (when emission drops to zero in only one component) is also possible (e.g., Wang et al., 2007; Shaifullah et al., 2018). Interestingly, nulling happens mostly for old pulsars[17] (e.g., Ritchings, 1976; Wang et al., 2007). Based on associated changes in the pulsar's spin-down rates during emitting and nulling states the phenomenon most likely originates in the pulsar magnetosphere (e.g., Kramer et al., 2006; Wang et al., 2007; Timokhin, 2010, etc.). Various explanations have been proposed, including instability of the magnetic field (e.g., Geppert et al., 2003); changing between curvature radiation and Compton

---

[17] Wang et al. (2007) wrote that the degree of nulling relates more to pulsar's age rather than its period

scattering (e.g., Zhang et al., 1997); or even missing the line of sight (e.g., Herfindal & Rankin, 2007).

1.4 A challenge in radio astronomy: Radio Frequency Interference

Radio Frequency Interference (RFI) is caused by human activities that utilize electronics and communication technology. It includes all types of the radio transmissions such as television, mobile, internet, as well as airplanes, and satellites, including the Global Positioning System (GPS), and is getting worse due to development and rapid increase in global demand. At the radio observatory RFI is produced both locally (e.g., local mobile phones, microwave ovens and other electronic devices), and off-site (e.g., Earth-borne and space-borne transmitters).

RFI causes loss of data and therefore loss of sensitivity and data quality. There are two most considered classes of RFI: persistent RFI that wipes out parts of the frequency band and the impulsive RFI that is mostly broadband (however sometimes it can be narrow-band) that wipes out signal in the time domain. RFI does not affect various astronomical signals equally, for example, RFI affects pulsar observations differently than spectral line and continuum observations. In pulsar observations, changes of signal and variations of signal amplitudes on short-time scales are important, thus RFI causes harm by adding more modulations or altering the signal. More importantly, often it is challenging to distinguish between impulsive RFI and, for example, bright pulses from a pulsar.

Figure 1.10 taken from Hobbs et al. (2020) shows the three radio-frequency (RF) bands of the Ultra-Wideband Low (UWL) receiver that were observed on 2019 February

24 at 22:48 UTC. Here we can see the potential impact of RFI[18] primarily in the form of transmission that occupies the large fraction of the band, especially for the 128 MHz-wide sub-bands with the center frequencies of 768 MHz, 896 MHz, 1024 MHz, and 1152 MHz. This loss of frequency band affects all observations.

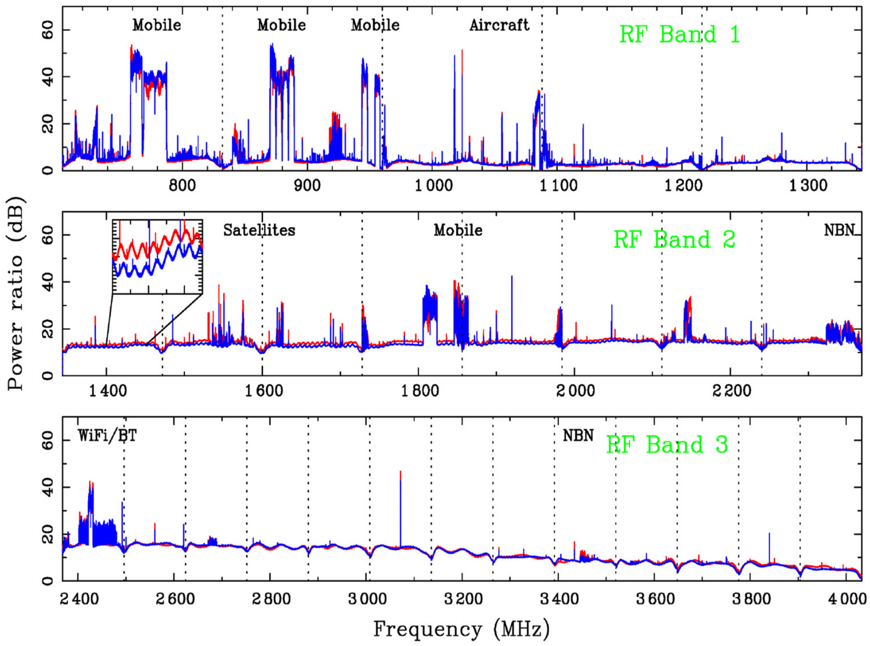

Figure 1.10: Three RF bands of the UWL receiver at the Parkes telescope from Hobbs et al. 2020. The dotted lines are the sub-band boundaries. The principal RFI transmissions are labelled. Here NBN and BT are, respectivelly, the National Broadband Network and Bluetooth.

Even such a mundane thing like a microwave oven can greatly compromise radio observations. For example, Burke-Spolaor et al. (2011) discovered the signals that shared some characteristics with an astrophysical signal called *Fast Radio Burst* (Lorimer et al., 2007). However, the fact that they appeared simultaneously in all 13 beams of the multi-beam receiver at Parkes (pointing at different patches of sky) clearly indicated a terrestrial origin. These signals were dubbed as "Perytons". Later more such signals were found, and not only in Parkes data, but also at the Bleinen Radio Observatory

---

[18] For example, in Chapter 4 we showed, that at low frequencies (e.g., in 128 MHz-wide sub-band with the center frequency of 768 MHz), where the most of RFI is due to the mobile phone towers, we lost up to 80% of the data.

(Saint-Hilaire et al., 2014).

Perytons were transient signals that generally lasted for about 250 ms across the observed band, at frequencies around 1.4 GHz. They mostly occurred during working hours, which points to their human-made nature; however, because the signal appeared dispersed (as expected for astronomical objects) they differed from the "usual" RFI. The mystery was resolved by Petroff et al. (2015) after installation of an RFI monitor at the Parkes observatory. The new RFI monitor helped to correlate between Peryton events and strong local RFI emission that occurred mostly at 2.3 - 2.5 GHz. The fact that most microwave ovens operate at these frequencies and the time of the day Perytons were detected gave the clue of the origin of the signals. Petroff et al. (2015) demonstrated that Perytons are generated by microwave ovens, especially when hungry users open them before they stop transmitting. They also proved the difference between fast radio bursts and Perytons, and that there is no relations between those events. Thus, all microwave ovens were removed from all ATNF radio observatories (Woolston, 2015).

Because of the large variety of radio telescopes, receivers, observing procedures, and the observational conditions, there is no one unified method for RFI mitigation. Instead, for different radio telescopes and receiver systems, a variety of techniques was developed by research groups and collaborations. From such broad variety of methods it is possible to generalize two main approaches (e.g., see Fridman & Baan, 2001):

- **Rejection in the temporal domain** which in general is used for strong spikes of RFI. In this case the simplified RFI cleanup is done in time domain (for example, spectral kurtosis method, Querol et al., 2019, Inter-Quartile Range Mitigation methods by Morello et al., 2022, Fourier domain excision by Maan et al., 2021, zero-dispersion measure filtering by Eatough et al., 2009).

- **Rejection in the frequency domain** is mostly good for long-lasting RFI signals.

Here the bandwidth is sub-divided into channels and channels with RFI are suppressed. This method may not be good for some type of observations (e.g., spectral line observations) because in certain unlucky circumstances the signal of interest can be rejected. However, the approaches with adaptive frequency rejection are used.

1.5 Observations with radio telescopes

To minimize the impact of RFI, the sites for radio observatories were carefully chosen in areas where the population density is low whenever it is possible[19]. A pulsar signal[20] is very weak; for example, the brightest pulsar has signal of order of Jy (e.g., Mignani et al., 2017), which is 10^{-26} W $m^{-2}Hz^{-1}$. There are two approaches to increase sensitivity of radio telescopes: by increasing the gain of the dish by increasing its collecting area, and by decreasing the temperature of the receiver (e.g., using cryogenic receivers) (Wilson et al., 2009). Then, the signal is further down-converted and digitized, after which we measure total powers in the observing bands.

In the next section we present brief introductions to the radio telescopes that produced the data used in this thesis.

1.5.1 Arecibo radio telescope (1963 - 2020)

The Arecibo radio telescope was a spherical-reflector radio telescope which was built inside a natural karst sinkhole at the Arecibo Observatory in Puerto Rico. The telescope main dish was 305 m in diameter, and had a 265-m radius of curvature (e.g., Goldsmith et al., 1995). The dish was stationary and its receivers and transmitters were positioned[21]

---

[19] However there are some exceptions, e.g., the Low Frequency Array (LOFAR) is located in highly populated areas of Europe.

[20] As any other astronomical signal

[21] Receivers and transmitters were mounted on the movable platform suspended from the cables (that were held by three tall towers) 150m above the surface of the dish.

to the required focal points for aiming at the targeted areas (see e.g., Cohen, 2009). For over 53 years it was the largest single-dish radio telescope in the world, and the data obtained on that facility are still on the cutting edge of science.

On 1 December 2020, after a series of devastating failures of support cables, the Arecibo radio telescope tragically ceased operations with the collapse of its receiver platform.

1.5.2 Parkes radio telescope

The Parkes radio telescope is a 64m-diameter parabolic dish-antenna that was built in 1961 (see e.g., Edwards, 2012) and still is at the cutting edge of the science due to its location in the Southern hemisphere and continuous sophisticated upgrades, such as introducing new receivers and improvements of the reflecting surface.

The Parkes radio telescope (Figure 1.11 shows the telescope as viewed via webcam), which is also known as "The Dish"[22] (Sitch, 2000), is situated at the Parkes Observatory, 25 km North of the town of Parkes, NSW in Australia. The observatory is built in a shallow valley to protect the facility from terrestrial RFI. The facility belongs to and is run by the Australia Telescope National Facility (ATNF) under the umbrella of the Commonwealth Scientific and Industrial Research Organisation (CSIRO). The Parkes observatory was added to the Australian National Heritage List on 10 August 2020 (*CSIRO, 2020*). Same year it was given a name of “Murriyang" in Wiradjuri language.

Throughout the history of the telescope it held a variety of receivers. At present it hosts the Ultra Wide-bandwidth Low (UWL), Methanol, MARS, and K-Band receivers to cover the wide range of frequencies. During this thesis, data from the UWL receiver were collected in the context of the long-term “Pulsar Radiation Emission Statistics Survey” (PRESS, P.I. van Straten).

---

[22] As it was one of the few radio telescopes that was receiving live broadcast from the Apollo 11 Moon landing. Later a film "The Dish", based of those events, was produced.

Figure 1.11: Parkes radio telescope as seen during a daytime observing session with good weather on-site. The screenshot was taken during the observations for the PRESS project via the live webcamera from the FROG telescope control software.

The **UWL receiver** (Hobbs et al., 2020) continuously covers the frequency range from 704 MHz to 4032 MHz using a novel feedhorn design (Dunning et al., 2015). The UWL frequency range is sub-divided into three bands:

- Low Band: 704 MHz - 1344 MHz
- Mid Band: 1344 MHz - 2368 MHz
- High Band 2368 MHz - 4032 MHz.

These three bands are digitised and further sub-divided, using critically-sampled polyphase filter banks, into 26 sub-bands of 128 MHz each. During observations, the channelised data are streamed to a signal-processor system based on Graphics Processor Units (GPUs) which is named MEDUSA[23]. MEDUSA's real-time processing capabilities include two special, pulsar-specific observing modes: *pulsar folding* and *pulsar search* modes. In **fold-mode** observations (which are based on synchronously averaging the data using a model to transform between the time and rotational pulse

---

[23] Named for the multiple applications the system can provide, as an analog to the mythological Medusa Gorgo who has many snakes on its head.

phase and termed ”folding“, more details are in Section 2.2), the incoming data are folded on the pulsar period. This observing mode is only good for pulsars with an accurate phase model, and when the science case does not involve studies of single pulses. In **search mode** observations the observed time-series of channelised intensities are recorded into file(s) (i.e., spectra as a function of time). The incoming voltage data are channelised and polarization products are formed, then averaged to some specified sampling intervals and re-quantised to 1, 2, 4, or 8 bits. This observing mode is useful for any pulsar (unknown or known) as well as for single pulse studies, such as ones presented in this thesis.

1.6 Analysis of single pulse data

For few bright pulsars, it is possible to detect the single pulses and their polarization characteristics well enough to study them in detail.

A number of analysis techniques and approaches were developed and applied to single-pulse analyses. For pulsars with *drifting subpulses* methods of folding over P_3 drift period were used since early studies. For example, Taylor et al. (1971) applied P_3-folding to pulsars with regular drifting behaviour. This approach is based on averaging several sequences of subpulses together as a function of drift cycle phase to improve signal-to-noise ratio and drift phase resolution.

To measure and analyse P_3 periods for any pulsar with drifting subpulses, methods such as the “longitude-resolved fluctuation spectrum” (LRFS) approach were developed by Backer (1973), and Backer et al. (1975). The LRFS is produced by computing the one-dimensional fast Fourier transform (FFT) of each time series single-pulse intensities at a specific pulse longitude, as a function of pulse longitude. This method is useful to estimate P_3 and for detecting and characterising drifting sub-pulses in a large population of pulsars. However, the LRFS does not determine P_2 and drift rate. Deshpande and

Rankin (2001) took a step further and developed an approach which is similar to the LRFS one, but in that case the FFT is applied along two dimensions: FFT of the pulse sequence along the same pulse longitude (first dimension), and then across each row of the complex LRFS (second dimension), i.e., did one-dimensional FFT twice. This method is known as harmonic-resolved fluctuation spectrum (HRFS). Edwards and Stappers (2002) then developed the similar approach (known as 2DFS) based on the two-dimensional FFT, i.e., did 2D FFT once. Later Edwards (2004) extended the LRFS to study the cross-spectral power between the four Stokes parameters, the “polarization LRFS” (PLRFS).

To study polarization properties such as the occurrence of OPMs, PA histograms derived from single-pulse analyses have been used since the discovery of pulsars (e.g., Ekers & Moffet, 1969; Taylor et al., 1975). With time, the approach was enriched with application of phase-resolved histograms of PA, applied by Stinebring et al. (1984), which allowed to retrieve more details about polarization modes (for example, it allows to study the evolution of OPM as a function of pulse longitude). Authors conducted a comprehensive study of the single-pulse polarization behaviour in a large number of pulsars and noticed that PA-histograms were broader than that expected due to instrumental noise. Based on the findings of the whole study Stinebring et al. (1984) distinguished between *superposed* and *disjoint* regimes of polarization mode combination. Here *disjoint* means that at a certain instant of time only one polarization mode is observed. *Superposed* means that the signal is an incoherent superposition of two polarization modes (Cordes et al., 1978).

Edwards and Stappers (2004) added an extra dimension to the study of the polarization vector orientation by applying two-dimensional phase-resolved histograms of the polarization state located on the Poincaré sphere. In their study, by plotting polarisation vectors on Lambert’s azimuthal equal-area projections of Poincaré sphere, they discovered an unexpected partial annular-shaped distribution that cannot be described by incoherent superposition of OPMs. They hypothesised that the annular shape was caused by generalised Faraday rotation. Generalised Faraday rotation (Kennett & Melrose, 1998) is the intrinsic Faraday rotation in the pulsar magnetospheres due to birefringence that arises in relativistic plasma.

1.7 Generalities of the statistical approach

Some of the aforementioned methods of studies of the properties of single-pulse emission have focused on the group of bright and slower pulsars, which comprise only a small fraction of the known population of pulsars. The majority of pulsars are too faint to detect single pulses, and thus, a lot of information is currently inaccessible. To address this issue statistical approaches were introduced.

Cordes et al. (1978) first suggested to use fourth moments of the electric field to distinguish between disjoint and superposed OPMs. Following this idea, other researchers developed and applied various statistical approaches to interpret phenomena related to OPMs (e.g., McKinnon & Stinebring, 2000; McKinnon, 2003a, 2006).

A new tool to study the polarization vectors with great potential to detect and characterize OPMs and possible deviations from orthogonality was independently proposed by Edwards and Stappers (2004) and McKinnon (2004). The method uses principal component analysis of 3×3 covariance matrices between the Stokes parameters Q, U, and V (see Section 2.1.0.2). This approach had more power and ability to detect deviations from OPM and characterize the distribution of the polarization vector in the Poincaré space.

Inspired by opportunities given by the fourth-order moments of the electric field, van Straten (2009) went further and introduced 4×4 covariance matrices, adding Stokes I. This approach improved the ability to interpret the observations and helped to eliminate some artificial assumptions (like the need to introduce additional randomly polarized radiation). However, it still had limitations because it only works when the components of the electric field vector are normally distributed, which is far from being realistic (e.g., most pulsars have exponential, log-normal, and power-law distributions of their flux density).

The idea of utilizing 4×4 covariance matrices was later expanded by van Straten and Tiburzi (2017) to overcome limitations by extending the method application to the non-normal distributions. Moreover, this method suggests to introduce a new type of occurrence of polarization modes to the already-cited superposed and disjoint. A third state, called *Composite*, can arise when disjoint modes are observed with insufficient resolution of the receiving instrumentation. In principle, fourth moments can be used to differentiate between the three mode regimes; however, the interpretation is complicated by amplitude modulation. Therefore, to further explore the interpretation and application of fourth moments statistics to real pulsar signals, this Thesis was designed to study known bright pulsars by applying this statistical approach and relate bright-pulsar methods (like histograms) to statistical methods (like Principal component analysis).

Outline of the thesis

The remainder of this thesis is organised as follows:

Chapter 2 introduces data processing and analysis approaches. It starts with an introduction to the polarimetry basics and terminology used in this thesis. Then we introduce techniques of data processing, RFI mitigation, and calibration used in this research (some techniques were developed during later stages of this project). The statistical methods on which this thesis is based are described at the end of this chapter.

Chapter 3 is a published article (Primak et al., 2022) and presents polarisation analysis of the pulsar PSR B1919+21. It reports on the new techniques that were added to our polarisation statistical analysis framework.

Chapter 4 introduces the pulsar radio emission statistics survey (PRESS) that was conceived by our team (i.e., Prof. van Straten, Dr. Tiburzi, and the author of this thesis) and developed into a large-scale international project. In this chapter, we verified the equations used to plan the PRESS observations and present further development and verification of statistical methods. An overview of the PRESS data processing pipeline (which is still under development) is given, jointly with preliminary outcomes of data analysis for pulsar PSR B1919+21, observed during the PRESS campaign, and obtained during pipeline developments.

Chapter 5 presents a summary, conclusions, and future work that has a good potential to germinate from this thesis.

Chapter 2

Data Processing and Analysis Approaches

In this chapter, the polarization review is based on Kliger et al. (1990); Jackson (1962); Born and Wolf (1999); van Straten (2009); van Straten and Tiburzi (2017). Unless other sources are noted, their notations and terminology are adapted for the following text.

2.1 Polarization basics

Since the first observations of pulsars (e.g., see Section 1.1), it was found that these sources are highly polarized (Lyne & Smith, 1968). Therefore, we explore the concepts of polarisation.

One set of solutions of Maxwell's equations in a vacuum is a plane transverse wave[1] (e.g., Chandrasekhar, 1960; Jackson, 1962). The wave consists of electric **E** and magnetic **B** oscillating fields orthogonal to each other.

There are two solutions of the Maxwell wave equations in terms of transverse

---

[1] a wave that oscillates perpendicular to its propagation.

components that represent 2 orthogonal values for polarization (e.g., Jackson, 1962). Thus, the radio receiving systems must differentiate between orthogonal polarization components to be able to describe the polarization state of the observed signal. Therefore, most radio telescope receivers are designed with two receptors that are ideally sensitive to orthogonal polarizations. For a monochromatic wave, the electric field can be presented mathematically as:

$$\mathbf{E}(\mathbf{r}, t) = \mathbf{E}_0 e^{\pm i(\mathbf{k}\cdot\mathbf{r} - \omega t)} \tag{2.1}$$

where $\mathbf{E}_0$ is the vector that represents the amplitudes and phases of the two wave components, $\mathbf{r}$ is the direction of the propagation, ω is the angular frequency, and $\mathbf{k}$ is the wave vector ($|\mathbf{k}| = \frac{\omega}{c} = \frac{2\pi}{\lambda}$), whose magnitude is the wave number.

The *polarization* of a monochromatic wave, describes the oscillation pattern of the electric field. In the case of *linear* polarization, $\mathbf{E}$ oscillates along a line. Observed *circular* polarization means that while oscillating, $\mathbf{E}$ draws a circle during each period of the wave (Figure 2.1 panels d and e). *Elliptical* polarization is a combination of linear and circular ones.

Linear and circular polarisation are special cases, as for pulsars polarization is mostly observed as elliptical, thus, let us consider this general case. Panel f) on Figure 2.1 shows the polarization ellipse with its main geometrical parameters such as: *orientation angle*, (or other term: *position angle, PA*) Ψ – the angle between the major axis of the ellipse and the x-axis of our Cartesian coordinate system ($-\frac{\pi}{2} \leqslant \Psi \leqslant \frac{\pi}{2}$), and the *ellipticity angle* χ, where $\tan\chi$ is the ratio of the ellipse's minor to major axis and $-\frac{\pi}{4} \leqslant \chi \leqslant \frac{\pi}{4}$ (the negative sign corresponds to counter-clockwise direction).

To describe polarization is common to utilize the Stokes parameters, which were introduced for astronomical use by Chandrasekhar (1947) and were named after George Gabriel Stokes who first defined them in the mid-nineteenth century (Stokes, 1851).

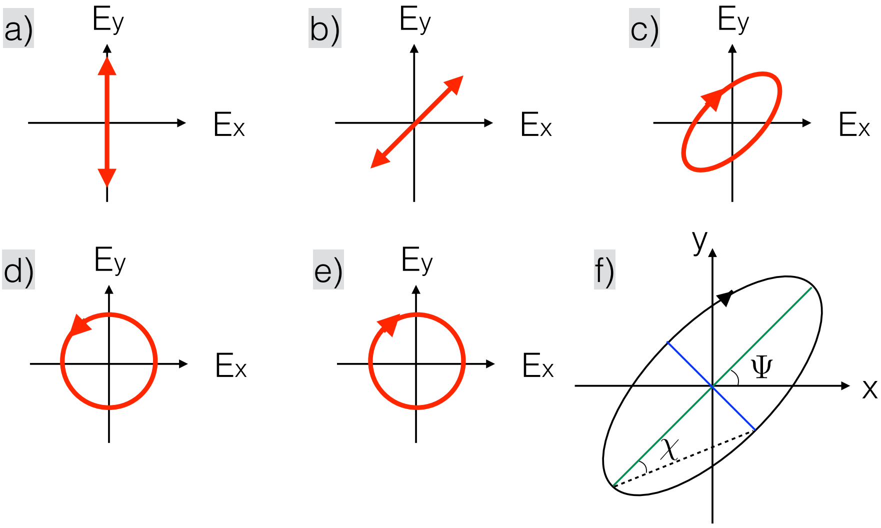

Figure 2.1: Example of polarization states of monochromatic waves. Panels a) and b) depict electric field vector over a complete cycle for linear polarization at two different orientations; panel c) depicts elliptical polarization (which occurs when there is a phase shift between horizontal and vertical polarization components); panels d) and e) depict circular polarization (phase shift is exactly ±90°) with opposite sign. Circular and elliptical polarisations can have either a clockwise or counterclockwise rotations of the field. Panel f) depicts the polarization ellipse with the position angle (orientation angle) Ψ and ellipticity angle χ; green and blue lines are major and minor axis of the ellipse respectively.

2.1.0.1 Stokes parameters.

Stokes parameters can be named as S_0, S_1, S_2, and S_3 or, alternatively, I, Q, U, and V. S_0, or I is the *total intensity*, S_1, S_2, or Q and U describe *linear polarization* whose intensity is defined as $L = \sqrt{Q^2 + U^2}$, and S_3, or V - describes *circular polarization*. The sign of V indicates whether the polarisation is left-handed (plus sign shows counter-clockwise rotation), LCP in other terms, or right-handed (minus sign shows clockwise rotation), RCP in other terms.

Stokes parameters are combined into the Stokes vector:

$$S = \begin{pmatrix} S_0 \\ S_1 \\ S_2 \\ S_3 \end{pmatrix} = \begin{pmatrix} \mathrm{I} \\ \mathrm{Q} \\ \mathrm{U} \\ \mathrm{V} \end{pmatrix}$$

A certain polarization state is presented by the polarization vector $\mathbf{I}_p = (S_1, S_2, S_3)$ = (Q, U, V), with magnitude $|\mathbf{I}_p|= \sqrt{\mathrm{Q}^2 + \mathrm{U}^2 + \mathrm{V}^2} = \sqrt{S_1^2 + S_2^2 + S_3^2}$.

The relation of the Stokes parameters to the polarization ellipse and the intensity of the signal can be expressed in various ways.

For example, for monochromatic waves, which are 100% polarized, the Stokes parameters can be conveyed through the spherical coordinates that express polarized flux $|\mathbf{I}_p|$, position angle Ψ, and ellipticity angle χ of the 3-dimensional vector on Cartesian coordinate system with axis S_1, S_2, S_3:

$S_0 = \mathrm{I}$

$S_1 = \mathrm{I} \cos 2\Psi \cos 2\chi$

$S_2 = \mathrm{I} \sin 2\Psi \cos 2\chi$

$S_3 = \mathrm{I} \sin 2\chi$

The aforementioned coordinate system is called *Poincaré space* and when the components of the polarization vector are normalized by the total intensity *Poincaré sphere* with unit radius (Figure 2.2). Because a monochromatic wave is 100% polarised, the normalised polarized flux, $\mathbf{I}_p/S_0$ (depicted with magenta arrow), becomes the unit radius in the Poincaré sphere.

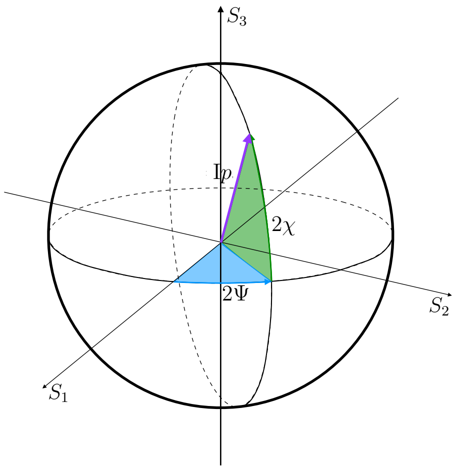

Figure 2.2: Polarization vector on the Poincaré sphere. The polarization vector $\mathbf{I}_p = (S_1, S_2, S_3)$ is depicted with magenta arrow. Three Stokes parameters S_1, S_2, and S_3 (or [Q, U, V]) are plotted in Cartesian coordinates. PA (Ψ) is shown with the blue color, ellipticity angle χ is shown with the green color.

In case of 100% *linear* polarisation, the vector will sit completely in the Equatorial (S_1S_2, or QU) plane of Poincaré sphere. The orientation of the linearly polarized vector, i.e., its PA, will be: $\Psi = \frac{1}{2}\tan^{-1}\frac{\mathrm{U}}{\mathrm{Q}} = \frac{1}{2}\tan^{-1}\frac{S_2}{S_1}$.

In case of *elliptically* polarized radiation, the circular polarization is contributing to the polarization state. In this case the ellipticity angle χ is:
$\chi = \frac{1}{2}\tan^{-1}\frac{\mathrm{V}}{\sqrt{\mathrm{Q}^2+\mathrm{U}^2}} = \frac{1}{2}\tan^{-1}\frac{\mathrm{V}}{\mathrm{L}} = \frac{1}{2}\tan^{-1}\frac{S_3}{\sqrt{S_1^2+S_2^2}}$.

Since non-monochromatic waves are most common in nature, it is helpful to adopt a statistical approach to describe polarization.

In general the emission is not monochromatic, and typically only partially polarised. In other words, the received signal is usually composed of polarised and unpolarised radiation. In this case we can apply the assumption of a quasi-monochromatic wave, where the Stokes parameters can be defined in terms of averaged components of electric field.To visualize these concepts, consider two orthogonal components of **E** in a Cartesian coordinate system E_x and E_y:
$\mathrm{I} = \langle E_x^2\rangle + \langle E_y^2\rangle$
$\mathrm{Q} = \langle E_x^2\rangle - \langle E_y^2\rangle$
$\mathrm{U} = 2\langle E_x^2\rangle\langle E_y^2\rangle\cos\Phi$
$\mathrm{V} = 2\langle E_x^2\rangle\langle E_y^2\rangle\sin\Phi$,
where Φ is the average phase difference between two orthogonal components of electric field (e.g., Lorimer & Kramer, 2012), and $\langle\rangle$ indicate time averages over a statistical sample of the electric field vector.

In case of partially polarized light, the degree of polarization is $\frac{|\mathbf{I}_p|}{\mathrm{I}}$; for 100% polarized wave $\mathrm{I} = \sqrt{\mathrm{Q}^2 + \mathrm{U}^2 + \mathrm{V}^2}$ (e.g., Burke & Graham-Smith, 2002; Lorimer & Kramer, 2012).

2.1.0.2 Jones vector, Jones matrix, and Mueller matrix representation

To describe linear transformations of the electric field, R. C. Jones (1941) developed a matrix calculus. This calculus involves complex values contained in two-dimensional column vectors - *Jones vector*, and 2×2 matrices - *Jones matrices* J.

The transverse electric field vector is described as:

$$\mathbf{e}(t) = \begin{pmatrix} e_0(t) \\ e_1(t) \end{pmatrix} \tag{2.2}$$

where $e_0(t)$ and $e_1(t)$ are complex-valued analytic signals associated with real-valued time series [2]. This provides the two instantaneous amplitudes and phases of the orthogonal polarization states.

The polarization of the electromagnetic wave is described by the second-order statistics of the electric field vector **e** through the complex coherency matrix (Born & Wolf, 1980; Born & Wolf, 1999):

$$\boldsymbol{\rho} \equiv \left\langle \mathbf{e} \otimes \mathbf{e}^{\dagger} \right\rangle = \begin{pmatrix} \langle e_0 e_0^* \rangle & \langle e_0 e_1^* \rangle \\ \langle e_1 e_0^* \rangle & \langle e_1 e_1^* \rangle \end{pmatrix} \tag{2.3}$$

where the angular brackets define an ensemble average, $\otimes$ represents a tensor product, $\dagger$ denotes the Hermitian transpose. The coherency matrix is Hermitian, $\boldsymbol{\rho} = \boldsymbol{\rho}^{\dagger}$.

The relations between complex two-dimensional space of coherency matrix and the real four-dimensional space of the Stokes parameters (van Straten, 2009) is:

$$\boldsymbol{\rho} = S_k \boldsymbol{\sigma}_k / 2 \tag{2.4}$$

$$S_k = \mathrm{tr}(\boldsymbol{\sigma}_k \boldsymbol{\rho}) \tag{2.5}$$

---

[2] From supplemental material from the Polarization Workshop held on November 2018 in Auckland, New Zealand.

In these two equations S_k is four Stokes parameters ($0 \leqslant k \leqslant 3$), tr is the matrix trace operator[3]; σ_0 is the identity matrix, and σ_{1-3} are Pauli matrices, i.e.,

$$\sigma_0 = \begin{pmatrix} 1 & 0 \\ 0 & 1 \end{pmatrix}, \sigma_1 = \begin{pmatrix} 1 & 0 \\ 0 & -1 \end{pmatrix}, \sigma_2 = \begin{pmatrix} 0 & 1 \\ 1 & 0 \end{pmatrix}, \sigma_3 = \begin{pmatrix} 0 & -i \\ i & 0 \end{pmatrix}. \tag{2.6}$$

Jones matrices can represent the instrument and the way it transforms the electric field. Thus, linear transformations of electric field vector can be expressed as:

$$\boldsymbol{e}' = \boldsymbol{J}\boldsymbol{e} \tag{2.7}$$

For the above transformation it is easy to see that the coherency matrix is subjected to the congruence transformation:

$$\boldsymbol{\rho}' = \left\langle \mathbf{e}' \otimes \mathbf{e}'^{\dagger} \right\rangle = \langle (\boldsymbol{J}\boldsymbol{e}) \otimes (\boldsymbol{J}\boldsymbol{e})^{\dagger}) \rangle = \langle \boldsymbol{J}\boldsymbol{e} \otimes \boldsymbol{e}^{\dagger}\boldsymbol{J}^{\dagger} \rangle = \boldsymbol{J} \langle \boldsymbol{e} \otimes \boldsymbol{e}^{\dagger} \rangle \boldsymbol{J}^{\dagger} = \boldsymbol{J}\boldsymbol{\rho}\boldsymbol{J}^{\dagger}.$$

As it was shown above, the two-dimensional space of coherency matrix can be transformed by Jones matrices, then we expect Stokes parameters to be transformed as well. The four-dimensional Stokes parameters transformation can be represented by 4×4 real-valued matrix, called *Mueller matrix* $\boldsymbol{M}$. The transformation then is:

$$S_i{}' = M_i^k S_k \tag{2.8}$$

Where by given a Jones matrix an equivalent Mueller matrix can be computed as:

$$M_i^k = \frac{1}{2} tr(\boldsymbol{\sigma}_i \boldsymbol{J} \boldsymbol{\sigma}_k \boldsymbol{J}^{\dagger}) \tag{2.9}$$

Transformations of the electric field can be described either by Jones or by Mueller

---

[3] Trace of the square matrix is the sum of elements on the main diagonal of this matrix.

matrices. Jones matrices have seven degrees of freedom, and describe only linear transformations of electric field. Mueller matrices have an additional nine degrees of freedom for description of impure or depolarizing transformations and describe linear transformations of the Stokes parameters (which are second moments of electric field, see e.g., van Straten, 2022).

2.2 Signal processing of received pulses

In this section, widely used techniques of data processing and analysis in pulsar astronomy are introduced.

2.2.1 Data processing approaches

Channelised time-series of the sample mean Stokes parameters are recorded at the telescope, and need to be processed for further analysis. The data processing usually consists of phase-resolved binning[4], which is known as "folding" in pulsar community, RFI mitigation, and calibration as described below.

Phase-resolved binning is based on synchronously averaging the data using a model to transform from time to rotational pulse phase (e.g., see Lorimer & Kramer, 2012). Pulse phase is usually measured in fraction of the rotation. If the data are re-sampled (or re-binned in other words) for a duration of one pulsar period, then the outcome will be an individual pulse profile. If the averaging over many periods is applied, then the output will be an average pulse profile. For successful phase-resolved binning, it is important to account for the pulsar's spin period as it would be observed from an inertial reference frame, such as the Solar System Barycenter[5] (which in turn requires an accurate model of the position of the Earth with respect to the Solar System Barycenter as a function of time) as well as a set of the individual pulsar parameters. Such information is contained in the *ephemeris* file which is used for the data processing. The information regarding pulsar's position on the sky in the ephemeris is important because, firstly, the Earth's orbital motion adds an annual variation of the Roemer delay of the pulsar signal. Due to proper motion and precession the coordinates of the pulsar change with time.

---

[4] Or it can be called as *phase-synchronous binning*.

[5] The Solar System barycenter is the center of mass of our Solar System.

To fold recorded pulsar signals, various software packages were developed. One of the popular software packages in the pulsar community, and one that was used in this research, is DSPSR (van Straten & Bailes, 2011). For the other data processing and analysis steps the software packages PSRCHIVE (Hotan et al., 2004; van Straten et al., 2012) and COASTGUARD/MEERGUARD (Lazarus et al., 2016 and Miles et al, paper in preparation) were used.

2.2.2 RFI mitigation

After phase-resolved binning process, data can be cleaned from the RFI. As mentioned previously in Chapter 1.4, anthropogenic RFI causes loss of data.

For the purposes of the PRESS[6] data processing, the majority of RFI was removed automatically during the initial folding process, and then manually after the initial folding. At the first stage the algorithm developed by Morello et al. (2019) which is based on the Inter-Quartile Range Mitigation approach was implemented into the pipeline. Then van Straten et al. (paper in preparation) extended existing methods with our own developed statistics and programmed an algorithm with more advanced techniques. It was found that for pulsars with intrinsic variability, or with mode changing, or with single pulse transient features, the newly developed RFI mitigation algorithms are still failing for single-pulse mitigation. Thus, an implementation of the **Gaussian Mixture Model** (GMM) approach was adopted (Sanderson & Curtin, 2017) which can be described as following.

The algorithm needs to identify what is varying in the data, so it is useful to model fluctuations from the mean as follows

- Compute the mean intensity profile over all sub-integrations and frequency channels: $\boldsymbol{S} = \langle \boldsymbol{P} \rangle$.

---

[6] See Chapter 4.

- Then for each sub-integration and channel, model the observed profile by subtracting a scaled and offset copy of the mean using ordinary least-squares to minimize the residual,

  $$\boldsymbol{R} = \boldsymbol{P} - a\boldsymbol{S} + b\mathbf{1}. \tag{2.10}$$

  Here $\boldsymbol{R}, \boldsymbol{P}, \mathbf{1}$, and $\boldsymbol{S}$ are N-dimensional vectors; a is a scale factor that compensates for gain variations, such as those arising from scintillation; and the offset b compensates for changes in the system equivalent flux density (SEFD).

- Third step is to compute the covariance matrix of the residuals $X = \left\langle \boldsymbol{R} \otimes \boldsymbol{R}^T \right\rangle - \langle \boldsymbol{R} \rangle \otimes \langle \boldsymbol{R} \rangle^T$

- Perform eigen decomposition of X. Then select the subset of eigenvectors of the covariance matrix $\boldsymbol{v}_j$, where $1 < j \leqslant M$ and $j \leqslant M \leqslant N$. Here M is the number of significant eigenvectors. Where λ_i are the eigenvalues of X sorted in descending order of magnitude, M is the index of the last eigenvalue with magnitude greater than the variance of the off-pulse baseline.

After the principal component analysis (PCA) step, the large dimensionality reduction is taking place[7]. Here we compute residual principal components: $\rho_j = \boldsymbol{v}_j \cdot \boldsymbol{R}$.

Then to these ρ_j the algorithm fits the GMM: the algorithm adds a progressively increasing number of Gaussian components and it selects the model that has the best Akaike Information Criterion[8]. And lastly, the algorithm computes the logarithm of the likelihood of ρ_j.

This algorithm was tested on the observed UWL data and compared against other algorithms as described in Chapter 4.

---

[7] This is done by projecting each residual vector onto one of the principal component eigenvectors.

[8] Which is a function of a number of free parameters k and natural logarithm of the likelihood $\hat{L}$, which is essentially a chi-square in a case of multivariate normal distribution: $AIC = 2k - 2\ln(\hat{L})$

2.2.3 Calibration

To allow further analysis of the pulsar polarization properties, it is important to correct the spurious effects introduced by imperfections of the receiving system. Such correction can be obtained by compiling a Jones matrix that offers a trustworthy representation of the system's imperfections, and that can be applied to the detected signal by inverting Equation 2.8. This important step is called *calibration*[9].

There are different ways of performing calibration, even within the same research field. Most general and common approach is the *First Order calibration* based on the *Ideal feed assumption*. More sophisticated methods are used to calibrate the data of the PRESS campaign, beginning with *Measurement Equation Modelling* (van Straten, 2004), where an astronomical source with unknown polarization is tracked throughout a large range of parallactic angles (i.e., the source is observed for many hours, ideally from rise to set). Those observations are then used to determine both the Stokes parameters of the unknown source itself and a subset of the parameters that describe the Jones matrix. After determining the polarisation of the source, it is used as a reference in the *Measurement Equation Template Matching* technique (van Straten, 2013). In this approach, relatively short observations can be used to solve for all seven degrees of freedom of the Jones matrix.

First Order Calibration and Ideal feed assumption:

An artificial, well-known source of polarized flux is installed in the receiver system (typically a noise diode), it is activated right before[10] a pulsar observation. The noise diode is switched on and off periodically and the channelised polarisation time series

---

[9] Most information about calibration in this section are adapted from the "Polarization Skills Workshop" held in AUT November 2018, as well as from discussions and brainstorm sessions with W. van Straten.

[10] Sometimes it can be done right after the pulsar observation.

are folded like a pulsar signal see Figure 2.3. Regular observations of the noise diode are important to model complex gain variations with time.

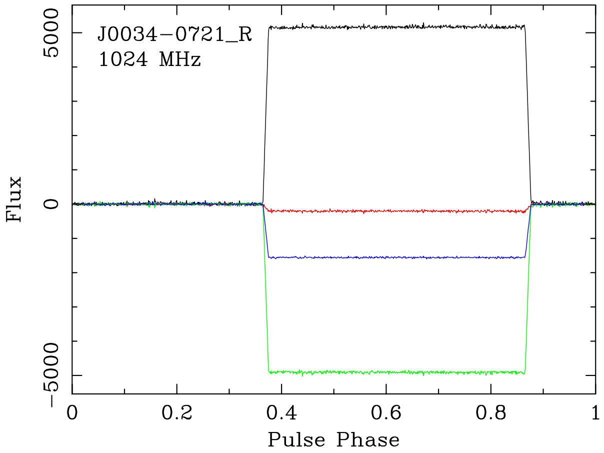

Figure 2.3: Calibration observation for the pulsar PSR J0034-0721 obtained during the PRESS observing campaign in a sub-band with center frequency 1024 MHz (i.e., out of number of channels n_{chan} = 128). Here red, green, blue colors correspond to Stokes Q, U, and V respectively, black color depict Stokes I.

This type of calibration makes an *ideal feed assumption*, where it is stated that:

- The receptors are orthogonal and there is no cross-coupling.

- The noise diode illuminates them equally in both amplitude and phase.

For the linearly polarised receptors, equal signal in x and y corresponds to 100% Stokes U, i.e., $\boldsymbol{S} = [1,0,1,0]\,C_0$, where C_0 is the flux density of the noise diode.

The instrumental response for our ideal feed can be expressed via Jones matrix (van Straten, 2004):

$$\boldsymbol{J} = G\boldsymbol{B}_{\hat{\boldsymbol{q}}}(\beta)\boldsymbol{R}_{\hat{\boldsymbol{q}}}(\phi), \tag{2.11}$$

Where G depicts the change in the absolute gain, ϕ is a differential phase, β is a differential gain, and $\hat{\boldsymbol{q}}$ corresponds to Stokes Q. Concerning the other parameters:

$$\boldsymbol{B}_{\hat{\boldsymbol{q}}}(\beta) = \cosh\beta\sigma_0 + \sinh\beta\hat{\boldsymbol{q}}\cdot\boldsymbol{\sigma} \tag{2.12}$$

is the Lorentz boost of the Stokes vector along Stokes Q axis by hyperbolic angle 2β, which describes the transformation that happens due to the differential gain, where $\boldsymbol{\sigma}$ is a three-vector whose components are the Pauli spin matrices, and

$$\boldsymbol{R}_{\hat{\boldsymbol{q}}}(\phi) = \cos\phi\sigma_0 + i\sin\phi\hat{\boldsymbol{q}}\cdot\boldsymbol{\sigma} \tag{2.13}$$

is a rotation of the Stokes polarization vector about Stokes Q axis by angle 2ϕ, due to the change in differential phase.

The measured Stokes parameters $\boldsymbol{S'}$ can then be expressed via Mueller matrix associated with the aforementioned Jones matrix $\boldsymbol{M_J}$ as following:

$$\boldsymbol{S'} = \boldsymbol{M_J}\boldsymbol{S}, \tag{2.14}$$

$$\boldsymbol{M_J} = \begin{pmatrix} \cosh 2\beta & \sinh 2\beta & 0 & 0 \\ \sinh 2\beta & \cosh 2\beta & 0 & 0 \\ 0 & 0 & \cos 2\phi & \sin 2\phi \\ 0 & 0 & \sin 2\phi & \cos 2\phi \end{pmatrix}$$

Therefore, $\boldsymbol{S'} = C_0\ G^2 \left[\cosh 2\beta, \sinh 2\beta, \cos 2\phi, \sin 2\phi\right]$. The parameters of the matrix can be obtained from the measured Stokes parameters (i.e., derived from the following ratios):

$$\tanh 2\beta = \frac{S_1}{S_0} = \frac{Q}{I} and \tag{2.15}$$

$$\tan 2\phi = \frac{S_3}{S_2} = \frac{V}{U}. \tag{2.16}$$

Using the measured β and ϕ the polarised data can be calibrated.

A similar set of equations can be used to derive β and ϕ of a non-ideal (real-life) feed. For this situation it should be assumed that polarisation vector is not all Stokes U as it is in Ideal feed (e.g., Ord et al., 2004). In this case Equation 2.14 is replaced by

$$\boldsymbol{S}' = \boldsymbol{M_J S_0} \tag{2.17}$$

Where $\boldsymbol{S}_0$ is non-ideal polarisation state of the noise diode, which for the UWL is coupled after the Orthomode transducer.

The conditions that satisfy the ideal feed assumption are not met in real-life observations; thus calibration can be done in other ways, for example, by fitting the data to a certain model. Two such approaches were developed by van Straten (2004) and van Straten (2013), implemented in the PSRCHIVE software (van Straten et al., 2012) and utilized in this research.

Measurement Equation Modeling - MEM (van Straten, 2004):

This approach is based on the idea that by observing an unknown source over a large range of parallactic angles[11], it is possible to model the observed variations in the polarization of the source, and thereby infer the instrumental response. In most cases this approach is better than using just the ideal feed assumption.

Pulsars are good sources for the MEM method due to their stability over long time periods. The method does not require the assumptions of truly orthogonal receptors, nor that the noise diode illuminates the receptors equally.

The observed Stokes parameters S' can be described by (van Straten, 2004):

$$S' = \boldsymbol{M R_v}(\psi) S,$$

---

[11] which happens because of the rotation of the receiver with respect to the celestial sphere

where $\boldsymbol{R_v}(\psi)$ is the rotation about the line of sight by the parallactic angle ψ, $\boldsymbol{M}$ is the Mueller matrix that describes the receiver, S', and S and are the observed and intrinsic Stokes parameters of the pulsar. Both $\boldsymbol{M}$ and S are unknown, thus there is no unique solution to this problem without additional assumptions and/or constraints. For example, Liao et al. (2016) encountered challenges when calibrating the 800 MHz receiver of the Green Bank Telescope, when they detected an unmodelled mixing between circular polarisation and total intensity. They solved the issue by using a number of known quasars as additional constraints.

Measurement Equation Template Matching - METM (van Straten, 2013):

This method uses observations of a known polarized source. At Parkes, PSR J0437-4715 is often used as a reference source for this method. The output of MEM is used to form a template. That template is then matched to a larger number of observations of the pulsar with shorter integration length. Then a penalized spline is used to model variations in time and frequency and smooth out the noise (The smoothing the noise is particularly important at high frequencies where pulsars have the weakest signals due to their steep SEDs).

After calibration, RFI mitigation, and processing, we can consider the off-pulse noise level of the resulting data as a "baseline". For successful data analysis this baseline should be subtracted from the signal.

2.3 Data Analysis

2.3.1 Statistical approach

In this subsection we will review the statistical approach introduced by van Straten (2009), then further developed by van Straten and Tiburzi (2017) to lay the basis for our current work. Unless other sources are noted, the notations and terminology are adapted from these works.

The aforementioned framework distinguishes between statistics of the *instantaneous*[12] and the *sample mean* Stokes parameters, which stresses the importance of the instrumental resolution when studying single pulse polarization properties. Instantaneous Stokes parameters are calculated from individual instances of the electric field and have been used to study auto- and cross-correlations of the Stokes parameters as a function of lag (e.g., Cordes, 1976; Cordes & Hankins, 1977; Hankins et al., 2003). Sample mean Stokes parameters are averages computed over finite samples of instances of the electric field and are the most typically used to study the polarization properties of both integrated pulse profiles and single pulses.

The statistical framework that we employ here, aims to describe the distribution of the Stokes parameters in four-dimensional space which in turn provides information on what causes temporal polarization fluctuations regarding pulsar emission. Theoretically expected distributions are derived using the Jones calculus and by exploiting the geometric relationships between the coherency matrix and the Stokes parameters, as described by Equations 2.4 and 2.5 in Section 2.1.0.2.

---

[12] Other terms that can be used: *unaveraged, unsmoothed.*

2.3.1.1 Distributions of the polarization vectors in the Poincaré space

As mentioned, our approach is based on the covariances between the instantaneous Stokes parameters or the covariances between the sample mean Stokes parameters. We begin by defining the *Stokes sample* as a finite sample of n instances of the electric field vector. The sample mean coherency matrix ($\bar{\boldsymbol{\rho}}$) and the sample mean Stokes parameters $\bar{S}$ can be expressed as

$$\bar{\boldsymbol{\rho}} \equiv \frac{1}{n}\sum_{i=1}^{n} \boldsymbol{e_i} \otimes \boldsymbol{e_i^\dagger} = \frac{1}{2}\bar{S}_\mu \boldsymbol{\sigma_\mu} \tag{2.18}$$

The 4×4 covariance matrix for the instantaneous Stokes parameters is expressed as:

$$\boldsymbol{C} \equiv \langle s \otimes s \rangle - S \otimes S, \tag{2.19}$$

where s is an instantaneous Stokes four-vector, and S represents population mean Stokes parameters. Figure 2.4 gives a schematic presentation of the covariance matrix.

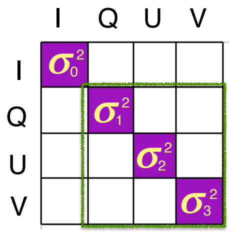

Figure 2.4: Schematic presentation of the 4×4 matrix for the instantaneous Stokes parameters. The cells enclosed by the green rectangle depict the 3×3 matrix of covariances between the elements of the polarization vector.

For a given phase bin (or pulse longitude) the ensemble of the sample mean Stokes parameters is derived from a series of sub-integrations. The covariances between the sample mean Stokes parameters are defined by the 4×4 covariance matrix:

$$\bar{\boldsymbol{C}} = \langle \bar{S} \otimes \bar{S} \rangle - S \otimes S, \tag{2.20}$$

where $S \equiv \langle \bar{S} \rangle = \langle s \rangle$ is again the population mean Stokes parameters.

For statistical and identically distributed instances of the electric field, the covariance matrix of the sample mean Stokes parameters can be expressed via the covariance matrix of the instantaneous Stokes parameters: $\bar{\boldsymbol{C}} = \boldsymbol{C}n^{-1}$, where n is the number of independent instances of the electric field in each Stokes sample.

In pulsar observations we can observe a number of emission regimes. In the simplest case, we receive emission from a single mode of radiation, that we are able to describe as *Single Mode* Stokes sample. In other cases, though, the combination of electromagnetic waves from two modes of emission arising from the same pulsars can be observed. In these circumstances we need to consider three special cases of Stokes sample types: *Disjoint*, *Composite*, and *Superposed.* To illustrate the characteristics of such radiation regimes, we make the following assumptions: (1) we consider emission where the polarized modes are incoherent[13], (2) with normally distributed electric fields, (3) equal population mean intensities I, (4) equal degrees of polarization p, and we assume that (5) the Stokes parameters are measured in the natural basis that are defined by OPMs, (6) modes are statistically independent, (7) the modes are orthogonal and therefore Stokes vectors are equal and point in opposite directions.

Single modes

In this case, the observer receives radiation characterized by an individual mode of emission (that can be associated to, e.g., an individual radiation region within the pulsar magnetosphere). The covariance matrix in the natural basis for the single mode regime

---

[13] By the "incoherent" in this case means that the voltages are uncorrelated.

is given by Equation 33 from van Straten and Tiburzi (2017):

$$\bar{C}_{\text{single}} = \frac{1}{2n}\begin{pmatrix} \|S\|^2 & 2I^2p & 0 & 0 \\ 2I^2p & \|S\|^2 & 0 & 0 \\ 0 & 0 & S^2 & 0 \\ 0 & 0 & 0 & S^2 \end{pmatrix}$$

Here, p denotes the degrees of polarisation, $\|S\|^2 = I^2(1+p)$, and $S^2 = I^2(1-p)$.

We note that S_1 is covariant with S_0, the variance of S_1 equals that of S_0, and that the variances of S_2 and S_3 are equal but lesser than the variances of S_0 and S_1. This means that the distribution of the sample mean Stokes polarization vectors forms a prolate spheroid (as it is shown in Figure 2.5). The ratio of axis in such spheroid is defined by degrees of polarization of the population mean Stokes parameters: $\epsilon = \left(\frac{1+p^2}{1-p^2}\right)^{1/2}$.

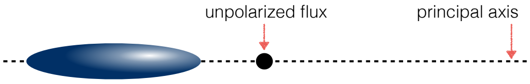

Figure 2.5: Distribution of the sample mean Stokes polarization vectors in the single mode. The principal axis is defined by the population mean polarization of the mode.

Disjoint modes

There are instances in which we receive electric field vectors that are associated with two distinct modes of emission, e.g., $\boldsymbol{e}_A$ and $\boldsymbol{e}_B$. Let assume that these modes are stationary and have population mean Stokes parameters A and B. For each mode the covariances between the sample mean Stokes parameters are $\bar{\boldsymbol{C}}_A = \boldsymbol{C}_A n^{-1}$ and $\bar{\boldsymbol{C}}_B = \boldsymbol{C}_B n^{-1}$ respectively. The electric field instances of the two modes do not necessarily need to have the same statistical distributions.

Disjoint sample modes can be observed when the polarization modes are mutually exclusive within the same Stokes sample, i.e., the integration time is shorter than the time of the mode switching. Thus, the observed instances of the electric field vector in a given Stokes sample belongs to only one of the two modes. In this case the sample mean Stokes parameters are given by either $\bar{A}$, or $\bar{B}$.

Then the covariance matrix in the natural basis defined by the modes is given by Equation 39 of van Straten and Tiburzi (2017):

$$\bar{\mathrm{C}}_{\mathrm{disjoint}} = \frac{1}{2n}\begin{pmatrix} \|S\|^2 & 0 & 0 & 0 \\ 0 & \|S\|^2 + 2nI^2p^2 & 0 & 0 \\ 0 & 0 & S^2 & 0 \\ 0 & 0 & 0 & S^2 \end{pmatrix}$$

In Poincaré space the distribution of the sample mean Stokes polarization vectors would form two ellipsoids in anti-parallel directions (see Figure 2.6).

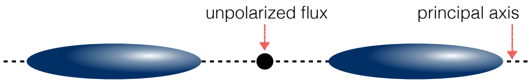

Figure 2.6: Distribution of the sample mean Stokes polarization vectors in the disjoint mode. The principal axis is defined by the population mean polarization vectors of the mode.

Figure 2.6 clearly shows that the distribution is bi-modal, which is not accurately described by a single multivariate normal distribution with a single covariance matrix. The term I^2p^2 that appears in the variance of the principal polarisation S_1 is due to the distance between the centers of the spheroids.

Composite modes

When two disjoint modes are unresolved (e.g, when the resolution of the instrument is coarser than the switching timescale between the modes), then each Stokes sample is made of instances coming from two populations of polarization modes. The composite sample mean Stokes parameters are equal to the weighted average of the sample mean Stokes parameters of each mode.

Then the covariance matrix in the natural basis for a composite mode is given by

Equation 44 from van Straten and Tiburzi (2017):

$$\bar{\mathrm{C}}_{\mathrm{composite}} = \frac{1}{2n}\begin{pmatrix} \|S\|^2 & 0 & 0 & 0 \\ 0 & \|S\|^2 & 0 & 0 \\ 0 & 0 & S^2 & 0 \\ 0 & 0 & 0 & S^2 \end{pmatrix}$$

In Poincaré space the Stokes polarization vectors create a prolate spheroidal distribution which is centered at the origin (e.g., Figure 2.7). The dimensions of the distribution in the Poincare' space for the composite mode regime is the same as for the individual, original modes that contribute to the composite samples. The principal polarization S_1 is no longer covariant with the total intensity S_0.

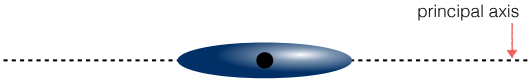

Figure 2.7: Distribution of the sample mean Stokes polarization vectors in the composite mode. The principal axis is defined by the population mean polarization vectors of the mode.

Superposed modes

When the electric field vectors in a Stokes sample are the sum of the electric field vectors from both modes A and B (before that the radiation is detected by the telescope), i.e., $\boldsymbol{e} = \boldsymbol{e}_A + \boldsymbol{e}_B$, then we are in the regime of "superposed" samples.

The covariance matrix in the natural basis for a superposed mode is given by Equation 42 from van Straten and Tiburzi (2017):

$$\bar{\mathrm{C}}_{\mathrm{superposed}} = \frac{1}{2n}\begin{pmatrix} 4I^2 & 0 & 0 & 0 \\ 0 & 4I^2 & 0 & 0 \\ 0 & 0 & 4I^2 & 0 \\ 0 & 0 & 0 & 4I^2 \end{pmatrix}$$

As shown by the covariance matrix, the modes have a spherically-symmetric distribution, see Figure 2.8.

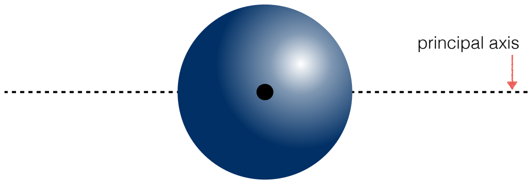

Figure 2.8: Distribution of the sample mean Stokes polarization vectors in the superposed mode. The principal axis is defined by the population mean polarization vectors of the modes.

Given only the population mean Stokes parameters it is challenging to distinguish between the disjoint, composite, and superposed regimes (because these regimes yield equal sample mean Stokes parameters under the aforementioned assumptions). To distinguish the various regimes, we study the covariance matrix of the Stokes parameters[14] through the *principal component analysis* (PCA) approach, which was introduced by Pearson (1901), i.e., we express the coherency matrix through eigendecomposition.

The 4×4 real-valued covariance matrix can be partitioned into the variance of the total intensity, 3×3 covariance matrix of the Stokes polarization vector, and the vector of covariances between the total intensity and the components of polarization vector, and then project Stokes vector to the basis defined by the eigendecomposition of 3×3 covariance matrix. The eigenvectors of the 3×3 matrix represent three axis of the spheroid (orientation of the distribution) and the eigenvalues of the covariance matrix are the measures of the shape of the distribution.

The $3{\times}3$ partition of the covariance matrix can be expressed as an eigen-decomposition

$$C^{3\times3} = \boldsymbol{R}\boldsymbol{D}\boldsymbol{R}^{T} \tag{2.21}$$

Where $\boldsymbol{R}$ is a three-dimensional rotation matrix of eigenvectors, $\boldsymbol{D}$ is a matrix with

---

[14] In other words, the fourth moment of the electric fields

eigenvalues on its diagonal

$$\boldsymbol{D} = \begin{pmatrix} \lambda_1 & 0 & 0 \\ 0 & \lambda_2 & 0 \\ 0 & 0 & \lambda_3 \end{pmatrix}$$

and $\lambda_1 \geqslant \lambda_2 \geqslant \lambda_3$ (see Figure 2.9).

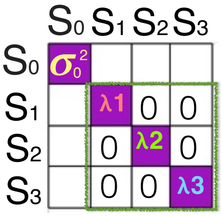

	S0	S1	S2	S3
S0	σ_0^2			
S1		λ1	0	0
S2		0	λ2	0
S3		0	0	λ3

Figure 2.9: Schematic presentation of the PCA outcome after applying it to the 4×4 matrix of covariances between the sample mean Stokes parameters. 3×3 part highlighted with the green rectangle is $\boldsymbol{D}$-matrix.

Figure 2.10 illustrate the PCA outcomes for a PSR B0820+02 observation from the Arecibo P1260 program[15] (Hankins & Rankin, 2010). The top panel exhibits the eigenvalues expected of an incoherent combination of amplitude modulated OPMs. In the case of this specific pulsar, the gap between the profiles of the standard deviation of the total intensity (black line) and λ_1 (red line) points to the presence of amplitude modulation ($\lambda_0 > \lambda_1$). The condition of $\lambda_1 > \lambda_2 \sim \lambda_3$ points to the *prolate* spheroidal distribution which is a very common configuration. Other relations between $\sigma_0, \lambda_1, \lambda_2$, and λ_3 point to the rare cases, as shown in Appendix C.

It is known that pulsar signal can be described as an amplitude-modulated noise (e.g., see Rickett, 1975) with the modulation index (β) represented by the ratio of the standard deviation to the mean of the total intensity. In van Straten and Tiburzi (2017) amplitude modulation is given by the Equation 48:

$$\mathrm{C}' = (\zeta_u^2 + 1)\mathrm{C} + \zeta_u^2 \, S \otimes S,$$

---

[15] `http://www.uvm.edu/~pulsar/P1260.`

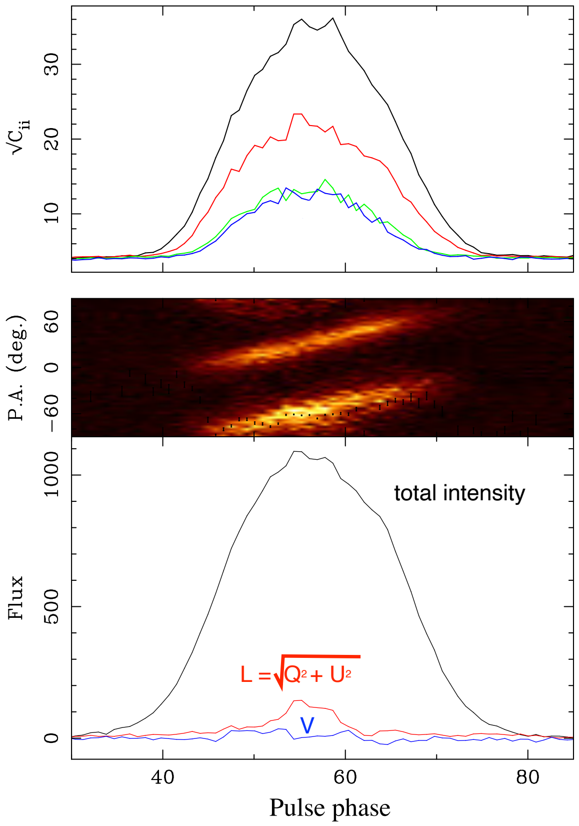

Figure 2.10: Phase-resolved eigendecomposition for the PSR B0820+02 observation from the Arecibo P1260 program (Hankins & Rankin, 2010). The upper panel presents the PCA output, where black is a standard deviation of the total intensity, red - λ_1, green - λ_2, and blue - λ_3; the middle panel is a PA histogram (black-yellow intensity where lightest yellow means the highest intensity); the lower panel is an averaged pulse profile with total intensity (black), linear and circular polarization components (red and blue accordingly).

where ζ_u^2 is the variance of statistically independent real-valued dimensionless scalar u which causes modulation; C is the covariance matrix of unmodulated instantaneous Stokes parameters, S is a population mean Stokes four-vector.

The last term of this equation, i.e., $S \otimes S$, is important in the interpretation of the PCA-output plots. For the **unpolarised** radiation that term shows that only the variance of the total intensity (σ_0^2) is increasing (not the other three Stokes parameters which do not contribute). In the PCA-output plots this is shown by the black lines that are above all other lines, see Figure 2.10 (upper panel) and Figure 2.11 (left and right panels). For the 100% **polarised** radiation both σ_0^2 and λ_1 increase identically. Middle panel of

Figure 2.11 demonstrates such case.

The given covariance matrices and equations that describe composite and superposed samples are applied to the case when the modes are statistically independent. However, the picture changes when any dependence between the modes occurs. Some examples of the possible independence loss are shown in Figure 2.11. Three regions of interest identified thanks to the PCA analysis and eigen-decomposition (at the bottom panels) are marked with ellipses. For pulsar PSR B1919+21 (left) we can identify a region where $\lambda_1 \simeq \lambda_2$, that implies an oblate distribution in the Poincare' sphere. PSR B1929+10 (middle) has a region where $\lambda_1 > \sigma_0$(total intensity). Finally, PSR B2044+15 has a region where $\lambda_1 \simeq \lambda_2$ which also points to an oblate distribution. These examples are to demonstrate the potential of the adopted approach in identifying interesting emission behaviours in the analysed pulsars.

Pulsars that feature exceptional behaviours in Figure 2.11 will be discussed with more details in Chapter 3 (left panel) and Chapter 4 (middle and right panels).

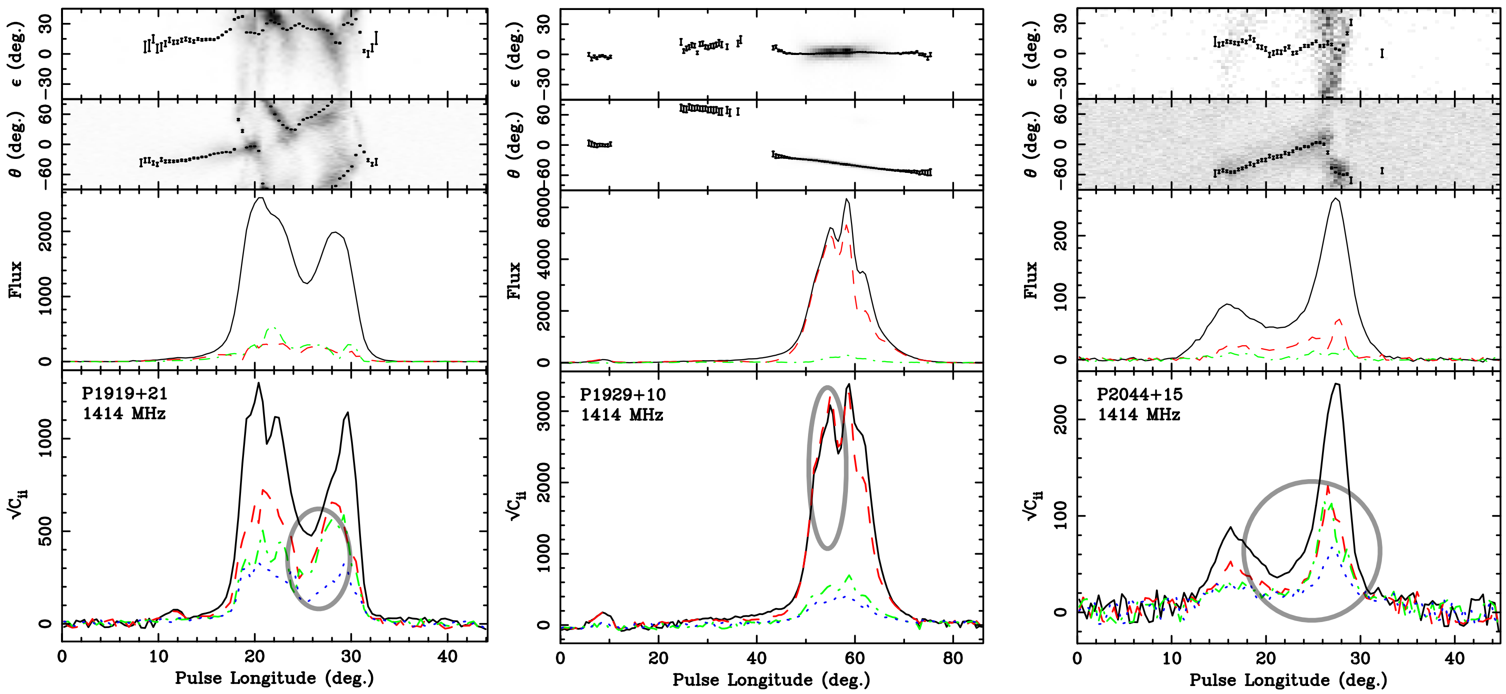

Figure 2.11: Examples of three pulsars that, according to their eigendecompositions, demonstrate deviations from the described sample modes. Their polarization vectors distribution shapes are supposed to differ from the distributions described by single, disjoint, superposed, or composite modes. Areas of interest are highlighted by the ellipses.

Each pulsar has four panels (from top to bottom): first panel shows both the ellipticity angle of the average Stokes parameters (points with error bars) and a histogram of the ellipticity angles of the individual pulses (greyscale intensity), the next panel presents both the position angle of the average Stokes parameters and a histogram of the position angles of the individual pulses, third panel is averaged profile in total intensity (black), linear (red) and circular polarisation (green). In the bottom panel the black solid line shows the standard deviation of the total intensity, and the red dashed, green dot-dashed, and blue dotted lines display the square roots of the eigenvalues (from largest to smallest, respectively) of the 3×3 partition of the covariance matrix that describes the fluctuations of the polarisation vector $\boldsymbol{S} = (Q, U, V)$.

Chapter 3

The polarisation of the drifting sub-pulses from PSR B1919+21

This chapter is based on *"The polarisation of the drifting sub-pulses from PSR B1919+21"* Primak, N., Tiburzi, C., van Straten, W., Dyks, J. & Gulyaev, S., A&A, 657, A34, (2022, January).

In this chapter the statistical methods of studying single-pulse emission for various types of pulsars are validated by the application to the brightest pulsar PSR B1919+21 and the simultaneous direct study of its longitude-resolved single pulse emission. In this study several methods of analysis and visualization are applied and compared. In particular: eigenvalue analysis of the longitude-resolved covariances between the Stokes parameters, longitude-resolved 3-dimensional scatter plots of the normalised Stokes vectors in the Poincaré sphere, auto- and cross-correlations between the Stokes parameters as a function of offset in pulse longitude and lag in pulse number, as well as mean drift bands of polarisation state created by averaging the Stokes parameters and quantities derived from them synchronously with the drifting sub-pulse modulation period are applied and compared.

3.1 Introduction

The physics of the pulsar magnetosphere, including the generation and propagation of the observed radio emission, remains poorly understood (Melrose & Yuen, 2016; Melrose et al., 2021). A viable physical model should explain the origin of coherent emission over a broad range of frequencies, the high degree of polarisation, and a wide range of characteristic phenomena, such as nulling (Backer, 1970), giant pulses (Romani & Johnston, 2001; Hankins et al., 2003; Knight et al., 2006), the occurrence of orthogonally polarised modes (e.g., Ekers & Moffet, 1969; Manchester et al., 1975; Stinebring et al., 1984), and sub-pulse drifting (Drake & Craft, 1968). The models proposed to date are able to explain some of the observed phenomena, but fail to describe others.

Drifting sub-pulses (Drake & Craft, 1968) are observed in almost half of the pulsar population (Weltevrede et al., 2006, 2007; Basu et al., 2019). In addition to the spin period of the pulsar (P_1), drifting is usually characterised by two periods: 1) the longitudinal interval or separation between successive drift bands (P_2); and 2) the modulation interval, or drift cycle, expressed in pulsar rotations between drift bands (P_3). Different methods exist to measure these periods. For example, Backer (1973) and Backer et al. (1975) introduce the longitude-resolved fluctuation spectrum (LRFS) method, based on one-dimensional Fourier transforms of single-pulse intensities as a function of pulse longitude. Deshpande and Rankin (2001) develops the harmonic-resolved fluctuation spectrum, and Edwards and Stappers (2002) elaborates an equivalent approach based on the two-dimensional Fourier transform. Edwards (2004) (hereafter, E04) extends the LRFS to study the cross-spectral power between the four Stokes parameters, the polarisation LRFS (PLRFS). Drifting sub-pulses are also studied using the longitude-resolved cross-correlation function (Prószyński & Wolszczan, 1986), two-dimensional auto-correlation function (Taylor et al., 1975), and P_3 folding (Taylor et al., 1971;

R. T. Edwards et al., 2003).

The origin of drifting sub-pulses is unclear. One scenario, known as the “rotating carousel” model (Ruderman & Sutherland, 1975; Rankin, 1993; Rankin et al., 2006), suggests that the observed radiation is produced by outflowing streams of charged particles that circulate around the magnetic pole due to **E** × **B** drift, where **E** and **B** are the electric and magnetic fields in the vicinity of the polar cap. Owing to the carousel motion, the streams drift across the primary beam of the pulsar, such that the associated sub-pulses appear to shift in pulse longitude as a function of time.

In relatively rare cases, sub-pulses are observed to periodically switch between orthogonally polarised states synchronously with the drift cycle of the modulated total intensity. OPM switching is evident as bi-modal distributions of single-pulse position angles (PAs), with peaks offset by 90° (Ekers & Moffet, 1969; Manchester et al., 1975; Ramachandran et al., 2002). Many pulsars exhibit OPM switching (Stinebring et al., 1984); however, to date, only five pulsars are reported to exhibit periodic OPM switching that is synchronised with the drifting sub-pulse modulation: PSRs B0809+74 (Taylor et al., 1971; Ramachandran et al., 2002; E04), B1237+25 (Rankin & Ramachandran, 2003), B0320+39, B0818−13 (E04), and B0031−07 (Ilie et al., 2020).

To explain the synchronicity of the OPM switching and drifting sub-pulses, Rankin and Ramachandran (2003) suggest a revision of the carousel model in which the emission is split into two rotating sub-beam structures, each corresponding to one of the observed OPMs. Owing to birefringence in the pulsar magnetosphere, the orthogonally polarised sub-beams are offset in both azimuthal and meridional directions with respect to the magnetic axis (Rankin et al., 2006), such that the observed switching between modes is synchronous with the modulation of total intensity caused by **E** × **B** drifting.

E04 presents examples of periodic modulations of the Stokes parameters in three pulsars with drifting sub-pulses that cannot be explained by cyclic switching between incoherently superposed OPMs (the result of which would have a linear distribution in

Poincaré space). Rather, two of the three pulsars exhibit periodic fluctuations such that the tip of the Stokes polarisation vector draws an ellipse in Poincaré space. E04 discovers and studies these drift-modulated elliptical variations of the Stokes polarisation vector through eigenvalue analysis of the PLRFS. Summing the spectral density tensor of the PLRFS over all harmonics is equivalent to computing the longitude-resolved covariances between the Stokes parameters, which can be used to study stochastic fluctuations of the Stokes parameters (McKinnon, 2004; Edwards & Stappers, 2004). van Straten (2009) and van Straten and Tiburzi (2017) develop the mathematical foundation required to interpret the 4×4 matrix of covariances between the Stokes parameters by considering three different regimes of incoherent mode superposition (disjoint, superposed, and composite) and the effects of amplitude modulation.

Analysing the covariances between the Stokes parameters provides a way to extend the study of single-pulse variability, such as drifting and OPM switching, to faint pulsars. For the majority of pulsars, individual pulses cannot be detected and it is not possible to directly study single-pulse variability using scatter plots of the Stokes parameters (McKinnon, 2004) or longitude-resolved histograms of polarisation state (Stinebring et al., 1984; Edwards & Stappers, 2004). For the typical pulsar, there is also insufficient signal to detect the local sub-pulse drift period P_3, which must be estimated in sufficiently short segments of time over which P_3 can be considered stable in order to average the Stokes parameters synchronously with the drift period (Taylor et al., 1971; Weltevrede et al., 2006). Therefore, to study the majority of pulsars, it is necessary to develop statistical descriptions of sub-pulse variability that can be used to integrate over a large number of pulses. These can be applied to develop a more complete picture of single-pulse variability across the entire pulsar population and provide a deeper understanding of the physics of radio wave emission and propagation in the pulsar magnetosphere.

To prepare to study weak sources, we must first study bright pulsars, whose single-pulse variability can be analysed using methods that are applicable only at high signal-to-noise ratio (histograms, scatter plots, P_3-folds, etc.) and connected with features derived from fourth-order moments (e.g. covariances between the Stokes parameters and the cross-correlations between them as a function of both longitudinal and temporal lags). These connections contribute toward the development of an interpretive framework from which we can infer the characteristics of single-pulse variability from statistical quantities that can be integrated over sufficiently long intervals.

In this article we present one further step in the development of such a framework through a case study of PSR B1919+21. As the first pulsar discovered by Jocelyn Bell (Hewish et al., 1968), PSR B1919+21 is among the most studied and, quite possibly as a consequence of such scrutiny, it has proven more exceptional than exemplary. For example, Rankin (1983) first regards its average profile as a “barely resolved conal-double”, in which the line of sight is neither tangential nor central to a hollow cone of emission. Rankin et al. (1989) later argue that PSR B1919+21 should be classified as a five-component multiple profile, based on evidence that the two main components are each composed of an unresolved pair of components produced as the line of sight crosses inner and outer cones, and that the saddle region between the two main components exhibits properties of core emission. With the caveat that there appears to be a weak trace of central core emission, Olszanski et al. (2019) classify PSR B1919+21 as having a conal quadruple profile produced by a line of sight that that cuts both inner and outer cones more centrally without passing near the core beam. With a spin-down energy of $\dot{E} \sim 2.2\times10^{31}$ erg s^{-1}, the radio signal from PSR B1919+21 is expected to be dominated by conal emission (Rankin et al., 2020). Core emission that supports a five-component multiple profile classification appears to be more evident at radio frequencies below 80 MHz (Bondonneau et al., 2021).

Compounding the challenges associated with classifying its emission, PSR B1919+21 shows no evidence of the radius-to-frequency mapping thought to be associated with outer-cone component pairs (Mitra & Rankin, 2002). Its main pulse is also preceded by weak emission (Weisberg et al., 1999) that appears more clearly at high radio frequencies as a separate leading component well beyond its putative outer cone (Olszanski et al., 2019). Furthermore, it is not possible to reliably constrain the magnetic field and viewing geometry of PSR B1919+21, owing to complex variations of its longitude-resolved position angle (P.A.) that depart significantly from the predictions of the rotating vector model (Radhakrishnan & Cooke, 1969). For many pulsars, deviations from the RVM can be described by transitions in the dominance of orthogonally polarised modes of emission, most clearly evident as jumps of 90° in the P.A. curve (Everett & Weisberg, 2001). However, at some radio frequencies, PSR B1919+21 exhibits a sharp 45° jump in P.A. near the profile peak, which can be interpreted as a sudden narrowing of the distribution of phase delay between the natural modes of wave propagation in the pulsar magnetosphere (Dyks, 2019). In Fig. 18 of Mitra et al. (2015), some of the smaller distortions of the P.A. profile appear to be associated with absorption features in the total intensity that were first detected at frequencies below 200 MHz (Hankins, 1973; Cordes, 1975). These striking features of both the single-pulse and average profiles of PSR B1919+21 remain poorly understood.

Although the first-discovered pulsar clearly warrants further study, none of the above difficulties or exceptions motivate its selection for this work. Rather, as described in Section 3.2, PSR B1919+21 was objectively selected owing to the anomalous distribution of its polarisation state, as identified by applying novel statistical methods to publicly available data. In Section 3.3 we report on the results of applying a wide variety of methods to analyse the variability of its single-pulse polarisation state. In Section 3.4 we discuss and interpret the results, which are summarised in Section 3.5.

3.2 Data set

The observations used in this article are part of a larger single-pulse dataset collected at the Arecibo Radio Telescope, mainly from 1988 to 1992, at multiple frequencies, and presented and described in detail by Hankins and Rankin (2010). From the polarisation-calibrated full Stokes data summarised in Table 2 of Hankins and Rankin (2010), we selected 32 pulsars observed at one or two central frequencies, 1414 MHz and 430 MHz, as part of the P1260 program.[1]

After computing the eigenvalues of the longitude-resolved covariances between the Stokes parameters for each observation, we searched for behaviour that is inconsistent with incoherent OPM superposition (van Straten & Tiburzi, 2017). That is, we searched for evidence of correlations between the Stokes parameters that are not consistent with a prolate spheroidal distribution of the polarisation vector. The observation of PSR B1919+21 at 1414 MHz clearly stands out as anomalous because, over a wide region of pulse longitude, the distribution of the Stokes polarisation vector is characterised by an oblate spheroid.

PSR B1919+21 produces complex patterns in the P.A. distributions of single pulse polarisation state (e.g., Fig. 18 of Mitra et al., 2015). It also exhibits sub-pulse drift with band separations $P_2 \approx 10 - 17$ ms and $P_3 \approx 4 - 4.4\ P_1$ (Backer, 1973; Hankins, 1973; Cordes, 1975; Wolszczan, 1978; Prószyński & Wolszczan, 1986; Weltevrede et al., 2007). It has three distinct drifting components that are not well separated in pulse longitude; that is, the sub-pulses from different components drift through shared regions of pulse longitude. The definitions of the drift-band region boundaries depend on radio frequency; however, P_3 is not frequency-dependent and is common to all three drift band regions (Prószyński & Wolszczan, 1986). Although the single-pulse polarisation and sub-pulse drifting properties of PSR B1919+21 have been separately analysed, the

---

[1] These data are located at `http://www.uvm.edu/~pulsar/P1260`.

connection between them has not been studied in detail.[2] Therefore, the remainder of our analysis focuses on PSR B1919+21.

3.3 Methods and results

The statistical methods applied in this work begin with an ensemble of sample mean Stokes 4-vectors

$$\mathrm{S}(\phi, t) = [\mathrm{I}(\phi, t), \mathrm{Q}(\phi, t), \mathrm{U}(\phi, t), \mathrm{V}(\phi, t)]^T \tag{3.1}$$

sampled as a function of pulse longitude ϕ, and pulsar rotation (or turn) t. Here, x^T denotes the transpose of vector x; i.e., the Stokes 4-vector is treated as a column vector. The sample mean Stokes parameters are averaged over a single interval of pulse longitude, which for the PSR B1919+21 data presented in this study is $\sim 0.325°$, or about 1.2 ms. The 4×4 matrix of cross-covariances between the Stokes parameters at two pulse longitudes, ϕ_1 and ϕ_2, as a function of time-lag in pulsar rotations $\tau > 0$ is given by

$$K(\phi_1, \phi_2; \tau) = \frac{1}{N_{\text{pulse}}} \sum_{t=\tau+1}^{N_{\text{pulse}}} \bar{S}(\phi_1, t - \tau) \otimes \bar{S}(\phi_2, t)^T, \tag{3.2}$$

where N_{pulse} is the number of pulses, $\bar{S}$ represents the Stokes parameters after subtracting a local mean value, and $\otimes$ represents an outer product. If $K_{\mu\nu}(\phi_1, \phi_2; \tau)$ is the element in row μ and column ν, then the cross-covariance at negative lag is given by transposing both μ and ν, and ϕ_1 and ϕ_2; i.e.

$$K_{\mu\nu}(\phi_1, \phi_2; -\tau) = K_{\nu\mu}(\phi_2, \phi_1; \tau). \tag{3.3}$$

---

[2] (Manchester et al., 1975) noted the possibility of correlation between polarisation state and the drifting sub-pulse structures.

3.3.1 Longitude-resolved covariances between the Stokes parameters

As in McKinnon (2004) and Edwards and Stappers (2004), we first studied the longitude-resolved 4×4 matrix of covariances between the Stokes parameters,

$$C(\phi) = K(\phi, \phi; 0) \tag{3.4}$$

by computing the eigendecomposition of the 3×3 partition of C corresponding to the three-dimensional polarisation vector, $\boldsymbol{S} = (\mathrm{Q}, \mathrm{U}, \mathrm{V})$. The eigenvectors and eigenvalues derived from this analysis describe the distribution of the polarisation vectors in Poincaré space. At a given pulse longitude ϕ, the eigenvectors define the principle axes of the distribution of the polarisation vectors; the eigenvalues λ_i, $i \in \{1, 2, 3\}$, are equal to the variances of the distribution in the directions of the corresponding eigenvectors. For example, when $\lambda_1 > \lambda_2 = \lambda_3$, the distribution of the polarisation vectors has a prolate spheroidal shape, as expected for incoherent OPM superposition (van Straten & Tiburzi, 2017).

The derived eigenvalues are shown in panel d) of Figure 3.1. Over the region of pulse longitude $-5° \lesssim \phi \lesssim 3°$, the eigenvalues indicate an unexpected and uncommon *oblate distribution* of the polarisation state, which is the primary focus of the following section. The longitude-resolved standard deviation of the total intensity also highlights a component around longitude $-12°$ that is most likely related to the precursor detected at 4.6 GHz (Olszanski et al., 2019). The phase-resolved modulation index of this component is ~ 1.2 to 1.3, around two to three times the modulation index in the main profile, which varies between ~ 0.4 and 0.7.

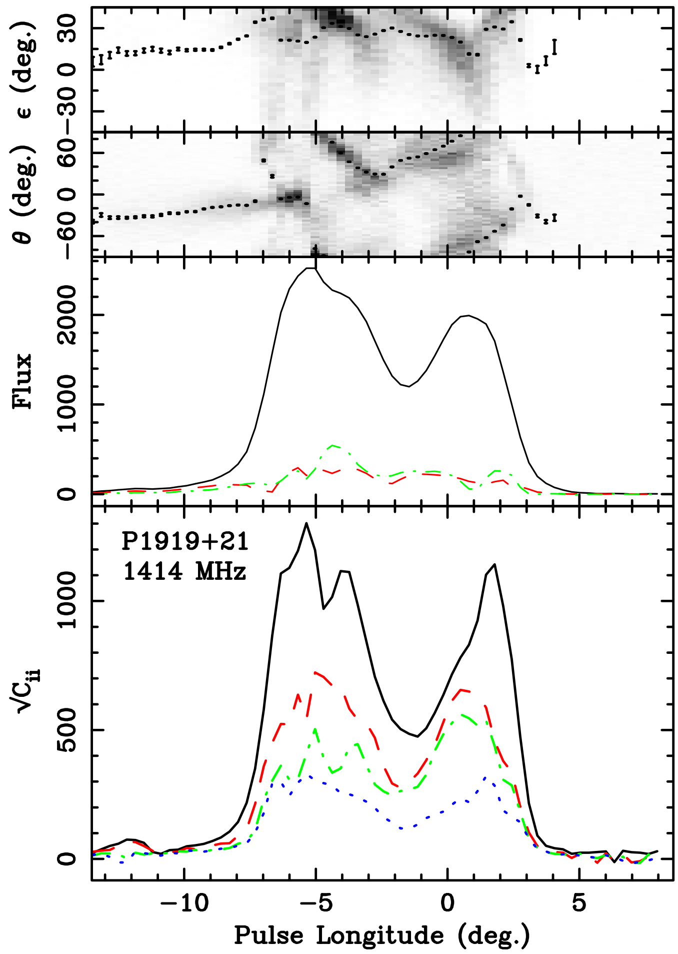

Figure 3.1: Longitude-resolved mean and variability of the polarised emission from PSR B1919+21 at 1414 MHz. Panel a) shows both the ellipticity angle of the average Stokes parameters (points with error bars) and a histogram of the ellipticity angles of the individual pulses (greyscale intensity). Similarly, panel b) shows both the position angle of the average Stokes parameters and a histogram of the position angles of the individual pulses. Panel c) shows the averaged profile in total intensity (black, upper solid), linear (red, dashed) and circular polarisation (blue, dot-dashed). These profiles were obtained by averaging together all the available data. In panel d), the black solid line shows the standard deviation of the total intensity, and the red dashed, green dot-dashed, and blue dotted lines display the square roots of the eigenvalues (from largest to smallest, respectively) of the 3×3 partition of the covariance matrix that describes the fluctuations of the polarisation vector $\boldsymbol{S} = (Q, U, V)$.

3.3.2 Distribution of the polarisation vectors

As in McKinnon (2004), we produced scatter plots of the Stokes polarisation vector using two-dimensional projections of the 3-dimensional Poincaré space. In Figure 3.2, one such projected scatter plot is divided into a 25×25 grid and the number of points in each pixel is integrated. Rather than the expected concentration of points near the origin, the polarisation states are concentrated on the circumference of a ring that is offset from the origin.

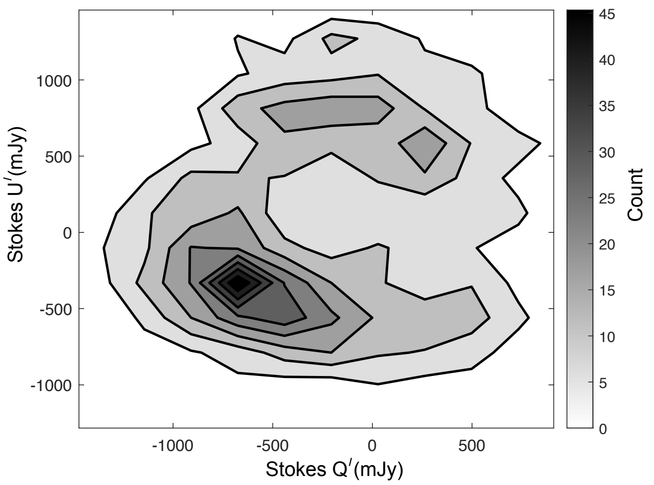

Figure 3.2: Integrated number of single-pulse polarisation states projected onto a two-dimensional plane that is normal to the minor axis of the oblate spheroidal distribution observed at pulse longitude 0°. The greyscale intensity represents the count of instances in each pixel after integrating 1100 single pulses; contours are spaced at intervals of 5 counts. The angle between the Stokes V axis and the normal to the Q'–U' plane is 7.2°.

If the Stokes vectors are normalised by the total intensity, then the normalised polarisation vectors will lie within a sphere of unit radius known as the Poincaré sphere. Visualising the polarisation state in the Poincaré sphere offers a couple of advantages: first, the length of the normalised polarisation vector indicates the degree of polarisation; second, assuming that all four Stokes parameters are modulated by the same function, normalisation by Stokes I reduces additional scatter due to amplitude-modulation that is intrinsic to the pulsar and/or owing to scintillation in the interstellar medium.

Normalisation by Stokes I is possible only for very bright single-pulse observations, where the total intensity is significantly different from zero. Therefore, to verify that this normalisation is valid, we plot histograms of Stokes I in the on-pulse regions of interest. As an example, Figure 3.3 shows that the total intensity is well above zero at ϕ = 0°, where the oblate distribution of the Stokes vectors is observed. The median of the off-pulse noise (i.e., the median value of the standard deviation estimated from the off-pulse longitudes of 200 consecutive pulses) varies as a function of time, most likely owing to the source moving away from the principal axis of the primary reflector. At the start of the observation, the median off-pulse noise is 75 mJy and at the end it was 134 mJy. The vertical dashed line in Figure 3.3 depicts the maximum value of the standard deviation of the off-pulse noise (at the end of the observation).

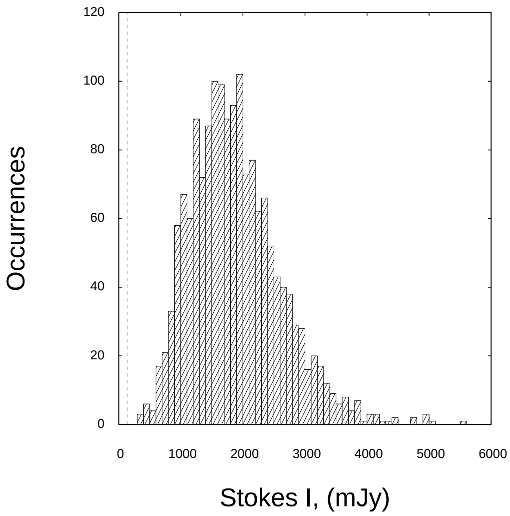

Figure 3.3: Total intensity histogram at pulse longitude 0°, where the Stokes parameters are toroidally distributed. This example demonstrates the validity of Stokes parameters normalisation. Stokes I has a similar behaviour throughout all pulse longitudes. The vertical dashed line shows the maximum value of the median off-pulse noise.

This figure shows that, at this pulse longitude, it is possible to visualise scatter plots of the polarisation state in either Poincaré space or within the Poincaré sphere. In Figure 3.4, the projected scatter plots of the normalised polarisation vectors at ϕ = 0° show that the distribution is not an oblate spheroid, but a torus of revolution.

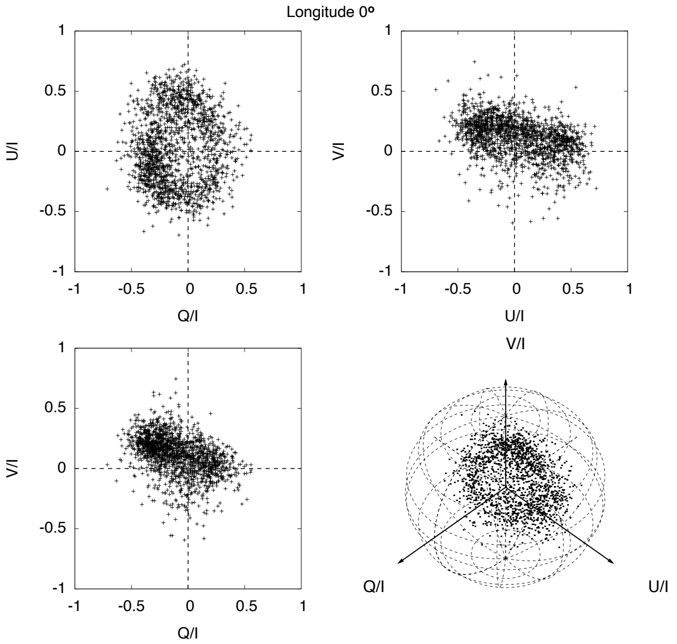

Figure 3.4: Distribution of the normalised Stokes parameters in the Poincaré sphere at ϕ 0.°. The two upper panels and the lower-left panel show the projected, 2D distribution of the Stokes parameters in the three planes normal to the basis vectors, and the 3D distribution is displayed in the lower-right panel.

A toroidal distribution is clearly detectable at $-0.8^\circ \lesssim \phi \lesssim 0.8^\circ$, and a partial torus appears to be visible in adjacent pulse ranges $-3.9^\circ \lesssim \phi \lesssim -1^\circ$, and $1^\circ \lesssim \phi \lesssim 1.6^\circ$. Scatter plots for four neighboring longitudes are presented in Figure A.1; these show that, as a function of pulse longitude, the torus changes orientation and shifts its center. Moreover, the centers of the toroidal distributions are offset from the origin of Poincaré sphere axis at all longitudes. For comparison, we also present projected scatter plots of the normalised Stokes polarisation vector observed at $\phi \simeq -6.8^\circ$ in Figure A.2. The distribution shown in this scatter plot is consistent with Figure 3.1, where the eigenvalues at this longitude indicate a prolate spheroid.

3.3.3 Correlations of Stokes parameters

Together with the 3D distributions of the Stokes parameters it is important to know whether the torus formed in an orderly or a random way. To this end, we explored the spatial and temporal relationships between the polarisation vectors via

(i) the longitude-offset cross-correlation function of the Stokes parameters with respect to a reference longitude; and

(ii) the longitude-resolved cross-correlation functions between two different Stokes parameters.

For each element of $R(\phi_1, \phi_2; \tau)$, we computed the Pearson correlation coefficient,

$$R_{\mu\nu}(\phi_1, \phi_2; \tau) = \frac{K_{\mu\nu}(\phi_1, \phi_2; \tau)}{\sigma_\mu(\phi_1)\sigma_\nu(\phi_2)} \tag{3.5}$$

where $\mu, \nu \in \{\text{I,Q,U,V}\}$, and the longitude-resolved variance is given by

$$\sigma_\mu^2(\phi) = C_{\mu\mu}(\phi) = K_{\mu\mu}(\phi, \phi; 0) \tag{3.6}$$

Prior to computing $R(\phi_1, \phi_2; \tau)$, we subtracted the moving average of the Stokes parameters from each pulse longitude, computed with a boxcar size of 100 pulse periods, which is smaller than the scintillation time at 1.4 GHz (~ 500 to 1500 s; Cordes, 1986; Bhat et al., 1999).

3.3.3.1 Longitude-offset cross-correlations for each Stokes parameter

Figures 3.5 and 3.6 present the longitude-offset cross-correlation coefficients,

$$R'_\mu(\Delta\phi, \tau; \phi_0) = R_{\mu\mu}(\phi_0, \phi_0 + \Delta\phi; \tau),$$

with $\mu \in \{\text{I,Q,U,V}\}$, as a function of lag τ and longitude offset $\Delta\phi$ with respect to the reference pulse longitude ϕ_0.

The reference longitude of Figure 3.5 is $\phi_0 \simeq -6.8°$, which is within a region of pulse longitude that is characterised by a prolate spheroidal distribution of the

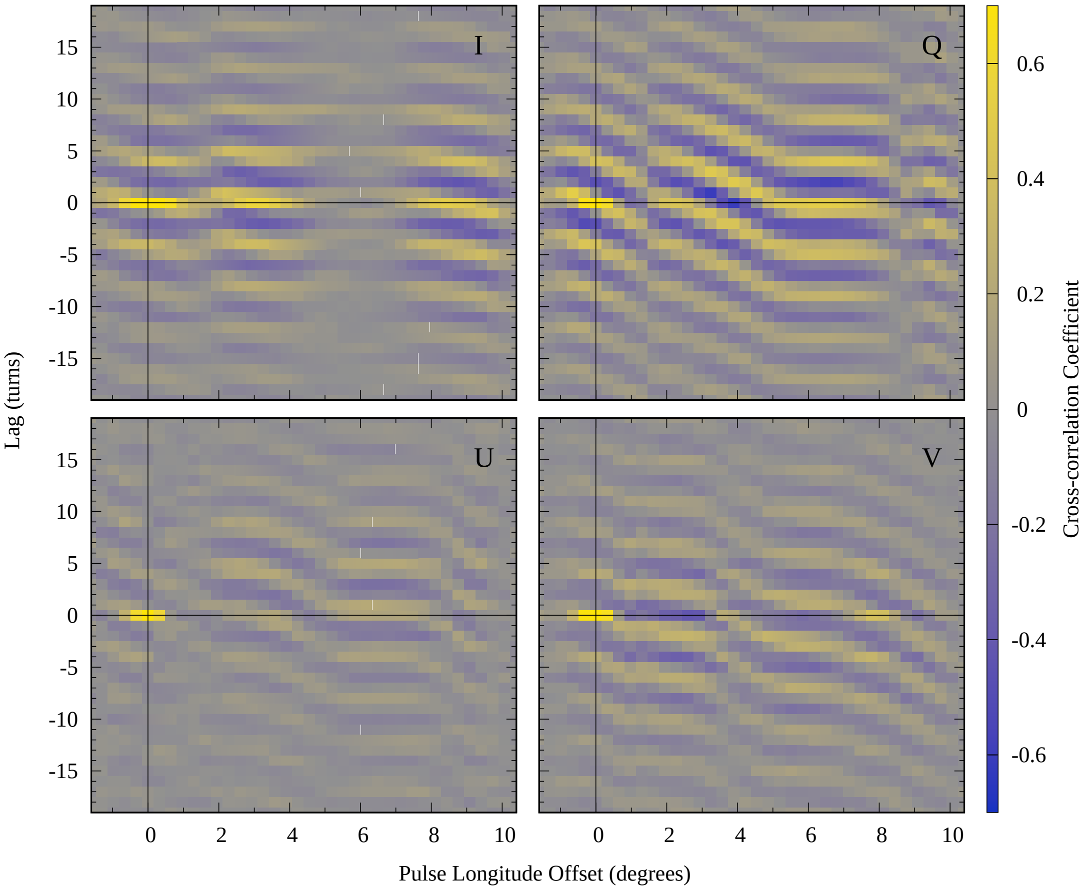

Figure 3.5: Longitude-offset cross-correlations of each Stokes parameter as a function of lag τ and longitude offset $\Delta\phi$ with respect to the reference pulse longitude $\phi_0 \simeq -6.8^\circ$. In each panel, a horizontal black line marks zero lag and a vertical black line marks zero longitude offset.

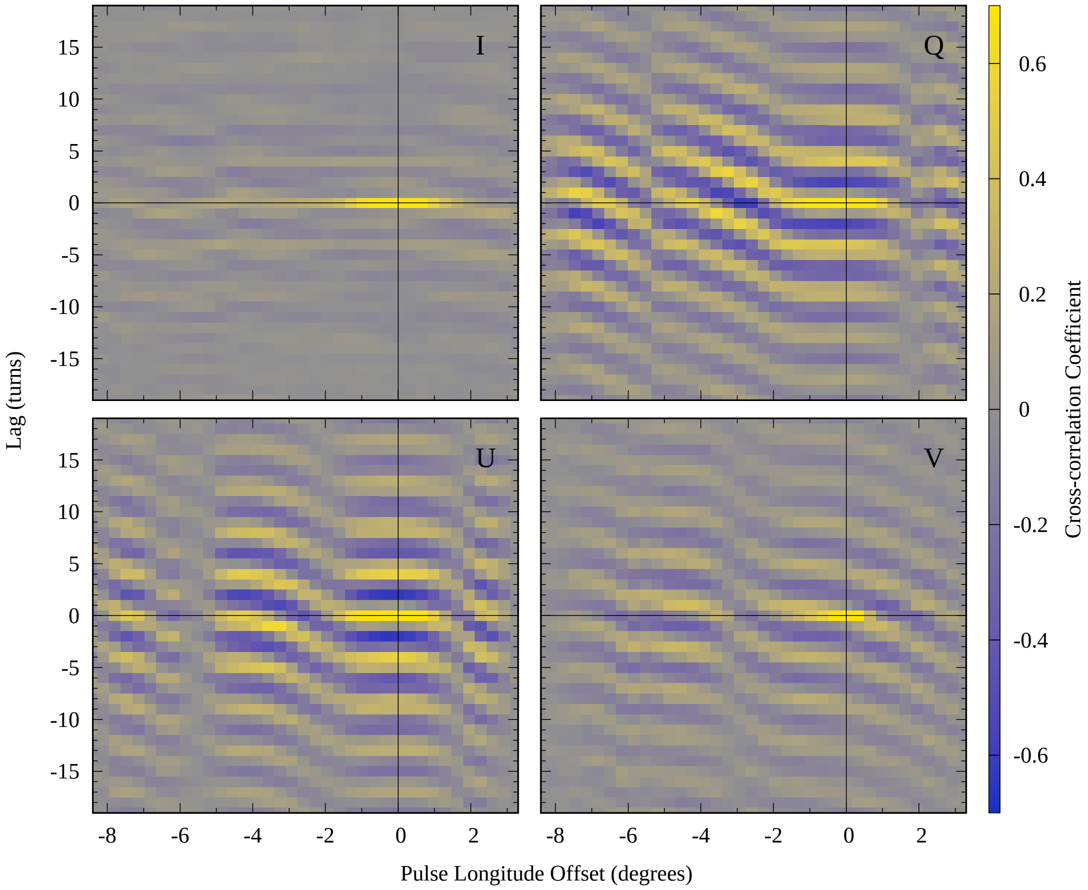

Figure 3.6: As for Figure 3.5, but for reference longitude $\phi_0 = 0°$, in the middle of the region where the toroidal distribution of the polarisation vector in the Poincaré sphere is observed.

Stokes parameters that is approximately centered at the origin of the Poincaré sphere. Figure 3.5 shows three main drift regions in total intensity, as first noted by Prószyński and Wolszczan (1986). In this plot, the first drift-band lies between the beginning of the on-pulse region and a pulse longitude of approximately -5.4° (corresponding to a longitude offset of 1.4°), the second drift band starts at the end of the first band and spans up to a longitude of about -2.6° (longitude offset 4.5°), and the third drift band lies approximately between longitudes -0.6° and 3°.

The periodic modulation of total intensity at the reference longitude is remarkably correlated with the modulation in the rest of the on-pulse region, even as far away as longitude offset $\Delta\phi \simeq 9.7^{\circ}$. However, this correlation is diminished over the saddle region $5^{\circ} \lesssim \Delta\phi \lesssim 7^{\circ}$ (corresponding to longitudes $-1.8^{\circ} \lesssim \phi \lesssim 0.2^{\circ}$). This region of diminished correlation in total intensity partially overlaps the region ($5.5^{\circ} \lesssim \Delta\phi \lesssim 7.5^{\circ}$) where the periodic modulations of Stokes Q and U exhibit little or no drifting (i.e., the slope is flat). The periodic modulations of Stokes Q, U, and V remain strong in this region.

The reference longitude of Figure 3.6 is $\phi_0 = 0^{\circ}$, which is in the center of the longitude region where the toroidal distribution of Stokes (Q, U, V) in the Poincaré sphere is observed. Figure 3.6 reaffirms that the total intensity in this region is not highly correlated with intensity in the rest of the on-pulse region. In both Figure 3.5 and Figure 3.6, the longitudinal discontinuity in the modulation pattern of Stokes Q at $\phi \simeq -5.4^{\circ}$ occurs at the transition between OPMs that is also evident in Figure 3.1.

3.3.3.2 Longitude-resolved Stokes Q,U,V cross-correlations

Figure 3.7 presents the longitude-resolved cross-correlation coefficients,

$$R'_{\mu\nu}(\phi,\tau) = R_{\mu\nu}(\phi,\phi;\tau),$$

with $(\mu, \nu) \in \{$(Q,U),(U,V),(V,Q)$\}$, as a function of lag τ and pulse longitude ϕ. Owing to symmetry, these three panels depict all of the information contained in the 6 off-diagonal components of the 4×4 matrix, $R'(\phi, \tau)$; furthermore, taking the one-dimensional Fourier transforms of the components of $R'(\phi, \tau)$ along the τ axis yields the PLRFS studied by E04. As in the PLRFS, the correlations between the Stokes parameters indicate their cyclic oscillation about an elliptical path in Poincaré space. They also indicate that the normal to this elliptical path precesses as a function of pulse longitude.

For example, over $-1.5^\circ \lesssim \phi \lesssim 1^\circ$, $R'_{\mathrm{QU}}(\phi, \tau)$ is antisymmetric about $\tau = 0$, which indicates that the oscillations of Stokes Q and U are 90° out of phase. This is consistent with the periodic cycling of the polarisation vector around an elliptical path in a plane that is only slightly offset from the Q–U plane[3] over this range of pulse longitudes.

At earlier pulse longitudes within this region, e.g. $-1.5^\circ \lesssim \phi \lesssim 0^\circ$, $R'_{\mathrm{VQ}}(\phi, \tau)$ is negative and symmetric about $\tau = 0$, which indicates that Stokes Q and V are anti-correlated (180° out of phase). This is consistent with the anti-correlation that is visible in the Q–V scatter plots in Figure 3.4 and the upper panels of Figure A.1. Furthermore, the oscillations of Stokes U and V are 90° out of phase, as indicated by the antisymmetry of $R'_{\mathrm{UV}}(\phi, \tau)$. Both the anticorrelation of Stokes Q and V and the antisymmetry of Stokes U and V are consistent with an axis of revolution of the torus that lies primarily in the Q-V plane, such that there is an apparently elliptical path projected into the U-V plane.

Similarly, at later pulse longitudes within this region, e.g. $0^\circ \lesssim \phi \lesssim 1^\circ$, $R'_{\mathrm{UV}}(\phi, \tau)$ is negative and symmetric about $\tau = 0$, which indicates that Stokes U and V are anti-correlated. This is consistent with the anti-correlation that is visible in the U–V scatter plots in Figure 3.4 and the lower panels of Figure A.1. Furthermore, the oscillations of Stokes Q and V are 90° out of phase, as indicated by the antisymmetry of $R'_{\mathrm{VQ}}(\phi, \tau)$.

---

[3] The offset varies from pulse longitude to pulse longitude.

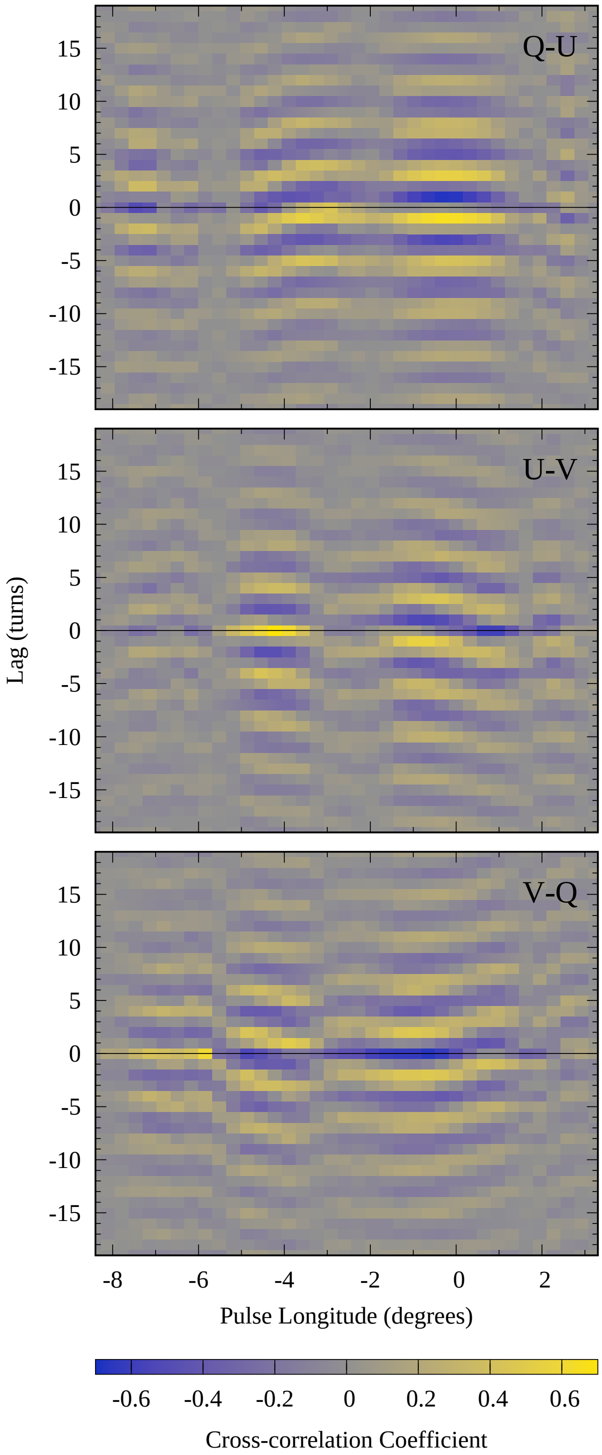

Figure 3.7: Longitude-resolved Stokes Q,U,V cross-correlations as a function of lag τ and pulse longitude ϕ. From top to bottom are plotted the correlations between Stokes Q and U, Stokes U and V, and Stokes V and Q. In each panel, a horizontal black line marks zero lag.

Both the anticorrelation of Stokes U and V and the antisymmetry of Stokes Q and V are consistent with an axis of revolution of the torus that lies primarily in the U-V plane, such that there is an apparently elliptical path projected into the Q-V plane. That is, as a function of pulse longitude, the axis of revolution of the torus precesses about the Stokes V axis, rotating from primarily in the Q–V plane to primarily in the U-V plane.

3.3.4 Average drift band

As in Taylor et al. (1971) and R. T. Edwards et al. (2003), we estimated the polarisation state of the mean drift bands by averaging the single-pulse Stokes parameters and quantities derived from them synchronously with the modulation period, $P_3 \simeq 4.2 P_1$, which was determined via short-time Fourier transform analysis. The results of P_3 folding the first 500 pulses in the data set are shown in Figure 3.8, which exhibits several noteworthy features.

In all panels, pulse longitude $\phi \simeq -5.4^\circ$ marks several significant changes in the sub-pulse modulation pattern. First, there is a 180° phase shift in the modulation of the total intensity associated with the transition from region 1 to region 2 of the mean drift band. The overlap of drift regions 1 and 2 leads to an apparent doubling of the modulation frequency, which is also detected in Fig. A.21 of Weltevrede et al. (2007), where it is described as "$P_3 = 2P_0$ flickering". Overlapping and offset drift regions also explain the reduced the longitude-resolved modulation index observed over this region of pulse longitude (Weltevrede et al., 2006).

The transition from drift region 1 to drift region 2 is accompanied by a longitudinal transition between orthogonally polarised modes, which is also clearly visible in the position angle histogram plotted in panel b) of Figure 3.1. Before this transition (over $-6.3^\circ \lesssim \phi \lesssim -5.4^\circ$), the position angle exhibits little modulation and has a mean value close to 0°. Immediately after this transition (over $-5.4^\circ \lesssim \phi \lesssim -4.7^\circ$), the position angle

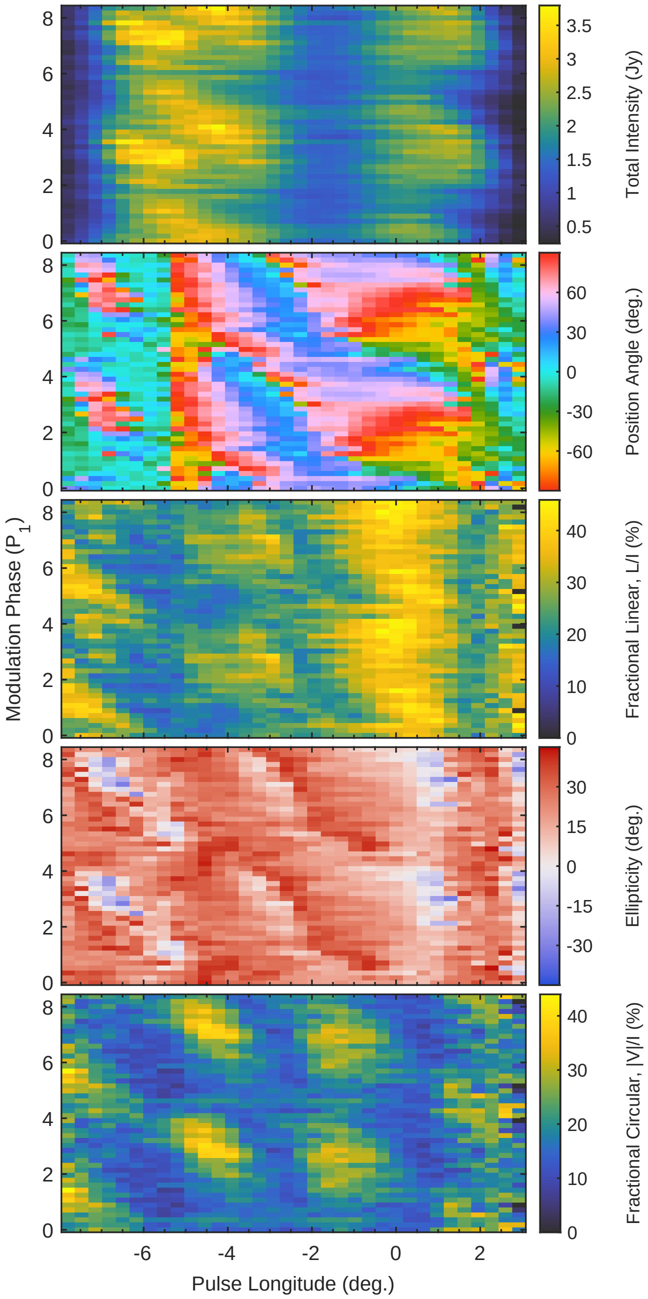

Figure 3.8: P_3-folded polarisation state of the first 500 pulses in the PSR B1919+21 dataset. From top to bottom are the total intensity; the position angle, $\theta = \tan^{-1}(U'/Q')/2$; the fractional linear polarisation, $\hat{L} = \sqrt{Q^2 + U^2}/I$; the ellipticity angle, $\epsilon = \sin^{-1}(V'/L')/2$; and the fractional circular polarisation, $\hat{C} = |V|/I$; where P_3-folded quantities are shown with primed symbols (e.g. Q' and U') and the symbols for single-pulse quantities are not primed (e.g. Q and U). That is, $\hat{L}$ and $\hat{C}$ are derived from the single-pulse Stokes parameters before P_3 folding and θ and ϵ are derived from the P_3-folded Stokes parameters. Furthermore, $\hat{L}$ and $\hat{C}$ are integrated only when the single-pulse total intensity exceeds 4 times the standard deviation of the of noise. In each panel, the modulation period ($P_3 \simeq 4.2\ P_1$) is plotted twice to better illustrate the continuity of the pattern.

varies between $\sim -60^\circ$ and $\sim 75^\circ$ as a function of modulation phase. The minimum degrees of polarisation (both fractional linear and fractional circular) in Figure 3.8 occur just before $\phi \simeq -5.4^\circ$. Shortly after this transition (over $-5.0^\circ \lesssim \phi \lesssim -3.7^\circ$) the ellipticity angle exhibits minimal modulation and remains greater than 15°; correspondingly, the fractional circular polarisation also reaches its maximum value in this pulse longitude range.

In the longitudes shortly before the OPM switch at $\phi \simeq -5.4^\circ$ (between approximately -7.6° and -6.3°) the P_3-folded position angle and ellipticity angle indicate variation between orthogonally polarised states as a function of modulation phase. However, as first noted for PSR B0809+74 (Taylor et al., 1971), the position angle does not jump discontinuously from one mode to the other, as expected for incoherent OPM superposition; rather, there is a continuous decrease followed by a continuous increase in position angle as a function of modulation phase. With reference to Figure A.2, the apparent continuous oscillation of the polarisation state could be explained by periodic switching along an axis that does not pass through the origin in the Q–U plane. A likely origin for such off-center switching is the incoherent transition between slightly non-orthogonal polarisation modes (McKinnon, 2003b). Similarly, continuous oscillation of position angle as a function of modulation phase is observed in the longitude range following the OPM transition, between approximately -5.4° and -3.6°. Here, there is also a clear systematic swing of position angle through each sub-pulse as a function of longitude and, as first noted for PSR B0809+74 (Taylor et al., 1971), this swing follows the sub-pulse structure as it drifts in longitude as a function of modulation phase. This swing gives rise to the continuous oscillation of position angle at a fixed longitude as a function of modulation phase.

Over the pulse longitudes that exhibit the toroidal and partially toroidal distributions (approximately $-3.6^\circ \lesssim \phi \lesssim 1.3^\circ$) the position angle no longer oscillates back and forth; rather, it cycles monotonically through the full spectrum of visible colours, clearly indicating the elliptical motion of the polarisation vector in the Q–U plane. Here, the degree of linear polarisation is also a maximum. Owing to the high degree of linear polarisation and the high signal-to-noise ratio of the individual pulses, the continuous cycling of the position angle over this range of pulse longitudes can also be clearly seen in the animations provided as supplementary material[4].

3.4 Discussion

In light of the complexities outlined in the introduction, it would be premature to interpret our results in terms of magnetospheric emission physics without a more comprehensive overview of single-pulse polarimetry across the radio spectrum. Instead, we aim to add valuable pieces to the puzzle and focus our discussion on two key features of the polarisation of the drifting sub-pulses: 1) the dramatic change in the modulation-resolved polarisation pattern seen in Figure 3.8 that coincides with the longitudinal transition between orthogonally polarised modes near $\phi \simeq -5.4°$; and 2) the toroidal distributions and cyclic drifting of polarisation state around an elliptical path as a function of modulation phase, observed over the region $-3.6° \lesssim \phi \lesssim 1.3°$.

First, the change in P_3-modulated polarisation near a pulse longitude of $\phi \sim -5.4°$ can be explained as a transition between primarily incoherent ($\phi \lesssim -5.4°$) and partially coherent ($\phi \gtrsim -5.4°$) mode superposition. At $\phi \lesssim -5.4°$, the distribution of polarisation states in the Poincaré sphere has, to first order, a prolate spheroidal shape as expected for the incoherent superposition of OPMs (e.g., Fig. A.2), van Straten and Tiburzi (2017). Over the region roughly defined by $-5.0° \lesssim \phi \lesssim -3.7°$, the polarisation state varies as a function of modulation phase between a low degree of polarisation (both linear and circular), as expected for an incoherent superposition of OPMs, and a high

---

[4] `https://www.dropbox.com/sh/1dbb3wnfrx1tt9j/AAB2hONBxf8ChwcdSleDJrJIa?dl=0`

degree of circular polarisation, as expected for a coherent superposition of linearly polarised natural modes in a highly relativistic plasma (Kennett & Melrose, 1998). Further evidence of coherent superposition is displayed on either side of this region. Over $-5.4^\circ \lesssim \phi \lesssim -4.7^\circ$, the position angle varies between approximately -60° and 75°; and over $-3.7^\circ \lesssim \phi \lesssim -3.6^\circ$, the position angle varies between approximately 30° and 75°. These approximately ±45° offsets can also be interpreted as transitions between incoherent OPM superposition, dominated by one mode, and a coherent superposition of linearly polarised modes (Dyks, 2019). The sign of the position angle offset is opposite on either side of the region where the degree of circular polarisation reaches its maximum, which can be interpreted as monotonic variation of the phase of the coherent superposition of linearly polarised natural modes as a function of drift phase (and hence pulse longitude), as also considered for PSR B1451−68 (Dyks et al., 2021).

Over $-0.8^\circ \lesssim \phi \lesssim 0.8^\circ$, the single-pulse polarisation state exhibits remarkable longitude-resolved toroidal distributions that are clear in both the integrated scatter plot shown in Figure 3.2 and the normalised scatter plots shown in Figures 3.4 and A.1. Furthermore, the polarisation state cycles around the elliptical path of the torus in a continuous periodic manner, rather than a stochastic one, modulated in phase with the drifting sub-pulse pattern observed in the total intensity. Cycling of the polarisation state around an elliptical path is demonstrated by the cross-correlations of Stokes Q and U in Figure 3.7 and in the P_3-folded position angle in Figure 3.8. The longitude-resolved cross-correlations between the Stokes parameters also indicate that the axis of elliptical revolution precesses about the Stokes V axis as a function of pulse longitude.

To date, continuous cyclic variation of the Stokes polarisation vector around an elliptical locus in Poincaré space has been observed in only three other sources, PSR B0320+39, PSR B0809+74, and PSR B0818−13 (observed at ~ 360 MHz, 1380 MHz, and 330 MHz, respectively; E04). For PSR B0320+39, E04 reports significant periodic fluctuations of the polarisation vector about an elliptical locus over a range of pulse longitude (~ 18° to ~ 19° in Figure 4 of E04) where periodic modulations of the total intensity are significantly diminished. In our analysis of PSR B1919+21, barely detectable modulation of total intensity is observed in the "saddle region" ($-2.3^\circ \lesssim \phi \lesssim -0.3^\circ$; cf. panels c) and d) of Figure 3.1 just prior to the range of pulse longitudes where the toroidal distributions are observed ($-0.8^\circ \lesssim \phi \lesssim 0.8^\circ$). As noted by (Backer, 1973), the decreased intensity modulation in this saddle region could be due to overlapping sub-pulses from the drift band regions on either side, especially if they differ by 180° in modulation phase. For PSR B0818−13, the elliptical locus reported by E04 appears to occur in a plane that is perpendicular to the Stokes Q–U plane and above it, as inferred from the positive ellipticity angles at pulse longitudes between ~ 38° and ~ 40° in Figure 2 of E04 and the meridional distribution of polarisation states in Figure 5 of E04. This is quite different to the toroidal distribution of polarisation states observed in our analysis of PSR B1919+21, for which the angle between the axis of revolution and the Stokes V axis varies between ~ 15° and ~ 45° (cf. Fig. A.1).

3.4.1 Origin of the toroidal distribution of polarisation state

We consider two plausible explanations for the observed toroidal distributions of polarisation state. These include 1) generalised Faraday rotation; and 2) four-mode mixing.

Generalised Faraday rotation – As in previous studies (Cheng & Ruderman, 1979; Kennett & Melrose, 1998; Edwards & Stappers, 2004; P. B. Jones, 2016; Dyks, 2017), consider a coherent superposition of orthogonally polarised *natural* modes, which have anti-parallel Stokes polarisation vectors that define an axis in Poincaré space. Phase-coherent superposition of the natural modes produces a new polarisation state that lies in a plane that is normal to this axis. The azimuthal direction of the new polarisation state in this normal plane depends on the phase relation between the orthogonal modes.

(In the special case of Faraday rotation, the natural modes have left-handed and right-handed circular polarisation, and birefringence-induced differential phase between these modes rotates the polarisation vector about the Stokes V axis.) If the phase difference between the modes varies smoothly between 0 and 2π during one drift cycle, then the polarisation state sweeps through a circle in the normal plane, creating a toroidal distribution.

Four-Mode Mixing – Consider the incoherent superposition of polarised radiation from two emission regions, $\mathcal{M}_1$ and $\mathcal{M}_2$. The emission from each region oscillates periodically between two orthogonally polarised states: M_1 and $-M_1$ from region $\mathcal{M}_1$, and M_2 and $-M_2$ from region $\mathcal{M}_2$, such that the radiation consists of an incoherent superposition of four modes in total (in contrast to the *coherent* superposition of four modes considered by Dyks et al., 2021). The primary axes defined by these pairs of OPMs in the Poincaré sphere are offset by some angle close to 90° (e.g. the emission from region $\mathcal{M}_1$ could oscillate between positive and negative Stokes Q and the emission from region $\mathcal{M}_2$ could oscillate between positive and negative Stokes U). On its own, amplitude modulation of a single pair of incoherently superposed OPMs would create a prolate distribution of polarisation states with its primary axis aligned with the axis defined by the OPMs in Poincaré space. If the two pairs of OPM oscillations are 90° out of phase with respect to each other, then their incoherent superposition will generate a toroidal distribution of polarisation vectors in the Poincaré sphere (as depicted in Figure A.3).

3.4.2 Origin of drifting sub-pulses

To explain the drifting of the observed sub-beams, we consider two physical models. These include 1) the refractive steering model; and 2) the rotating carousel model.

Refractive Steering Model – In this model, sub-beams are steered across the primary beam owing to refraction in the pulsar magnetosphere (Barnard & Arons, 1986; Lyubarskii & Petrova, 1998; Petrova & Lyubarskii, 2000). Each sub-beam consists of a coherent superposition of natural modes and, as the beam is steered, the relative phase difference between the modes slowly varies, causing the resulting polarisation state to move in an arc around the primary axis defined by the OPM pair. Because the magnetospheric conditions that determine the refracted ray path of each sub-beam (Fussell & Luo, 2004; Petrova, 2000) may also determine the polarisation state (e.g., through birefringent effectsCheng & Ruderman, 1979; Lyubarskii & Petrova, 1999), it seems plausible that periodic modulation of these magnetospheric conditions would result in temporal correlation between the angle at which the refracted sub-beam leaves the pulsar magnetosphere and the polarisation state of the sub-beam. However, more detailed modeling is required to explain how the relative phase between the natural modes cycles through approximately 2π per drift cycle. Furthermore, at pulse longitudes $-0.8^\circ \lesssim \phi \lesssim 0.8^\circ$, the polarisation state rotates in a plane that is offset by only a small angle from the Q–U plane. This seems to suggest that the natural modes of the magnetospheric plasma that is responsible for the birefringence are highly circularly polarised, which is inconsistent with the properties of a highly relativistic plasma for which the natural modes are expected to be linearly polarised (Kennett & Melrose, 1998). This inconsistency could be resolved by introducing two different birefractive regions in the pulsar magnetosphere, both with linearly polarised natural modes, such that the first region introduces the torus and the second region rotates the primary axis of the torus out of the Q–U plane.

Rotating Carousel Model – In the rotating carousel model, charged particle streams circulate around the magnetic poles owing to **E**×**B** drift, causing sub-beams to drift across the primary beam (Ruderman & Sutherland, 1975; Rankin, 1993; Rankin et al., 2006). (Rankin & Ramachandran, 2003) extend this model such that each sub-beam is split (e.g. owing to birefringence) into two spatially separated beams; as our line of sight passes from one sub-beam to the next, the polarisation state switches between OPMs. For elliptical cycling of polarisation state to arise requires a fortuitous incoherent superposition of two distinct rotating carousels, one carousel comprised of the OPM pair from region $\mathcal{M}_1$ and the other comprised of the OPMs from region $\mathcal{M}_2$ (as described in the four mode mixing model). The sub-beams in the $\mathcal{M}_1$ carousel must also be offset in magnetic longitude from the sub-beams in the $\mathcal{M}_2$ carousel, such that the polarisation state periodically cycles through the four modes and completes a full 360° rotation with each drift cycle. It is important to note that, if the sub-beams are as well resolved as shown in Figure 6 of (Rankin & Ramachandran, 2003), then the total intensity would cycle through four maxima in the time required for the polarisation state to complete one circle. This would not be consistent with our observations; e.g. Figure 3.6 shows that the total intensity is only weakly modulated compared to the much deeper modulations of Stokes Q, U, and V. This can be explained if the sub-beams observed in the toroidal region are unresolved (i.e. the width of each sub-beam is comparable to the spacing between them) such that any remaining modulation in intensity arises from the (possibly small) differences in the peak intensities of the beams along the line of sight that cuts through them (as depicted in Figure A.3).

In principle, four-mode mixing by a pair of unresolved or partially resolved carousels is consistent with either the barely resolved conal quadruple (Olszanski et al., 2019) or the five-component multiple (Rankin et al., 1989) classifications that have been applied to describe the mean profile of PSR B1919+21. In this interpretation, the first and third drift-bands represent the leading and trailing edges of the outer cone, the second drift-band represents the leading edge of the inner cone, the trailing edge of the inner cone is unresolved, and the inner and outer cones represent the $\mathcal{M}_1$ and $\mathcal{M}_2$ carousels of orthogonally polarised sub-beams. As noted in the introduction, quantitatively testing this interpretation of the beam geometry is challenging.

First, it is not possible to model the entire P.A. curve, plotted in panel b) of Figure 3.1, using the RVM. Therefore, to apply the RVM it is necessary to apply judgement and model only limited regions of pulse longitude (Everett & Weisberg, 2001). We identify two candidate regions: A) the steepest, negative slope of the P.A. profile ranging from $-5°$ to $-2.5°$ in pulse longitude; and B) the shallow, positive slope from $-13°$ to $+2°$, excluding $-7.5°$ to $-2°$. Region A exhibits the highest degree of circular polarisation and the P.A. in this region most likely represents a distortion produced by coherent superposition of natural modes rather than a regular RVM swing (Dyks, 2019). Moreover, assuming that the leading component centred at $-12°$ can be neglected as anomalous, the steepest slope of P.A. swing in region A leads the centre of the total intensity profile, which conflicts with the expected effects of aberration and retardation (Blaskiewicz et al., 1991). Regardless of the selected region, the best-fit value for the colatitude of the magnetic axis α approaches $0°$, which is inconsistent with the observed narrow pulse width. Therefore, we abandon any further interpretation of the beam geometry based on the P.A. profile.

To measure the apparent longitudinal offset between the centres of the putative inner and outer cones of emission, we model the mean total intensity pulse profile as a sum of six components, each described by a von Mises function (Weltevrede & Johnston, 2008). The derived difference of $0.36°$ in relativistic phase shifts corresponds to an offset in the inner and outer cone emission heights of ~ 200 km (Dyks et al., 2004); therefore, relativistic aberration is a plausible explanation for the overlapping trailing components of the inner and outer cones.

3.5 Conclusions

The brightness of PSR B1919+21, combined with the sensitivity of Arecibo, enables a variety of approaches to studying the polarisation of its drifting sub-pulses. The methods adopted in this study facilitated the discovery of toroidal and partially toroidal distributions of the Stokes parameters. Further investigation showed that, over the range of pulse longitudes that exhibit toroidal distributions, the polarisation state rotates continuously and synchronously with the sub-pulse drift period.

This analysis is one step forward in the development of a framework that can be used to interpret the fourth-order statistics of the Stokes parameters in weaker sources. Eigenvalues can be used to identify rare oblate distributions of the Stokes polarisation vectors, and the cross-correlations between the Stokes parameters can reveal the continuous cycling of polarisation state around an elliptical path, synchronous with the intensity modulation of drifting sub-pulses. In the Arecibo observations of PSR B1919+21, these interpretations are supported by visualisation of the single pulses using methods that are applicable only at high S/N. For example, the scatter plots of the normalised Stokes parameters clearly show the toroidal distribution of polarisation states and the P_3-folded position angle confirms the continuous cycling of polarisation state.

Our study demonstrates that novel statistical methods can facilitate the discovery of relatively rare phenomena, even when analysing decades-old archival observations of the most studied pulsars. Although only 6 pulsars are currently known to exhibit drift-synchronous modulation of polarisation state, we speculate that more such sources remain to be discovered. To obtain a large sample of uniformly studied pulsars, we are conducting the Pulsar Radio Emission Statistics Survey (PRESS)[5], an observing campaign that will record single-pulse observations of around 200 pulsars using the ultra-wide bandwidth low-frequency (UWL) receiver at the Parkes Observatory (Hobbs et al., 2020). These data will be made public as soon as they are calibrated and various quality assurance checks have been performed. All of the software required to perform the analysis presented in this paper is freely available as part of PSRCHIVE, an open-source C++ development library for the analysis of pulsar astronomical data (Hotan et

---

[5] `https://sites.google.com/view/psr-press`

al., 2004; van Straten et al., 2012).

Chapter 4

PRESS project

4.1 Introduction to PRESS

The Pulsar Radio Emission Statistics Survey (PRESS) project was initiated by Prof. van Straten, Dr. Tiburzi, and the candidate with the aim of applying the statistical methods introduced by van Straten (2009), and developed by van Straten and Tiburzi (2017), to the study of pulsar emission. The PRESS project team currently includes 28 investigators from different institutions around the world.

4.1.1 PRESS Science Goals

The two main scientific goals of PRESS are to study

- the physics of broadband radio wave emission and propagation in the pulsar magnetosphere; and
- the variability of pulsar emission and propagation properties across the entire pulsar population, from millisecond pulsars to radio-emitting magnetars.

By studying single-pulse emission with high time resolution across a wide frequency range, PRESS aims to unveil the beam geometry (e.g., Dyks et al., 2016) of pulsar emission, to derive the properties of strong plasma turbulence in the pulsar magnetosphere (e.g., Asseo & Porzio, 2006), to measure its birefringent properties (e.g., Suresh & Cordes, 2019), and characterise the energy distribution of impulsive emission phenomena (e.g., Burke-Spolaor et al., 2012).

Throughout the pulsar population, important properties such as magnetic field strength and spin-down luminosity vary by about seven orders of magnitude. PRESS is set to study the instantaneous pulsar emission properties and their evolution across the entire pulsar population.

4.2 Preparations for PRESS observations

4.2.1 Source Selection Criteria and Process

To study single pulse dynamics via the fourth moments of the electric field using observations that span frequencies above 2 GHz, where pulsars are dim owing to their steep spectrum (e.g., Jankowski et al., 2018), necessitates long integration times to achieve a sufficient signal-to-noise ratio (S/N) in the elements of the covariance matrix. At the same time, PRESS aims to study a large number of pulsars to include a large variety of physical properties of neutron stars, and this demands shorter integration lengths (to fit more pulsars into granted time).

The instrument used in the project, the UWL receiver at the Parkes radio telescope (Hobbs et al., 2020), provides a wide bandwidth of about 3 GHz, from 704 to 4032 MHz. This instrument has a flexible digital backend (MEDUSA) which enables recording the pulsar signal at high time resolution.

We prioritised to have greater sensitivity at high frequencies at the cost of observing a smaller number of pulsars. One advantage of this strategy is to complement the MeerKAT 1000 Pulsar Array project, which studies pulsar emission over a narrower frequency range and much larger sample. Since our novel, wide-band single-pulse studies are conducted through the analyses of the fourth moments of the electric fields, or the covariance matrix of the Stokes parameters (van Straten, 2009; van Straten & Tiburzi, 2017), the first step was to predict the integration lengths required to achieve sufficient S/N in the elements of the matrices. Thus, we derived a new radiometer equation (van Straten et al. in preparation), and used single-pulse observations of PSR J0437-4715 (Osłowski et al., 2014) to verify our derivations.

The fourth-moment equation was used to estimate the integration length required to achieve a signal-to-noise ratio of 100 for the fourth moments of the electric field for a bandwidth of 1.2 GHz at a central frequency of 2.4 GHz. After that we applied the equation to all the known pulsars visible from Parkes and sorted them in ascending order of integration length. Then we selected those sources up to the point where integration length exceeded nine hours, striking a balance between having sufficient sensitivity and observing as many pulsars as possible. The final selection counted 234 pulsars, with integration lengths ranging from ~5 minutes to ~8 hours (for PSR J0437-4715 and PSR J1851+1259 respectively). It is important to note, for the sake of our observing strategy, that the integration time does not need to be reached in an individual pointing. The required integration time can be obtained over multiple observing sessions, by making the reasonable assumption that the pulsar emission characteristics are stationary over a small number of months.

4.2.2 Integration time estimations

Radiometer equation for the sample mean intensity

To determine the integration length (τ) for detecting continuous sources with a certain S/N at a certain bandwidth $\Delta\nu$, the *radiometer equation* is used, and its general form (e.g., see Lorimer & Kramer, 2012) can be expressed as:

$$R = \frac{S_{\mathrm{src}}}{S_{\mathrm{sys}}}\sqrt{\Delta\nu\tau} \tag{4.1}$$

Where S_{src} is the flux density of the continuous source and S_{sys} is the *System Equivalent Flux Density* (SEFD), that describes the combined impact of the telescope systems and the sky background. However, pulsars are not continuous sources, and are observed as periodical emitters. Therefore, we can derive a new expression for the radiometer equation as following.

First consider the observation of *n* Nyquist-sampled instances (e.g., Stiltz, 1961 Oppenheim et al., 1999, Léna et al., 2012) of the complex-valued electric field. Here $n = \tau\Delta\nu$ (where τ is the observation length, and $\Delta\nu$ is bandwidth). The pulsar signal is approximated as a periodic rectangular waveform, with a duty cycle δ_{on} (i.e., the fraction of the period when the signal is on) and an on-pulse intensity I_{on}.

For this signal, we define the detection significance of the estimated periodic signal intensity $\bar{S}$ (where $\bar{S} = \bar{I}_{\mathrm{on}} - \bar{I}_{\mathrm{off}}$, $\bar{I}_{\mathrm{off}}$ is the sample mean intensity of off-pulse instances) as its S/N, R:

$$R \equiv \frac{\bar{S}}{\sigma'_{\bar{S}}}. \tag{4.2}$$

Here $\sigma'_{\bar{S}}$ is the standard deviation that describes the uncertainty of a given measurement of $\bar{S}$, $\left\langle \bar{I}_{\mathrm{off}} \right\rangle = S_{\mathrm{sys}}$. The flux densities of pulsars (S) are typically recorded as though from a source of constant intensity, such that S_{src} is usually averaged over one pulse period. For the aforementioned rectangular signal $S'_{\mathrm{src}} = \delta_{\mathrm{on}}S$.

We can express the ratio of averaged flux density to the SEFD as $r' = \frac{S'_{\mathrm{src}}}{S_{\mathrm{sys}}}$, and the radiometer equation for pulsars will take form as:

$$R = r'\sqrt{2n\frac{1-\delta}{\delta}}, \tag{4.3}$$

where $\delta_{\text{on}} = \delta$.

Radiometer equation for the sample variance

To determine the sensitivity of the fourth moments of the electric field, we need to derive a radiometer equation which is based on the noise statistics for the amplitude-modulated signal. Very briefly, the derivation can be described as follows:

- First, we continue from the notions of the radiometer equation for the sample mean (i.e., Equation 4.3), replacing the variances of the sample means, I_{on} and I_{off}, with the variances of sample variance of the instantaneous intensity in the on-pulse and the off-pulse signals: $\Upsilon_{\text{on}} \equiv \bar{\sigma}^2_{\text{on}}$ and $\Upsilon_{\text{off}} \equiv \bar{\sigma}^2_{\text{off}}$.
- The observed on-pulse signal is a sum of the intrinsic pulsar signal and noise. Therefore, it is necessary to compute an unbiased estimator of the source-intrinsic variance of the intensity.
- We find the S/N of the sample variance estimator of the instantaneous intensity, taking into consideration the modulation index (see Chapter 2.3.1.1) of the signal.
- We consider the division of the large sample of n instances into sub-samples that are composed of m instances of intensity, because in typical observations the intensity is sampled at lower than the Nyquist rate.
- The final radiometer equation then will take into account the modulation index of the sub-sample mean intensity instead of the modulation index at the Nyquist interval.

These steps are described in detail in van Straten et al. (paper in preparation) and below brief mathematical highlights are given.

From van Straten and Tiburzi (2017) (equation 42), an unbiased estimator of the variance of the subsample mean signal intensity is given by:

$$\bar{\Upsilon}_S = \bar{\Upsilon}_{\text{on}} - \bar{\Upsilon}_{\text{off}} - m^{-1}(I_{\text{on}} - I_{\text{off}})I_{\text{off}}, \tag{4.4}$$

Where m is the number of instances of the intensity that were averaged. The S/N of sample variance of the sub-sample mean intensity is

$$R_{\bar{\Upsilon}} \equiv \frac{\bar{\Upsilon}_S}{\sigma_{\bar{\Upsilon}_S}} = \beta^2_{m\tau'} r^2 \left(2mn\delta(1-\delta)\right)^{1/2}, \tag{4.5}$$

where $\beta_{m\tau'}$ is the modulation index of the sub-sample mean intensity over the interval $m\tau' = \frac{m}{\Delta\nu}$.

The ideas used for Equation 4.5 are based on the unnatural assumption that the periodic signal has a rectangular waveform. Furthermore, the modulation index typically varies as a function of a pulse phase ϕ (e.g., Weltevrede et al., 2006). Thus, for the sample variance radiometer equation $\beta^2_{m\tau'}$ was replaced by its weighted mean value of:

$$\bar{\beta}^2 \equiv \frac{\sum_{\phi\in\Phi_{\text{on}}} {\beta^2}_{m\tau'}(\phi) I_S^2(\phi)}{\sum_{\phi\in\Phi_{\text{on}}} I_S^2(\phi)} \tag{4.6}$$

Where Φ_{on} defines the set of on-pulse rotational phases.

For the PRESS observing campaign we used $\bar{\beta}^2 = 1$, which we estimated from a sample of pulsars observed at Arecibo (Hankins & Rankin, 2010).

4.2.3 Equations verification

To verify Equation 4.5, we used data collected with the Parkes radio telescope, consisting of 2 hours of single-pulse observations of PSR J0437-4715 (Osłowski et al., 2014). These data were observed at a central frequency of 1382 MHz with a bandwidth $\Delta\nu$ of 400 MHz. The pulsar's spin period is $P \sim 5.8$ ms, and every pulse was subdivided into 1024 phase bins. Since $m = (P/nbin)\cdot\Delta\nu$, in our case we have that $m \simeq 2250$ instances per sub-sample. The set of 1.2 million single pulses was divided into non-overlapping sub-sets that span 60s.

We computed the sample variance of the mean intensity for each subset and measured the S/N of the sample variance profile. We also estimated the expected S/N, given the weighted mean modulation index $\bar{\beta}^2 \simeq 1$, the intensity ratio r' varied between 4×10^{-3} and 5.7×10^{-3}, and the profile width at 10% of the peak flux density $\delta \simeq 0.125$.

This predicted S/N was then compared with the measured S/N, as shown in Figure 4.1. Ideally, the linear fit for predicted vs measured data (dotted line) should have a slope of unity (i.e., as the identity line shown by the dashed line), and we can see that overall the measured values of S/N are close to the predicted. The small deviation from ideal may be caused by the arbitrary choice of δ 10% of the peak flux density, the rectangular pulse assumption, or the use of $\bar{\beta} \sim 1$.

The next step was to investigate the behaviour of the S/N while increasing the sample size *n*, and the sub-sample size *m*. For the first case we computed sample variances for subset of the duration of 2, 4, 8, 16, and 32 minutes. For the second case we computed sample variances after averaging contiguous sets of 2, 4, 8, 16, 32, and 64 single pulses.

It is expected that with the increase of the sample size, the S/N will vary as $\sqrt{n}$, and the slope of this dependence on log-log plot is expected to be 0.5. When the sub-sample size is larger than the size of sub-pulse structures, then the sub-sample will be averaged

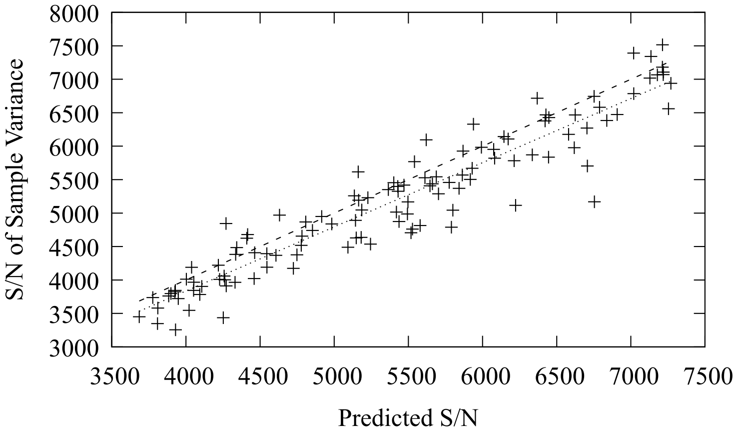

Figure 4.1: Comparison of predicted and measured S/N of the sample variance profiles derived for PSR J0437−4715. The dashed line is the line of identity (i.e., $45°$). The dotted line is a liner fit to the data set.

over some number of statistically-independent sub-pulses, as it is argued in Appendix A of van Straten and Tiburzi (2017). In that case, $\beta_{m\mathcal{T}'} \propto m^{-\frac{1}{2}}$ will be less than the pulsar's natural modulation index, and then the S/N is predicted to follow an inverse square-root behaviour, $\frac{1}{\sqrt{m}}$ and the slope of this dependence is expected to be -0.5.

The final results for both varying sizes of n and m are shown in Figures 4.2 and 4.3 respectively, where the measured S/N are in a good agreement with the expected slopes.

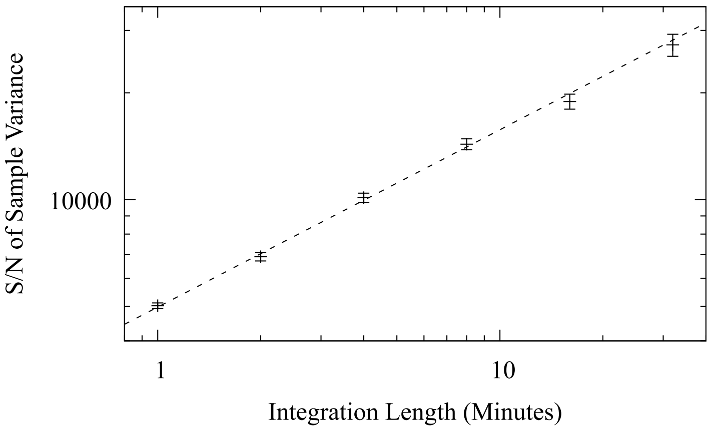

Figure 4.2: S/N of the sample variance of the sub-sample mean intensity, R_{Υ}, as a function of integration length for PSR J0437−4715. The dashed line has the expected slope of 0.5, each point is the mean value derived from $N \simeq (\text{observation duration})/(\text{integration length on x} - \text{axis})$ independent estimates of the sample variance, and the error bars are the standard deviations of the estimates, divided by the square root of the number of estimates.

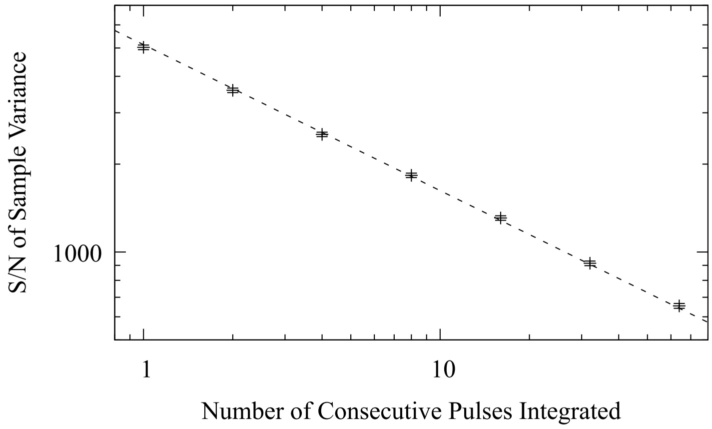

Figure 4.3: S/N of the sample variance of the sub-sample mean intensity, $R_{\bar{\Upsilon}}$, as a function of the number of integrated single pulses from PSR J0437−4715. The dashed line has the expected slope of -0.5, each point is the mean value derived from 125 independent estimates of the sample variance, and the error bars are the standard deviations of the estimates, divided by the square root of the number of estimates.

4.3 PRESS observing campaign

The PRESS observing campaign took place from 1 April 2020 to 21 October 2021. Out of the awarded 420 hours, 350 hours yielded useful data for our program. Some observing time was missed due to either poor weather conditions (such as thunderstorms with large amount of on-site lightning, sandstorm, or extremely high winds), or telescope or receiver breakdown. (Some fraction of time is also lost during antenna slews, and/or setup of the system.)

Out of the planned 234 pulsars, we completed the desired integration time for 176, while for 7 we partially completed the observations. The source list (Table B.1) had to be revised in the last observing semester, because many of the targeted pulsars are located in the Galactic Plane, and the time slots when the Galactic Plane is visible from Parkes are usually in high demand among the observing projects. This led to a situation where the Galactic Plane was not always visible during the observing slots allocated to PRESS. Therefore, after two observing semesters all of our selected pulsars that are not located in the Galactic Plane were fully observed, and thus we had to alter the initial source list by adding off-plane pulsars. The silver lining of the challenges caused by time allocation, is that some pulsars (in Table B.1 they have negative values in "To-do" column) were observed for longer than originally planned, which compensates for time lost to RFI.

I took charge in managing the PRESS observations, organizing the observers (located around the world), preparing the schedules and personally performing the majority of the observations.

4.4 Arecibo data analysis as a pilot for PRESS

4.4.1 Arecibo data

The statistical analysis that we aim to apply to the PRESS data was tested and verified using observations recorded at the Arecibo telescope (Hankins & Rankin, 2010), as part of the P1260 program[1]. Principal component analysis (PCA), described in Chapter 3, was applied to all of the pulsars observed in the program and a search was conducted for any unexpected and/or unconventional emission statistics. When it was possible, the pulsar candidates with interesting behaviour were inspected more closely.

Figures C.1, trough C.7 display the results of this study. The top panel of each plot shows both the ellipticity angle of the average Stokes parameters (points with error bars) and histogram of the ellipticity angles of the individual pulses (greyscale intensity). The next panel down shows both the position angle of the average Stokes parameters and a histogram of the position angles of the individual pulses. The third panel shows the averaged profile in total intensity (black, upper solid), linear (red, dashed) and circular polarisation (green, dot-dashed). These profiles were obtained by averaging all of the available data. In the bottom panel the black solid line shows the standard deviation of the total intensity (σ_0^2), and the red dashed, green dot-dashed, and blue dotted lines display the square roots of the eigenvalues $\lambda_1, \lambda_2, \lambda_3$ (from largest to smallest, respectively) of the 3×3 partition of the covariance matrix that describes the fluctuations of the polarisation vector S = (Q, U, V). These eigenvalues describe the shape of the polarisation vector distribution at each pulse longitude (see Section 2.3.1 for more details) and were used to choose candidate pulsars for follow-up research.

In general, with a few exceptions, at all pulse longitudes the pulsars exhibit the expected prolate spheroidal distribution of the Stokes parameters (when $\lambda_1 > \lambda_2 \gtrsim \lambda_3$) and increased modulation of Stokes I (relative to Q, U, and V) due to amplitude

---

[1] These data are located at `http://www.uvm.edu/~pulsar/P1260`

modulation (when $\sigma_0^2 > \lambda_1$).

Quick review of interesting pulsars

Evidence of OPMs

Pulsars **PSR B0820+02** at 430 MHz (Figure C.2), **PSR B1133+16** at 430 MHz and 1414 MHz (Figure C.2), **PSR B1821+06** at 1414 MHz (Figure C.3), **PSR B1923+04** at 430 MHz (Figure C.5), **PSR B2020+28** at 1414 MHz (Figure C.6), **PSR B2016+28** at 430 MHz (Figure C.6) and **PSR B2110+27** at 1414 MHz (Figure C.6), demonstrate bimodal distributions of PA.

Evidence of disjoint modes

Some pulsars show that Stokes I and the major polarisation (black and red lines at the bottom panels) have similar variances, i.e., $\sigma_0^2 \sim \lambda_1$; for example:

- **PSR B0611+22** at 430 MHz (Figure C.1 upper-right) visible throughout the whole pulse,
- **PSR B1737+13** at 430 MHz (Figure C.3 upper-middle) visible on the leading pulse component,
- **PSR B1842+14** at 1414 MHz (Figure C.3 lower-right) visible at the leading edge of the pulse,
- **PSR B1929+10** at 1414 MHz (Figure C.5 upper-middle) visible approximately throughout the majority of the pulse,
- **PSR B2020+28** at 430 MHz (Figure C.6 upper-middle) visible at almost all pulse longitudes in both components.

The observed condition may indicate that either i) there is very little amplitude modulation; or ii) that the variance in the primary polarisation is enhanced by the occurrence of the disjoint OPMs (see Equation 39 from van Straten & Tiburzi, 2017); or iii) that the emission is highly polarised. The last explanation is the most plausible for the pulsars PSR B0611+22, PSR B1842+14, and PSR B1929+10, where strong linear polarisation correlates with pulse longitudes that show $\sigma_0^2 \sim \lambda_1$.

However, in PSR B1737+13, the leading pulse longitudes show a PA jump which correlates with a region of depressed linear polarisation indicating the presence of OPMs, which can also be seen in the phase-resolved histogram of PA. Therefore, over these pulse longitudes, the near equality of σ_0^2 and λ_1 can be explained by disjoint modes. After that OPM jump $\sigma_0^2 \sim \lambda_1$ can be explained by the high degree of polarisation.

For PSR B2020+28 high linear polarisation correlates with $\sigma_0^2 \sim \lambda_1$ only at the first pulse component, but then around pulse longitude $32°$ (where there is a possible second pulse component merged with the first one) a PA jump occurs which depresses the linear polarisation; and after that the rest of the pulse may be explained by disjoint modes.

Non-prolate polarisation vector distributions

Together with the interesting findings for **PSR B1919+21** described in Chapter 3, it is worth to mention here a few pulsars that have pulse longitude intervals with non-prolate distributions of the polarization vectors (e.g., regions where $\lambda_1 \approx \lambda_2 > \lambda_3$). For example,

- **PSR B0626+24** at 1414 MHz (Figure C.1 lower-middle), around pulse longitudes $\sim 18° - 22°$ and $\sim 28° - 34°$,
- **PSR B1821+05** at 430 MHz (Figure C.3 upper-right), around pulse longitudes $\sim 15° - 25°$, $\sim 35° - 45°$,
- **PSR B1821+05** at 1414 MHz (Figure C.3 lower-left), around pulse longitudes $\sim 18° - 25°$,
- **PSR B1842+14** at 1414 MHz (Figure C.3 lower-right) starting from pulse longitude ~ 25,
- **PSR B1920+21** at 1414 MHz (Figure C.4 lower-right) before pulse longitude 20 and around pulse longitudes $\sim 24° - 34°$, and

PSR B2044+15 at 1414 MHz (Figure C.6 lower-left) from pulse longitude ~ 20° till the end of pulse exhibits weakly polarised emission emission (visible in the third panel) at pulse regions where the eigenvalues λ_1 and λ_2 are close to each other. This points to the presence of oblate distributions of polarisation vectors.

By investigating such pulsars one needs to find whether there are similarities in their emission behaviours (i.e., by exploring correlograms as it was described in Chapter 3) to those found in PSR B1919+21. To date, only five other pulsars (see Chapter 3) together with PSR B1919+21 are known to exhibit periodic OPM switching that is synchronised with the drifting sub-pulse modulation. Possibly there are more pulsars that have the same behaviour, and this would potentially set them into a separate class of drifters, but due to their faint emission they were not noticed yet.

For pulsar **PSR B1839+09** at 1414 MHz (Figure C.3 lower-middle) most of the pulse longitudes show that all the eigenvalues are close to each other, which indicates a spherical distribution of polarisation vectors at those pulse longitudes.

Another interesting example is **PSR B1842+14** at 1414 MHz (Figure C.3 lower-right) that displays a pulse with two components with an interesting behaviour. In the leading edge of the first pulse component (before pulse longitude ~ 20°), $\lambda_1 \sim \sigma_0^2$, which is explained by the high linearly polarised emission (shown in the third panel), and an absence of OPMs; then in its trailing edge and the whole second component, all eigenvalues are close to each other ($\lambda_1 \simeq \lambda_2 \simeq \lambda_3$), which indicates unpolarised emission. However, the signal is polarised at all longitudes, which is inconsistent with a spherical distribution.

The most peculiar among the Arecibo pulsars is **PSR B1929+10**, whose PCA result plot is shown in Figure C.5 (upper-middle panel). At the leading edge of its pulse

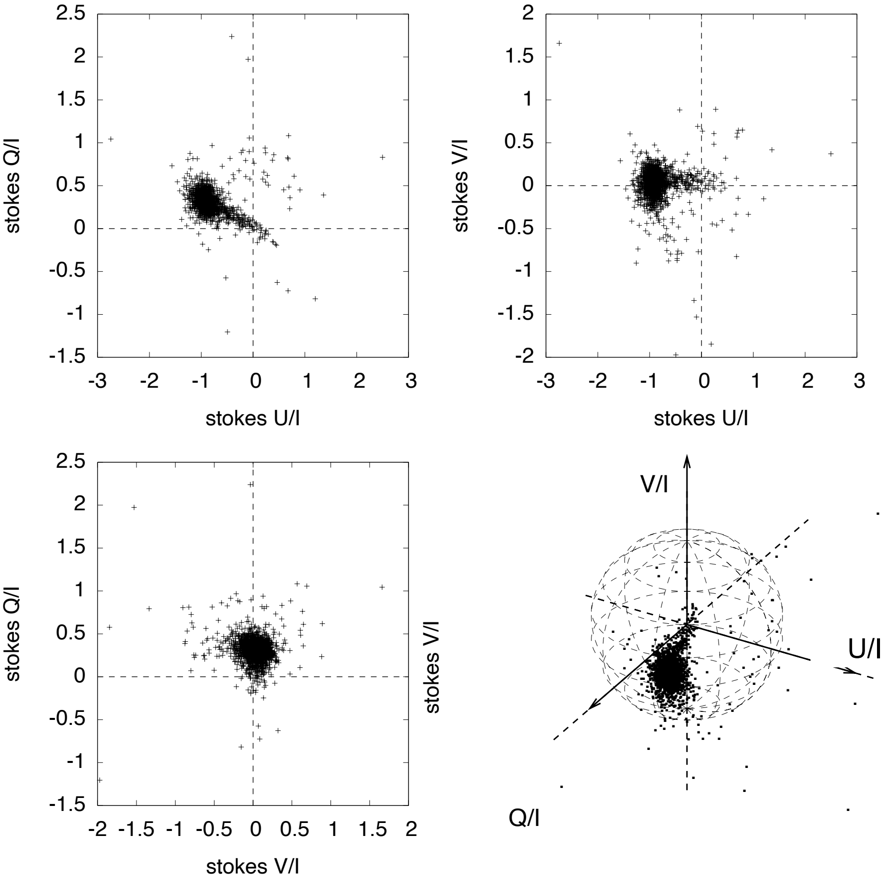

Figure 4.4: Distribution of the normalised Stokes parameters in the Poincaré sphere for pulsar PSR B1929+10. The two upper panels and the lower-left panel show the projected, 2D distribution of the Stokes parameters in the three planes normal to the basis vectors, and the 3D distribution is displayed in the lower-right panel.

$\lambda_1 > \sigma_0^2$. We can speculate that this condition may point to the occurrence of disjoint modes. However, PA and ellipticity 2-D histograms show no such evidence, and seem to display the presence of only one mode. Moreover, the mean profile (third panel) looks 100% polarised, while the presence of OPMs should typically de-polarise the radiation. At the same time though, the 3-dimensional polarization vectors distribution in the Poincaré sphere at the indicated pulse longitudes shows an interesting shape, as it is displayed in Figure 4.4 (for producing this figure data instances where $S_0 \leqslant 0$ were removed), that is in theory incompatible with a 100% polarised emission. In 3-D plot and its 2-D projections we see evidence of a highly-polarised state (the cluster offset from the origin) and an unpolarised state, (the cluster near the origin). It looks like the emission does not switch between two OPMs; rather, it switches between two states of polarisation: highly polarised state and unpolarised state.

The peculiar distribution of this pulsar will be studied in future work.

Table 4.1: Division of the UWL frequency range into sub-bands

Band	Freq. range (MHz)	Central Freq. (MHz)	Band	Freq. range (MHz)	Central Freq. (MHz)	Band	Freq. range (MHz)	Central Freq. (MHz)
Low	704 - 832	768	Mid	1344 - 1472	1408	High	2368 - 2496	2432
	832 - 960	896		1472 - 1600	1536		2496 - 2624	2560
	960 - 1088	1024		1600 - 1728	1664		2624 - 2752	2688
	1088 - 1216	1152		1728 - 1856	1792		2752 - 2880	2816
	1216 - 1344	1280		1856 - 1984	1920		2880 - 3008	2944
				1984 - 2112	2048		3008 - 3136	3072
				2112 - 2240	2176		3136 - 3264	3200
				2240 - 2368	2304		3264 - 3392	3328
							3392 - 3520	3456
							3520 - 3648	3584
							3648 - 3776	3712
							3776 - 3904	3840
							3904 - 4032	3968

4.5 Preliminary analyses of the PRESS data

Before digitisation, the UWL frequency range is divided into three bands by analog filters: Low (704 - 1344 MHz), Mid (1344 - 2368 MHz), and High (2368 - 4032 MHz) (Hobbs et al., 2020). These bands have different RFI levels and, to mitigate its impact, they are separately digitised with different effective dynamic ranges before they are divided into 26 narrower sub-bands using a poly-phase filter bank that is also built into the receiver[2]. Finally, each sub-band is divided into 128 frequency channels by the MEDUSA software.

A pipeline to process the PRESS data is being developed based on the *DSPSR* (van Straten & Bailes, 2011) and *PSRCHIVE* (Hotan et al., 2004; van Straten et al., 2012) software packages and is known as *psrpl*[3]. The diagram in Figure 4.5 depicts an overview of the current PRESS pipeline. Data processing is carried in two independent stages. In Stage 1 the search mode data are “folded” [4] into average profiles with integration lengths of ~ 10 seconds, and in Stage 2 the raw data are divided and re-sampled into single pulse profiles. Separately, polarization calibration solutions are

---

[2] Both hardware are included into the so-called “UWL receiver package”.

[3] https://psrchive.sourceforge.net/manuals/psrpl/

[4] I.e., the *phase-resolved binning* described in Section 2.2.1 is performed on data.

derived from Parkes observations of PSR J0437-4715. This step is shown in Figure 4.5 as a standalone process between Stage 1 and Stage 2 and its results are applied to both stages.

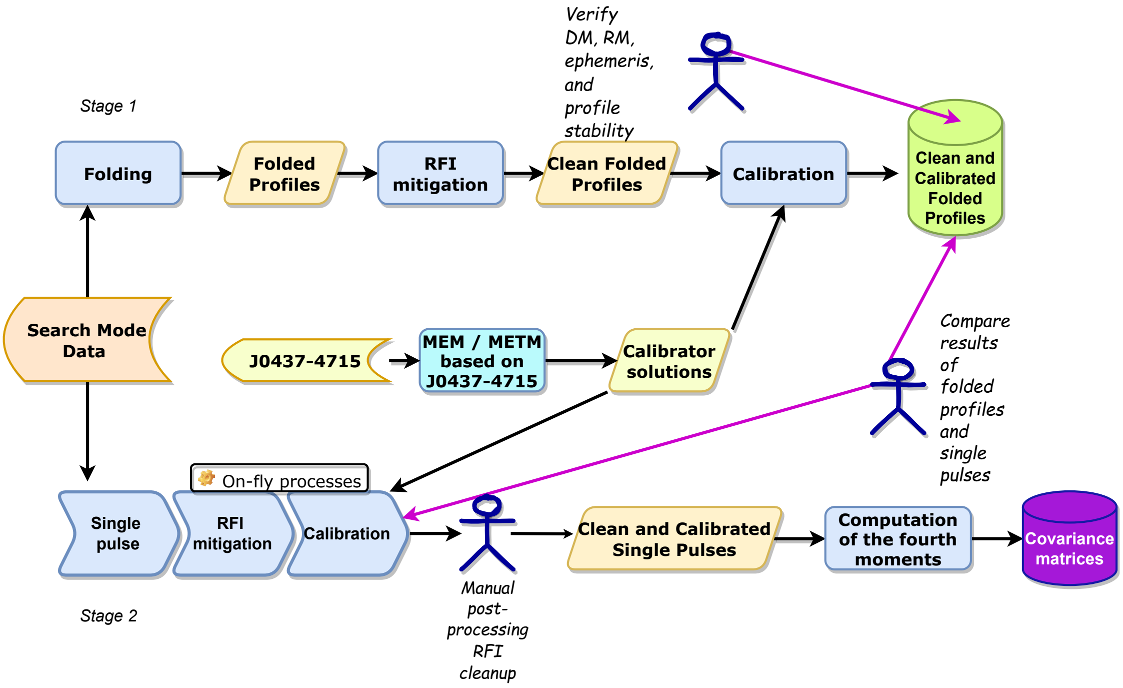

Figure 4.5: Diagram showing the current stages of the PRESS pipeline, as it is described in the main text.

Below are described the data processing steps implemented in the PRESS pipeline and the challenges we met. For testing and verification of the pipeline performance we used the following set of pulsars: PSR J0034-0721, PSR J0738-4042, PSR J1056-6258, PSR J1136+1551, PSR J1456-6843, PSR J1731-4744, PSR J1921+2153, PSR J1932+1059, and PSR J2048-1616.

4.5.1 Stage 1 of data processing: folded data

4.5.1.1 Folding

The recorded UWL time samples of the sample mean Stokes parameters are integrated into $N_{\rm bin}$ longitude intervals. To this array, the pipeline continues to add time samples for 10 consecutive seconds of observations. As a result, a longitude-resolved average with 10 seconds long sub-integrations in each sub-band are ready to undergo the RFI excision.

4.5.1.2 RFI excision from folded data

RFI-mitigation algorithms are then applied to the sub-integrations, to detect outliers and eliminate corrupted channels. At this processing stage, an outlier detection and rejection routine using interquartile range, as described in *CLFD* by Morello et al. (2022), is applied (further we will call it *PSRCHIVE tfzap*). Next, the cleaned 10-second sub-integrations are added into 5-minute sub-integrations. The procedure in the pipeline is based on the *psradd* routine. Lastly, the 5-minute sub-integration files are time-averaged into a total archive.

4.5.1.3 Visual inspection of summary images

During the development of *psrpl*, it was important to visually verify the quality of the RFI mitigation approach. This revealed issues with the initial RFI mitigation techniques based on the application of generalised least squares and triggered the development of a new outlier-detection statistic based on a Gaussian-mixture model (GMM).

Figure 4.6 gives an example of the image generated for such quality verification. Panels from left to right demonstrate a pulse-stack of the whole observing session, frequency evolution of the signal within a sub-band, and the fully frequency- and time-averaged pulse profile. In the case of corrupted (or poorly cleaned) data the left and middle panels will show horizontal bands with RFI as artifacts. Low level artifacts which were not visible in these panels will manifest in the right panel as a crooked baseline, or random off-pulse spikes.

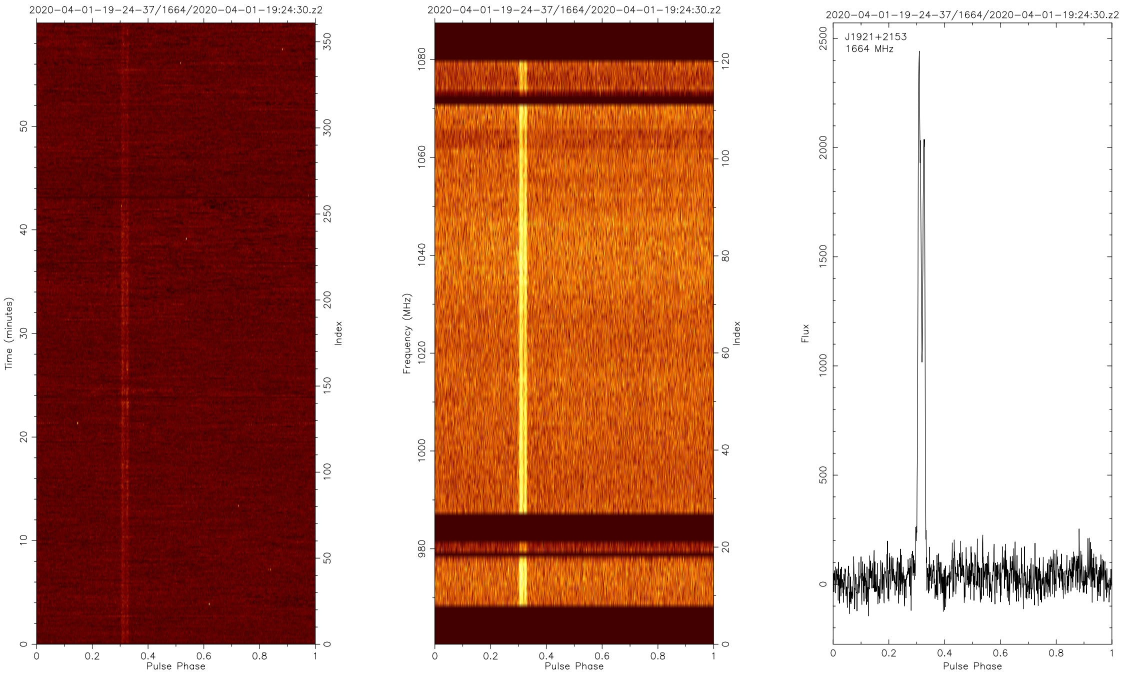

Figure 4.6: Example of images produced for folding and RFI mitigation quality verification after applying *tfzap*. The left panel gives a pulse-stack of the whole observing session, where x-axis show pulse phase and y-axis show time in minutes. The middle panel represents a frequency evolution of the signal within a sub-band, where x-axis show pulse phase and y-axis show frequency. The right panel is the fully frequency- and time-averaged pulse profile, where x-axis show pulse phase and y-axis show pulsar brightness.

Later[5] when we saw that our current RFI-mitigation approach was not working effectively for the Stage 2, we adopted *MEERGUARD* (see more details in the description of Stage 2.). Therefore, recently we decided to add this second way of RFI cleanup to Stage 1, to produce two types of folded profiles produced by the two algorithms of RFI cleanup. Examples that compare the performances of both the RFI mitigation approaches are available in Figures C.8 and C.9

4.5.1.4 Calibration of folded, RFI-cleaned data

All calibration developments were done by van Straten (paper in preparation); therefore, in this section a very brief summary is provided.

---

[5] During the Stage 2 development

First, an absolute flux calibration should be performed by using observations of the astronomical source with well-known parameters, such as flux density and spectral index, throughout the wide frequency range. Quasar QSO B0407-65 was used for PRESS absolute flux calibration. It was observed with the UWL during 91 sessions from 8 April 2019 to 24 August 2022. During calibration observations, the noise diode was operating producing the square wave (switching on and off). The observations were organised as the following set of pointings (each two minutes in duration): - North of the source - on Source - South of the source - on Source - North of the source. A detailed description of the flux calibration algorithms is given in van Straten et al. (2012).

To calibrate the polarisation of each pulsar observation, a noise diode was switched on and off with a period of ~ 89.9 milliseconds for two minutes before the pulsar observation. The final step of the calibration process is to create an individual calibrator database for each pulsar. After that, calibration solutions were applied.

Pulsar PSR J0437-4715 was used to produce the calibration solutions for the Parkes observations. This pulsar is regularly observed with the UWL, covering a large range of parallactic angles for the purpose of producing Measurement Equation Modelling (MEM; van Straten, 2004); solutions for a number of pulsar observing projects at Parkes. For our purposes observations of PSR J0437-4715 conducted from 5 November 2018 to 1 September 2022 were used. This period contains 177 observing sessions whose duration varied from ~ 1 hour to 9.6 hours.

First, MEM was used to create calibration solutions for 28 of these sessions. Then the calibrated pulsar observations were combined to produce a single high S/N template. Secondly, using the template as a polarised reference source, Measurement Equation Template Matching (METM; van Straten, 2013) was used to produce solution for all 177 sessions. Apparent rotations of the instrument around the line of sight caused by ionospheric Faraday rotation are built-in to those solutions due to the absence of a good model of the ionosphere. Therefore, new software was developed (by van Straten) to estimate and correct the Faraday rotation variations in the METM fits.

After RM-correction, seven of the free model parameters (four that describe receptor cross-coupling, and three that describe the polarization of the noise diode signal), are smoothed using a two-dimensional penalized spline (a function of time and radio frequency) - one spline for each model parameter. These splines are used to interpolate the calibration solution at the time of any PRESS observation, and used to calibrate the PRESS data in both Stages 1 and 2. The smoothing (details are in van Straten et all, paper in preparation) is done to: i) interpolate over gaps in data, and ii) to de-noise the data (at high frequencies the signal-to-noise ratio of the pulsar observation is lower; therefore, the uncertainties of estimated model parameters are greater).

4.5.1.5 Verifying DM, RM, and ephemeris

Another important step is to validate the calibrated outcomes and verify that the DM, RM, and ephemeris are consistent with our observations.

For this step, the *pdmp* tool was used; it generates images with information that compares derived and catalogue parameters (such as barycentric period, topocentric period, and DM). Figure 4.7 is an example of the DM verification step. The text above the image panels gives the catalogue values, and the text below the two middle panels gives the measured values. For example, for the observations of PSR J1921+2153 taken on 13 April 2020, the estimated DM = 12.8 ± 0.9 pc/cm^3 does not conflict with the catalogue DM = 12.444(6) pc/cm^3.

For the RM verification, the PSRCHIVE tool *rmfit* was used. For all considered pulsars, the estimated RM was within an acceptable range of the catalogue value given variations in ionospheric Faraday rotation which have a standard deviation of ±2 rad/m^2 (e.g., Porayko et al., 2019). Figure 4.8 presents differences of measured and catalogue RM (left panel) and DM (right panel) values for test pulsars, which can be seen in Tables B.2 and B.3 respectively.

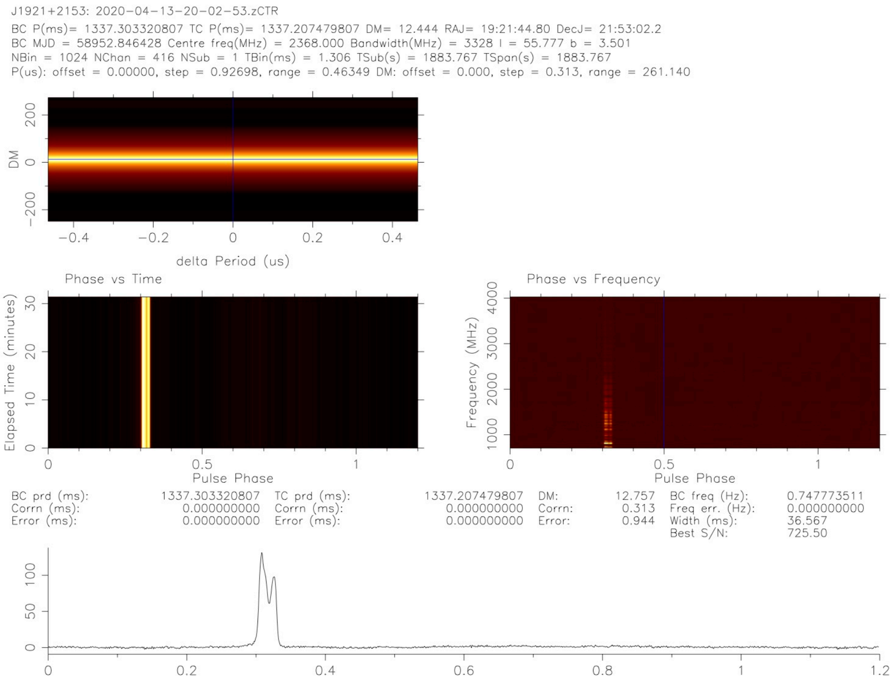

```
J1921+2153: 2020-04-13-20-02-53.zCTR
BC P(ms)= 1337.303320807 TC P(ms)= 1337.207479807 DM= 12.444 RAJ= 19:21:44.80 DecJ= 21:53:02.2
BC MJD = 58952.846428 Centre freq(MHz) = 2368.000 Bandwidth(MHz) = 3328 l = 55.777 b = 3.501
NBin = 1024 NChan = 416 NSub = 1 TBin(ms) = 1.306 TSub(s) = 1883.767 TSpan(s) = 1883.767
P(us): offset = 0.00000, step = 0.92698, range = 0.46349 DM: offset = 0.000, step = 0.313, range = 261.140
```

```
BC prd (ms):        1337.303320807  TC prd (ms):        1337.207479807  DM:      12.757  BC freq (Hz):     0.747773511
Corrn (ms):            0.000000000  Corrn (ms):            0.000000000  Corrn:    0.313  Freq err. (Hz):   0.000000000
Error (ms):            0.000000000  Error (ms):            0.000000000  Error:    0.944  Width (ms):       36.567
                                                                                          Best S/N:         725.50
```

Figure 4.7: Example of images produced by *pdmp* for checking the measured vs catalogue DM. Above graphs, data for the catalogue pulsar parameters is given. The top panel of the figure is a colour map of the delta of the barycentric period (us; x-axes) vs delta DM (y-axes) vs S/N (colour). Blue cross-hair shows the highest S/N value. Middle panels demonstrate colour maps of phase (x-axes) vs integration time (y-axes) on the left and phase (x-axes) vs frequency (y-axes) on the right plots. After the middle panel are the results of fitting the best DM and barycentric period which give the highest DM. The bottom panel presents a total intensity pulse profile integrated over the frequency with the new best period and DM (x-axes is a pulse phase, and y-axes is the pulsar brightness).

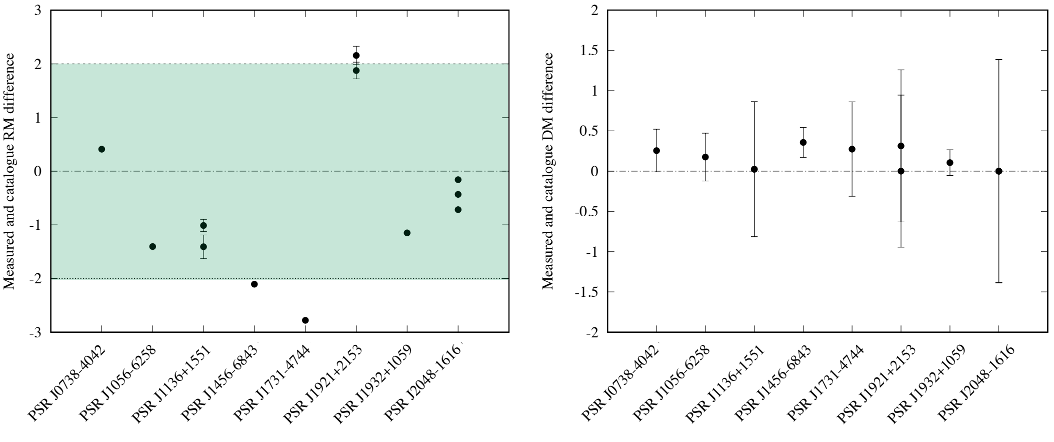

Figure 4.8: Comparison of measured and catalogue RM (left panel) and DM (right panel). Here x-axes show test pulsar names and y-axes are the differences between measured and catalogue values. The green-colored section at left panel depicts the the ionospheric Faraday rotation influence withing the standard deviation range from −2 to +2 rad/m^2.

4.5.1.6 Second visual inspection

To validate the quality of the profiles throughout the wide frequency range, the subbands of the folded data were grouped into three frequency bands (as listed in Table 4.1) and then time-averaged plots of the pulse profiles for each band were generated (see Figure 4.9 as an example) for visual inspection. Good profiles without issues, such as RFI that was missed, are then ready to be further analysed.

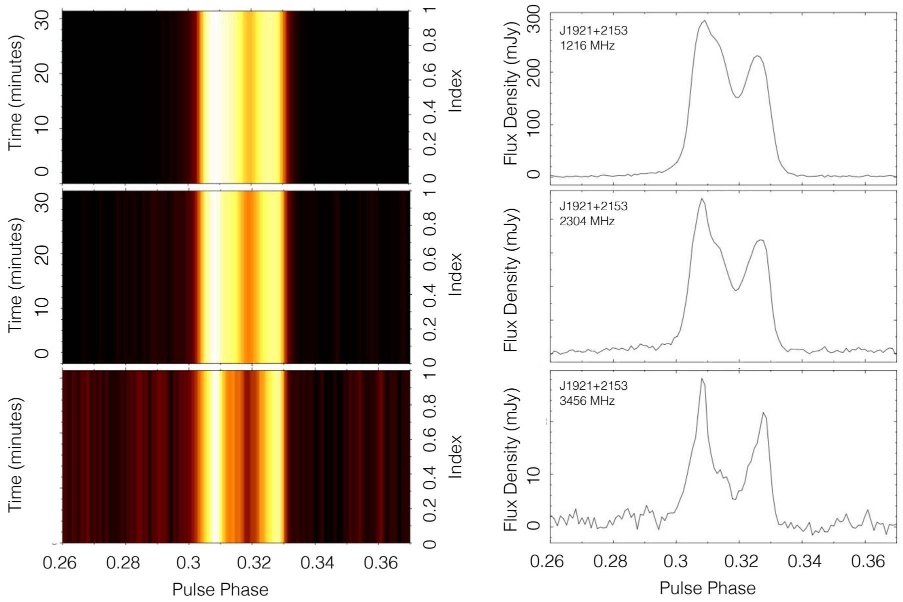

Figure 4.9: Example of images produced for checking the stability of the profile. The left panels are pulsar time series, and the right panels are averaged pulse profiles. From top to bottom, frequency bands are: Low, Mid, and High.

4.5.2 Stage 2 of data processing: single pulses

After verifying the quality of the data and the validity of the pipeline, including polarization calibration and RFI mitigation, we started single-pulse processing.

4.5.2.1 Producing cleaned and calibrated single-pulse archives

For the first step of this stage, DSPSR is used to resample the recorded timeseries, which consists of samples at regular intervals defined by the observatory clock, into phase bins which are regular time intervals in the reference frame of the pulsar. At the same time it organises the data into arrays, where each array represents one rotation of the pulsar and has a single pulse profile. Then these arrays are calibrated and written to file, separately for each band. Then these calibrated archives[6] are cleaned using two RFI-mitigation routines based on *PSRCHIVE tfzap* and *MEERGUARD* (Miles et al, paper in preparation) producing two types of cleaned data archives.

---

[6] Typically, in the pulsar community pulsar data are called *data archives*.

4.5.2.2 Comparing folded and single-pulse archives

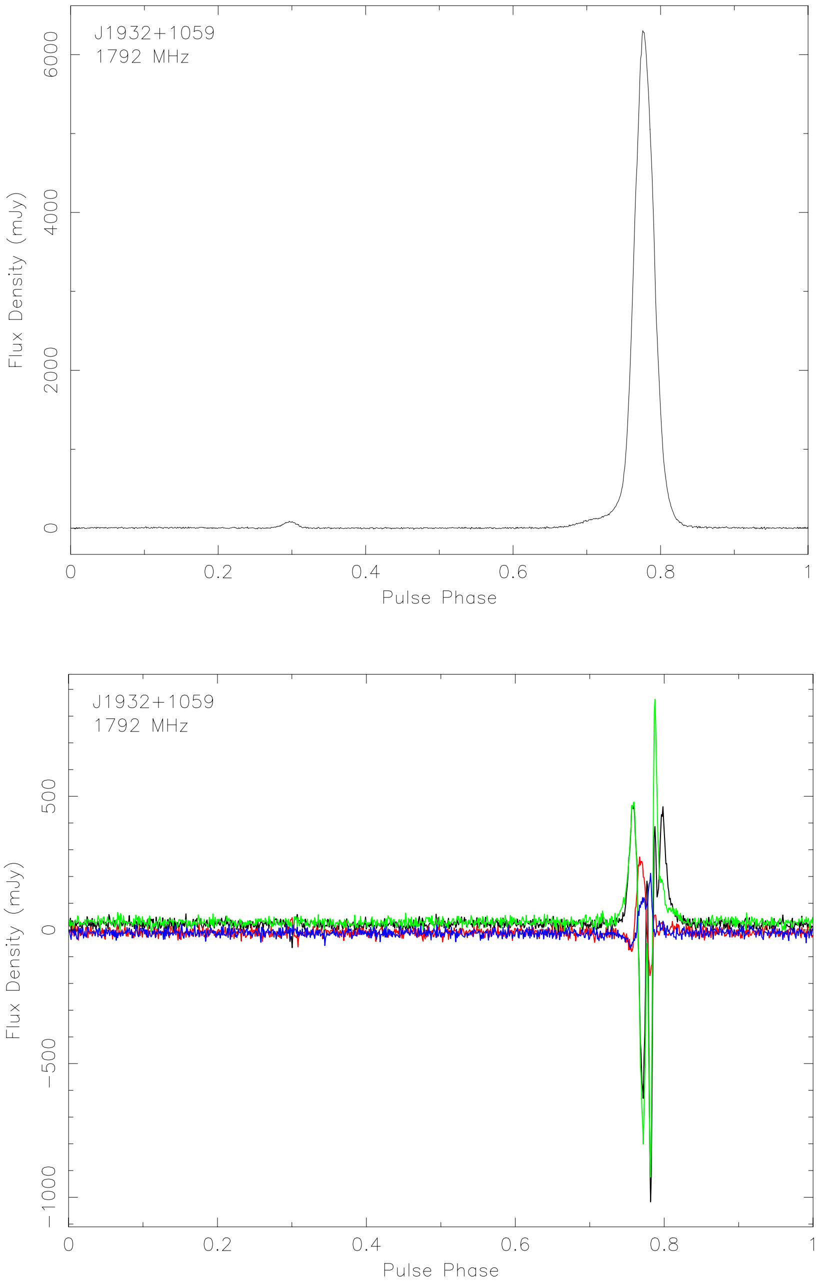

Figure 4.10: Example of the results for the folded and single-pulse processed data for PSR J1932+1059 (PSR B1929+10), which was done after the first run of the Stage 2 of *psrpl*. Top panel shows the averaged folded pulse profile at 1792 MHz. Bottom panel is the difference of folded and single-pulse processed results. There Stokes I, Q, U, and V are shown by black, red, blue, and green colours respectively. Such example alerted us about issues with RFI mitigation and triggered further research in that direction and then developments of the RFI-excision approaches described in Section 4.5.3.2

The next step is to verify that the single-pulse production procedure is performing correctly and whether the RFI algorithms are erroneously removing the brightest single pulses. Such verification was done by subtracting the fully-averaged profile obtained from the single-pulse data from the fully-averaged profile from the folded profiles and inspecting the residuals.

This important step was repeated over several iterations of refinement due to the large differences that were initially found between the folded and the single pulse data. It was found, for example, that indeed the original RFI routine was removing giant pulses from PSR J1056-6258. Thanks to this validation phase, we improved the RFI mitigation and calibration routines. Figure 4.10 shows an example of comparison of the *psrpl* results for the folded and single-pulse processed data for PSR J1932+1059 (PSR B1929+10), which was done before the developments of the *tfzap* RFI-excision algorithms and ultimate adoption of *MEERGUARD*. Here the difference between folded and single-pulse profiles can be seen between pulse longitudes ~ 0.73 and ~ 0.83 where all Stokes parameters are highly deviating from the zero in positive and negative directions.

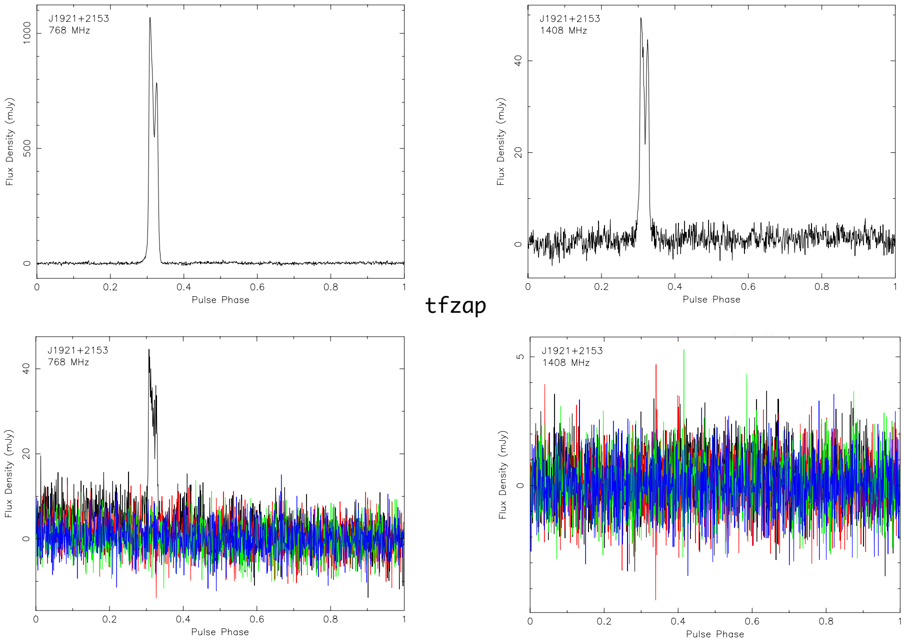

Figure 4.11: Example comparison of the results with the *PSRCHIVE tfzap* RFI excision on folded and single-pulse data for PSR J1921+2153 (PSR B1919+21). Stokes I, Q, U, and V are shown by black, red, blue, and green colours respectively. Top panel shows the averaged pulse profiles of corresponding sub-bands (left side 768 MHz, right side 1408 MHz), bottom panel is the difference between folded and single-pulse processed results. The bottom-right panel shows no difference between folded and single pulse processed data; while the bottom-left panel points to differences in Stokes I.

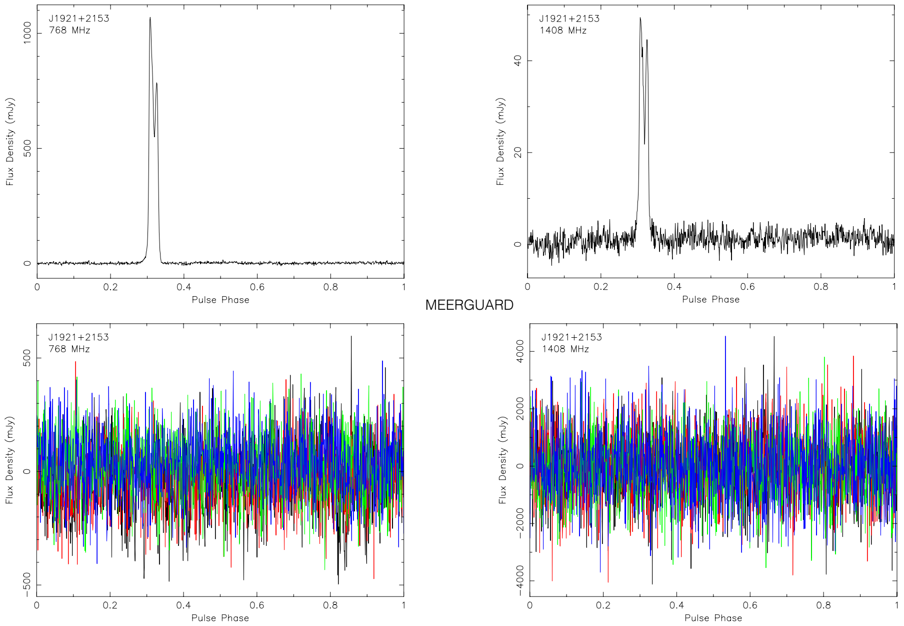

Figure 4.12: Example comparison of the results with the *MEERGUARD* RFI-cleanup folded and single-pulse processed data for PSR J1921+2153 (PSR B1919+21). Stokes I, Q, U, and V are shown by black, red, blue, and green colours respectively. Top panel shows the averaged pulse profiles of corresponding sub-bands (left side 768 MHz, right side 1408 MHz), bottom panel is the difference between folded and single-pulse processed results. Both panels show no difference between folded and single pulse data.

After development and implementation of the GMM statistics for RFI detection, the averaged profiles for folded and single-pulse data were more consistent, (Figure 4.11). Although some sub-bands continued to exhibit differences, as shown in the example for PSR J1921+2153 (PSR B1919+21) at 768 MHz (bottom-left panel). Here we see a peak of Stokes I that occurs in the on-pulse region, which means that one of the data archives, in this case folded, has more signal there than the other. That may mean that RFI algorithm zapped some single-pulse features (like a bright pulse for this pulsar, or giant pulse as we saw for other pulsars) in the single-pulse data and saved in the folded. The bottom right panel (1408 MHz) of this figure shows the consistency in the data processing for both Stages of *psrpl*.

Figure 4.12 demonstrates the application of the *MEERGUARD* on this pulsar. Here the folded and single-pulse data differences (i.e., the same sub-bands and same epoch of observation) indicate no significant differences between folded and single-pulse processed results.

4.5.2.3 Post-processing RFI cleanup

Currently, no automated RFI mitigation algorithm is able to detect and flag all affected data. The residual RFI significantly affects the quality of the fourth moments, which are squared intensities and therefore more susceptible to outliers. Therefore, manual cleanup is still important. More details for this are given in Section 4.5.3.2.

4.5.2.4 4th-moment computation in the subbands and result combination

Finally, the single-pulse data are ready to undergo the first step of our statistical data processing, and we can compute the phase-resolved covariances between the Stokes parameters. This step utilises the PSRCHIVE routine *psr4th* for each sub-band. The output files contain phase-resolved covariances between the Stokes parameters. For each epoch, the fourth moments of every sub-band are combined into three frequency bands (see Table 4.1), and all epochs are combined into one file for each frequency band, producing the following data products:

- Fourth moment output datafiles for Low, Mid, and High bands of all observed data
- Fourth moment output datafiles for Low, Mid, and High bands for individual epochs
- Fourth moment output datafiles for each sub-band in individual epochs

Images and datafiles will be made available for public access on the CSIRO Data Access Portal (DAP) after our data analysis pipeline is fully tested and its results are demonstrated to be reproducible.

4.5.3 Encountered Challenges

During the pipeline development for PRESS data processing, our team encountered a large number of challenges due to the facts that the UWL was a new instrument, sometimes some changes to the instrument were necessary in the middle of observing session(s), and PRESS utilizes novel single-pulse study approaches. These issues implied a large amount of software-development from the P.I. of the project, that I was further testing and validating. During work on RFI challenges at each stage of RFI-mitigation developments and trials I performed all manual cleanup. Below I report a brief list of the major challenges that demanded a lengthy timeline for resolving and code development.

4.5.3.1 First challenges with PRESS pipeline

Initially data processing for Stage 1 was planned as follows: a) data folding, b) verification of DM and RM, c) RFI excision, and d) calibration of the folded profiles. After this, it was planned to run the single pulse processing pipeline Stage 2, that produces single pulse archives from which covariance matrices of polarisation vectors fluctuations are derived.

However, after carrying out the initial folding step on a small sample of pulsars, the DM values reported using *pdmp* were found to be far from the catalogue values.

The main reason for this was the impact of RFI, and the lack of flux calibration, which made it difficult for the *pdmp* routine to estimate the correct DM values. This software searches for the optimal DM as a function of trial DM, and during fitting it searches for the peak in signal-to-noise ratios after combining all frequencies. However, for the uncalibrated UWL data the low frequency part of the band by design has much lower values of the uncalibrated flux density than at higher frequencies. Therefore, before flux calibration, the low frequency channels have negligible impact on the integrated total. However, low frequency channels provide the greatest constraint on the DM because the dispersive delay is greatest there. The most important part of the band for accurate estimation of DM was suppressed by UWL attenuation of the band most impacted by RFI (e.g., see Figure 1.10 in Chapter 1.4).

As a solution, we revised the pipeline steps and re-scheduled verification of DM and RM values after excising RFI and calibrating the folded profiles.

4.5.3.2 RFI mitigation challenges

RFI mitigation challenges caused most issues in our data processing and took a very long time to deal with. Currently issues with automated RFI excision are still not solved completely, and at this stage of the pipeline development a manual post-processing cleanup is needed.

Below we'll describe two groups of RFI challenges based on the processing stage we encountered them in chronological order.

RFI mitigation for folded data in Stage 1 Our initial approach was based on a built-in *PSRCHIVE* (van Straten et al., 2012) routine for detecting outliers in the folded profiles. It uses various thresholds based on the interquartile range of some computed statistics such as: the range of values, $max - min$; sum of detrended outliers; sum of harmonic outliers; the reduced χ^2 (distance between each profile and the average); and generalised χ^2 for each frequency channel and sub-integration. Issues with the application of this approach were found for observations with more than 25% corrupted data (such that the median and interquartile range are biased), and pulsars with interesting behaviour (e.g., the mode changing pulsar PSR J0034-0721, and the giant pulse emitting pulsar PSR J1056-6258). In these cases, the generalised least square approach either removed the useful signal, or missed a large fraction of RFI, or both.

As a solution, the P.I. of PRESS (van Straten et al., in preparation) developed a new outlier-detection statistics based on the the Gaussian Mixture Model (GMM). Later, we found that simply masking the on-pulse signal when searching for outliers, which is done by *COASTGUARD* (Lazarus et al., 2016) preserves more single-pulse phenomena (such as bright or giant pulses). Therefore, *MEERGUARD*, which is based on the *COASTGUARD* routines and was developed for the MeerTime project (Miles et al, paper in preparation), was adopted for PRESS. However, it is not the perfect remedy. It does a better job for some pulsars (see an example in Figure C.9 of Appendix C) but some RFI remains in the output.

RFI mitigation for single-pulse data in Stage 2 Compared to the more stable folded profiles, single pulses are highly variable. Therefore, we encountered issues that were not noticed or did not cause noticeable outliers in Stage 1.

For the initial single pulse processing we used the same RFI mitigation routine that was applied to the cleanup of folded data. However, a large amount of RFI was missed by the algorithm; therefore, all post-processed data must be manually cleaned. Owing to the very wide frequency band of the UWL, this is a labor-intensive task.

It was noticed that some pulsars (e.g., drifters or mode changing) lost their signal intensity after single pulses were added and then compared with the same data of folded profiles, as it is shown in bottom-left panel of Figure 4.11. Our best hypothesis is that that the outlier detection was cutting off the on-pulse signal for some bright single pulses, (e.g., giant pulses or intermediate single pulse features).

Experimentation with the chosen RFI detection thresholds revealed that when the value of thresholds were increased, the single-pulse on-pulse signal was recovered (not excised). However, more RFI remained in the data. When the thresholds were lowered, the output data contained much less RFI, but some (or many, depending on the pulsar) of the brightest single pulses were also excised. It was found that the optimal threshold levels are different for each pulsar; moreover, for a given pulsar, they vary with the epoch of observation. At the current stage of development, the optimal thresholds cannot be determined automatically.

Therefore, we decided to test a different approach, based on masking the on-pulse signal and detecting RFI using only the off-pulse phase bins, and applied[7] *MEERGUARD* (Miles et al, paper in preparation).

Single-pulse data then was reprocessed using two RFI-mitigation algorithms: with previously described *PSRCHIVE tfzap* zapping algorithm and the *MEERGUARD* cleaning routine. Comparison revealed that the *MEERGUARD* cleaning routine is best (Figure 4.13). However, the output still requires manual post-processing cleanup. Figure 4.13 demonstrates an example of $\simeq 14.31$ minutes (858.8 seconds) of observations, which contain 643 sub-pulses, for 1792 MHz sub-band.

---

[7] Chronologically first time *MEERGUARD* was used during the Stage 2, later in time it was added to the Stage 1

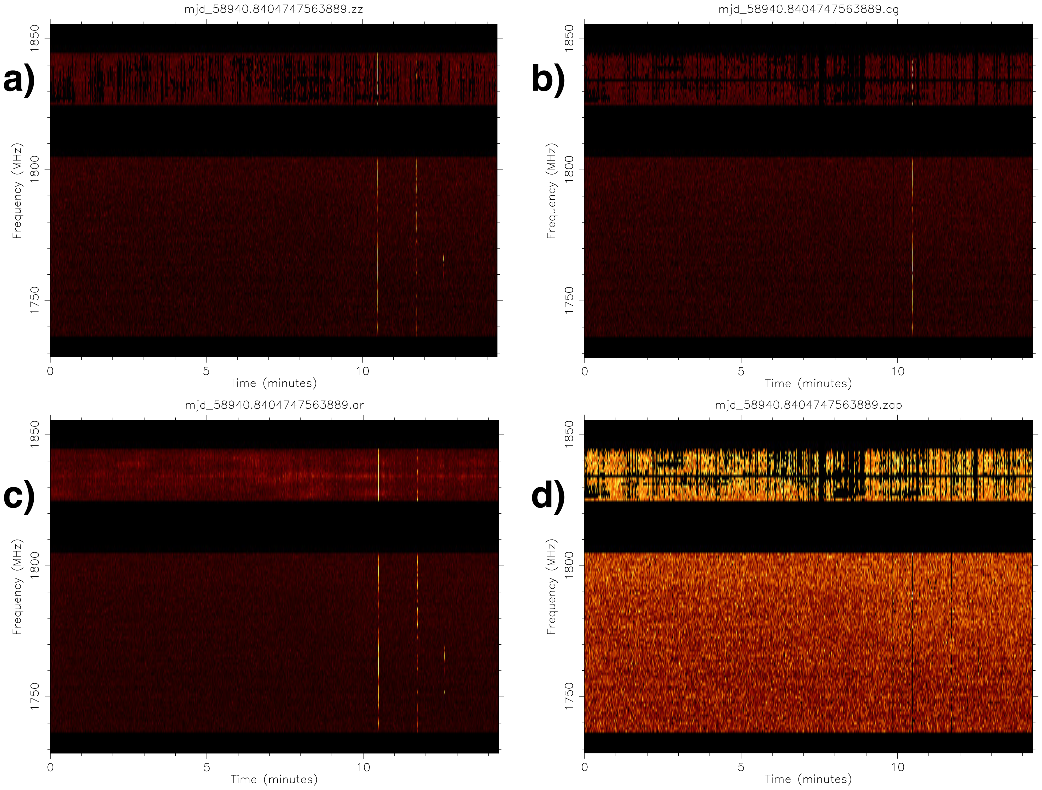

Figure 4.13: Comparison of single-pulse RFI excision routines for the 1792 MHz sub-band. For all panels, x-axis are time, y-axis are frequency, and the intensity of the colors are the range of the profile amplitudes ($max - min$). Panel a) is the result of *PSRCHIVE tfzap* zapping routine and panel b) is the result of algorithm based on the *MEERGUARD* approach. Panel c) depicts data before RFI mitigation, while panel d) is the final result after manual post-processing cleaning of the file from panel b).

The goal of the PRESS pipeline data processing is to perform automated data processing with the least possible manual intervention. At the same time the best possible RFI excision is highly important for further PCA and obtaining the most accurate covariance matrices of the fourth moments of electric field for further research.

4.5.3.3 Calibration Challenges

All calibration developments were done by van Straten (paper in preparation); therefore, in this section a brief description of the calibration challenges is provided.

Measurement Equation Modeling (MEM)

- PACKETS DROPPED BY MEDUSA

  In the stream of packets between the digitiser and the GPU cluster, the two polarisations are sent in different packets and the loss of packets in one stream incorrectly introduces a time offset between them. This time offset completely depolarises Stokes U and V. This is observed as an extremely noisy estimate of the differential phase. Figure 4.14 illustrates the issue.

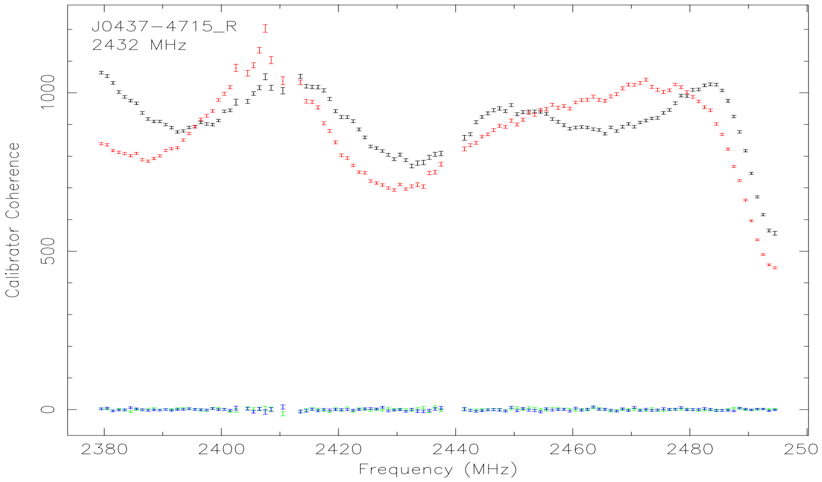

Figure 4.14: Packets dropped by Medusa are seeing in the“raw” noise diode Stokes parameters calibrator spectrum. Stokes U and V (green and blue points respectively) should be as high as the intensity in X and Y polarisations (black and red points).

  As a solution, the PSRCHIVE routine *pcm* was updated to ignore or excise observations of the noise diode with less than 50% polarised flux.

- MEDUSA RECORDS WHILE NOISE DIODE IS OFF

  Medusa starts recording data while the noise diode is turned off. At the end of the observation the noise diode turns off while Medusa is still recording. Figure 4.15 illustrates the issue.

  As a solution, the processing pipeline code was developed to remove sub-integrations in which the S/N of the noise diode is anomalously low.

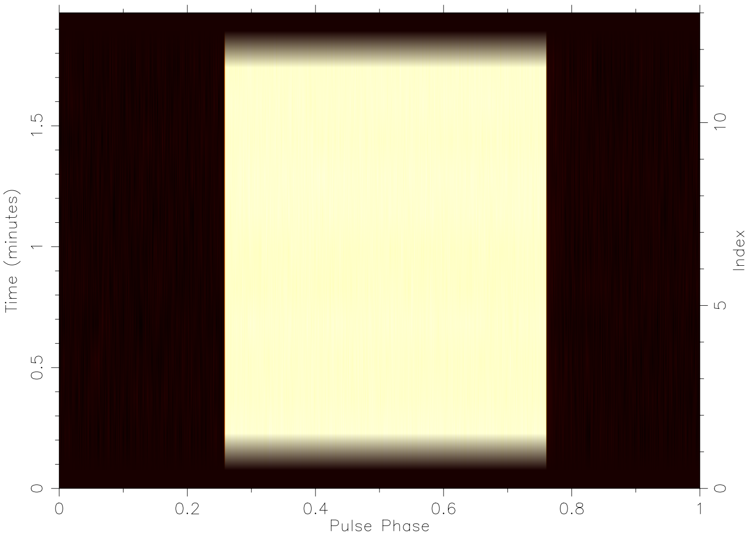

Figure 4.15: Demonstration that Medusa starts before and stops after the noise diode was turned on and off. Here the first and last subintegrations have lower flux (the x-axis shows the pulse phases, y-axis shows integration time, and color depicts the intensity; black is low and yellow is high).

- DIFFERENTIAL PHASE JUMPS

  The differential phase between the two nominally orthogonal receptors of the UWL receiver were observed to change during some of the observing sessions. Apparently, modifications were made to the instrumental configuration and, judging from the change in the slope of the linear variation of differential phase with frequency, in some cases the lengths of the cables used to propagate the two polarizations were changed. Figure 4.16 illustrates the issue. Here during a single observing session, the differential phase slope changes its direction several times during a single observing session. The image panels are organised by time from top to bottom in the left column followed by top to bottom in the right column (timestamps of each observation are provided in the right-bottom corner of each panel).

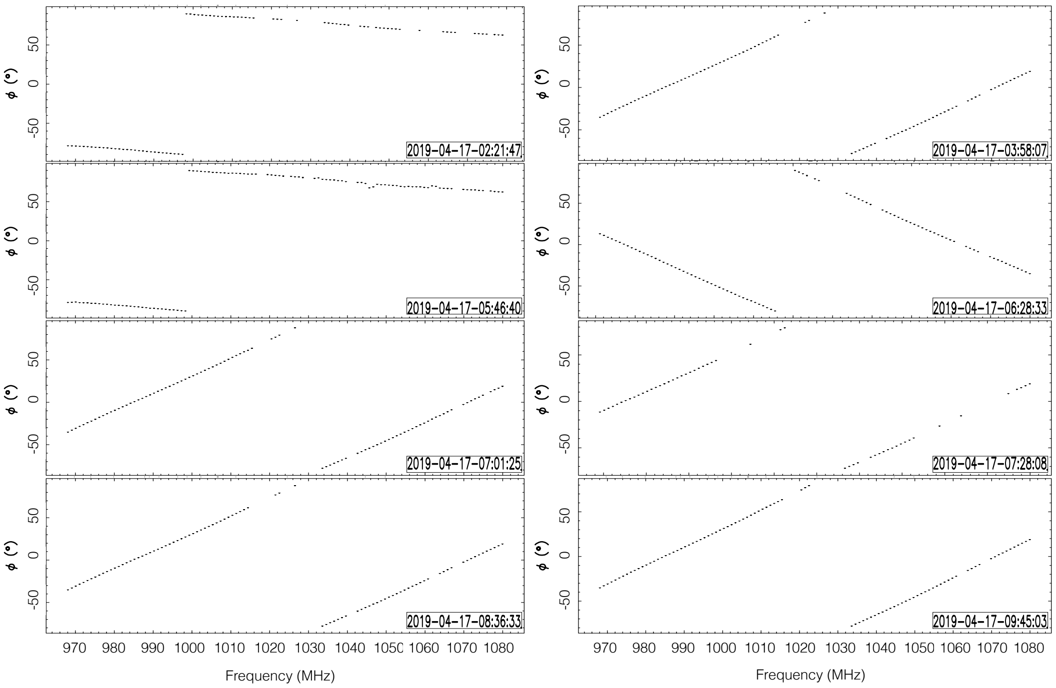

Figure 4.16: Differential phase changes during one observing session. Here x-axis of each panel depicts radio frequency, y-axis of each panel is differential phase in degrees.

From December 2018 to August 2022, jumps in differential phase were detected automatically in 36 separate observing sessions. In 19 of these cases, the jump was detected in only 1 or 2 of the 26 UWL sub-bands, and could be explained by random fluctuations of the detection statistic. On 2019 April 17 (the example shown Figure 4.16), the jump was detected in 25 of the 26 sub-bands. As late as 2022 February 20, differential phase jumps were detected in 5 of the 26 sub-bands; therefore, it appears that experimentation with instrumental configuration continued beyond the early commissioning phase of the receiver.

As a solution, the processing software was modified to detect and account for the introduced instrumental changes by inserting step functions in the model.

Measurement Equation Template Matching (METM)

- LARGE NUMBERS OF REJECTED SOLUTIONS AT HIGH FREQUENCIES

METM generates a median of 180 solutions for each frequency band. The pipeline culls what it considers a bad fit, and at 3968 MHz only 17 solutions survived the cull, due to large error bars on parameter estimates. Figure 4.17 illustrates the issue; here the top two panels show that at the highest frequencies errorbars have the largest spread (which means that the pulsar signal is the weakest and therefore, the constrains on the model parameters are weakening).

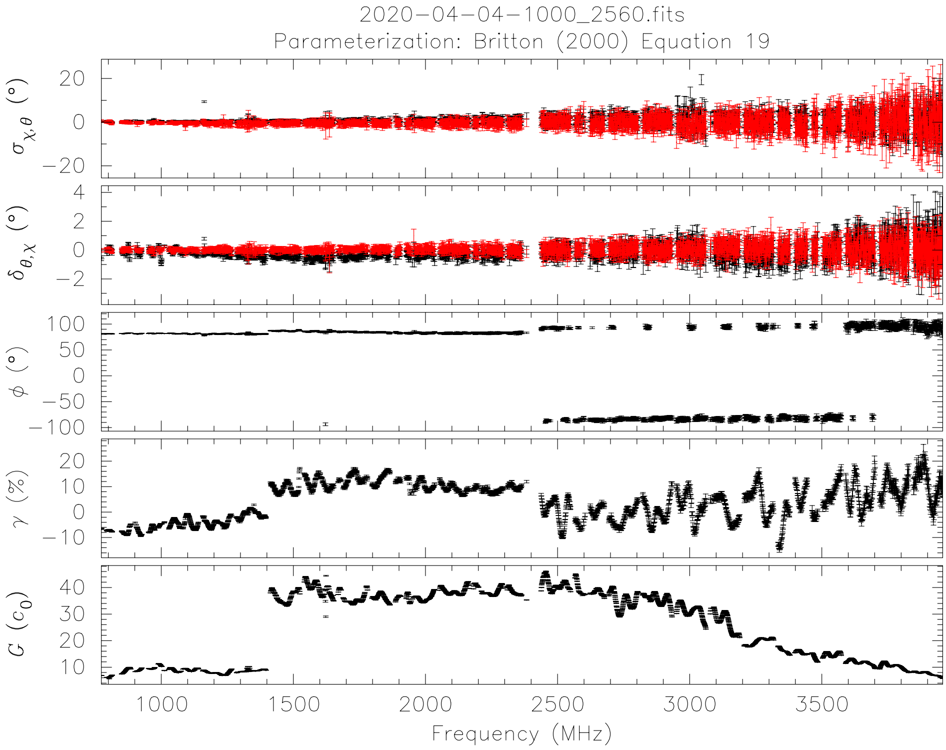

Figure 4.17: Parametrisation of the flux calibration. Top panel shows the sum of the ellipticities χ (black) and the orientations θ (red); second panel shows differences between the orientations θ (black) and the ellipticities χ (red); third panel shows differential phases; fourth panel shows differential gain; and the last panel shows the absolute gain.

To address this issue, spline-based smoothing of the solutions was implemented.

- THE SMOOTHING SPLINES DISPLAY TOO MUCH STRUCTURE

Initially, to smooth the solutions using *penalized splines*[8], a smoothing factor was chosen using *Generalized Cross Validation* (GCV). For data with low S/N, the

---

[8] Penalized splines are regression splines fit through least-squares with a roughness penalty.

GCV function creates smoothing splines that overfit data in about 10% to 20% of the trials.

As a solution, the PRESS P.I. (van Straten et al., in preparation) programmed a technique based on m-fold cross-validation, as described in Clark (1977). In a nutshell, the technique chooses the best smoothing factor based on following:

- All data is divided at random into two samples: the *estimation sample*, i.e., the set of data to which we fit the spline, and *validation sample*, i.e., the set of data that does not overlap with the first set.
- Then by using some given value of the smoothing factor, the smoothing spline is fit to the *estimation sample* and creates the estimator as a cross-validation mean-square-error (Chi-square) .
- After that it estimates the goodness of fit (which is a data minus model squared, averaged over all of the data) by computing the difference between the model and the *validation sample* (data that was not used to estimate the spline).
- The aforementioned steps are then repeated for various partitions, i.e., keep re-sampling at random the data set and test how well best-fit splines fit the validation data.

The above steps are repeated for each trial value of the smoothing factor. Then the optimal value of the smoothing factor is chosen.

- IONOSPHERIC RM BUILT-IN TO NOISE DIODE STOKES U

In the early spline fits to the model Stokes parameters of the noise diode, Stokes U was much less stable than Stokes Q and V. There is an apparent rotation of the linear polarization about the line of sight caused by ionospheric Faraday rotation, which varies with hour angle, total electron content of the ionosphere, and geomagnetic field (as the line of sight through the ionosphere changes). Due to the absence of a reliable ionospheric model, the best-fit rotation of the receiver about the line of sight (σ_θ from equation 19 of Britton, 2000) and the Stokes U of the noise diode were corrupted. In the model used by the software, Stokes Q of the noise diode has an ideal value of 1 and Stokes U has an ideal value near zero, therefore, in this reference frame $Q \propto \cos\theta \propto 1 - \theta^2/2$ and $U \propto \sin\theta \propto \theta$, where θ is the apparent rotation about the line of sight.

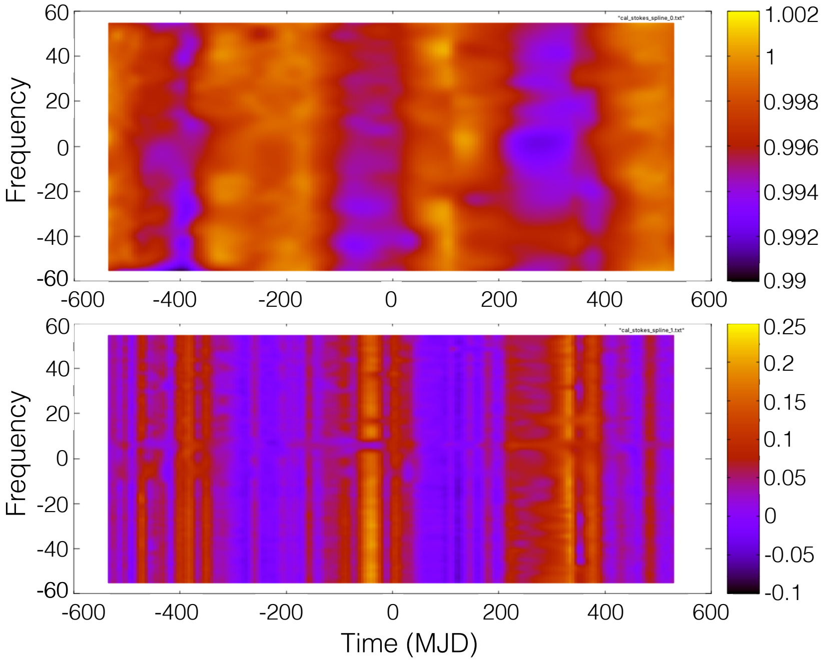

Figure 4.18: Stokes Q (upper panel) and Stokes U (lower panel) of the noise diode over ~ 3 years of observations. Here x-axis is time offset in MJD, y-axis is frequency offset in MHz with the central frequency of 1152 MHz. Both plots were produced from ionospheric RM-corrupted data.

Figure 4.18 illustrates the issue, where the variations in U are larger than the variations in Q. The variations in Stokes U are covariant with the variations in σ_θ because they are caused by the same apparent rotation about the line of sight.

To eliminate this covariance, we enabled the option to model the noise diode as coupled after the frontend (Hobbs et al., 2020); following this correction, the ionosphere no longer impacted the modelled Stokes parameters of the noise diode.

4.5.3.4 DM verification for the folded profiles of PSR J0034-0721

After RFI excision and calibration, most of the pulsars of our test subset showed an acceptable DM. However, in the mode-changing pulsar J0034-0721, the measured DM is off (by about 6 to 7 pc cm^3 depending on the epoch of observation) from the catalogue value even after improving and changing Stage 1 of *psrpl* (Figure 4.19 shows an example of one observing epoch).

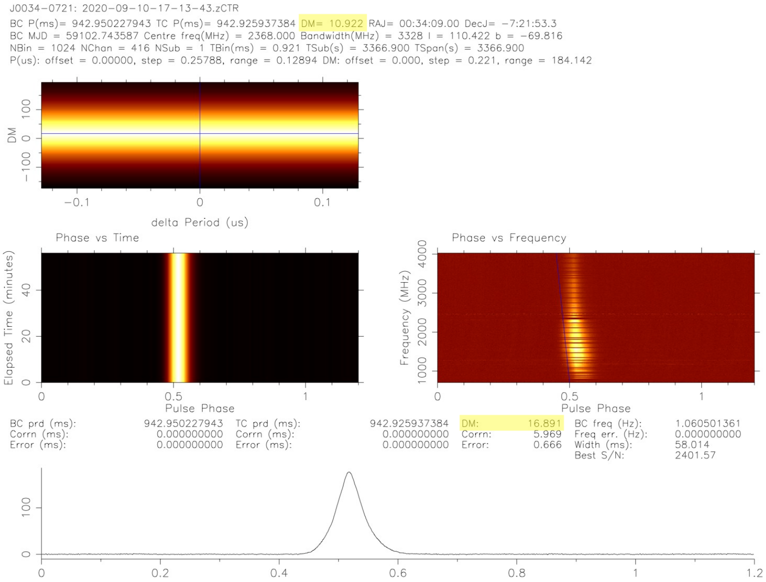

```
J0034-0721: 2020-09-10-17-13-43.zCTR
BC P(ms)= 942.950227943 TC P(ms)= 942.925937384 DM= 10.922 RAJ= 00:34:09.00 DecJ= -7:21:53.3
BC MJD = 59102.743587 Centre freq(MHz) = 2368.000 Bandwidth(MHz) = 3328 l = 110.422 b = -69.816
NBin = 1024 NChan = 416 NSub = 1 TBin(ms) = 0.921 TSub(s) = 3366.900 TSpan(s) = 3366.900
P(us): offset = 0.00000, step = 0.25788, range = 0.12894 DM: offset = 0.000, step = 0.221, range = 184.142
```

```
BC prd (ms):    942.950227943  TC prd (ms):   942.925937384  DM:       16.891  BC freq (Hz):     1.060501361
Corrn (ms):       0.000000000  Corrn (ms):      0.000000000  Corrn:     5.969  Freq err. (Hz):   0.000000000
Error (ms):       0.000000000  Error (ms):      0.000000000  Error:     0.666  Width (ms):       58.014
                                                                               Best S/N:         2401.57
```

Figure 4.19: Example of images produced for checking the measured vs catalog DM for PSR J0034-0721. See Figure 4.7 for details.

At this stage of development we decided to drop from the processing PSR J0034-0721 because in pulsar astronomy, the problem of disentangling the effects of DM, scattering and spectral evolution of the pulse profile is still unsolved.

4.5.3.5 Baseline issues while computing the fourth moments

After computing the covariance matrices for the single pulse data, we encountered new challenges in the form of RFI-induced structures in the baseline of the *psr4th* output.

Owing to RFI, the apparent SEFD of the signal output from the UWL is constantly changing, even on the timescale of a single pulse period. This is observed as a ramp in the off-pulse baseline of the Stokes parameters (see top panel of Figure 4.20), in some data. Accurate estimation of the mean off-pulse Stokes parameters is required to compute the source-intrinsic covariances between the Stokes parameters (see Equation 4.4).

The RFI impact on the baseline is clearly shown in the observation performed on PSR J1921+2153 on 13 April 2020 at 1536 MHz, see Figures 4.20 and 4.21 for folded profile and Stokes parameters. These figures report the same data, but with different levels of RFI cleanups, and it is obvious that the baseline with the less performing RFI mitigation has a noticeable baseline ramp in Stokes Q, U, and V. It is worth to note that even if *MEERGUARD* cleanup looks much better (top panel of Figure 4.21 where ramp disappeared), the baselines of the Stokes parameters still have prominent structures (bottom panels), which indicate to the presence of missed RFI[9].

When we compute fourth moments, the baseline plays a crucial role. Figure 4.22 illustrates another issue caused by baseline distortions.

Because the baseline is highly variable on sub-pulse timescales, we need to subtract it from every profile. The way the baseline is subtracted is important, as we have found that if we keep the baseline window fixed (i.e., the same phase bins were always used to estimate the baseline), then we result with underestimation of variance on these phase bins.

The RFI influence on the baseline of the covariance matrices can be described as following: when the baseline window is fixed and the off-pulse baseline is computed from the same phase bins in every single pulse, then a degree of freedom is removed from those phase bins, which biases the variance towards lower values. However, this bias is very small if the intensities in the off-pulse phase bins are uncorrelated with each other. In our case, the RFI introduces correlated structures on sub-pulse timescales, and

---

[9] Baseline plots can be used as bench tests for RFI cleanup quality control.

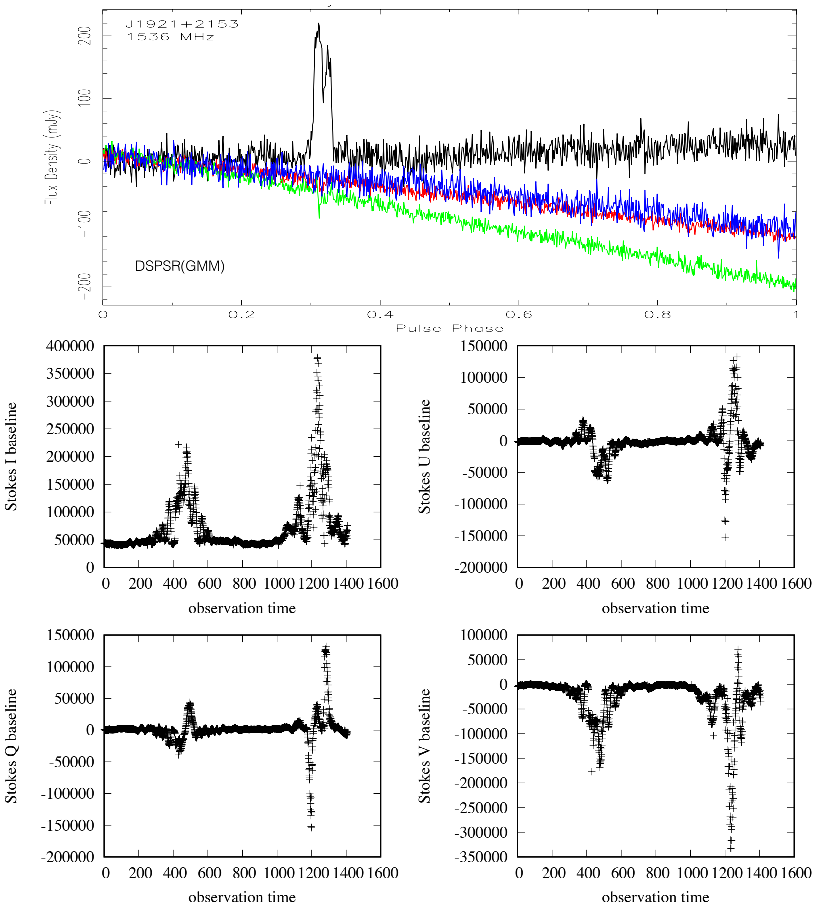

Figure 4.20: Folded profile and Stokes parameters with their baselines for PSR J1921+2153 observed on 13-th of April 2020 at 1536 MHz. These data had tfzap RFI mitigation.
Top panel is a pulse profiles in Stokes I, Q, U, and V (black, red, blue, and green respectively). Middle and bottom panels present baselines for each Stokes parameter.

the correlation introduced in neighbouring off-pulse phase bins increases the bias and introduces the dip that appears in the PCA results, as shown in Figure 4.22. Here for better demonstration, we chose a fixed baseline window around pulse phase 0.85, where a dip is clearly visible.

While improving the RFI mitigation in *psrpl*, we discovered that improved RFI cleaning reduces the baseline distortions, but at the current stage of the pipeline development, and with the current on-site RFI situation we have not been able to clean data completely.

As a solution, we decided to not remove the baseline calculated from each single

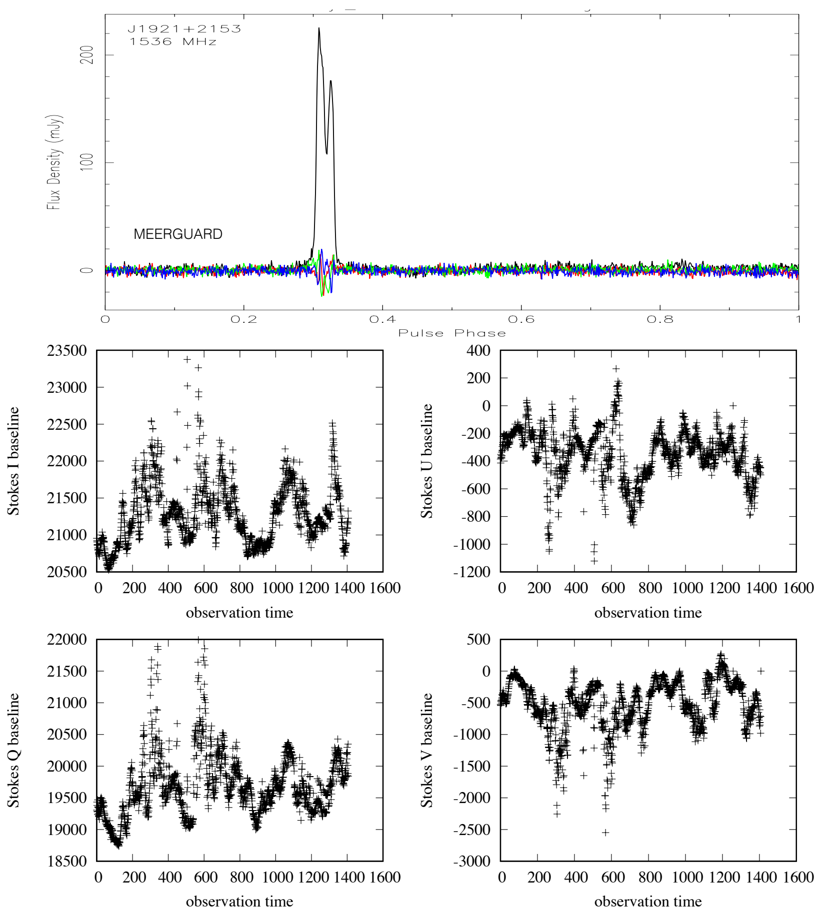

Figure 4.21: Folded profile and Stokes parameters with their baselines for PSR J1921+2153 observed on 13-th of April 2020 at 1536 MHz. These data had MEERGUARD RFI mitigation.
Top panel is a pulse profiles in Stokes I, Q, U, and V (black, red, blue, and green respectively). Middle and bottom panels present baselines for each Stokes parameter.

pulse, but to remove a baseline computed as a running mean computed over a certain number of pulses (usually 100 pulses for the first epoch of PSR J1921+2153 observations) throughout the off-pulse window.

Figure 4.23 shows a comparison of the two baseline removal approaches in PSR J1821+2153, when the baseline computed as a running mean over 100 pulses and the baseline computed from each pulse. The data had the best-to-date RFI removal.

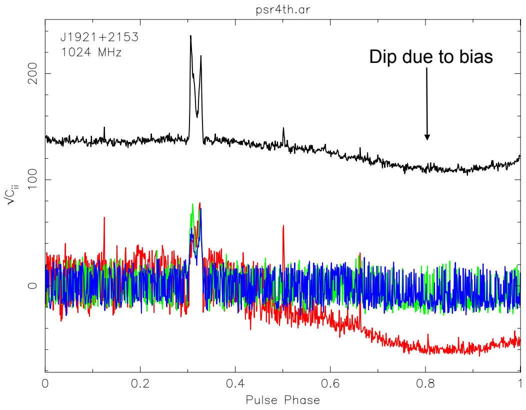

Figure 4.22: Example of the encountered issues with removing the baseline in the PCA outcome from the 1024 MHz-centered sub-band. The black curve shows the standard deviation of the total intensity, while red, blue, and green are the eigenvalues λ_1, λ_2. and λ_3 respectively.

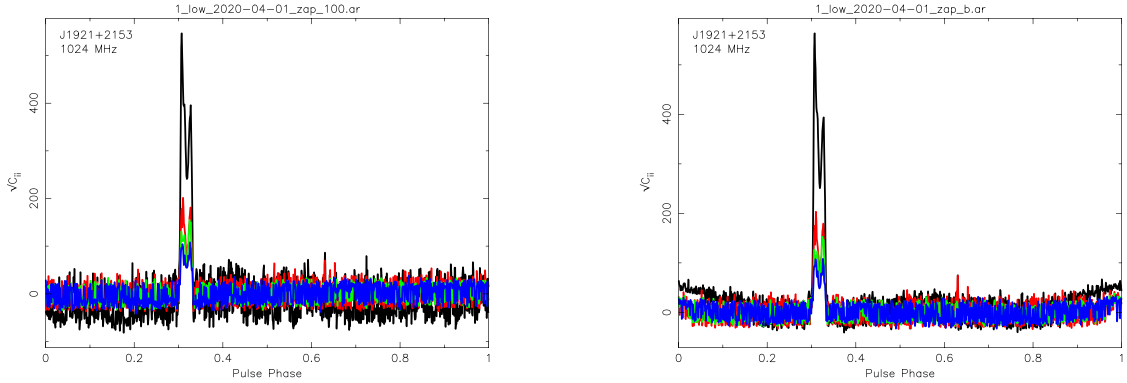

Figure 4.23: Comparison of the two baseline removal approaches in the PCA output for the 1024 MHz-centered sub-band. The black curve shows the standard deviation of the total intensity, while red, blue, and green are the eigenvalues λ_1, λ_2. and λ_3 respectively. The left panel shows the result of removing of a running mean baseline computed over 100 pulses, while the right panel shows the result of removing a baseline computed from each pulse.

4.6 Preliminary outcomes

During the development of *psrpl*, for testing and validating the pipeline performance we used PSR J1921+2153 (PSR B1919+21)[10]. It was chosen for these purposes due to the previous thorough studies of its polarisation properties using Arecibo data (see Chapter 3) and the interesting single-pulse behaviour, which makes it a good candidate for verifying the quality of the data processing.

---

[10] We also used other pulsars but in a smaller extent, mostly at the initial stages of the *psrpl* developments.

Within the PRESS project, this pulsar was observed on 1 and 13 April 2020 with integration lengths of 60 and 31 minutes respectively. The targeted integration length of 91 minutes was derived through Equation 4.5. Both of the observational epochs have different RFI and scintillation conditions, which caused the baselines for each epoch to be very different, and introduced complications when adding these two epochs together. Work on this issue is still in progress; therefore, in this chapter we will report the preliminary results derived for only the first epoch (which has the longest integration time).

4.6.1 Comparison of measured and predicted off-pulse noise

The integration length for the first observing epoch was 60 minutes; however, after the RFI cleanup, both the effective integration time and effective bandwidth are reduced. They are also reduced differently for each sub-band due to different RFI in each sub-band. Table B.4 shows the amount of data lost to RFI mitigation for the individual sub-bands. Therefore, in many sub-bands the targeted signal-to-noise ratio for the sample variance was not achieved (which may be supported by our preliminary results).

We now proceed to compare the standard deviation of the off-pulse baseline predicted by the radiometer equations (described in Section 4.2.2) to the one measured in each frequency sub-band. For this purpose we use Equation 4.3, with parameter values taken from the observed data, taking into account the amount of data lost to RFI. For this purpose the observed number of instances of total intensity should be multiplied by the fraction kept after RFI excision, such that: $n' = \tau \Delta\nu K$, where $\tau = 3600$s, $\Delta\nu = 128{\cdot}10^6$ Hz, and K is the fraction of kept data. In each sub-band, K was computed by counting all channels and subintegrations kept after RFI excision, and then dividing this amount by the product of all channels and subintegrations.

The r' from Equation 4.3 in our case is the ratio of the integrated flux under the pulse and the average flux under the baseline (or, in other words, the off-pulse mean flux, or SEFD). The duty cycle δ was estimated from the data by computing the full width of the pulse at 10% of the peak intensity. For PSR J1921+2153 $\delta \sim 0.032$, which is consistent with the value reported by Posselt et al. (2021)[11].

We compared predicted and measured RMS of the off-pulse baseline of the non-weighted data. The predicted RMS=SEFD $\sqrt{n_{bin}/(2\,n')}$, where $n_{bin} = 1024$ phase bins.

As shown in column 4 of Table 4.2, ratios for measured and predicted RMS are close to 1 for all sub-bands which is consistent with expectations.

Frequency MHz	Measured RMS	Predicted RMS	$\frac{Measured}{Predicted}$
768	4.63	4.41	1.05
896	2.48	2.51	0.99
1024	2.04	1.75	1.16
1152	2.86	2.00	1.43
1280	2.13	2.10	1.01
1408	1.58	1.42	1.11
1536	1.82	1.64	1.11
1664	1.67	1.41	1.18
1792	1.85	1.58	1.16
1920	1.65	1.50	1.10
2048	1.72	1.43	1.20
2176	1.67	1.57	1.07
2304	2.11	1.97	1.07

---

[11] https://www.atnf.csiro.au/research/pulsar/psrcat/expert.html

Table 4.2: Comparison of predicted and measured RMS of sample mean in the Low and Mid bands on the first epoch of observations of PSR J1921+2153.
The first column is the central frequency for each sub-band, column 2 is the measured RMS, column 3 is the predicted RMS, column 4 is the ratio of measured versus predicted RMS.

Measured RMS was derived from the data on which our best RFI excision was performed. It is worth to note that some sub-bands were heavily corrupted by RFI. The worst affected by RFI is the 768 MHz sub-band for which approximately 80% of its data was removed (see Table B.4), and it was not certain that all RFI was mitigated. It was challenging to find the limit when to stop excision.

4.6.2 Comparison of the PCA outputs

Despite the volume of data lost to RFI mitigation, we obtained preliminary PCA results for the Low frequency band (that spans 704 MHz to 1344 MHz) which are shown in Figure 4.24. Here the largest panel shows the PCA of the S/N-weighted mean of the covariance matrices computed for five sub-bands with center frequencies of 768 MHz, 896 MHz, 1024 MHz, 1152 MHz, and 1280 MHz. In the smaller panels are the PCA results for each sub-band.

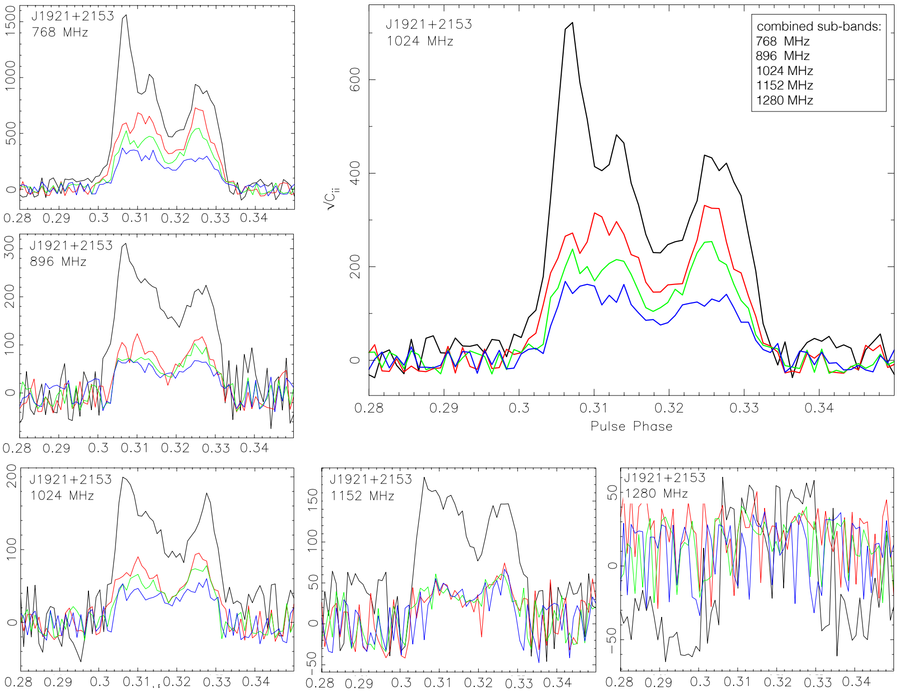

Figure 4.24: Preliminary PCA results for the first epoch of observation of PSR J1921+2153 at Low frequency with the best RFI-cleanup as of the end of November 2022.
The largest panel present the PCA results derived from the sum of covariance matrices for five sub-bands with center frequencies of 768 MHz, 896 MHz, 1024 MHz, 1152 MHz, and 1280 MHz. The smaller panels depict the PCA results for each sub-band individually. For each panel the y-axis is the standard deviation in Jy and x-axis is the pulse phase in fractional turns. For each panel, the black solid line shows the standard deviation of the total intensity, and the red, green, and blue lines display the square roots of the eigenvalues (from the largest to the smallest, respectively) of the 3×3 lower-right partition of the covariance matrix that describes the distribution of the polarisation vector $\boldsymbol{S} = (Q, U, V)$.

As evident from Figure 4.24, for the first epoch of observation, the S/N becomes insufficient for sub-bands with central frequencies above 1280 MHz. The PCA of individual sub-bands (where S/N allows) and of the combined Low band shows that throughout the pulse profile we do not see the prolate distribution. At the pulse phases around 0.321 and 0.324 fractional turns there is an indication of an oblate distribution of the polarisation vector, which is consistent with the results reported in Chapter 3 (see Figure 3.1 for comparison), where it was shown that this phase interval exhibits polarisation fluctuations characterized by a toroidal distribution of Stokes Q, U, V in the observations made with the Arecibo telescope.

By comparing the sub-bands, the difference in the flux density of the 768 MHz sub-band and the rest is very noticeable. This may have several explanations, one of them being the steepness of the pulsar's SED combined with the different scintillation effects in the individual sub-bands, whose behaviour varies with both time and frequency. The scintillation behaviour in the Low band for this observation is shown in Figure 4.25. Here we can see a very bright "scintle" (an island of enhanced intensity in the time-frequency domain) appears around the end of the observing session at frequencies approximately from ~730 MHz to ~870 MHz. Scintillation for individual sub-bands of Low and Mid bands are shown in Appendix C Figures C.10 and C.11 respectively.

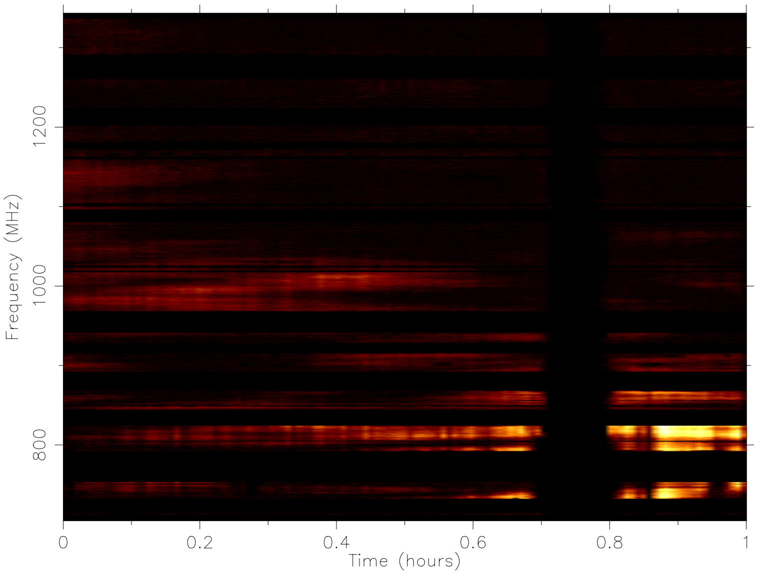

Figure 4.25: Scintillation for PSR J1921+2153 in the Low frequency band for one hour-long observation made on 1 April 2020. The image shows a time (x-axis) vs frequency (y-axis) plot of the dynamic signal-to-noise spectrum for RFI-cleaned data.

It is worth noting that our Arecibo study was done at 1414 MHz; however, the sample of PRESS data presented here is at a lower frequency range. Figure 4.24 shows that the polarisation behaves in a similar manner at lower and higher frequencies. In our analysis of the Arecibo data there is also a possible oblate distribution at 430 MHz (see Figure C.4 lower-left panel), but due to the lower signal-to-noise ratio and to the fact that a fraction of single pulses had flux density close to zero, we did not perform further studies (i.e., in the Poincaré sphere) of the polarisation behaviour at that frequency. However, at this stage we are not able to compare the Arecibo and PRESS PCA results at the same frequencies.

Chapter 5

Summary, conclusions, and future work

This chapter briefly summarises the research reported in this thesis, the consequences of the reported findings, and future research that builds on these results. Novel results were obtained by applying our statistical approach to Arecibo observations, and new techniques were developed to establish the PRESS project and undertake the initial analysis of its data.

5.1 Summary

5.1.1 Application of our statistical approach to Arecibo data

During our initial studies of pulsar emission using the adopted statistical approach, and following the preparations for the PRESS project, we used a high-quality (high S/N and low RFI) data set collected with the Arecibo radio telescope and published by Hankins and Rankin (2010). The aim was to test our interpretations of the Stokes covariance matrix by comparing our expectations of the Stokes parameters behaviour described by the PCA of said matrix with the direct study of polarisation fluctuations in the Poincaré sphere. The PCA approach and detailed study of polarisation fluctuations indeed showed that our interpretation of the PCA outcomes is aligned with the polarisation vector distributions. For the large majority of the studied pulsars, we see the expected prolate distributions (if modes are orthogonal and, in the case of superposed, they do not have equal intensities) alongside the effects of amplitude modulation, while other sources show evidence of disjoint modes, as detailed in Section 4.4.1. Our statistical method also enabled us to detect unexpected oblate distributions (see Section 4.4.1), which led to the study presented in Chapter 3.

5.1.2 New findings for PSR B1919+21

PSR B1919+21 was the first pulsar discovered (Hewish et al., 1968), it is very bright and relatively well-studied. However, our research discovered a polarisation behaviour that was previously unreported, as it showed that PSR B1919+21 exhibits both OPM switching and cycling of the polarisation vector around an elliptical path, synchronous with the drifting sub-pulse modulation. Drift-synchronous switching between nearly orthogonal polarized states has been observed for only five other pulsars, while elliptical cycling of the polarization state has been reported only once before (Edwards, 2004).

We also discovered a dramatic change in the modulation-resolved polarisation pattern of drifting subpulses that coincides with the pulse longitude where a transition between OPM occurs.

These observed effects are not predicted, and we explored a few models to offer a possible explanation.

To explain the abrupt change in P_3-modulated polarisation of PSR B1919+21 we suggested that at that “border” (i.e., at $\phi \sim -5.4^\circ$ shown in Figure 3.8) there was a transition from a primarily incoherent OPM superposition into a partially coherent OPM superposition.

To explain the observed toroidal distributions of the polarisation vectors we suggested a couple of hypothesis, such as *Generalised Faraday rotation* and *Four-Mode Mixing*.

According to the first explanation, the origin of the observed toroidal distributions and drift-synchronous elliptical cycling of polarisation state may arise from pulsar magnetospheric effects. We suggested that the beam consists of sub-beams, each of them composed of the partially coherent superposition of natural modes, where the natural modes are defined by the birefringent properties of the magnetosphere. Refraction in the magnetosphere then steers those sub-beams across the main beam. When the index of refraction changes, the beam varies its direction, and the relative phase of the coherent mode superposition also changes, causing the polarisation state to cycle around an elliptical path.

Another explanation is based on the *Rotating Carousel Model*, where we suggested the presence of two distinct rotating carousels that incoherently superpose. Each carousel is composed of sub-beams that alternate between orthogonally polarised states. (as described in *Four-Mode Mixing*). These two carousels may be offset in magnetic longitude.

To narrow down our hypothesis and retrieve a more accurate description of the physics behind the observed phenomena, we need more detailed studies of this pulsar. Therefore, we included PSR B1919+21 in the PRESS project, and focused primarily on the analysis of its observation.

5.1.3 Preparation of the PRESS project and testing the sample variance radiometer equation

To conduct a study of the covariance matrices of the Stokes parameters in the general pulsar population, we needed a new equation to calculate the observation time required to achieve sufficient S/N in the fourth moments of the electric field. Intuitively, such an integration length is going to be longer than what is needed to detect the mean Stokes parameters. Therefore, Prof. van Straten derived a new radiometer equation to estimate the observing time needed to achieve a given S/N in the sample variance of the subsample mean intensity (van Straten et al., paper in preparation).

The equation was derived theoretically, based on a number of assumptions, and verified with the data of PSR J0437-4715 observed by Osłowski et al. (2014) at a center frequency of 1382 MHz and a bandwidth of 400 MHz at the Parkes telescope. We then used the newly derived radiometer equation for predicting the required integration times and selecting pulsars for the PRESS observations.

For our equation we also assumed a square wave-form of the pulse, and the same amplitude modulation throughout the whole frequency range. However, in real situation we deal with non-square wave, and it may be more useful to approximate it with Gaussian. Moreover, the amplitude modulation is likely to be different at different radio frequencies, and the modulation index is not recorded in the pulsar catalogue. Derivation of an improved radiometer equation for the sample variance is planned for future research.

5.1.4 PRESS observations, lessons learned

Based on the results of the PRESS observation campaign, the following lessons were learned for further improvements in planning new observing campaigns oriented to collect data for calculating the fourth moments of the electric field. While developing the analysis pipeline for the PRESS data, *psrpl*, we achieved preliminary results that gave us the opportunity to test the radiometer equations that we derived for the standard sample variance of the single-pulse observations.

To compare predicted and measured S/N for sample mean and sample variance, we learned important lessons regarding the prior assumptions that we used to derive Equations 4.3 and 4.5. In these equations the effective number of sampled instances of total intensity n, is decreased by data lost to RFI mitigation, and the increase of the off-pulse variance of the sample variance profiles due to the different methods and levels chosen for RFI mitigation. For a more accurate estimation of the observing time we need to include time overheads for RFI. These days the RFI issue on-site is quite prominent and even increasing with the introduction of the 5G network (which currently transmits in Australia on frequency ranges of 703 MHz - 748 MHz, 758 MHz - 803 MHz, and 2500 - 2690 MHz)[I] and new launches of the Starlink and cubesats satellites (all together they operate at frequency ranges from S-band, 2 - 4 GHz, to Ka-band,[II] 26 - 40 GHz). During data processing a lot of the observed data in the time and frequency domains was rejected during the RFI cleanup, which artificially decreased the integration time used for pulsar observations (see example for PSR J1921+2153 in Table B.4, where approximately ~ 15% to ~ 85% of the data is lost in different sub-bands), and thus, it lowered the S/N with respect to the values we were aiming for (e.g., from ~1.3 to ~6 times off, see Chapter 4.6.1).

Furthermore, owing to scintillation, the data are non-uniformly weighted as a function of time and frequency. Firstly, scintillation causes variations in observed flux density; secondly, to maximise the S/N we computed weighted means, where each profile was weighted by $(\mathrm{S/N})^2$.

[I] https://www.spectrummonitoring.com/frequencies.php/frequencies.php?market=AUS

[II] https://docs.fcc.gov/public/attachments/DA-21-34A1.pdf and Akyildiz et al. (2019)

Find a long-term large data storage for the raw data in advance. During the observations we generated high volume of data (over 289 TB) that proved to be difficult to store. Together with other solutions to this issue, we decided to remove millisecond pulsars from the observing list because they require the highest sampling rate; an hour of millisecond pulsar observations may generate ~ 198.9 TB). To prevent the exclusion of some types of pulsars in future, extra data storage is vital.

5.1.5 PRESS data processing during pipeline developments

In the reported work, I focused on validation, testing, and quality assurance of the outputs of the PRESS data processing pipeline (through manual investigation of intermediate products of the pipeline). Analysis and discussion with the project PI (van Straten) to study the results of these tests and fix problems enabled alternative solutions to the encountered challenges. A large amount of time and effort was dedicated to the on-going challenges posed by RFI, some of which are left for future research projects.

Although the pipeline development continues, we achieved preliminary results on PSR B1919+21 that can be compared with the results of the Arecibo data analysis. This gave us clues for further improvements of the data processing that will be implemented for the upcoming first Data Release (DR1 in prep.).

5.2 Future opportunities and work

With the initiation of the PRESS project and further developments in the single-pulse analysis statistical approach reported in this thesis, we set the foundation for future research projects. Below is a brief list of the projects that stem from this thesis.

5.2.1 Future research on pulsars demonstrating peculiar features in the fourth moments

As it was described in Chapter 4 (Section 4.4.1) we found a number of pulsars that exhibit interesting behaviours in the fourth moments in the Arecibo data set, which can be studied in future projects. For example,

- pulsars PSR B1737+13 and PSR B2020+28 have similar variances of total intensity (σ_0^2) and the first eigenvalue (λ_1), but the degree of polarization is not nearly 100%; therefore, these pulsars might exhibit evidence of disjoint modes.;
- pulsars PSR B0626+24, PSR B1821+05, and PSR B2044+15 indicate the presence of non-prolate distributions of polarisation vectors;

PSR B1929+10 (PSR J1932+1059)

While studying the Arecibo P1260 pulsars through the lens of the fourth moments of the electric field, we also found the polarisation behaviour of PSR B1929+10 to be surprising. Its PCA results (Figure C.5 upper-middle panel) stand out from the whole set of pulsars (see Section 4.4.1 for details). The distribution of polarisation vectors in the Poincaré sphere may indicate that the emission is switching between highly polarised and unpolarised states. (Section 4.4.1).

5.2.2 Further research on PSR B1919+21 (J1921+2153)

As shown in the Chapter 3, our methodology is capable of detecting previously undiscovered properties of well-studied pulsars. For pulsar PSR B1919+21, it laid the foundation for new research projects that will utilize our tools.

The PCA method is able to detect highly variable (i.e., highly modulated in its amplitude) profile components that may not be detected in their weak average emission. As it was mentioned in Chapter 3, with PCA we found a pre-pulse feature of PSR B1919+21 at low frequencies where it had not been detected. Previously, that emission feature was noticed only in a dedicated 4.6 GHz, high-sensitivity Arecibo single-pulse survey by Olszanski et al. (2019)[III]. Together with detecting such pre-pulse emission feature, PCA shows that the distribution of the polarisation vectors from the pre-pulse in the Poincaré space is different (prolate) to that of the main pulse (ellipsoidal and oblate spheroidal).

PSR B1919+21 has both a complicated beam geometry and drifting sub-pulse dynamics that require further dedicated study. For example, motivated by the findings of this thesis, Castelltort (2023) has extended the Polarization Longitude Resolved Fluctuation Spectra (PLRFS) analysis introduced by Edwards (2004) so that it can be applied to study the quasi-periodic drifting of PSR B1919+21.

This pulsar was also observed in the framework of the PRESS project and used as a validation tool during the pipeline developments. Therefore, when the PRESS data will be completely processed and ready to use, it will provide a novel opportunity to study the evolution of the polarisation variances of this pulsar throughout the wide frequency range of about 3 GHz of the UWL.

[III] Currently, the Olszanski et al. (2019) data have the highest single-pulse sensitivity due to the large effective area of the Arecibo telescope, and the low-level of RFI due to the site location.

5.2.3 Future developments for PRESS RFI mitigation

During the PRESS data processing our team encountered RFI mitigation challenges that turned out to be more complicated and nontrivial than we initially anticipated. The established and most widely used RFI mitigation routines failed to eliminate the wide variety of RFI in the UWL band. The initial novel developments to automate RFI cleanup for the PRESS data are described in Section 4.5. It is vital to continue the development of automated RFI mitigation to perform an accurate statistical study of the single pulse emission.

This PhD research indicated that for RFI mitigation in folded profiles and single pulses the approach should be different. Here we identified the major issue such as the way in which we detect outliers and how we distinguish RFI from the variability of the single pulses.

For the first PRESS data release, more sophisticated RFI cleanup is necessary.

5.2.4 Planned PRESS release of data

Our team plans to release PRESS data products for free access once the RFI challenges are solved and the pipeline is able to perform automated RFI mitigation with an acceptable level of quality. The first data release (DR1) will include:

- Archives with folded profiles of pulsars[IV] for each epoch of observations and each sub-band, as well as for combined observing epochs, if any, and for the three frequency bands (Low, Mid, and High)
- Archives with single-pulse profiles of pulsars for each epoch of observations and each sub-band
- Archives with covariance matrices in the PSRCHIVE *psr4th* data format for each

---

[IV] See the list of PRESS pulsars in Table B.1

epoch and each sub-band, as well as for combined epochs and three frequency bands (Low, Mid, and High). These archives contain both sample mean and sample variance data.

DR1 products will be uploaded to the CSIRO Data Access Portal. We also plan to publish a paper that describes the data, how they were obtained, processed, and how they can be accessed by public.

5.2.5 PRESS-X

As it was found in preliminary results, the RFI artificially increased the integration time needed to achieve targeted sensitivity for the sample variance detection (e.g., Section 4.6). Moreover, PRESS started with a number of assumptions (Section 4.2.2) to derive a radiometer equation, but in these assumptions we did not consider the scintillation effects and the RFI influence.

Therefore, we aim to carry out an extension of the PRESS observations (i.e., PRESS-X) to level out the differences between achieved and estimated S/N.

PRESS-X will complete the observing campaign for unfinished observations of pulsars (see Table B.1); and add more integration time for already observed pulsars to achieve an acceptable signal-to-noise ratio in the sample variance for pulsars that have lost data in the time- and frequency- domains due to the RFI cleanup. The data recorded for PRESS-X will be appended to the DR1 data, and later it is planned to produce the second data release, DR2.

5.3 Conclusion

This thesis presents important steps that lead to the foundation of the PRESS project: the verification of the methods on real data that proved the validity of the methodology; and finally, the observed single-pulse pulsar survey based on the developed methodology.

During the first part of the research, we found and studied the toroidal distributions of the polarisation vector in the Poincaré sphere and its cycling around elliptical paths synchronously with the drifting in intensity for PSR B1919+21.

Together with providing the scientific potential of the PRESS data and methodology, we identified the need for future software developments, especially in the area of automated RFI mitigation.

Following the work done in the thesis, we plan to deliver a PRESS DR1 that will be freely accessible. The larger research community will benefit from new ways of analysing previously unavailable polarisation information of faint pulsars via the statistical analysis described in this thesis.

References

Akyildiz, I. F., Jornet, J. M. & Nie, S. (2019). A new cubesat design with reconfigurable multi-band radios for dynamic spectrum satellite communication networks. *Ad Hoc Networks*, *86*, 166-178. doi: https://doi.org/10.1016/j.adhoc.2018.12.004

Asseo, E. & Porzio, A. (2006). Strong langmuir turbulence in a pulsar emission region: statistical analysis. *Monthly Notices of the Royal Astronomical Society*, *369*(3), 1469-1490. doi: 10.1111/j.1365-2966.2006.10386.x

Baade, W. & Zwicky, F. (1934). On super-novae. *Proceedings of the National Academy of Science*, *20*(5), 254-259. doi: 10.1073/pnas.20.5.254

Backer, D. C. (1970). Correlation of subpulse structure in psr 1237+25. *Nature*, *228*, 752–755.

Backer, D. C. (1970). Pulsar nulling phenomena. *Nature*, *228*, 42-43. doi: 10.1038/228042a0

Backer, D. C. (1973). Pulsar fluctuation spectra and the generalized drifting-subpulse phenomenon. *Astrophysical Journal*, *182*, 245-276. doi: 10.1086/152134

Backer, D. C., Rankin, J. M. & Campbell, D. B. (1975). Pulsar fluctuation spectra and the generalized drifting-subpulse phenomenon. ii. *Astrophysical Journal*, *197*, 481-487. doi: 10.1086/153533

Backer, D. C., Rankin, J. M. & Campbell, D. B. (1976). Orthogonal mode emission in geometric models of pulsar polarisation. *Nature*, *263*, 202-207.

Baiotti, L., Hawke, I., Montero, P. J., Löffler, F., Rezzolla, L., Stergioulas, N., … Seidel, E. (2005). Three-dimensional relativistic simulations of rotating neutron-star collapse to a kerr black hole. *Physical Review D*, *71*(2), 024035. doi: 10.1103/PhysRevD.71.024035

Barnard, J. J. & Arons, J. (1986). Wave propagation in pulsar magnetospheres: Refraction of rays in the open flux zone. *Astrophysical Journal*, *302*, 138.

Basu, R. & Mitra, D. (2018). Subpulse drifting, nulling, and mode changing in psr j18222256. *Monthly Notices of the Royal Astronomical Society*, *476*(1), 1345-1355. doi: 10.1093/mnras/sty297

Basu, R., Mitra, D. & Melikidze, G. I. (2017). Meterwavelength single-pulse polarimetric emission survey. III. the phenomenon of nulling in pulsars. *The Astrophysical Journal*, *846*(2), 109. doi: 10.3847/1538-4357/aa862d

Basu, R., Mitra, D., Melikidze, G. I., Maciesiak, K., Skrzypczak, A. & Szary, A. (2016). Meterwavelength single-pulse polarimetric emission survey. ii. the phenomenon of drifting subpulses. *The Astrophysical Journal*, *833*(1), 29. doi: 10.3847/

1538-4357/833/1/29

Basu, R., Mitra, D., Melikidze, G. I. & Skrzypczak, A. (2019). Classification of subpulse drifting in pulsars. *Monthly Notices of the Royal Astronomical Society*, *482*(3), 3757-3788. doi: 10.1093/mnras/sty2846

Bhat, N. D. R., Rao, A. P. & Gupta, Y. (1999). Long-term scintillation studies of pulsars. i. observations and basic results. *The Astrophysical Journal Supplement Series*, *121*, 483-513.

Blaskiewicz, M., Cordes, J. M. & Wasserman, I. (1991). A relativistic model of pulsar polarization. *Astrophysical Journal*, *370*, 643-669.

Bombaci, I. (1996). The maximum mass of a neutron star. *Astronomy and Astrophysics*, *305*, 871.

Bondonneau, L., Grießmeier, J. M., Theureau, G., Cognard, I., Brionne, M., Kondratiev, V., … Tasse, C. (2021). Pulsars with NenuFAR: Backend and pipelines. *Astronomy and Astrophysics*, *652*, A34. doi: 10.1051/0004-6361/202039339

Born, M. & Wolf, E. (1980). *Principles of optics: electromagnetic theory of propagation, interference and diffraction of light*. New York: Pergamon.

Born, M. & Wolf, E. (1999). *Principles of optics*.

Britton, M. C. (2000). Radio astronomical polarimetry and the lorentz group. *Astrophysical Journal*, *532*(2), 1240-1244. doi: 10.1086/308595

Burke, B. F. & Graham-Smith, F. (2002). *An introduction to radio astronomy: Second edition*.

Burke-Spolaor, S., Bailes, M., Ekers, R., Macquart, J.-P. & Crawford, F., III. (2011). Radio bursts with extragalactic spectral characteristics show terrestrial origins. *The Astrophysical Journal*, *727*, 18. doi: 10.1088/0004-637X/727/1/18

Burke-Spolaor, S., Johnston, S., Bailes, M., Bates, S. D., Bhat, N. D. R., Burgay, M., … van Straten, W. (2012). The high time resolution universe pulsar survey - v. single-pulse energetics and modulation properties of 315 pulsars. *Monthly Notices of the Royal Astronomical Society*, *423*(2), 1351-1367. doi: 10.1111/j.1365-2966.2012.20998.x

Castelltort, A. (2023). *Spectral Analysis of the Polarization of Drifting Subpulses* (Master's Thesis). Auckland University of Technology, New Zealand.

Chandrasekhar, S. (1947). The transfer of radiation in stellar atmospheres. *Bulletin of the American Mathematical Society*, *53*(7), 641–711.

Chandrasekhar, S. (1960). *Radiative transfer*. New York: Dover, 1960.

Cheng, A. F. & Ruderman, M. (1979). A theory of subpulse polarization patterns from radio pulsars. *Astrophysical Journal*, *229*, 348-360.

Clark, R. M. (1977). Non-parametric estimation of a smooth regression function. *Journal of the Royal Statistical Society. Series B (Methodological)*, *39*(1), 107–113.

Clayton, D. D. (1983). *Principles of stellar evolution and nucleosynthesis*.

Cohen, M. H. (2009). Genesis of the 1000-foot arecibo dish. *Journal of Astronomical History and Heritage*, *12*(2), 141-152.

Condon, J. J. & Ransom, S. M. (2016). *Essential radio astronomy*.

Cordes, J. M. (1975). Pulsar psr 1919+21: notches, drifting subpulses, microstructure, and other emission. *Astrophysical Journal*, *195*, 193-202. doi: 10.1086/153318

Cordes, J. M. (1976). Correlation analyses of microstructure and noiselike intensity fluctuations from pulsar 2016 + 28. *Astrophysical Journal*, *208*, 944–954.

Cordes, J. M. (1978). Observational limits on the limits of pulsar emission regions. *Astrophysical Journal*, *222*, 1006-1011.

Cordes, J. M. (1986). Space velocities of radio pulsars from interstellar scintillations. *Astrophysical Journal*, *311*, 183-196.

Cordes, J. M. & Chernoff, D. F. (1998). Neutron star population dynamics. ii. three-dimensional space velocities of young pulsars. *Astrophysical Journal*, *505*(1), 315-338. doi: 10.1086/306138

Cordes, J. M. & Hankins, T. H. (1977). Pulsar polarization fluctuations at 430 MHz with microsecond time resolution. *Astrophysical Journal*, *218*, 484-503.

Cordes, J. M., Rankin, J. M. & Backer, D. C. (1978). Orthogonal modes of polarization from pulsar PSR 2020+28. *Astrophysical Journal*, *223*, 961-972.

Csiro, 2020. (2020, Aug). Retrieved from `https://www.csiro.au/en/News/News-releases/2020/CSIRO-Parkes-radio-telescope-added-to-National-Heritage-List`

Davidson, K. & Ostriker, J. P. (1973). Neutron-star accretion in a stellar wind: Model for a pulsed x-ray source. *Astrophysical Journal*, *179*, 585-598. doi: 10.1086/151897

Deshpande, A. A. & Rankin, J. M. (2001). The topology and polarization of sub-beams associated with the 'drifting' sub-pulse emission of pulsar b0943+10 - i. analysis of arecibo 430- and 111-mhz observations. *Monthly Notices of the Royal Astronomical Society*, *322*, 438–460.

Drake, F. D. & Craft, H. D. (1968). Second periodic pulsations in pulsars. *Nature*, *220*, 231-235.

Dunning, A., Bowen, M., Bourne, M., Hayman, D. & Smith, S. L. (2015). An ultra-wideband dielectrically loaded quad-ridged feed horn for radio astronomy. In *2015 ieee-aps topical conference on antennas and propagation in wireless communications (apwc)* (p. 787-790). doi: 10.1109/APWC.2015.7300180

Dyks, J. (2017). The origin of radio pulsar polarization. *Monthly Notices of the Royal Astronomical Society*, *472*(4), 4598-4617. doi: 10.1093/mnras/stx2101

Dyks, J. (2019). Radio pulsar polarization as a coherent sum of orthogonal proper mode waves. *Monthly Notices of the Royal Astronomical Society*, *488*(2), 2018-2040. doi: 10.1093/mnras/stz1690

Dyks, J., Rudak, B. & Harding, A. K. (2004). On the Methods of Determining the Radio Emission Geometry in Pulsar Magnetospheres. *Astrophysical Journal*, *607*, 939-948.

Dyks, J., Serylak, M., Osłowski, S., Saha, L., Guillemot, L., Cognard, I. & Rudak, B. (2016). A model for distortions of polarisation-angle curves in radio pulsars. *Astronomy and Astrophysics*, *593*, A83. doi: 10.1051/0004-6361/201628516

Dyks, J., Weltevrede, P. & Ilie, C. (2021). Circular polarization in radio pulsar PSR B1451-68: coherent mode transitions and intrabeam interference. *Monthly*

Notices of the Royal Astronomical Society, *501*(2), 2156-2173. doi: 10.1093/mnras/staa3762

Eatough, R. P., Keane, E. F. & Lyne, A. G. (2009). An interference removal technique for radio pulsar searches. *Monthly Notices of the Royal Astronomical Society*, *395*(1), 410-415. doi: 10.1111/j.1365-2966.2009.14524.x

Edwards. (2004). The polarization of drifting subpulses. *Astronomy and Astrophysics*, *426*, 677-686. doi: 10.1051/0004-6361:20041029

Edwards. (2012). Fifty years in fifteen minutes: The impact of the parkes observatory. *arXiv e-prints*, arXiv:1210.2138.

Edwards & Stappers. (2002). Drifting sub-pulse analysis using the two-dimensional fourier transform. *Astronomy and Astrophysics*, *393*, 733-748. doi: 10.1051/0004-6361:20021067

Edwards & Stappers. (2004). Ellipticity and deviations from orthogonality in the polarization modes of PSR B0329+54. *Astronomy and Astrophysics*, *421*, 681-691.

Edwards, R. T., Stappers, B. W. & van Leeuwen, A. G. J. (2003). Unusual subpulse modulation in PSR B0320+39. *Astronomy and Astrophysics*, *402*, 321-329.

Ekers, R. D. & Moffet, A. T. (1969, October). Polarization of Pulsating Radio Sources. *The Astrophysical Journal*, *158*, L1. doi: 10.1086/180419

Ergma, E. & van den Heuvel, E. P. J. (1998). On the initial progenitor masses of stellar mass black holes and neutron stars. *Astronomy and Astrophysics*, *331*, L29-L32.

Everett, J. E. & Weisberg, J. M. (2001). Emission beam geometry of selected pulsars derived from average pulse polarization data. *Astrophysical Journal*, *553*, 341–357.

Fridman, P. A. & Baan, W. A. (2001). Rfi mitigation methods in radio astronomy. *Astronomy and Astrophysics*, *378*, 327-344. doi: 10.1051/0004-6361:20011166

Fussell, D. & Luo, Q. (2004). The effect of differential refraction on wave propagation in rotating pulsar magnetospheres. *Monthly Notices of the Royal Astronomical Society*, *349*(3), 1019-1026. doi: 10.1111/j.1365-2966.2004.07581.x

Gedalin, M. E. & Machabeli, G. Z. (1982). The role of turbulence of the relativistic electron-positron plasma in generating in the prepulses of the crab radio pulsar. *Soviet Astronomy Letters*, *8*, 153-157.

Geppert, U., Rheinhardt, M. & Gil, J. (2003). Spot-like structures of neutron star surface magnetic fields. *Astronomy and Astrophysics*, *412*, L33-L36. doi: 10.1051/0004-6361:20034605

Geyer, M., Karastergiou, A., Kondratiev, V. I., Zagkouris, K., Kramer, M., Stappers, B. W., … Sobey, C. (2017). Scattering analysis of lofar pulsar observations. *Monthly Notices of the Royal Astronomical Society*, *470*(3), 2659-2679. doi: 10.1093/mnras/stx1151

Ginzburg, V. L., Zheleznyakov, V. V. & Zaitsev, V. V. (1969). Coherent mechanisms of radio emission and magnetic models of pulsars. *Astrophysics and Space Science*, *4*, 464-504. doi: 10.1007/BF00651351

Goldsmith, P. F., Baker, L. A., Davis, M. M. & Giovanelli, R. (1995). Multi-feed systems for the arecibo gregorian. In D. T. Emerson & J. M. Payne (Eds.), *Multi-feed systems for radio telescopes* (Vol. 75, p. 90-98).

Green, D. A. (2017). Vizier online data catalog: A catalogue of galactic supernova remnants (green 2017). *VizieR Online Data Catalog*, *7278*.

Gullón, M., Miralles, J. A., Viganò, D. & Pons, J. A. (2014). Population synthesis of isolated neutron stars with magneto-rotational evolution. *Monthly Notices of the Royal Astronomical Society*, *443*(3), 1891-1899. doi: 10.1093/mnras/stu1253

Hankins, T. H. (1973). Notches in the average pulse profile of the pulsar psr 191+21. *Astrophysical Journal*, *181*, L49. doi: 10.1086/181182

Hankins, T. H., Kern, J. S., Weatherall, J. C. & Eilek, J. A. (2003). Nanosecond radio bursts from strong plasma turbulence in the Crab pulsar. *Nature*, *422*.

Hankins, T. H. & Rankin, J. M. (2010). Arecibo Multi-Frequency Time-Aligned Pulsar Average-Profile and Polarization Database. *Astronomical Journal*, *139*, 168-175. doi: 10.1088/0004-6256/139/1/168

Hankins, T. H. & Wolszczan, A. (1987). The drifting subpulse phenomenon observed in three pulsars with triple profiles. *Astrophysical Journal*, *318*, 410. doi: 10.1086/165377

Helfand, D. J., Manchester, R. N. & Taylor, J. H. (1975). Observations of pulsar radio emission. III. Stability of integrated profiles. *Astrophysical Journal*, *198*, 661-670.

Herfindal, J. L. & Rankin, J. M. (2007). Periodic nulls in the pulsar b1133+16. *Monthly Notices of the Royal Astronomical Society*, *380*, 430-436. doi: 10.1111/j.1365-2966.2007.12089.x

Hewish, A., Bell, S. J., Pilkington, J. D. H., Scott, P. F. & Collins, R. A. (1968). Observation of a rapidly pulsating radio source. *Nature*, *217*, 709-713.

Hobbs, G., Manchester, R. N., Dunning, A., Jameson, A., Roberts, P., George, D., … Whiting, M. (2020). An ultra-wide bandwidth (704 to 4 032 mhz) receiver for the parkes radio telescope. *Publications of the Astronomical Society of Australia*, *37*, e012. doi: 10.1017/pasa.2020.2

Hotan, A. W., van Straten, W. & Manchester, R. N. (2004). PSRCHIVE and PSRFITS: An Open Approach to Radio Pulsar Data Storage and Analysis. *Publications of the Astronomical Society of Australia*, *21*, 302-309.

Huguenin, G. R., Taylor, J. H. & Troland, T. H. (1970). The radio emission from pulsar mp 0031-07. *The Astrophysical Journal*, *162*, 727. doi: 10.1086/150704

Hulse, R. A. & Taylor, J. H. (1975). Discovery of a pulsar in a binary system. *Astrophysical Journal*, *195*, L51-L53. doi: 10.1086/181708

Ibrahim, A. I., Safi-Harb, S., Swank, J. H., Parke, W., Zane, S. & Turolla, R. (2002). Discovery of Cyclotron Resonance Features in the Soft Gamma Repeater SGR 1806-20. *Astrophysical Journal*, *574*, L51-L55.

Ilie, C. D., Weltevrede, P., Johnston, S. & Chen, T. (2020). The drifting sub-pulses of psr b0031-07 and its synchronously modulated radio polarization. *Monthly Notices of the Royal Astronomical Society*, *491*(3), 3385-3394. doi: 10.1093/mnras/stz3167

Jackson, J. D. (1962). *Classical electrodynamics*. Wiley.

Jankowski, F., van Straten, W., Keane, E. F., Bailes, M., Barr, E. D., Johnston, S. &

Kerr, M. (2018). Spectral properties of 441 radio pulsars. *Monthly Notices of the Royal Astronomical Society*, *473*, 4436-4458. doi: 10.1093/mnras/stx2476

Jones, P. B. (2016). Circular polarization shows the nature of pulsar magnetosphere composition. *Monthly Notices of the Royal Astronomical Society*, *455*(4), 3814-3819. doi: 10.1093/mnras/stv2654

Jones, R. C. (1941). New calculus for the treatment of optical systems. i. description and discussion of the calculus. *Journal of the Optical Society of America (1917-1983)*, *31*(7), 488.

Kaspi, V. M. & Wolszczan, A. (1993). A preliminary analysis of pulse profile stability in PSR 1257+12. In J. A. Phillips, S. E. Thorsett & S. R. Kulkarni (Eds.), *Planets around pulsars* (Vol. 36, p. 81-85). Astronomical Society of the Pacific Conference Series.

Kennett, M. & Melrose, D. (1998). Propagation-induced circular polarisation in synchrotron sources. *Publications of the Astronomical Society of Australia*, *15*, 211-216.

Kijak, J., Gupta, Y. & Krzeszowski, K. (2007). Turn-over in pulsar spectra around 1 GHz. *Astronomy and Astrophysics*, *462*, 699-702. doi: 10.1051/0004-6361:20066125

Kijak, J. & Maron, O. (2004). High-frequency Turnover in Pulsar Spectra. In (p. 339).

Kliger, D. S., Lewis, J. W. & Randall, C. E. (1990). *Polarized light in optics and spectroscopy*.

Kloumann, I. M. & Rankin, J. M. (2010). On the long and short nulls, modes and interpulse emission of radio pulsar b1944+17. *Monthly Notices of the Royal Astronomical Society*, *408*(1), 40-52. doi: 10.1111/j.1365-2966.2010.17114.x

Knight, H. S., Bailes, M., Manchester, R. N., Ord, S. M. & Jacoby, B. A. (2006, April). Green Bank Telescope Studies of Giant Pulses from Millisecond Pulsars. *Astrophysical Journal*, *640*, 941-949.

Komesaroff, M. M. (1970). Possible mechanism for the pulsar radio emission. *Nature*, *225*, 612-614.

Kramer, M., Lyne, A. G., O'Brien, J. T., Jordan, C. A. & Lorimer, D. R. (2006). A periodically active pulsar giving insight into magnetospheric physics. *Science*, *312*, 549-551. doi: 10.1126/science.1124060

Kulkarni, S. R. (2020). Dispersion measure: Confusion, constants & clarity. *arXiv e-prints*, arXiv:2007.02886.

Lazarus, P., Karuppusamy, R., Graikou, E., Caballero, R. N., Champion, D. J., Lee, K. J., … Kramer, M. (2016). Prospects for high-precision pulsar timing with the new effelsberg psrix backend. *Monthly Notices of the Royal Astronomical Society*, *458*(1), 868-880. doi: 10.1093/mnras/stw189

Léna, P., Rouan, D., Lebrun, F., Mignard, F. & Pelat, D. (2012). *Observational astrophysics*. doi: 10.1007/978-3-642-21815-6

Lewandowski, W., Dembska, M., Kijak, J. & Kowalińska, M. (2013). Pulse broadening analysis for several new pulsars and anomalous scattering. *Monthly Notices of the Royal Astronomical Society*, *434*(1), 69-83. doi: 10.1093/mnras/stt989

Lewandowski, W., Kowalińska, M. & Kijak, J. (2015). The analysis of the largest sample of multifrequency pulsar scatter time estimates. *Monthly Notices of the*

Royal Astronomical Society, *449*(2), 1570-1583. doi: 10.1093/mnras/stv385

Liao, Y.-W., Chang, T.-C., Kuo, C.-Y., Masui, K. W., Oppermann, N., Pen, U.-L. & Peterson, J. B. (2016). Accurate polarization calibration at 800 mhz with the green bank telescope. *Astrophysical Journal*, *833*(2), 289. doi: 10.3847/1538-4357/833/2/289

Löhmer, O., Mitra, D., Gupta, Y., Kramer, M. & Ahuja, A. (2004). The frequency evolution of interstellar pulse broadening from radio pulsars. *Astronomy and Astrophysics*, *425*, 569-575.

Lominadze, J. G., Machabeli, G. Z. & Usov, V. V. (1983). Theory of NP 0532 pulsar radiation and the nature of the activity of the Crab Nebula. *Astrophysics and Space Science*, *90*, 19-43. doi: 10.1007/BF00651544

Lorimer, D. R., Bailes, M., McLaughlin, M. A., Narkevic, D. J. & Crawford, F. (2007). A bright millisecond radio burst of extragalactic origin. *Science*, *318*, 777. doi: 10.1126/science.1147532

Lorimer, D. R. & Kramer, M. (2012). *Handbook of pulsar astronomy*.

Lorimer, D. R., Yates, J. A., Lyne, A. G. & Gould, D. M. (1995). Multifrequency flux density measurements of 280 pulsars. *Monthly Notices of the Royal Astronomical Society*, *273*, 411-421.

Lyne, A. G. & Smith, F. G. (1968). Linear polarization in pulsating radio sources. *Nature*, *218*, 124-126.

Lyne, A. G., Smith, F. G. & Graham, D. A. (1971). Characteristics of the radio pulses from the pulsars. *Monthly Notices of the Royal Astronomical Society*, *153*, 337. doi: 10.1093/mnras/153.3.337

Lyubarskii, Y. E. & Petrova, S. A. (1998). Refraction of radio waves in pulsar magnetospheres. *Astronomy and Astrophysics*, *333*, 181–187.

Lyubarskii, Y. E. & Petrova, S. A. (1999). On the circular polarization of pulsar radiation. *Astrophysics and Space Science*, *262*, 379-389.

Lyutikov, M. (1999). Beam instabilities in a magnetized pair plasma. *Journal of Plasma Physics*, *62*, 65-86. doi: 10.1017/S0022377899007837

Maan, Y., van Leeuwen, J. & Vohl, D. (2021). Fourier domain excision of periodic radio frequency interference. *Astronomy & Astrophysics*, *650*, A80. doi: 10.1051/0004-6361/202040164

Manchester, R. N., Hobbs, G. B., Teoh, A. & Hobbs, M. (2005). The australia telescope national facility pulsar catalogue. *The Astronomical Journal*, *129*(4), 1993-2006. doi: 10.1086/428488

Manchester, R. N., Taylor, J. H. & Huguenin, G. R. (1975). Observations of pulsar radio emission II. Polarisation of individual radio pulses. *Astrophysical Journal*, *196*, 83-102.

Maron, O., Kijak, J., Kramer, M. & Wielebinski, R. (2000). Pulsar spectra of radio emission. *Astronomy and Astrophysics*, *147*, 195–203.

McKinnon, M. M. (2003a). Three-Dimensional Statistics of Radio Polarimetry. *Astrophysical Journal, Suppl. Ser*, *148*, 519-526.

McKinnon, M. M. (2003b). The Transition between Nonorthogonal Polarization Modes in PSR B2016+28 at 1404 MHz. *Astrophysical Journal*, *590*, 1026-1034.

McKinnon, M. M. (2004). On the Excess Dispersion in the Polarization Position Angle of Pulsar Radio Emission. *Astrophysical Journal*, *606*, 1154-1166.

McKinnon, M. M. (2006). Orientation angles of a pulsar's polarization vector. *Astrophysical Journal*, *645*, 551-555.

McKinnon, M. M. & Stinebring, D. R. (2000). The Mode-separated Pulse Profiles of Pulsar Radio Emission. *Astrophysical Journal*, *529*, 435–446.

McSweeney, S. J., Bhat, N. D. R., Tremblay, S. E., Deshpande, A. A. & Ord, S. M. (2017). Low-frequency observations of the subpulse drifter PSR J0034-0721 with the murchison widefield array. *Astrophysical Journal*, *836*(2), 224. doi: 10.3847/1538-4357/aa5c35

Melrose, D. B. & Gedalin, M. E. (1999). Relativistic plasma emission and pulsar radio emission: A critique. *The Astrophysical Journal*, *521*, 351-361. doi: 10.1086/307539

Melrose, D. B. & Rafat, M. Z. (2017). Pulsar radio emission mechanism: Why no consensus? *Journal of Physics: Conference Series*, *932*(1), 012011. Retrieved from `http://stacks.iop.org/1742-6596/932/i=1/a=012011`

Melrose, D. B., Rafat, M. Z. & Luo, Q. (2009). Linear acceleration emission. i. motion in a large-amplitude electrostatic wave. *The Astrophysical Journal*, *698*, 115-123. doi: 10.1088/0004-637X/698/1/115

Melrose, D. B., Rafat, M. Z. & Mastrano, A. (2021). Pulsar radio emission mechanisms: a critique. *Monthly Notices of the Royal Astronomical Society*, *500*(4), 4530-4548. doi: 10.1093/mnras/staa3324

Melrose, D. B. & Yuen, R. (2016). Pulsar electrodynamics: an unsolved problem. *Journal of Plasma Physics*, *82*(2), 635820202. doi: 10.1017/S0022377816000398

Mignani, R. P., Paladino, R., Rudak, B., Zajczyk, A., Corongiu, A., de Luca, A., … Marconi, G. (2017). The first detection of a pulsar with alma. *Astrophysical Journal*, *851*(1), L10. doi: 10.3847/2041-8213/aa9c3e

Mitra, D., Arjunwadkar, M. & Rankin, J. M. (2015). Polarized quasiperiodic structures in pulsar radio emission reflect temporal modulations of non-stationary plasma flow. *Astrophysical Journal*, *806*(2), 236. doi: 10.1088/0004-637X/806/2/236

Mitra, D. & Rankin, J. M. (2002). Toward An Empirical Theory of Pulsar Emission. VII. On the Spectral Behavior of Conal Beam Radii and Emission Heights. *Astrophysical Journal*, 322–336.

Morello, V., Barr, E. D., Cooper, S., Bailes, M., Bates, S., Bhat, N. D. R., … Tiburzi, C. (2019). The high time resolution universe survey - xiv. discovery of 23 pulsars through gpu-accelerated reprocessing. *Monthly Notices of the Royal Astronomical Society*, *483*(3), 3673-3685. (Introduces clfd) doi: 10.1093/mnras/sty3328

Morello, V., Rajwade, K. M. & Stappers, B. W. (2022). IQRM: real-time adaptive RFI masking for radio transient and pulsar searches. *Monthly Notices of the Royal Astronomical Society*, *510*(1), 1393-1403. doi: 10.1093/mnras/stab3493

Olszanski, T. E. E., Mitra, D. & Rankin, J. M. (2019). Arecibo 4.5/1.4/0.33-GHz polarimetric single-pulse emission survey. *Monthly Notices of the Royal Astronomical Society*, *489*(2), 1543-1555. doi: 10.1093/mnras/stz2172

Oppenheim, A. V., Schafer, R. W. & Buck, J. R. (1999). *Discrete-time signal processing* (Second ed.). Prentice-hall Englewood Cliffs.

Oppenheimer, J. R. & Volkoff, G. (1939). On massive neutron cores. *Physical Review*, *55*, 374-381.

Ord, S. M., van Straten, W., Hotan, A. W. & Bailes, M. (2004). Polarimetric profiles of 27 millisecond pulsars. *Monthly Notices of the Royal Astronomical Society*, *352*(3), 804-814. doi: 10.1111/j.1365-2966.2004.07963.x

Osłowski, S., van Straten, W., Bailes, M., Jameson, A. & Hobbs, G. (2014). Timing, polarimetry and physics of the bright, nearby millisecond pulsar psr j0437-4715 - a single-pulse perspective. *Monthly Notices of the Royal Astronomical Society*, *441*, 3148-3160. doi: 10.1093/mnras/stu804

Pearson, K. (1901). LIII. on lines and planes of closest fit to systems of points in space. *The London, Edinburgh, and Dublin Philosophical Magazine and Journal of Science*, *2*(11), 559-572. doi: 10.1080/14786440109462720

Pennucci, T. T., Possenti, A., Esposito, P., Rea, N., Haggard, D., Baganoff, F. K., … Minter, A. (2015). Simultaneous multi-band radio and x-ray observations of the galactic center magnetar sgr 1745-2900. *Astrophysical Journal*, *808*(1), 81. doi: 10.1088/0004-637X/808/1/81

Petroff, E., Keane, E. F., Barr, E. D., Reynolds, J. E., Sarkissian, J., Edwards, P. G., … Bhandari, S. (2015). Identifying the source of perytons at the parkes radio telescope. *Monthly Notices of the Royal Astronomical Society*, *451*, 3933-3940. doi: 10.1093/mnras/stv1242

Petrova, S. A. (2000). The effect of magnetospheric refraction on the morphology of pulsar profiles. *Astronomy and Astrophysics*, *360*, 592–602.

Petrova, S. A. (2002). Towards explanation of pulsar radio spectra. *Astronomy and Astrophysics*, *383*, 1067-1075. doi: 10.1051/0004-6361:20011829

Petrova, S. A. & Lyubarskii, Y. E. (2000). Propagation effects in pulsar magnetospheres. *Astronomy and Astrophysics*, *355*, 1168–1180.

Pilkington, J. D. H., Hewish, A., Bell, S. J. & Cole, T. W. (1968). Observations of some further pulsed radio sources. *Nature*, *218*(5137), 126-129. doi: 10.1038/218126a0

Porayko, N. K., Noutsos, A., Tiburzi, C., Verbiest, J. P. W., Horneffer, A., Künsemöller, J., … Wucknitz, O. (2019). Testing the accuracy of the ionospheric faraday rotation corrections through LOFAR observations of bright northern pulsars. *Monthly Notices of the Royal Astronomical Society*, *483*(3), 4100-4113. doi: 10.1093/mnras/sty3324

Posselt, B., Karastergiou, A., Johnston, S., Parthasarathy, A., Keith, M. J., Oswald, L. S., … Venkatraman Krishnan, V. (2021). The thousand-pulsar-array programme on meerkat - vi. pulse widths of a large and diverse sample of radio pulsars. *Monthly Notices of the Royal Astronomical Society*, *508*(3), 4249-4268. doi: 10.1093/mnras/stab2775

Primak, N., Tiburzi, C., van Straten, W., Dyks, J. & Gulyaev, S. (2022). The polarisation of the drifting sub-pulses from PSR B1919+21. *Astronomy and Astrophysics*, *657*, A34. doi: 10.1051/0004-6361/202140811

Prószyński, M. & Wolszczan, A. (1986). A cross-correlation analysis of subpulse drift in PSR 0809+74, PSR 1237+25 and PSR 1919+21. *Astrophysical Journal*, *307*, 540-544.

Querol, J., Perez, A. & Camps, A. (2019). A review of rfi mitigation techniques in microwave radiometry. *Remote Sensing*, *11*(24). Retrieved from `https://www.mdpi.com/2072-4292/11/24/3042` doi: 10.3390/rs11243042

Radhakrishnan, V. & Cooke, D. J. (1969). Magnetic poles and the polarization structure of pulsar radiation. *Astrophysical Letters*, *3*, 225-229.

Ramachandran, R., Rankin, J. M., Stappers, B. W., Kouwenhoven, M. L. A. & van Leeuwen, A. G. J. (2002). Pulsar “drifting”-subpulse polarization: No evidence for systematic polarization-angle rotations. *Astronomy and Astrophysics*, *381*, 993-999.

Rankin, J. M. (1983). Toward an empirical theory of pulsar emission: II. On the spectral behavior of component width. *Astrophysical Journal*, *274*, 359-368.

Rankin, J. M. (1986). Toward an empirical theory of pulsar emission. III. Mode changing ,drifting subpulses and pulse nulling. *Astrophysical Journal*, *301*, 901–922.

Rankin, J. M. (1993). Toward an empirical theory of pulsar emission. vi - the geometry of the conal emission region. *The Astrophysical Journal*, *405*, 285-297. doi: 10.1086/172361

Rankin, J. M., Olszanski, T. E. E. & Wright, G. A. E. (2020). Arecibo investigations of pulsar B0823+26. i. plasma source changes configure its bright and quiet modes. *Astrophysical Journal*, *890*(2), 151. doi: 10.3847/1538-4357/ab67cb

Rankin, J. M. & Ramachandran, R. (2003). Toward an Empirical Theory of Pulsar Emission. VIII. Subbeam Circulation and the Polarization-Modal Structure of Conal Beams. *Astrophysical Journal*, *590*, 411-423.

Rankin, J. M., Ramachandran, R., van Leeuwen, J. & Suleymanova, S. A. (2006). Phenomenology of pulsar B0809+74’s rotating subbeam system. ii. “Carousel” configuration and polarization. *Astronomy and Astrophysics*, *455*, 215-221. doi: 10.1051/0004-6361:20054417

Rankin, J. M., Stinebring, D. R. & Weisberg, J. M. (1989). Arecibo 21 centimeter polarimetry of 64 pulsars: A guide to classification. *Astrophysical Journal*, *346*, 869-897.

Redman, S. L., Wright, G. A. E. & Rankin, J. M. (2005). Pulsar PSR B2303+30: a single system of drifting subpulses, moding and nulling. *Monthly Notices of the Royal Astronomical Society*, *357*, 859-872.

Reville, B. & Kirk, J. G. (2010). Linear acceleration emission in pulsar magnetospheres. *The Astrophysical Journal*, *715*, 186-193. doi: 10.1088/0004-637X/715/1/186

Rickett, B. J. (1975). Amplitude-modulated noise: an empirical model for the radio radiation received from pulsars. *Astrophysical Journal*, *197*, 185-191. doi: 10.1086/153501

Rickett, B. J. (1977). Interstellar scattering and scintillation of radio waves. *Annual review of astronomy and astrophysics*, *15*, 479-504.

Ridley, J. P. & Lorimer, D. R. (2010). Isolated pulsar spin evolution on the diagram.

Monthly Notices of the Royal Astronomical Society, *404*(2), 1081-1088. doi: 10.1111/j.1365-2966.2010.16342.x

Ritchings, R. T. (1976). Pulsar single pulse intensity measurements and pulse nulling. *Monthly Notices of the Royal Astronomical Society*, *176*, 249-263. doi: 10.1093/mnras/176.2.249

Romani, R. & Johnston, S. (2001). Giant pulses from the millisecond pulsar b1821-24. *Astrophysical Journal*, *557*, L93.

Rowe, E. T. (1995). A self-consistent treatment of linear acceleration emission. *Astronomy and Astrophysics*, *296*, 275.

Ruderman, M. A. & Sutherland, P. G. (1975). Theory of pulsars - Polar caps, sparks, and coherent microwave radiation. *The Astrophysical Journal*, *196*, 51–72. doi: 10.1086/153393

Saint-Hilaire, P., Benz, A. O. & Monstein, C. (2014). Short-duration radio bursts with apparent extragalactic dispersion. *The Astrophysical Journal*, *795*, 19. doi: 10.1088/0004-637X/795/1/19

Sanderson, C. & Curtin, R. (2017). An open source C++ implementation of multi-threaded gaussian mixture models, k-means and expectation maximisation. In *2017 11th international conference on signal processing and communication systems (icspcs)* (p. 1-8). doi: 10.1109/ICSPCS.2017.8270510

Scheuer, P. A. G. (1968). Amplitude variations of pulsed radio sources. *Nature*, *218*, 920-922.

Schopper, R., Ruhl, H., Kunzl, T. A. & Lesch, H. (2002). The free electron maser in pulsar magnetospheres. In W. Becker, H. Lesch & J. Trümper (Eds.), *Neutron stars, pulsars, and supernova remnants* (p. 193).

Shaifullah, G., Tiburzi, C., Osłowski, S., Verbiest, J. P. W., Szary, A., Künsemöller, J., … Vocks, C. (2018). Multifrequency behaviour of the anomalous events of PSR J0922+0638. *Monthly Notices of the Royal Astronomical Society*, *477*(1), L25-L29. doi: 10.1093/mnrasl/sly049

Shapiro, S. L. & Teukolsky, S. A. (1983). *Black holes, white dwarfs and neutron stars. The physics of compact objects.* New York: Wiley–Interscience.

Sieber, W. (1973). Pulsar spectra – a summary. *Astronomy and Astrophysics*, *28*, 237-252.

Sitch, R. (2000). *The dish.* New York: The Dish Film Productions.

Smits, J. M., Mitra, D., Stappers, B. W., Kuijpers, J., Weltevrede, P., Jessner, A. & Gupta, Y. (2007). The geometry of PSR B0031−07. *Astronomy and Astrophysics*, *465*, 575-586.

Stiltz, H. (1961). *Aerospace telemetry* (No. v. 1). Prentice-Hall. Retrieved from `https://books.google.co.nz/books?id=8o1CnQEACAAJ`

Stinebring, D. R., Cordes, J. M., Rankin, J. M., Weisberg, J. M. & Boriakoff, V. (1984). Pulsar polarization fluctuations. I. 1408 MHz statistical summaries. *Astrophysical Journal, Suppl. Ser*, *55*, 247-277.

Stokes, G. G. (1851). On the composition and resolution of streams of polarized light from different sources. *Transactions of the Cambridge Philosophical Society*, *9*, 399.

Suresh, A. & Cordes, J. M. (2019). Induced polarization from birefringent pulse splitting in magneto-ionic media. *Astrophysical Journal*, *870*(1), 29. doi: 10.3847/1538-4357/aaf004

Sutton, J. M., Staelin, D. H., R.M., P. & Weimer, R. (1970). Three pulsars with marching subpulses. *Astrophysical Journal*, *159*, L89-L94.

Taylor, J. H., Huguenin, G. R., Hirsch, R. M. & Manchester, R. N. (1971). Polarisation of the drifting subpulses of pulsar 0809+74. *Astrophysical Letters*, *9*, 205-208.

Taylor, J. H., Manchester, R. N. & Huguenin, G. R. (1975). Observations of pulsar radio emission. I. Total–intensity measurements of individual pulses. *Astrophysical Journal*, *195*, 513.

Timokhin, A. N. (2010). A model for nulling and mode changing in pulsars. *Monthly Notices of the Royal Astronomical Society*, *408*, L41-L45. doi: 10.1111/j.1745-3933.2010.00924.x

Trümper, J., Pietsch, W., Reppin, C., Voges, W., Staubert, R. & Kendziorra, E. (1978). Evidence for strong cyclotron line emission in the hard X-ray spectrum of Hercules X-1. *Astrophysical Journal*, *219*, L105-L110.

Usov, V. V. & Melrose, D. B. (1995). Pulsars with strong magnetic fields: polar caps, bound pair creation and nonthermal luminosities. *Australian J. Phys*, *48*, 571-612.

van Straten, W. (2004). Radio astronomical polarimetry and point-source calibration. *The Astrophysical Journal Supplement*, *152*(1), 129-135. doi: 10.1086/383187

van Straten, W. (2009). The statistics of radio astronomical polarimetry: Bright sources and high time resolution. *The Astrophysical Journal*, *694*, 1413-1422. doi: 10.1088/0004-637X/694/2/1413

van Straten, W. (2013). High-fidelity radio astronomical polarimetry using a millisecond pulsar as a polarized reference source. *The Astrophysical Journal Supplement*, *204*(1), 13. doi: 10.1088/0067-0049/204/1/13

van Straten, W. (2022). Introduction to radio astronomical polarimetry. *arXiv e-prints*, arXiv:2202.07818.

van Straten, W. & Bailes, M. (2011). Dspsr: Digital signal processing software for pulsar astronomy. *Publications of the Astronomical Society of Australia*, *28*(1), 1-14. doi: 10.1071/AS10021

van Straten, W., Demorest, P. & Oslowski, S. (2012). Pulsar data analysis with psrchive. *Astronomical Research and Technology*, *9*(3), 237-256.

van Straten, W. & Tiburzi, C. (2017). The statistics of radio astronomical polarimetry: Disjoint, superposed, and composite samples. *The Astrophysical Journal*, *835*, 293. doi: 10.3847/1538-4357/835/2/293

van Straten, W., Demorest, P. & Osłowski, S. (2012). Pulsar data analysis with PSRCHIVE. *Astronomical Research and Technology*, *9*(3), 237–256.

Vietri, M. & Stella, L. (1998). A gamma-ray burst model with small baryon contamination. *Astrophysical Journal*, *507*, L45-L48.

Vivekanand, M. & Joshi, V. (1997). The drifting behavior of PSR B0031−07. *Astrophysical Journal*, *477*, 431.

Wang, N., Manchester, R. N. & Johnston, S. (2007). Pulsar nulling and mode changing.

Monthly Notices of the Royal Astronomical Society, *377*, 1383–1392. doi: 10.1111/j.1365-2966.2007.11703.x

Weisberg, J. M., Cordes, J. M., Lundgren, S. C., Dawson, B. R., Despotes, J. T., Morgan, J. J., … Backer, D. C. (1999). Arecibo 1418 MHZ polarimetry of 98 pulsars: Full stokes profiles and morphological classifications. *Astrophysical Journal, Suppl. Ser*, *121*, 171-217.

Weltevrede, P. (2016). Investigation of the bi-drifting subpulses of radio pulsar B1839-04 utilising the open-source data-analysis project PSRSALSA. *Astronomy and Astrophysics*, *590*, A109. doi: 10.1051/0004-6361/201527950

Weltevrede, P., Edwards, R. T. & Stappers, B. W. (2006). The subpulse modulation properties of pulsars at 21 cm. *Astronomy and Astrophysics*, *445*, 243-272.

Weltevrede, P. & Johnston, S. (2008). Profile and polarization characteristics of energetic pulsars. *Monthly Notices of the Royal Astronomical Society*, *391*, 1210-1226. doi: 10.1111/j.1365-2966.2008.13950.x

Weltevrede, P., Stappers, B. W. & Edwards, R. T. (2007). The subpulse modulation properties of pulsars at 92 cm and the frequency dependence of subpulse modulation. *Astronomy and Astrophysics*, *469*, 607-631. doi: 10.1051/0004-6361:20066855

Wheaton, W. A., Doty, J. P., Primini, F. A., Cooke, B. A., Dobson, C. A., Goldman, A., … Scheepmaker, A. (1979). An absorption feature in the spectrum of the pulsed hard X-ray flux from 4U0115 + 63. *Nature*, *282*, 240-243.

Williamson, I. P. (1972). Pulse broadening due to multiple scattering in the interstellarmedium. *Monthly Notices of the Royal Astronomical Society*, *157*, 55+.

Wilson, T. L., Rohlfs, K. & Hüttemeister, S. (2009). *Tools of radio astronomy*. doi: 10.1007/978-3-540-85122-6

Wolszczan, A. (1978). PSR 1919+21: a temporal variability of the p_3 period. *Astronomy and Astrophysics*, *63*, 425-427.

Woolston, C. (2015). Microwave oven blamed for radio-telescope signals. *Nature*, *521*, 129. Retrieved from `https://doi.org/10.1038/521129f`

Woosley, S. E. (1987). The birth of neutron stars. In D. J. Helfand & J.-H. Huang (Eds.), *The origin and evolution of neutron stars, IAU symposium 125* (p. 255-272). Dordrecht: Reidel.

Woosley, S. E. & Weaver, T. A. (1986). Theoretical models for type i and type ii supernova. In J. Audouze & N. Mathieu (Eds.), *Nato asic proc. 163: Nucleosynthesis and its implications on nuclear and particle physics* (p. 145-166).

Woosley, S. E. & Weaver, T. A. (1992). In R. Pines D. Tamagaki & S. Tsuruta (Eds.), *The structure and evolution of neutron stars* (pp. 235–249). Redwood City, California: Addison-Wesley.

Wright, G. A. & Fowler, L. A. (1981). Mode-changing and quantized subpulse drift-rates in pulsar PSR 2319+60. *Astronomy and Astrophysics*, *101*, 356-361.

Yao, J. M., Manchester, R. N. & Wang, N. (2017). A new electron-density model for estimation of pulsar and frb distances. *Astrophysical Journal*, *835*(1), 29. doi: 10.3847/1538-4357/835/1/29

Zhang, B., Qiao, G. J., Lin, W. P. & Han, J. L. (1997). Three modes of pulsar inner gap. *The Astrophysical Journal*, *478*, 313-321. doi: 10.1086/303787

Appendix A

Additional Figures for Chapter 3

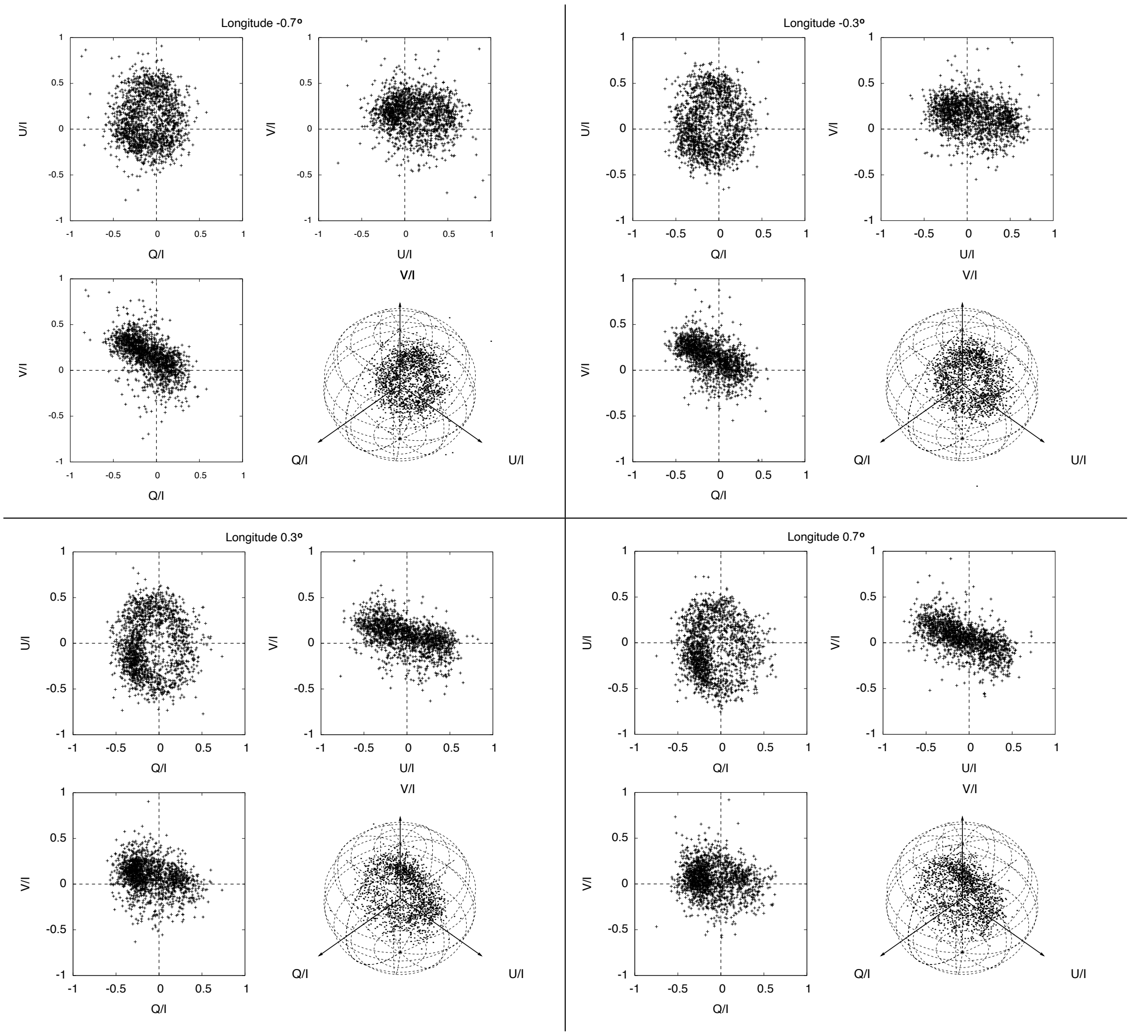

Figure A.1: Distributions of the normalised Stokes parameters in the Poincaré sphere at pulse longitudes of approximately $-0.7°$ (upper left), $-0.3°$ (upper right), $0.3°$ (lower left), and $0.7°$ (lower right). In each quadrant, the two upper panels and the lower-left panel show the projected, 2D distribution of the normalised Stokes parameters in the major planes of Poincaré space, and the 3D distribution is displayed in the lower-right panel.

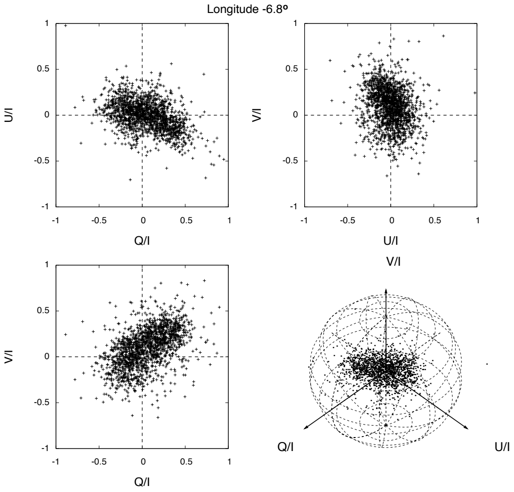

Figure A.2: Prolate spheroidal distribution of the normalised Stokes parameters in the Poincaré sphere at pulse longitude ~ −6.8°. The two upper panels and the lower-left panel show the projected, 2D distribution of the normalised Stokes parameters in the major planes of Poincaré space, and the 3D distribution is displayed in the lower-right panel.

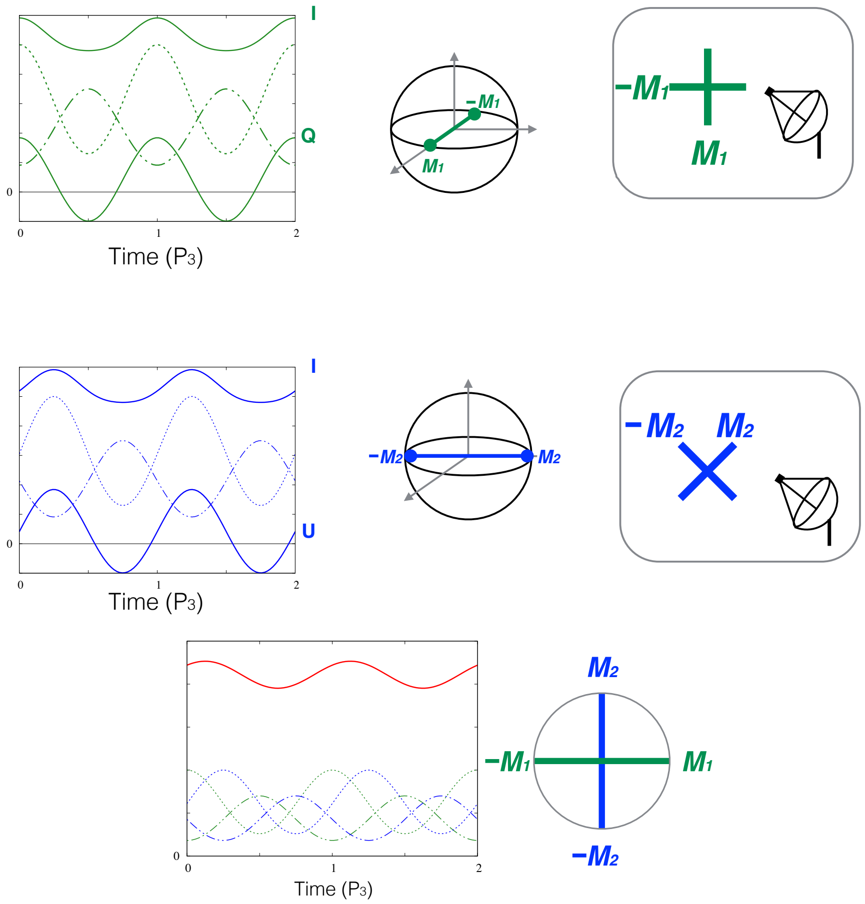

Figure A.3: Four-mode mixing model. *Top row*: signal from emission region $\mathcal{M}_1$; *middle row*: signal from emission region $\mathcal{M}_2$; and *bottom row*: incoherent superposition of $\mathcal{M}_1$ and $\mathcal{M}_2$. *Upper two rows*: from right to left, the right-most panels depict the OPM pairs as linearly polarised states in the $x - y$ plane orthogonal to the line of sight of the antenna; the middle panels depict the OPM pairs in the Poincaré sphere; and the left-most panels depict the modulated time series produced by the OPM pairs over two drift cycles, where the dashed lines represent the positive OPM state, the dash-dot lines represent the negative OPM state, the upper thick lines represent the total intensity, and the lower thick lines represent the superposed polarisation state. *Bottom row*: the right panel depicts the four modes in the equatorial plane of the Poincaré sphere and the left panel depicts the modulated time series produced by the incoherent superposition the OPM pairs over two drift cycles (colours and line types are the same as for the upper two rows, and the resultant total intensity is shown in red.

Appendix B

Additional information for Chapter 4

B.1 List of PRESS observed pulsars

Pulsars that were observed in the scope of the PRESS project (first column, their LST rise and set times (columns 2 and 3), target integration times derived by Equation 4.5 (column 4), sampling rates in μs (column 5), pulsar completion status (column 6), and remaining time to observe (column 7). Negative values in column 7 show extra time that pulsars were observed over the targeted time.

Pulsar name	Rise (LST)	Set (LST)	Target (min)	t_samp (us)	Done	To-do (min)
J0034-0721	20:40:00	04:28:17	120	64	TRUE	-120
J0134-2937	20:49:53	06:18:43	67	16	TRUE	7
J0151-0635	21:59:22	05:43:23	691	64	FALSE	239
J0152-1637	21:35:02	06:09:19	69	64	TRUE	-21
J0255-5304	21:28:22	08:23:30	31	64	TRUE	0
J0304+1932	01:04:35	05:04:30	95	64	TRUE	-38
J0401-7608	21:37:04	10:26:38	530	64	TRUE	-32
J0437-4715	23:20:17	09:54:13	5	4	TRUE	0
J0448-2749	00:07:48	09:29:34	31	64	TRUE	0
J0452-1759	00:32:21	09:12:46	37	64	TRUE	0
J0536-7543	23:13:27	11:59:34	150	64	TRUE	-122
J0601-0527	02:13:05	09:50:52	386	64	TRUE	-45
J0624-0424	02:38:26	10:10:13	510	64	TRUE	0
J0627+0649	03:19:52	09:35:54	640	64	TRUE	81
J0630-2834	01:48:27	11:13:11	85	64	TRUE	0
J0646+0905	03:47:52	09:45:09	62	64	TRUE	2
J0656-2228	02:26:32	11:26:27	84	64	TRUE	0
J0659+1414	04:25:58	09:33:38	184	64	TRUE	-26
J0729-1836	03:07:56	11:51:08	496	64	TRUE	0

J0738-4042	02:33:22	12:43:41	26	64	TRUE	0
J0742-2822	03:00:50	12:24:47	11	16	TRUE	0
J0745-5353	02:16:00	13:14:08	507	16	FALSE	507
J0749-68	01:50:21	13:51:19	62	64	TRUE	0
J0758-1528	03:44:01	12:12:56	47	64	TRUE	0
J0818-3232	03:28:24	13:08:27	148	64	TRUE	-28
J0820-1350	04:09:48	12:31:04	85	64	TRUE	0
J0823+0159	04:57:20	11:48:59	59	64	TRUE	-9
J0835-4510	03:22:06	13:48:34	6	16	TRUE	0
J0837-4135	03:30:36	13:44:06	51	64	TRUE	0
J0837+0610	05:26:28	11:47:43	87	64	TRUE	0
J0846-3533	03:50:23	13:41:48	76	64	TRUE	-6
J0856-6137	03:12:49	14:41:09	66	64	TRUE	0
J0902-6325	03:14:35	14:50:29	134	64	TRUE	0
J0907-5157	03:41:43	14:32:48	17	16	TRUE	0
J0908-1739	04:49:09	13:28:06	37	64	TRUE	0
J0908-4913	03:48:03	14:29:07	22	16	TRUE	0
J0909-7212	02:59:15	15:19:56	93	64	TRUE	0
J0922+0638	06:13:27	12:31:00	29	64	TRUE	0
J0924-5814	03:47:10	15:01:51	50	64	TRUE	0
J0934-5249	04:07:21	15:01:34	99	64	TRUE	0
J0942-5552	04:09:26	15:15:05	45	64	TRUE	0
J0942-5657	04:08:01	15:17:47	553	64	TRUE	0
J0952-3839	04:50:52	14:53:41	94	64	TRUE	0
J0953+0755	06:49:34	12:56:44	17	16	FALSE	17
J0959-4809	04:40:49	15:18:03	392	64	TRUE	-175

J1001-5507	04:30:15	15:33:00	98	64	TRUE	0
J1012-5857	04:34:02	15:51:34	87	64	TRUE	0
J1013-5934	04:33:32	15:53:30	176	64	TRUE	0
J1016-5345	04:47:41	15:45:21	210	64	TRUE	0
J1019-5749	04:43:20	15:56:24	83	16	FALSE	83
J1034-3224	05:44:33	15:24:06	79	64	TRUE	0
J1038-5831	05:00:25	16:16:14	45	64	TRUE	0
J1041-1942	06:17:35	15:05:36	201	64	TRUE	0
J1047-6709	04:50:57	16:43:59	223	16	FALSE	223
J1048-5832	05:10:17	16:26:08	8	16	TRUE	0
J1056-6258	05:09:25	16:43:25	29	64	TRUE	0
J1057-5226	05:31:34	16:24:23	50	16	FALSE	50
J1110-5637	05:35:46	16:44:14	38	64	TRUE	0
J1112-6103	05:29:15	16:55:13	427	4	FALSE	427
J1114-6100	05:31:29	16:57:15	60	64	TRUE	0
J1116-4122	06:10:20	16:23:05	64	64	TRUE	4
J1133-6250	05:47:08	17:20:34	509	64	TRUE	-30
J1136-5525	06:04:05	17:07:58	25	64	TRUE	0
J1136+1551	09:11:22	14:00:43	81	64	TRUE	0
J1141-3322	06:50:06	16:33:19	67	64	TRUE	7
J1146-6030	06:04:15	17:28:00	131	64	TRUE	0
J1157-6224	06:11:26	17:43:03	27	64	TRUE	0
J1202-5820	06:24:55	17:40:01	41	64	TRUE	0
J1224-6407	06:34:52	18:13:52	15	16	TRUE	0
J1243-6423	06:53:13	18:33:21	27	64	TRUE	0
J1253-5820	07:15:55	18:31:01	64	16	FALSE	64

J1306-6617	07:12:13	19:01:03	161	64	TRUE	0
J1307-6318	07:20:12	18:55:37	339	64	TRUE	0
J1312-6400	07:22:52	19:01:21	448	64	TRUE	0
J1320-3512	08:25:09	18:15:15	57	64	TRUE	0
J1326-5859	07:48:08	19:05:48	33	64	TRUE	-33
J1326-6700	07:29:54	19:22:11	37	64	TRUE	0
J1327-6222	07:41:33	19:13:00	36	64	TRUE	0
J1328-4357	08:17:03	18:39:09	36	64	TRUE	0
J1338-6204	07:53:04	19:23:14	85	64	TRUE	0
J1357-62	08:11:30	19:43:20	31	64	TRUE	0
J1359-6038	08:17:51	19:42:05	9	16	TRUE	0
J1401-6357	08:12:44	19:51:00	58	64	TRUE	0
J1410-7404	07:53:28	20:26:46	75	64	TRUE	0
J1413-6307	08:26:12	20:00:50	221	64	TRUE	0
J1428-5530	08:56:18	20:00:33	39	64	TRUE	0
J1430-6623	08:36:02	20:25:19	54	64	TRUE	0
J1453-6413	09:03:51	20:43:14	12	16	TRUE	0
J1456-6843	08:55:32	20:56:27	18	64	TRUE	0
J1512-5759	09:35:50	20:49:36	99	16	FALSE	99
J1522-5829	09:44:52	21:00:32	27	64	TRUE	0
J1534-5334	10:05:38	21:02:37	93	64	TRUE	0
J1535-4114	10:29:10	20:41:23	97	64	TRUE	0
J1539-5626	10:05:20	21:13:07	17	16	TRUE	0
J1543-0620	11:52:09	19:34:51	173	64	TRUE	0
J1544-5308	10:17:17	21:12:41	21	16	FALSE	21
J1550-5418	10:21:02	21:20:46	141	64	TRUE	0

J1555-3134	11:07:07	20:43:28	54	64	TRUE	0
J1559-4438	10:47:25	21:11:58	18	16	TRUE	0
J1600-5044	10:37:36	21:24:10	13	16	TRUE	0
J1602-5100	10:38:32	21:26:04	59	64	TRUE	0
J1603-2712	11:23:26	20:42:49	339	64	FALSE	339
J1604-4909	10:43:57	21:24:48	22	64	TRUE	0
J1605-5257	10:37:54	21:32:37	45	64	TRUE	0
J1611-5209	10:45:10	21:36:55	105	16	FALSE	105
J1622-4950	11:01:04	21:44:25	295	64	TRUE	0
J1630-4733	11:13:06	21:48:08	39	64	TRUE	0
J1632-4621	11:17:27	21:48:12	414	64	FALSE	414
J1633-4453	11:21:04	21:46:29	215	64	TRUE	0
J1633-5015	11:10:35	21:55:24	24	64	TRUE	0
J1640-4715	11:23:13	21:57:12	314	64	FALSE	314
J1644-4559	11:30:07	21:59:30	31	64	TRUE	0
J1645-0317	13:02:25	20:27:39	26	64	TRUE	0
J1646-6831	10:46:58	22:46:50	122	64	TRUE	0
J1651-4246	11:42:55	22:00:42	58	64	TRUE	0
J1651-5222	11:25:25	22:18:00	43	64	TRUE	0
J1652-2404	12:19:42	21:26:15	116	64	FALSE	56
J1653-3838	11:52:16	21:55:03	79	64	TRUE	0
J1653-4249	11:44:41	22:02:39	42	64	TRUE	-11
J1700-3312	12:09:34	21:52:11	192	64	FALSE	81
J1701-3726	12:02:07	22:00:29	168	64	TRUE	0
J1703-3241	12:13:03	21:53:42	83	64	TRUE	0
J1705-1906	12:42:53	21:28:18	20	64	TRUE	0

J1705-3423	12:12:10	21:59:14	42	16	FALSE	42
J1705-4108	11:59:23	22:11:17	87	64	TRUE	0
J1707-4053	12:01:51	22:12:52	40	64	TRUE	0
J1709-1640	12:52:11	21:26:41	45	64	TRUE	0
J1709-4401	11:58:32	22:20:50	164	64	TRUE	0
J1709-4429	11:57:43	22:21:42	7	16	TRUE	0
J1713+0747	14:09:41	20:17:57	197	4	FALSE	197
J1717-3425	12:23:46	22:10:54	88	64	TRUE	0
J1717-4054	12:12:05	22:23:39	61	64	TRUE	1
J1721-3532	12:25:52	22:17:13	19	64	TRUE	0
J1722-3207	12:32:48	22:11:17	33	64	FALSE	33
J1722-3712	12:24:14	22:21:43	92	16	FALSE	92
J1731-4744	12:13:50	22:49:33	57	64	TRUE	0
J1733-2228	13:03:29	22:03:23	184	64	FALSE	124
J1733-3716	12:34:33	22:32:20	227	64	FALSE	227
J1735-0724	13:40:48	21:29:21	297	64	FALSE	297
J1738-3211	12:49:31	22:28:16	52	64	TRUE	0
J1739-1313	13:30:51	21:49:04	89	64	TRUE	0
J1739-2903	12:56:16	22:22:51	22	64	TRUE	0
J1739-3131	12:51:19	22:27:29	36	64	TRUE	0
J1740-3015	12:54:54	22:26:13	41	64	TRUE	0
J1740+1000	14:45:46	20:35:05	50	16	FALSE	50
J1740+1311	15:00:47	20:19:26	162	64	TRUE	0
J1741-3927	12:38:25	22:44:11	35	64	TRUE	0
J1743-3150	12:54:55	22:32:17	165	64	TRUE	0
J1745-3040	12:59:29	22:32:23	25	64	TRUE	0

J1746-2850	13:03:12	22:29:00	389	64	FALSE	389
J1749-3002	13:03:59	22:34:27	438	64	FALSE	438
J1751-4657	12:35:15	23:08:08	51	64	TRUE	0
J1752-2806	13:11:31	22:34:25	38	64	TRUE	0
J1756-2435	13:22:36	22:31:19	337	64	FALSE	337
J1757-2421	13:23:35	22:31:23	20	16	TRUE	0
J1759-2205	13:30:14	22:28:33	350	64	FALSE	350
J1759-3107	13:12:03	22:46:40	467	64	FALSE	467
J1801-2920	13:17:55	22:45:38	216	64	FALSE	216
J1803-2137	13:35:42	22:32:00	37	16	FALSE	37
J1807-0847	14:09:40	22:05:35	11	16	TRUE	0
J1812-1733	13:53:00	22:31:31	37	64	FALSE	37
J1817-3618	13:20:01	23:14:10	132	64	TRUE	0
J1817-3837	13:15:37	23:18:22	38	64	TRUE	0
J1818-1422	14:06:30	22:30:16	407	64	FALSE	407
J1818-1519	14:04:07	22:32:22	155	64	FALSE	155
J1819+1305	15:40:02	20:59:50	262	64	FALSE	142
J1820-0427	14:34:51	22:06:53	41	64	TRUE	1
J1822-2256	13:52:02	22:53:55	128	64	FALSE	128
J1823-1115	14:19:24	22:27:56	81	64	TRUE	2
J1823-3106	13:36:28	23:11:05	19	64	TRUE	0
J1824-1945	13:59:51	22:48:09	13	16	TRUE	0
J1825-0935	14:25:28	22:25:32	52	64	TRUE	0
J1825-1446	14:12:12	22:37:53	97	64	TRUE	0
J1829-1751	14:09:48	22:49:37	21	64	TRUE	0
J1830-1059	14:27:10	22:34:24	28	64	TRUE	0

J1832-0644	14:40:17	22:25:07	58	64	TRUE	0
J1832-0827	14:35:33	22:29:40	44	64	TRUE	0
J1833-0338	14:50:02	22:17:21	263	64	FALSE	263
J1833-0827	14:36:35	22:30:44	229	16	FALSE	229
J1835-1020	14:34:01	22:37:54	90	64	TRUE	0
J1836-0436	14:50:24	22:23:18	286	64	FALSE	286
J1836-1008	14:35:27	22:38:20	40	64	TRUE	0
J1837-0653	14:44:24	22:30:04	130	64	FALSE	130
J1840-0809	14:44:18	22:36:48	65	64	TRUE	0
J1840-0815	14:43:42	22:36:45	229	64	FALSE	229
J1841-0425	14:55:10	22:27:00	192	16	FALSE	192
J1842-0359	14:57:45	22:27:07	194	64	FALSE	194
J1843-0000	15:11:00	22:15:55	60	64	TRUE	0
J1844-0538	14:54:42	22:33:28	201	16	FALSE	201
J1844+00	15:13:39	22:14:42	39	64	TRUE	1
J1845-0434	14:59:13	22:31:55	103	64	FALSE	103
J1846-7403	12:29:41	01:02:46	333	64	TRUE	0
J1847-0402	15:02:35	22:32:10	41	64	TRUE	0
J1848-0123	15:11:32	22:25:14	45	64	TRUE	0
J1849-0636	14:57:00	22:41:12	174	64	FALSE	174
J1851+1259	16:10:50	21:31:36	467	64	FALSE	467
J1852-0635	15:00:54	22:45:00	36	64	TRUE	0
J1852+0031	15:21:46	22:23:08	149	64	FALSE	149
J1853+0545	15:41:47	22:06:09	36	16	TRUE	0
J1859+00	15:29:14	22:30:17	456	64	FALSE	456
J1900-2600	14:23:32	23:38:02	42	64	TRUE	0

J1901-0906	15:03:07	23:00:39	122	64	FALSE	122
J1901+0331	15:41:02	22:22:01	198	64	TRUE	0
J1901+0435	15:44:56	22:18:08	47	64	TRUE	0
J1903+0135	15:36:20	22:30:39	50	64	TRUE	0
J1906+0641	15:57:59	22:15:11	50	64	TRUE	0
J1906+0746	16:02:35	22:11:02	201	16	FALSE	201
J1909+1102	16:19:52	21:59:44	136	64	FALSE	136
J1910+0358	15:51:17	22:29:00	159	64	FALSE	159
J1912+2104	17:25:13	21:00:13	152	64	TRUE	0
J1913-0440	15:27:15	23:00:33	56	64	TRUE	0
J1914+0219	15:49:44	22:39:02	405	64	FALSE	345
J1915+1009	16:21:33	22:09:26	270	64	FALSE	270
J1917+1353	16:42:00	21:53:19	13	16	TRUE	0
J1918+1444	16:47:23	21:49:24	81	64	TRUE	-3
J1919+0134	15:52:31	22:46:55	109	64	TRUE	1
J1921+2153	17:41:37	21:01:52	91	64	TRUE	0
J1929+1357	16:53:50	22:04:30	139	64	TRUE	0
J1932+1059	16:42:06	22:22:22	15	16	TRUE	0
J1935+1616	17:13:40	21:57:55	24	64	TRUE	0
J1939+2134	17:56:42	21:22:35	401	4	FALSE	283
J1941-2602	15:03:42	00:18:18	114	64	TRUE	-6
J1946+1805	17:36:26	21:57:19	30	64	TRUE	0
J2006-0807	16:10:06	00:02:26	416	64	TRUE	0
J2046-0421	17:00:16	00:31:43	106	64	TRUE	-2
J2046+1540	18:20:56	23:12:22	202	64	TRUE	0
J2048-1616	16:32:15	01:04:55	134	64	TRUE	0

J2053-7200	14:44:02	03:03:31	1220	64	TRUE	0
J2144-3933	16:41:07	02:47:16	581	64	TRUE	0
J2251-3711	17:52:59	03:50:28	828	64	FALSE	470
J2324-6054	17:41:47	05:07:07	160	64	TRUE	0
J2330-2005	19:05:35	03:55:18	360	64	TRUE	-64
J2346-0609	19:55:59	03:37:41	171	64	TRUE	-60

Table B.1

B.2 Verifying DM and RM

Measured and catalogue RM comparison. The first column is the pulsar name, the second column is the measured RM (values produced by rmfit), the third column is the estimated error of the measured RM, and the fourth column is the value of RM from the pulsar catalogue (Manchester et al., 2005).

Pulsar (PSR Jname)	Measured RM (rad/cm^2)	Error of measured RM	Catalogue RM (rad/cm^2)
J0738-4042	12.5097	0.00385	12.1
J1056-6258	6.99594	0.00615473	8.4
J1136+1551	2.95853	0.133172	3.97
J1136+1551	2.56307	0.229561	3.97
J1456-6843	-2.11528	0.00914489	-0.01
J1731-4744	-445.778	0.00831358	-443
J1921+2153	-14.8323	0.177943	-16.99
J1921+2153	-15.114	0.163165	-16.99
J1932+1059	-8.01836	-0.00624322	-6.87
J2048-1616	-10.7156	0.0113001	-10
J2048-1616	-10.4323	0.0284425	-10
J2048-1616	-10.1586	0.0137431	-10

Table B.2

Measured and catalogue DM comparison. The first column is the pulsar name, the second column is the measured DM (values produced by pdmp), the third column is the estimated error of the measured DM, and the fourth and fifth columns are the value of DM and its estimated uncertainty recorded in the pulsar catalogue

Pulsar (PSR Jname)	Measured DM (pc/cm^3)	Error of measured DM	Catalogue DM (pc/cm^3)	Error of catalogue DM
J0738-4042	161.1516	0.2647	160.896	0.003
J1056-6258	320.7951	0.2983	320.62	0.03
J1136+1551	4.864	0.8387	4.84066	0.00034
J1136+1551	4.864	0.839	4.84066	0.00034
J1456-6843	8.9705	0.186	8.613	0.004
J1731-4744	123.33	0.586	123.056	0.004
J1921+2153	12.444	0.9442	12.44399	0.00063
J1921+2153	12.7575	0.9442	12.44399	0.00063
J1932+1059	3.2894	0.1599	3.18321	0.00016
J2048-1616	11.456	1.385	11.456	0.005
J2048-1616	11.456	1.385	11.456	0.005
J2048-1616	11.456	1.385	11.456	0.005

Table B.3

B.3 Fraction of data lost to RFI for the first epoch of PSR J1921+2153

Amount of lost to RFI signal for individual sub-bands in regards with the integration length for both epochs of observations. First column is the epoch of observation, (column 2) is a central frequency of the sub-band, (column 2) is a number of lost profiles, and (column 4) is a fraction of lost data.

2020-04-01	Frequency (MHz)	Number of profiles lost	Fraction of profiles lost
	1024	105096	0.31
	1152	158679	0.46
	1280	178656	0.52
	1408	51994	0.15
	1536	114894	0.33
	1664	79607	0.23
	1792	126753	0.37
	1920	80708	0.23
	2048	46954	0.14
	2176	92209	0.27
	2304	162838	0.47
	768	288080	0.84
	896	216739	0.63
2020-04-13			
	1024	43008	0.24
	1152	90115	0.50
	1280	86693	0.48
	1408	40246	0.22

1536	81255	0.45
1664	39045	0.22
1792	84438	0.47
1920	44044	0.24
2048	24133	0.13
2176	70928	0.39
2304	104023	0.58
2432	179310	0.99
768	145588	0.81
896	114751	0.64

Table B.4

Appendix C

Additional Figures for Chapter 4

C.1 Images with PCA analysis for Arecibo P1260 pulsars

In this section all images of longitude-resolved mean and variability of the polarised emission from pulsars of the P1260 Arecibo program (Hankins & Rankin, 2010) are presented.

Each image have similar settings: panel a) shows both the ellipticity angle of the average Stokes parameters (points with error bars) and a histogram of the ellipticity angles of the individual pulses (greyscale intensity). Similarly, panel b) shows both the position angle of the average Stokes parameters and a histogram of the position angles of the individual pulses. Panel c) shows the integrated profile in total intensity (black, upper solid), linear (red, dashed) and circular polarisation (green, dot-dashed). These profiles were obtained by averaging together all the available data. In panel d), the black solid line shows the standard deviation of the total intensity, and the red dashed, green dot-dashed, and blue dotted lines display the square roots of the eigenvalues (from largest to smallest, respectively) of the 3×3 partition of the covariance matrix that describes the fluctuations of the polarisation vector $\boldsymbol{S} = (Q, U, V)$.

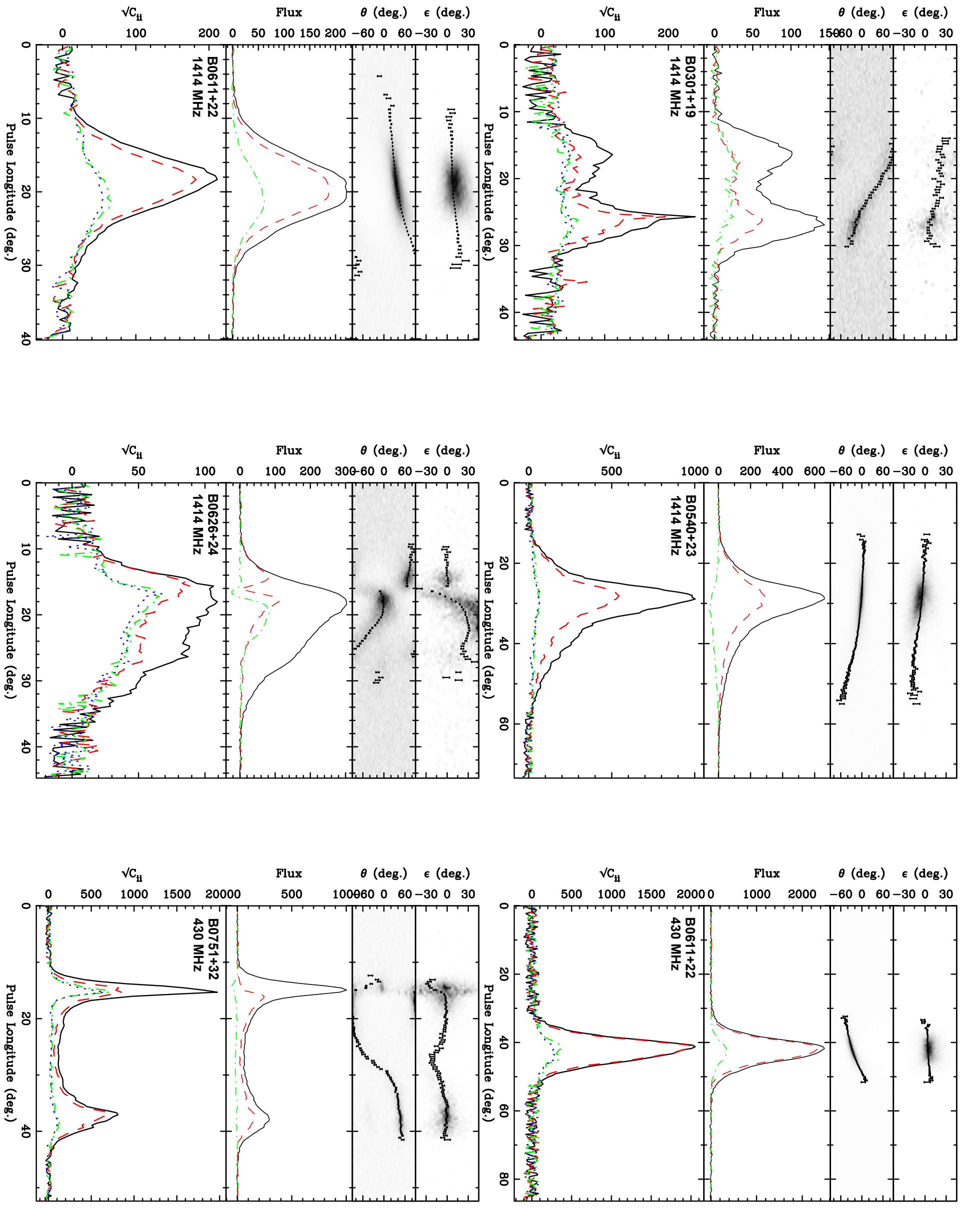

Figure C.1: Arecibo P1260 pulsars

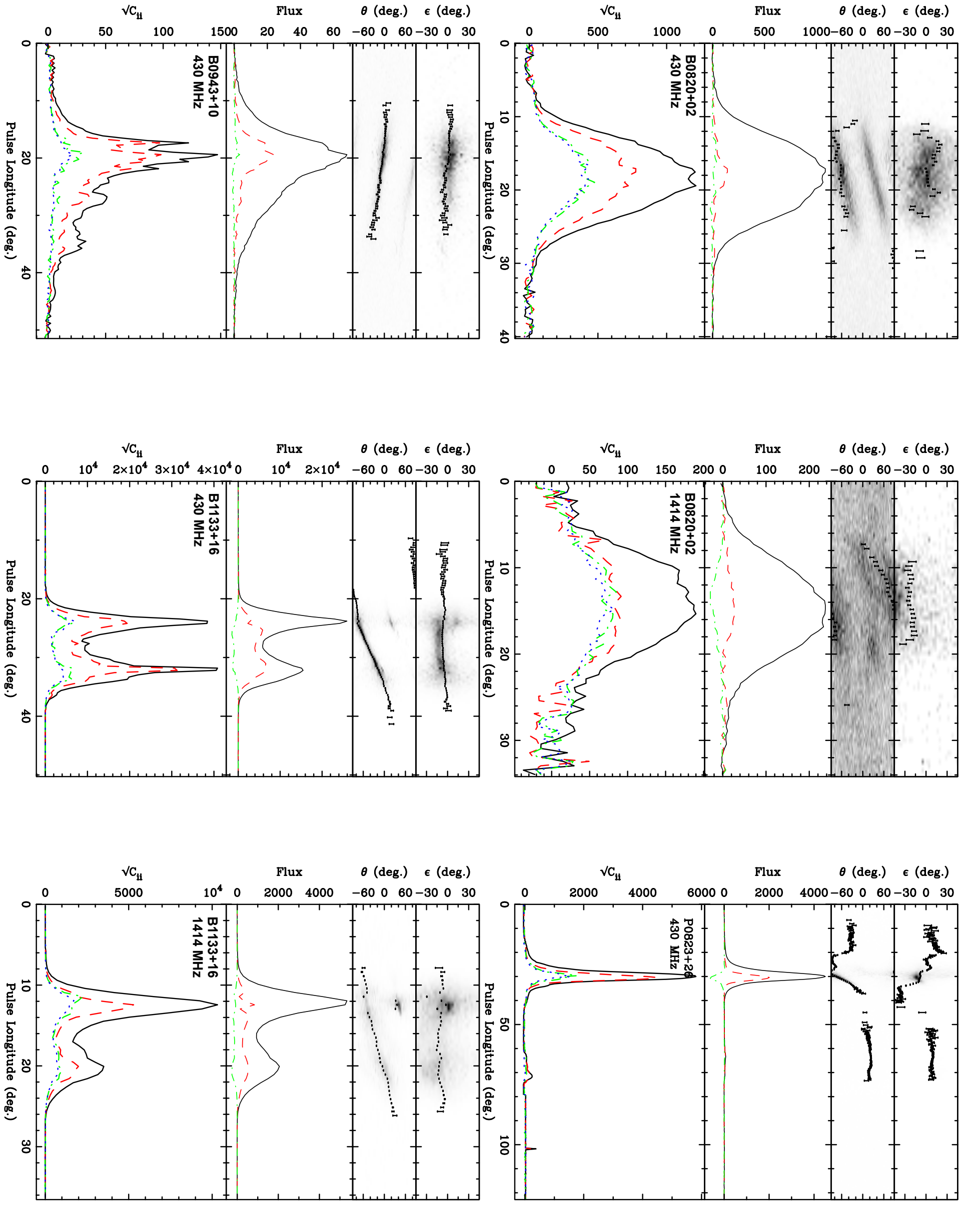

Figure C.2: Arecibo P1260 pulsars

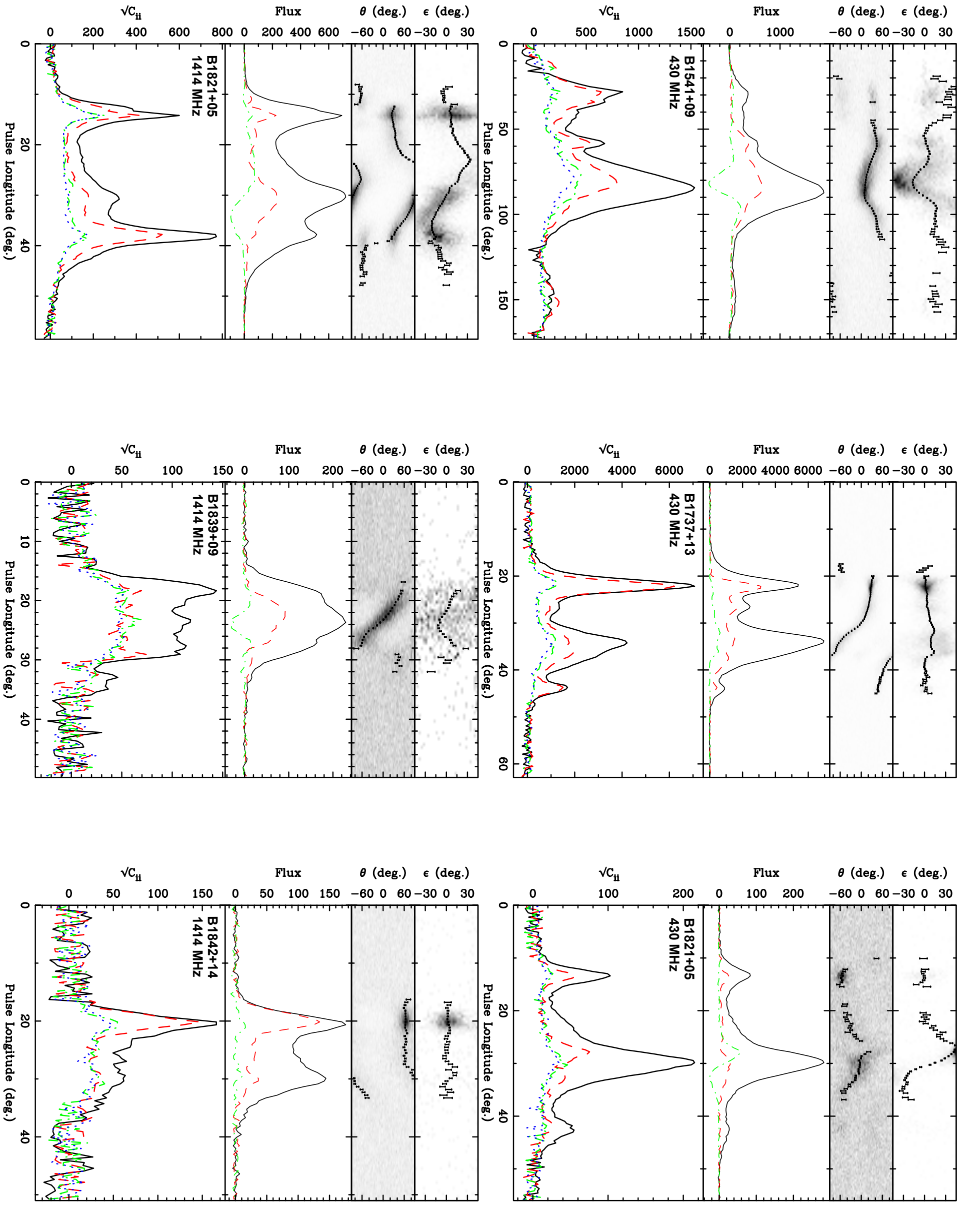

Figure C.3: Arecibo P1260 pulsars

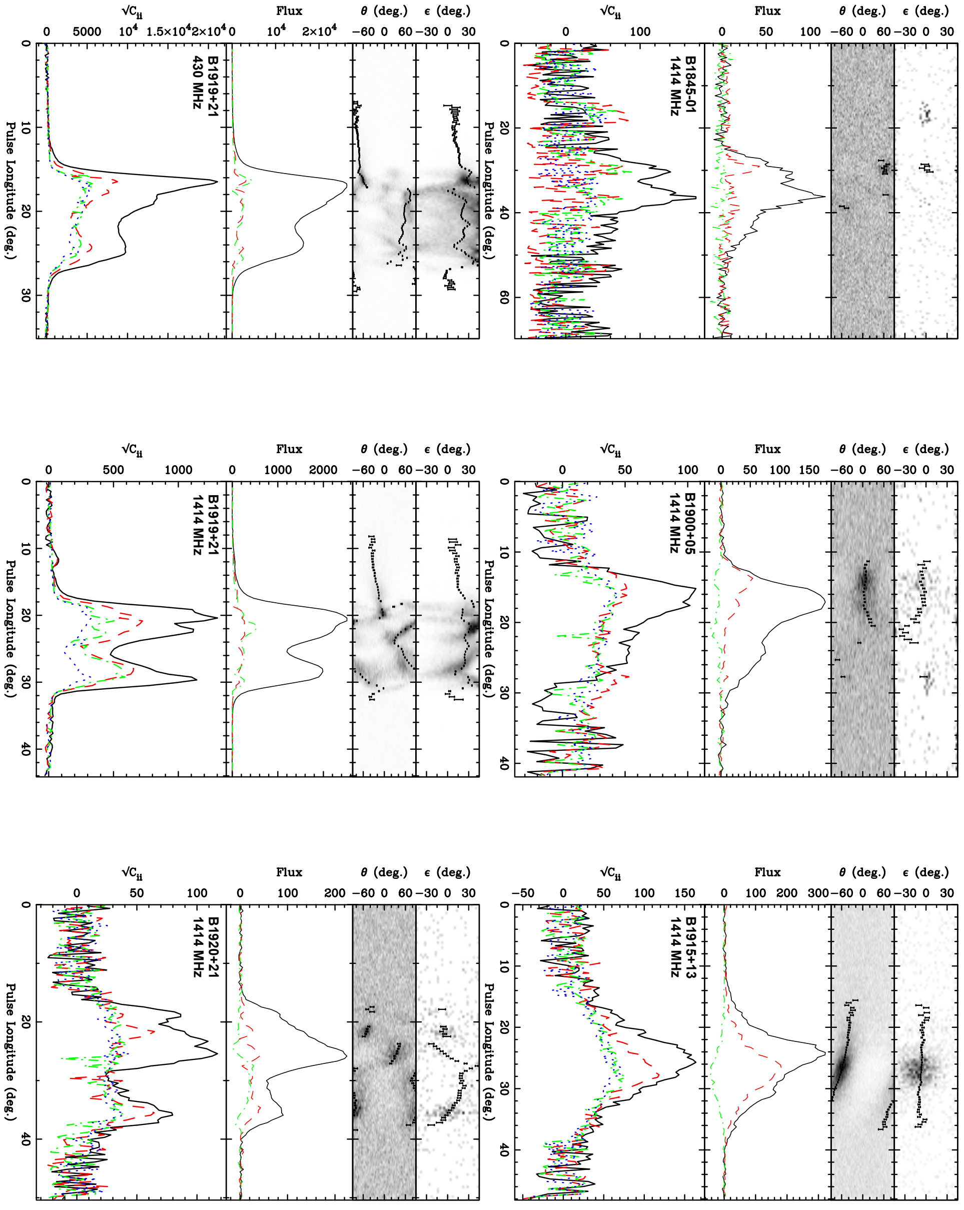

Figure C.4: Arecibo P1260 pulsars

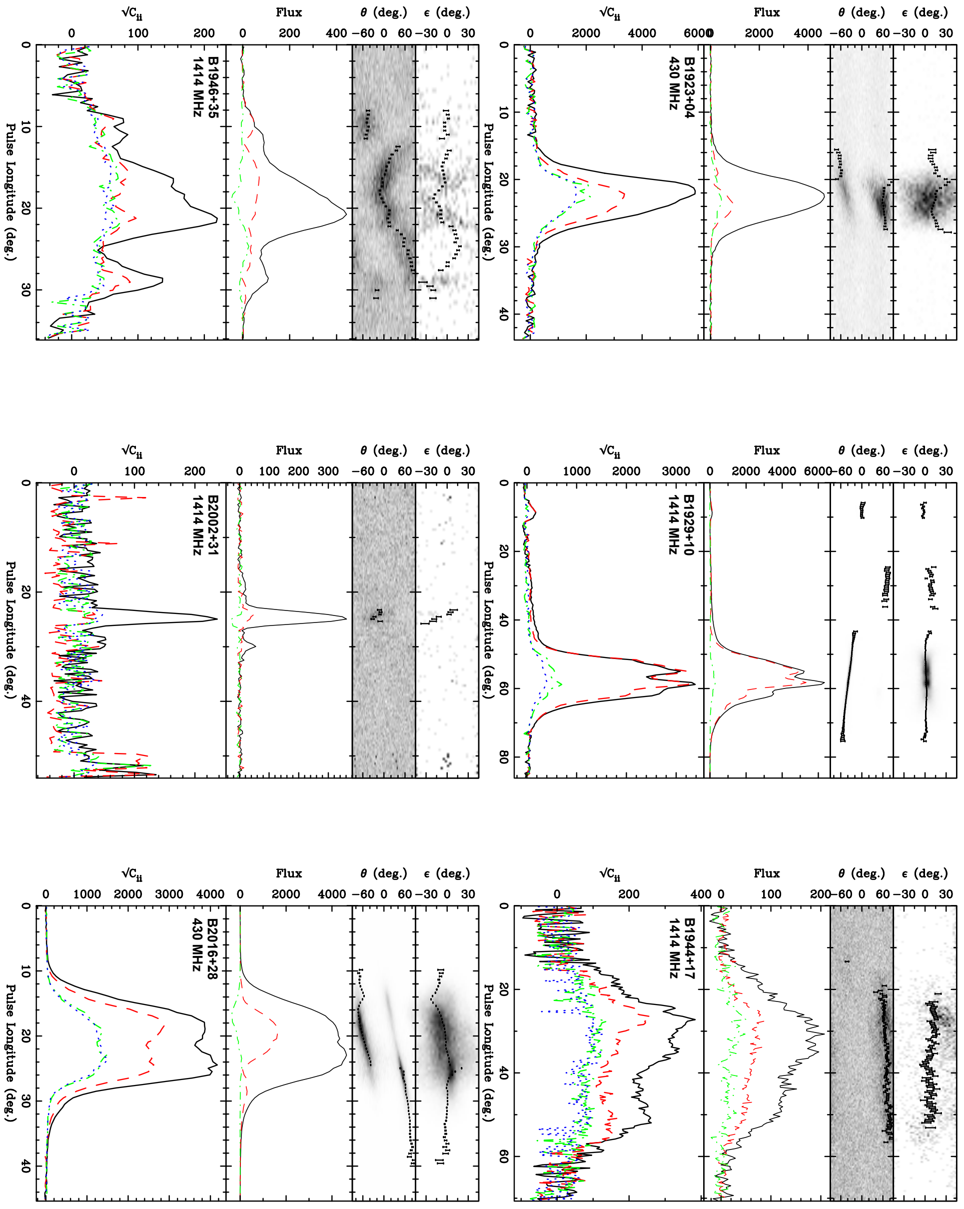

Figure C.5: Arecibo P1260 pulsars

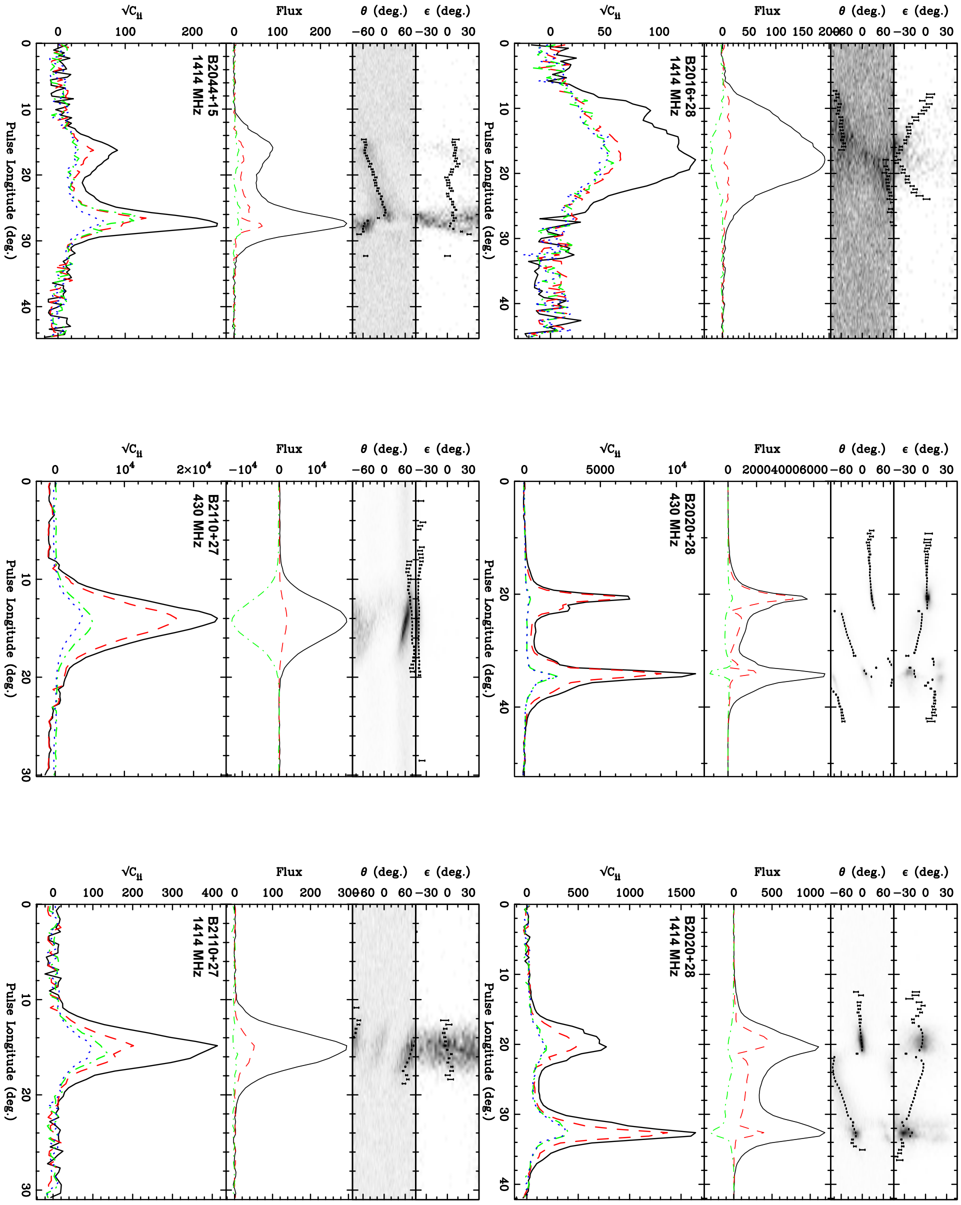

Figure C.6: Arecibo P1260 pulsars

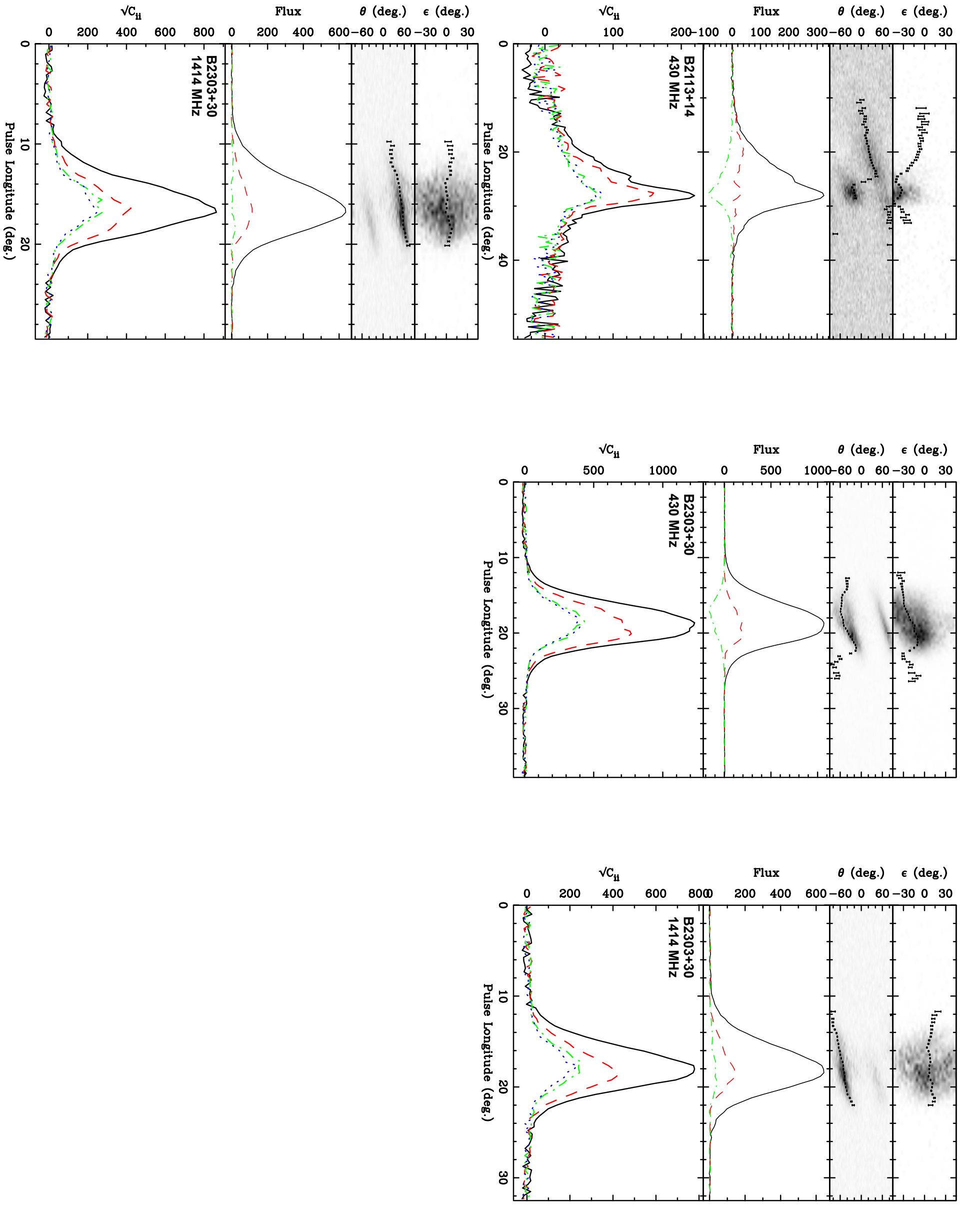

Figure C.7: Arecibo P1260 pulsars

C.2 Comparison of routines for RFI excision

Following images illustrate **folded** data before the RFI mitigation, and the quality of automated RFI-excision of two routines applied in *psrpl*: *PSRCHIVE tfzap* and MEERGUARD. For some data (e.g., PSR J1456-6843 at 768 MHz) *PSRCHIVE tfzap* zapped everything, while MEERGUARD cut only a handful of frequency channels, but also let a lot of RFI in.

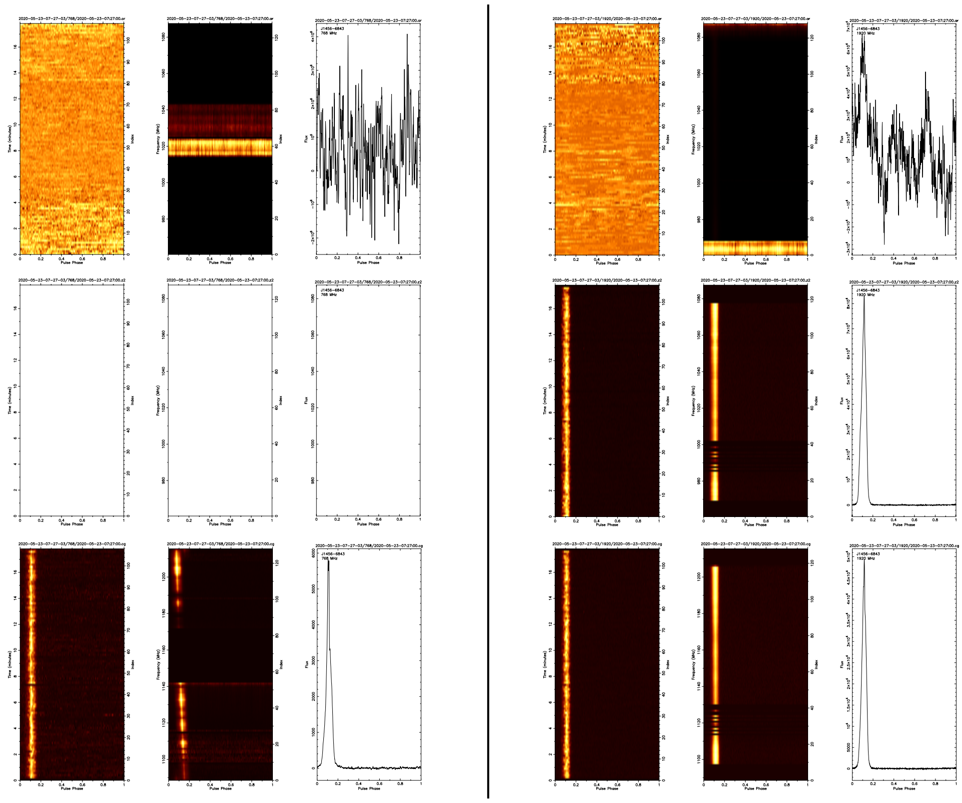

Figure C.8: Comparison between *tfzap* zapping and *MEERGUARD* RFI-mitigation routines for **folded** data of PSR J1456-6843 at 768 MHz (left column) and 1920 MHz (right column). For each column, top panel: folded data **before** RFI mitigation, middle panel: results of *tfzap* mitigation, and bottom panel: *MEERGUARD* excision.

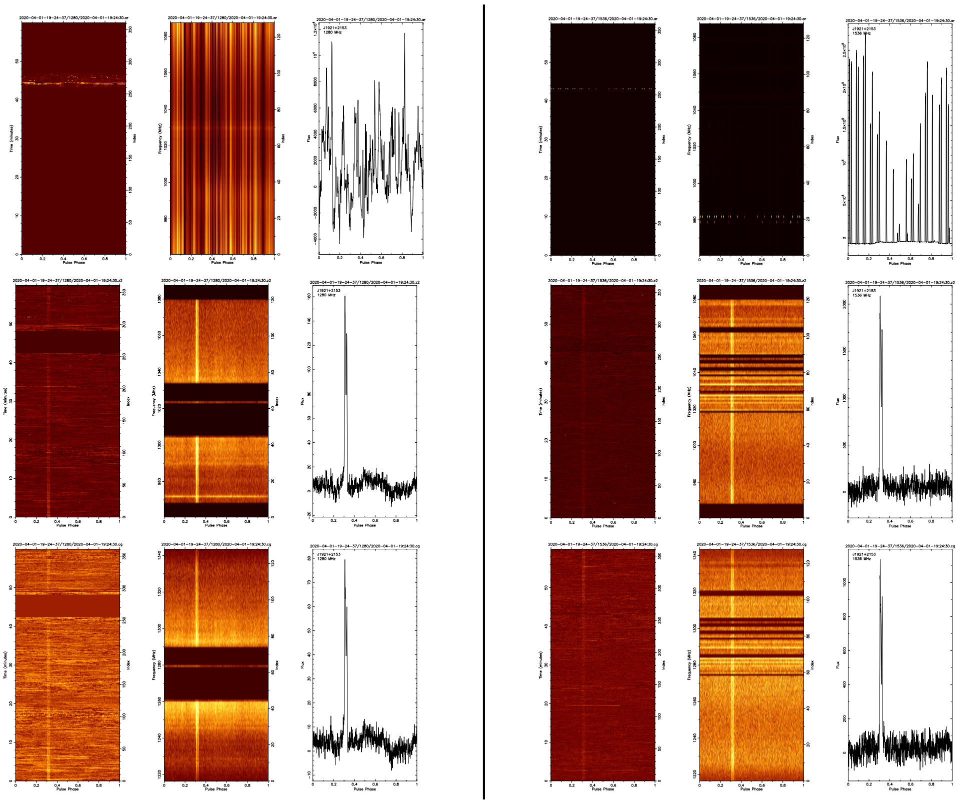

Figure C.9: Comparison between *tfzap* zapping and *MEERGUARD* RFI-mitigation routines for **folded** data of PSR J1921+2153 at 1280 MHz (left column) and 1536 MHz (right column). For each column, top panel: folded data **before** RFI mitigation, middle panel: results of *tfzap* mitigation, and bottom panel: *MEERGUARD* excision.

C.3 Scintillation of PSR J1921+2153

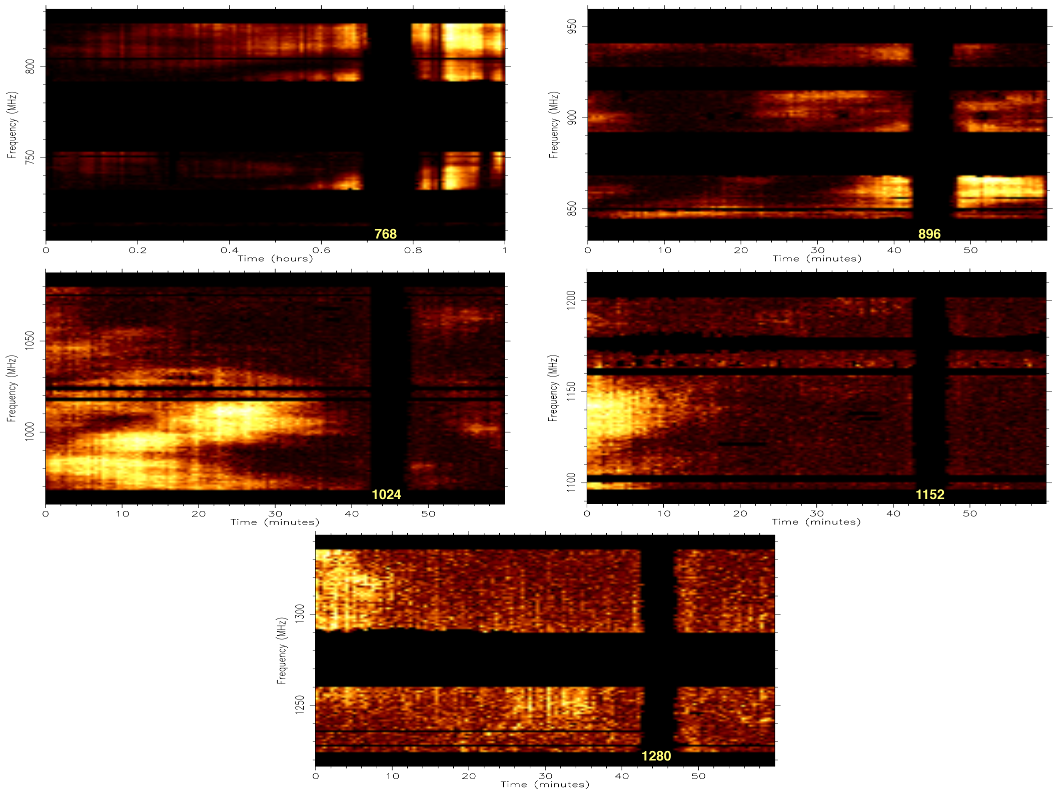

Figure C.10: Scintillation of PSR J1921+2153 at low frequency during an hour-long observation on 1 April 2020. Each panel shows time (x-axis) vs frequency (y-axis) plots of dynamic signal-to-noise spectrum for RFI-cleaned data. The yellow digits placed around 45minutes indicate the central frequency of each sub-band.

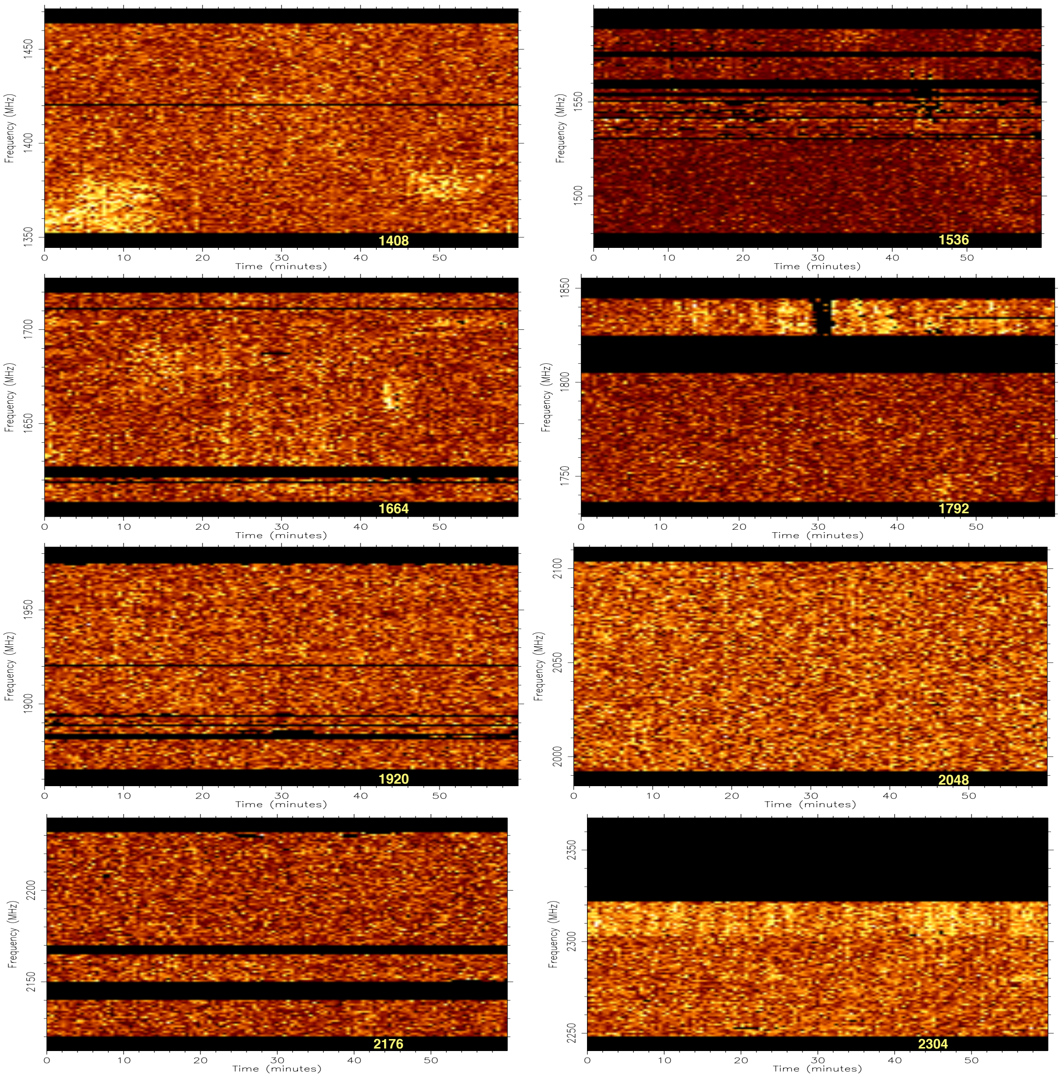

Figure C.11: Scintillation of PSR J1921+2153 at mid frequency during an hour-long observation on 1 April 2020. Each panel shows time (x-axis) vs frequency (y-axis) plots of dynamic signal-to-noise spectrum for RFI-cleaned data. The yellow digits placed around 45minutes indicate the central frequency of each sub-band.